

**NANO- AND MICRO-PARTICLES FOR BREAST CANCER
DETECTION AND TREATMENT**

JOHN DAVID OBAYEMI

ID. NUMBER: 70049

**A THESIS
PRESENTED TO THE FACULTY
OF AFRICAN UNIVERSITY OF SCIENCE AND TECHNOLOGY
IN CANDIDACY FOR THE DEGREE OF
DOCTOR OF PHILOSOPHY (PhD)**

**RECOMMENDED FOR ACCEPTANCE
BY THE DEPARTMENT OF
MATERIALS SCIENCE AND ENGINEERING**

ADVISER: PROFESSOR WINSTON O. SOBOYEJO

CO-ADVISER: DR. OLUSHOLA S. ODUSANYA



© MARCH 2015

© Copyright by John David Obayemi, 2015.

All rights reserved.

Preface

With much love,

this dissertation is dedicated to God Almighty who has seen me through the ups and
downs of life and to my family:

my parents, Mr David Obayemi and Mrs. Deborah Obayemi,

my brothers, Mr. Oluwatope David O., Mr. Daniel David O. and Mr. Solomon David O.,

My Sisters, Mrs. Taiwo Adzoge., Mrs. Ruth O. and Miss. Bukola David O.

my loving and caring wife, Mrs. Adenike Omole Obayemi

Abstract

This dissertation shows the use of material science and engineering approaches in developing solutions to problems in the life science with focus in nano and micro-particles for the detection and treatment of cancer. It presents the results of experimental and theoretical studies of magnetite, gold nanoparticles and injectable multi-functional biodegradable polymer-loaded microparticles. Biocompatible magnetite nanoparticles (BMNPs) were produced from Magnetospirillum magneticum (M.M.) bacteria that respond to magnetic fields. The BMNP concentrations were characterized with UV-visible (UV-Vis) spectroscopy, while the nanoparticle shapes, sizes and polydispersity were elucidated via transmission electron microscopy (TEM) and dynamic light scattering (DLS), respectively. The structure of the particles was also studied using X-ray diffraction (XRD). Carbodiimide reduction was also used to functionalize the BMNPs with a molecular recognition unit (Luteinizing Hormone Releasing Hormone, LHRH). The resulting nanoparticles were examined using Fourier Transform Infrared (FTIR) spectroscopy and quantitative image analysis. Furthermore, the adhesion between BMNPs and chemically synthesized magnetite nanoparticle (CMNPs) were demonstrated and their potentials for specific targeting of breast cancer cells were explored in the treatment of cancer. Also, in-depth examination of molecular recognition units that attach specifically to receptors on breast cancer cells and anti-cancer drug to test the assorted targeting methods of the gold nanoparticles via atomic force microscopy (AFM) techniques were explored. Further study of the effects of adhesion between gold nanoparticles and surfaces that is relevant to the potential applications in cancer detection and treatment were presented. Finally, in the case of polymer-loaded microparticles, a biosynthesized cancer drug prodigiosin and paclitaxelTM that was tested as a control were encapsulated using a single emulsion solvent evaporation technique (SESET). The dependence of the particle size and morphology, and the in-vitro release of the cancer drugs with respect to their morphology were studied using a combination of scanning electron microscopy (SEM), differential scanning calorimetry (DSC), UV-visible spectrophotometry (UV-Vis) and Atomic Force Microscopy (AFM). The implications of the results are discussed for the development of nanoparticles and injectable microparticles for specific targeting and localized drug delivery in the treatment of breast cancer.

Acknowledgments

All thanks to the omniscience, omnipresence and omnipotent God who is the reason why I am alive today. I remain very grateful to God for all His good works and favor over my life. My sincere special gratitude goes to a mentor, father and my indefatigable supervisor, Professor Wole Soboyejo. His patience, understanding, guidance and mentorship lead to the successful completion of this phase of my research. Words cannot truly express my joy and appreciation for knowing and being thought by a great personality like him. I strongly believe in all ramifications that the Almighty God will continue to protect, guide, increase and favor him and his lovely, loving, caring and wonderful family in Jesus Name.

My special thanks go to my co-advisor, Dr. Shola Odusanya. Where everyone had an advisor, I have a director, friend and uncle who was not only supervising and guiding me, but was always criticizing, encouraging and assisting me during the period of my research. I also wish to appreciate my mum and dad, Mr. David Obayemi and Mrs. Deborah Obayemi, through whose union, perseverance, parental love, encouragement and prayers, I am gradually getting to the ‘promise land’. A big thank you goes also to my brothers, Mr. Oluwatope David O., Mr. Daniel O., Mr. Solomon David O. and to my sisters Mrs. Taiwo Adeoye, Mrs. Ruth David and Miss Bukola David O.

To every successful man, there is a caring and encouraging woman. My special love and thanks to my wife “Sweetheart” Mrs. Adenike Omole Obayemi, for standing and believing in our future together all through my PhD program. My sincerest gratitude goes to my uncle, Dr. Gilbert

Olatunji Obajemu, his wife Mrs. Titilayo Obajemu and my in-laws (Arch. and Mrs. Omole) for the inestimable support and advice.

Special thanks go to Dr. Karen Malatesta, Dr. Nicolas Anuku, Dr. Yusuf Oni and Prof. Nan Yao of Princeton University for their useful scientific and technical assistance. Also, very big thanks to Prof. Eric Garfunkel, Dr. Johanna Bernstein, the Uhrich group (Prof. Kathryn E. Uhrich, Wei Yu (Connie), Yingyue Zhang (Joanna)) and Prof. Gene S. Hall of Rutgers University for their help and support in the usage of experimental facilities. I would also like to thank Prof. A. O. Adeyeye of the National University of Singapore (NUS) for the VSM measurements and useful technical discussions.

I would also like to express my gratitude to the World Bank STEP B program for financial support. My appreciation is also extended to the World Bank Africa Centers of Excellence Program, the African Capacity Building Foundation (ACBF), the Nelson Mandela Institution (NMI), the African University of Science and Technology (AUST) and the African Development Bank (AfDB) for financial their support. My sincere gratitude also goes to Princeton University, Princeton, USA and the Sheda Science and Technology Complex (SHESTCO), Biotechnology Advanced Laboratories, Abuja, Nigeria.

Table of Contents

Abstract	iv
Acknowledgments	v
Table of Contents	vii
List of Tables	xii
List of Figures	xiii
Chapter 1	1
1.0 Introduction	1
1.1 Background and Motivation	1
1.2 Research Objectives	5
1.3 Scope and Organization of Thesis	7
References	9
Chapter 2	14
2.0 Literature Review	14
2.1 Introduction	14
2.2 Magnetite and Gold Nanoparticles (AuNPs)	15
2.2.1 Nanoparticle Synthesis	17
2.2.1.1 Microemulsion Method	17
2.2.1.2 Sol-gel Method	18
2.2.1.3 Co-precipitation Method	19
2.2.1.4 Thermal Decomposition	19
2.2.1.5 Solvothermal Synthesis	20
2.2.1.6 Biological Synthesis	21
2.3 Magnetite and Gold Nanoparticles for Cancer Detection and Treatment	23
2.3.1 Magnetic Nanoparticles for Cancer Detection and Treatment	23

2.3.2	Gold Nanoparticles for Cancer Detection and Treatment	24
2.3.3	Passive and Active Targeting	25
2.3.4	Magnetic Resonance Imaging (MRI)	26
2.3.5	Hyperthermia	27
2.3.6	Plasmon Resonance	29
2.3.7	Adhesion Mechanism and Theory	29
2.4	Polymer Drug Microspheres	32
2.4.1	Drug Delivery	33
	References	36
	Chapter 3	62
3.0	Biosynthesis and the Conjugation of Magnetite Nanoparticles with Luteinizing Hormone Releasing Hormone (LHRH) for the Specific Targeting of Breast Cancer Cells	62
3.1	Introduction	62
3.2	Experimental Procedures	68
3.2.1	Sample Preparation:	68
3.2.2	Synthesis of Magnetite Nanoparticles	69
3.2.3	Structure of Nanoparticles	70
3.2.4	Ligand Conjugation	71
3.2.5	Characterization of Nanoparticle Sizes and Shapes	72
3.2.6	Vibrating Sample Magnetometry (VSM)	73
3.3	Results and Discussion	74
3.3.1	Nanoparticle Synthesis and Structure	74
3.3.2	Magnetic Properties	78
3.3.3	Characterization of Conjugated Magnetite Nanoparticles	79
3.3.4	Nanoparticle Formation	80

3.4 Implications	81
3.5 Summary and Concluding Remarks	83
References	85
Chapter 4	116
4.0 Magnetite Nanoparticles for Cancer Detection and Treatment: The Role of Adhesion	116
4.1 Background and Motivation	116
4.2 Adhesion Theory	120
4.3 Experimental Procedures	121
4.3.1 Materials	121
4.3.2 Adhesion and Characterization of Conjugated Nanoparticles to Breast Cancer Cells	121
4.4.1 AFM Tip and Substrate Characterization	125
4.4.2 Adhesion Measurements	125
4.5 Implications	127
4.6 Summary and Concluding Remarks	129
References	131
Chapter 5	144
5.0 Gold Nanoparticles for Cancer Detection and Treatment: The Role of Adhesion	144
5.1 Introduction	144
5.2 Theory	147
5.3. Materials and Methods	148
5.3.1 Materials	148
5.3.2 AFM Experiments	149
5.3.2.1 AFM Tip and Substrate Coating/Characterization	149
5.3.2.2 AFM Force-Displacement Measurements	150
5.4 Results and Discussion	151

5.4.1	AFM Tip and Substrate Characterization	151
5.4.2	Adhesion Forces	151
5.5	Implications	155
5.6	Conclusions	156
	References	158
Chapter 6		172
6.0	Injectable, Biodegradable Microparticles Loaded with Prodigiosin for Localized Anticancer Drug Delivery in the Treatment of Cancer	172
6.1	Background and Motivation	172
6.2	Materials	175
6.3	Experimental Methods	175
6.3.1	Synthesis and Purification of Prodigiosin (PG)	175
6.3.2	Preparation of Polymer-loaded Microspheres	177
6.3.3	Materials Characterization	179
6.3.4	Standard Curve and Drug Concentration	181
6.3.5	<i>In-vitro</i> Drug Release from Microparticles	182
6.4	Results and Discussion	183
6.4.1	Microsphere Morphology and Physicochemical Properties	183
6.4.2	Purity of Extracted Prodigiosin and Standard Calibration Curves	184
6.4.3	<i>In-vitro</i> Drug Release From Prodigiosin/Paclitaxel TM -Loaded PLGA Microspheres	186
6.5	Implications	189
6.6	Summary and Concluding Remarks	190
	References	192
Chapter 7		215

7.0	Concluding Remarks and Suggestions for Future Work	215
7.1	Summary and Concluding Remarks	215
7.2	Suggestions for Future Work	218
7.2.1	Biosynthesized Magnetite Nanoparticles for Early Cancer Detection and Treatment	218
7.2.2	AFM Adhesion Measurement for Cancer Detection and Treatment.	220
7.2.3	Drug Polymer for Localized Drug Delivery in the Treatment of Cancer	220

List of Tables

Table 3.1: Commercially available SPION/MNPs contrast enhancement and their specific indication place. (http://mr-tip.com/).	111
Table 3.2: List of some microorganisms that have been used to synthesize magnetite nanoparticles.	112
Table 3.3: The mean particle size at pH 6.5 at different reaction time for <i>Magnetospirillum magneticum</i> strain.	113
Table 3.4: The mean particle size at pH 7.0 at different reaction time for <i>Magnetospirillum magneticum</i> strain.	113
Table 3.5: The mean particle size at pH 7.5 at different reaction time for <i>Magnetospirillum magneticum</i> strain.	114
Table 3.6: The mean particle size at pH 9.5 at different reaction time for <i>Magnetospirillum magneticum</i> strain.	114
Table 3.7: Diameter of some selected BMNPs from TEM and DLS (Z-average) characterization synthesized at pH (a) 6.5 (b) 7.0 (c) 9.5 and (d) functionalized BMNPs-LHRH with their polydispersity index for sample concentration diluted with 0.05 and 0.1 mL PBS solution respectively.	115
Table 3.8: Peaks that revealed the absence of characteristic bands of $-NH_2$ present in the LHRH, unbound nanoparticles and bound particles.	115
Table 4.1: Spring constants of the bare/coated AFM tips.	143
Table 4.2: Adhesion forces between coated/uncoated AFM tips and breast cancer cells.	143
Table 5-I: Substrates and coated tips used in AFM study.	169
Table 5-II: Spring constants of the bare and coated tips.	169
Table 5-III: Comparison of adhesion interactions for LHRH with and without thiols.	169
Table 5-IV: Comparison of adhesion interactions for paclitaxel (taxol) with antibody, gold or LHRH.	170
Table 5-V: Comparison of adhesion interactions for Gold with and without thiols.	170
Table 5-VI: Comparison of adhesion interactions for LHRH with and without thiols.	170
Table 5-VII: Comparison of adhesion interactions of the nanocomposite components with thiols.	
Table 6.1: Formulations parameters and characteristics of investigated prodigiosin and paclitaxel –loaded PLGA microspheres	214

List of Figures

Figure 2.1: Inverse spinel structure of magnetite.....	58
Figure 2.2: Passive and active targeting of nanocarriers. Nanocarriers can reach tumors selectively through the leaky vasculature surrounding the tumors. Ligands grafted at the surface of nanocarriers bind to receptors (over)-expressed by cancer cells (green) or angiogenic endothelial cells (pink). Adapted from Ref [103]......	59
Figure 2.3: Schematic Setup of an AFM in (a) Contact Mode and (b) Tapping Mode (Adapted from Ref. [144])......	60
Figure 2.4: Schematic of Typical Deflection-Displacement Plot with Corresponding Stages of Force-Displacement Behavior (Adapted from Ref. [145])......	61
Figure 3.1: UV-Vis scan of magnetite nanoparticles. Arrow represents the existence of a peak at a wavelength, λ_{max} , of 450 nm.	96
Figure 3.2: Schematic of reaction pathway for the functionalization of magnetite nanoparticles.	97
Figure 3.3: Standard absorbance-concentration curve for biosynthesized magnetite nanoparticles.	98
Figure 3.4: Plots of nanoparticle concentration versus pH exposure for different durations to <i>Magnetospirillum magneticum</i> strain.	99
Figure 3.5: TEM micrographs of MNPs produced after exposure at a pH of 6.5 for (a) 24, (b) 48, (c) 72, (d) 96 and (e) 120 hours respectively. (f) Statistical analysis showing the mean particle size distribution after exposure to <i>Magnetospirillum magneticum</i> at a pH of 6.5 for different duration.	100
Figure 3.6: Some TEM micrographs for better illustration of MNPs shape produced after exposure at a pH of 7.0 for durations of (a) 24, (b) 48, (c) 72, (d) 96 and (e)/(f) 120 hours, respectively.	101
Figure 3.7: TEM micrographs of MNPs produced after exposure at a pH of 7.5 for (a) 24, (b) 48, (c) 72, (d) 96 and (e) 120 hours respectively. (f) Statistical analysis showing the mean particle size distribution after exposure to <i>Magnetospirillum magneticum</i> at a pH of 7.5 for different duration.	102
Figure 3.8: TEM micrographs of MNPs produced after exposure at a pH of 9.5 for (a) 24, (b) 48, (c) 72, (d) 96 and (e) 120 hours respectively. (f) Statistical analysis showing the mean particle	

size distribution after exposure to <i>Magnetospirillum magneticum</i> at a pH of 9.5 for different duration.	103
Figure 3.9 (a) Intensity particle size distributions of some selected BMNPs synthesized at pH (a) 6.5 (b) 7.0 (c) 9.5 and (d) functionalized BMNPs-LHRH particles for sample concentration diluted with 0.05 mL PBS solution.	104
Figure 3.9 (b) Intensity particle size distributions of some selected BMNPs synthesized at pH (a) 6.5 (b) 7.0 (c) 9.5 and (d) functionalized BMNPs-LHRH particles for sample concentration diluted with 0.1 mL PBS solution.	105
Figure 3.10: TEM micrographs of BMNPs produced at (a) pH of 6.5 for 48 hours (c) pH of 7.0 after 96 hours (e) pH of 9.5 after 72 hours, with (b), (d) and (f) as their respective ligand conjugated nanoparticles (BMNPs-LHRH).	106
Figure 3.11: EDS of biosynthesized MNPs produced by <i>Magnetospirillum magneticum</i> at a pH 7.0 after exposure for 96 hours.	107
Figure 3.12: X - ray diffraction pattern of the biosynthesized magnetite particles (BMNPs).	108
Figure 3.13: VSM results showing the hysteresis loops of the magnetic moments (emu/g) against the In-plane Field (Oe) for the (a) Biosynthesized magnetite nanoparticles obtained at pH 7.0 after 96 hours (b) Chemically synthesized magnetite nanoparticles (one pot synthesis).	109
Figure 3.14: Fourier transformation infrared spectrum of LHRH, biosynthesized magnetite nanoparticles (BMNPs) synthesized at pH 7.0 after 96 hours and LHRH-BMNPs.	110
Figure 4.1: Ligand/receptor interactions. In the experimental setup, ligands on the dip-coated AFM tip interact with surface receptors on breast cancer cells (MDA-MB-231) seeded on a Petri dish.	137
Figure 4.2: Schematic of typical force–displacement plot with corresponding stages of force displacement behavior (Modified from Ref. 56). In one approach-retract cycle, the AFM tip approaches the surface of the sample (A), jumps to contact with the surface when significant van der Waals forces are felt (B), and undergoes elastic bending and is retracted (C, D). Due to adhesive interactions, the tip does not detach from the substrate until a force sufficient to pull the tip off of the surface is achieved (E). (Adapted from Ref [45])	138
Figure 4.3: Electron diffraction spectroscopy (EDS) spectrum of a bare AFM tip showing 98.9 wt % Si.	139
Figure 4.4: Sample SEM images of the AFM tips: (a) LHRH-coated AFM tip before adhesion measurement; (b) LHRH-coated AFM tip after adhesion measurement; (c) BSA-coated AFM tip before adhesion measurement; (d) BSA-coated AFM tip after adhesion measurement. Boxes	

show coating on apex tip and side edges. (e) Chemically synthesized magnetite nanoparticles-LHRH coated AFM tip before adhesion measurement; (f) Chemically synthesized magnetite nanoparticles-LHRH coated AFM tip after adhesion measurement; (g) Biosynthesized magnetite nanoparticles-LHRH coated AFM tip before adhesion measurement; (h) Biosynthesized magnetite nanoparticles-LHRH coated AFM tip after adhesion measurement. 140

Figure 4.5: EDS Spectrum of LHRH conjugated magnetite nanoparticles coated on AFM tip showing 28.5 wt% Si, 53.1 wt% C, 10.5 wt% O and 7.9 wt% Fe. 141

Figure 4.6: Summary of pull-off force measurements for different configuration with breast cancer (MDA-MB-231) cells. 142

Figure 5.1: Possible schematics of a nanoparticle-based drug delivery/detection system. 162

Figure 5.2: Schematic of an atomic force microscope force-displacement behavior: (a) Load-displacement plot, (b) Tip/Surface Interaction. In one cycle, tip approaches the surface of the substrate (A), jumps to contact with substrate as significant van der Waals forces are felt (B), undergoes elasticity as it is displaced further in the same direction (C), displacements are reversed upon retraction as loads reduce to zero (D), tip does not detach at zero load due to the effects of adhesion until sufficient force is applied to pull the tip off the surface (E)..... 163

Figure 5.3: Sample SEM Images of the AFM tips: (a) Bare AFM tip; (b) Gold nanoparticles-coated AFM tip before adhesion measurement; (c) Gold nanoparticles-coated AFM tip after adhesion measurement; (d) LHRH-coated AFM tip before adhesion measurement; (e) LHRH-coated AFM tip after adhesion measurement; (f) BSA-coated AFM tip before adhesion measurement; (g) BSA-coated AFM tip after adhesion measurement. Boxes show coating on apex tip and side edges. 164

Figure 5.4: Typical AFM force-displacement behavior for coated tips on substrates..... 165

Figure 5.5: Adhesion interactions of components in a drug delivery system. 166

Figure 5.6: Comparison of adhesion interactions for gold with and without thiols. 166

Figure 5.7: Comparison of adhesion interactions for LHRH with and without thiols..... 167

Figure 5.8: Comparison of adhesion interactions for paclitaxel (taxol) with and without thiols. 167

Figure 5.9: Comparison of adhesion interactions of the nanocomposite components with thiols. 168

Figure 6.1: Structural formula of (a) prodigiosin (PG) (IUPAC/Chemical Name: 4-methoxy-5-[(Z)-(5-methyl-4-pentyl-2H-pyrrol-2-ylidene)methyl]-1H,1'H-2,2'-bipyrrole) (b) paclitaxel TM (PT).	200
Figure 6.2: UV scans of (a) prodigiosin and (b) paclitaxel TM . Arrow represents the existence of respective peaks at wavelength corresponding to λ_{max}	201
Figure 6.3: Concentration-Absorbance standard curves of (a) prodigiosin and (b) paclitaxel TM	202
Figure 6.4: SEM micrographs and mean particle size distributions of PLGA prodigiosin-loaded microspheres for homogenizer speed of 18000 rpm ((a) & (c)) and 22000 rpm ((b) & (d)) with a uniform PVA concentration of 0.5 %, respectively.	203
Figure 6.5: SEM micrographs and mean particle size distributions of paclitaxel TM -loaded PLGA microspheres for homogenizer speed of 18000 rpm ((a) & (c)) and 22000 rpm ((a) & (d)) with a uniform PVA concentration of 0.5 %, respectively.	204
Figure 6.6: SEM micrographs and mean particle size distributions of prodigiosin-loaded PLGA microspheres for 0.5% PVA ((a) & (c)) and 3% PVA ((c) & (d)) with a uniform homogenizer speed of 18000 rpm, respectively.	205
Figure 6.7: SEM micrographs and mean particle size distributions of paclitaxel TM -loaded PLGA microspheres using 0.5% PVA ((a) & (c)) and 3% PVA ((b) & (d)) with a uniform homogenizer speed of 18000 rpm, respectively.	206
Figure 6.8: DSC results of (a) Plain (non-loaded) PLGA microspheres (b) PG-loaded PLGA and (c) PT-loaded PLGA microspheres.	207
Figure 6.9: HPLC Analysis of Sample Purity: (a) Standard Prodigiosin and (b) Tested Sample (Prodigiosin), respectively at 535 nm.	208
Figure 6.10: In-vitro release profiles of different formulations based on homogenization speed of 18000 and 22000 rpm for drug formulation 1 to 4 for 8 days, respectively.	209
Figure 6.11: Optical micrographs of prodigiosin (PG) and paclitaxel (PT) drug-loaded microspheres after day 1 (24 hours) to day 8 (192 hours) stages of drug release respectively. .	212
Figure 6.12: AFM images of a section of paclitaxel-loaded PLGA microsphere (a & c) and prodigiosin-loaded PLGA microsphere (b & d) after 1 day (24 hours) and after 7 days (168 hours) of drug release.	213

Chapter 1

1.0 Introduction

1.1 Background and Motivation

Cancer is a major public health problem and was once considered an incurable disease, but today most patients diagnosed with early stage cancer will survive their illness. Cancer is currently the second leading cause of death after cardiovascular diseases [1,2], while breast cancer is the second most common cause of cancer death in women [2]. Current trends also suggest that cancer will become the leading cause of death by 2030 [1,2]. Cancer is projected to result in more deaths than deaths from AIDS, tuberculosis and malaria combined [3]. Even if the current trends in cancer should remain unchanged, the statistics suggest that two thirds of the entire global incidence of cancer should occur in low and middle income countries [4].

In most cases, the major challenge is detection of cancer before metastasis [5,6] as well as the side effects associated with the treatment methods available [7]. In the absence of a cure, the real clinical challenge is early detection. However, the early detection of breast cancer is limited by the spatial resolution of the methods that are currently used to diagnose cancer. The current detection techniques in breast cancer (mammograms, ultrasound, magnetic resonance imaging (MRI) and different types of scan) are not yet considered effective for early stages in cancer diagnosis [8]. These types of diagnosis are often made too late to effectively administer the current treatments [9].

In the case of cancer treatment, most patients who undergo the bulk systemic cancer treatment

(chemotherapy, surgery, radiation therapy, hormonal therapy etc.), often experience significant short and long term side effects [10]. Such treatment is also expensive and beyond the reach of most people in developing countries [7]. Furthermore, chemotherapy affects normal cells, while reducing the therapeutic index of the drugs [11]. Many of the existing cancer drugs also lack selectivity and specificity. Hence, incremental improvements in breast cancer therapy are unlikely to address the challenges associated with the cost and side effects of breast cancer treatment. However, in recent years, there has been increasing interest in the development of magnetic nanoparticles for the detection and treatment of cancer [12-14]. These include: MRI enrichment/contrast agents [13,14] and nanoclusters for the localized delivery of cancer drugs [11]. Microspheres are usually defined as small spherical particles, with diameters in the micrometer scale (1 μm - 1000 μm (1 mm)). The term microspheres are sometimes referred to as microparticles. Microparticles in a polymeric drug-loaded microparticles form have been used effectively in the treatment of prostate cancer [15], atherosclerosis [16] and breast cancer [17], by localized drug delivery. This is due to their uniqueness in the delivery of drugs within the therapeutic window [18,19,].

Nanotechnology and nanoscience have been employed as one of the most exciting fields and subjects that have provided a solution to the challenges associated with current methods of cancer diagnosis and treatment. Nanotechnology is the design, characterization, production and application of structures, devices and systems by controlling shape and size at nanometer scale. Nanoscience is the study of phenomena and manipulation of materials at atomic, molecular and macromolecular scales [20]. Nanoparticles are engineered particulate materials or structures whose sizes ranges from 1 to 100 nanometers. The study of materials at a nanoscale has provided

solutions to some critical problems in the areas of energy generation [21,22], information storage [23], environmental remediation [24,25] and biological application [26] to mention but a few. In the recent years, there has been increasing interest in the development of nanoparticles for potential and emerging applications in medicine [27]. These include potential emerging applications in disease detection and treatment [28,29], biological labelling [30], biosensors [31] and drug delivery [32].

In the case of magnetite nanoparticles (MNPs) with clinical sizes (1 to 80 nm), there have been significant efforts to develop these nanoparticles for application in cancer detection via magnetic resonance imaging (MRI) [33] and treatment by hyperthermia [34]. In MRI, the current spatial resolution of detection is of the order of a few millimeters [35]. Their potential has also been explored for use as contrast enhancement agent during MRI of tumour tissue [36] and localized hyperthermia [34] during cancer treatment. Magnetic nanoparticles have been reported to have the ability of binding to drugs, proteins, enzymes, antibodies, or nucleotides. They can also be directed to an organ, tissue, cells or tumors using an external magnetic field or be heated by alternating magnetic fields for use in hyperthermia [36-38].

The success of any biomedical device depends on many factors including: material, size and location (internal/external). However, adhesion of MNPs and gold nanoparticles is an important concept that also plays a very important role in the success of a drug delivery device and the ability of a device to get to the specific site of interest without the architecture being altered. Furthermore, since nano-medicine requires the specific targeting of diseased cells, there is,

therefore a need to develop a basic understanding of the adhesion of nanoparticles to diseased cells (cancer cells) at a nanoscale.

The use of polymer-based microparticles as a colloidal drug-delivery system has certain advantages, such as augmented effectiveness and reduced toxicity of the incorporated agents to non-targeted cells and tissues. However, there are also disadvantages: microspheres are denatured within several weeks and are, therefore, relatively unstable. Thus, they are not easily mass-produced [39]. Microspheres are synthesized from characteristically free-flowing powders consisting of proteins/synthetic polymers that are biodegradable. Ideally, they have a particle size less than 200 μm . Biodegradable microspheres can be utilized to direct drugs to organ(s) by depositing them in the end organ vessels at a control rate and time. Microsphere formulations of paclitaxel are particularly well suited to the local treatment of diseases. They are injectable and the drug encapsulation tends to occur at a high efficiency with a release that is slow over a period of time [40-43].

To establish understanding in the development of nanoparticle and microparticle as well as their applications in cancer detection and treatment, a careful characterization of nanoparticles is very crucial. A couple of methods have been used to characterize nanoparticles and microparticles that are suited for biomedical applications. The common types of techniques used to characterize the shape and size of nanoparticles include; Atomic Force Microscopy (AFM) [44], Transmission Electron Microscopy (TEM) [45,46], Scanning Electron Microscopy (SEM) [47], Dynamic Light Scattering (DLS) [44,48] and ordinary Optical Microscopy (OM). The technique widely used to reveal the chemical composition and crystallographic structure of

nanoparticles/microparticles is X-ray Diffraction (XRD) [49,50]. Fourier Transform Infrared Spectroscopy (FTIR) [50] is used to study the composition of nanoparticles/microparticles, the chemical bonds between component and their surface modification coatings/constituent. The Vibrating Sample Magnetometer (VSM) is used to determine the magnetic properties of the nanoparticles.

However, the development, functionalization, characterization of nano- and micro-particles in the form of magnetite nanoparticles, gold nanoparticles and poly(lactic-*co*-glycolic acid) (PLGA) drug-loaded microparticles is very crucial and significant for the detection and treatment of cancer.

1.2 Research Objectives

The thesis presents a combination of experimental and theoretical studies that provide new insights for the development of nano-(magnetite and gold) and micro-(PLGA drug-loaded) particles that have great potential for the detection and treatment of cancer. The following are the objectives of the current work:

- To biosynthesize magnetite nanoparticles from *Magnetospirillum magneticum* with clinically relevant particle sizes between 10 and 60 nm.
- To understand the mechanism of the formation of magnetite nanoparticles intracellularly in *M. magneticum*.
- To give new insights into the effects of pH and processing time on the sizes and shapes of biosynthesized magnetite nanoparticles.
- To obtain monodispersed successfully conjugated biosynthesized magnetite nanoparticles to LHRH ligands that have potential biomedical relevance.

- To explore the effects of adhesion between magnetite nanoparticles and surfaces that is relevant to the potential applications in cancer detection and treatment.
- To study the adhesion forces obtained for dip-coated magnetite nanoparticles that interact with peptide or antibody-based molecular recognition units (MRUs) that attach specifically to breast cancer cells.
- To explore the effects of adhesion between magnetite/gold nanoparticles and surfaces that are relevant to the potential applications in cancer detection and treatment.
- To study the adhesion forces obtained for simple dip-coated magnetite/gold nanoparticles that interact with peptide or antibody-based molecular recognition units (MRUs) that attach specifically to breast cancer cells.
- To measure the adhesion between magnetite/gold nanoparticles and the constituents of cancer drug/MRU's that are required to deliver nanoparticle/drug into the body for the specific detection and localized treatment of cancer.
- To biosynthesize, purify, characterized and quantify prodigiosin from *Serratia marcescens subsp. marcescens*.
- To develop multi-functionalized polymeric drugs for effective localization at preselected target(s) in therapeutic concentrations.
- To develop cost effective injectable polymeric drug microspheres for localized breast cancer treatment.
- To study the initial cancer drug release from the polymeric microspheres with implications for localized breast cancer treatment.
- To prepare and characterize porous prodigiosin-loaded injectable microspheres.

1.3 Scope and Organization of Thesis

The scope and the organization of this thesis begin with Chapter 1 which includes the background and motivation as well as the scope and organization of the work. This is followed by a review of relevant literature in the development and application of magnetite nanoparticles, gold nanoparticles and PLGA drug-loaded microparticles for cancer detection and localized drug delivery in treatment of cancer as Chapter 2. Chapter 3 presents biosynthesis and the conjugation of magnetite nanoparticles with luteinizing hormone releasing hormone (LHRH) for the specific targeting of breast cancer cells. This chapter highlights the results of an experimental study of the biosynthesis of magnetite nanoparticles (BMNPs) with clinically relevant particle sizes between 10 nm and 60 nm for the specific targeting and treatment of breast cancer.

Chapter 4 proceeds to show the experimental results of an atomic force microscopy (AFM) study of the adhesion between dip-coated magnetite nanoparticles (biosynthesized and chemically conjugated magnetite nanoparticles) that interact with breast cancer cells. Chapter 5 further presents consolidated results of an experimental study of the effects of adhesion between gold nanoparticles and surfaces that are relevant to the potential applications in cancer detection and treatment. Here, adhesion forces are obtained for dip-coated gold nanoparticles that interact with drug, peptide or antibody-based molecular recognition units (MRUs) that attach specifically to breast cancer cells were also explored. The implications of the results are then discussed for the design of robust gold nanoparticle clusters and for potential applications in localized drug delivery and hyperthermia.

In Chapter 6, the results of an experimental study of the synthesis and physicochemical characterization of injectable multi-functional biodegradable polymer-loaded microparticles with sizes $\sim 1 - 60 \mu\text{m}$ were elucidated. These were loaded with a biosynthesized cancer drug prodigiosin (PG) (that was obtained from bacteria, *Serratia marcescens subsp. marcescens*) for localized cancer drug delivery for the treatment of cancer. In Chapter 7, a salient summary and concluding remarks arising from the study is presented along with suggestions for future work.

References

- [1] B. Peter and L. Bernard. “The World Cancer Report” World Health Organization. 2008.
- [2] D. Cutierrez. “Cancer Facts and Figures. 2nd Edition. America Cancer Society, 2008.
- [3] D. C. Mathers and D. Loncar. Updated Projections of Global Mortality and Burden of Disease, 2002-2030; Data Sources, Methods and Results. World Health Organization. (2005) 6.
- [4] J. Ferlay, H. R. Shin, F. Bray, D. Forman, C. D. Mathers and D. Parkin. GLOBOCAN 2008, Cancer Incidence and Mortality Worldwide: IARC Cancer-Base No.10 [Internet]. Lyon, France: International Agency for Research on Cancer. 2010; Available from: <http://globocan.iarc.fr>.
- [5] L. A Nagahara, Ferrari M, Grodzinski P. MRS Bulletin 2009;34:406-14.
- [6] P. Grodzinski, Silver M, Molnar LK. Expert Rev Mol Diagn 2006;6:307-18.
- [7] David Needhama, Mark W. Dewhirst. The development and testing of a new temperature-sensitive drug delivery system for the treatment of solid tumors. Advanced Drug Delivery Reviews. Elsevier, 2001; 53, 285–305.
- [8] B. Hildebrandt, W.P. Ceelen and P. Wust in: (Ed), “Peritoneal Carcinomatosis: A Multidisciplinary Approach”, Springer, New York, (2007) 185.
- [9] Stewart BW, Kleihues. Le Cancer Dans le Monde, ed. C.I.d.R.s.I.C. (CIRC).
- [10] Irvine D, Vincent L, Graydon JE, Bubela N and Thompson L. Cancer Nursing 1994;17(5):367-78.
- [11] Ms Rajput et al: Microspheres in cancer therapy, Indian journal, 2010.
- [12] J. W. M. Bulte, M. Cuyper, D. Despres and J. A. Frank, Journal of Magnetism and Magnetic Materials 194 (1999) 204.

- [13] H. Pardoe, P. R Clark, T. G St Pierre, P. Moroz, S. K Jones. *Magnetic Resonance Imaging*. (2003) 21:483–488.
- [14] F. J. Lazaro, A. R. Abadia, M. S. Romero, L. Gutierrez, J. Lazaro and M. P. Morales. *Biochim Biophys Acta*. (2005) 1740:434–45.
- [15] Jackson, J.K., Gleave, M.E., Yago, V., Beraldi, E., Hunter, W.L., Burt, H.M., 2000b. The suppression of human prostate tumor growth in mice by the intratumoral injection of a slow release polymeric paste formulation of paclitaxel. *Cancer Res*. 60, 4146–4151.
- [16] David Martin. M and Boyle F. J: Drug eluting stents for coronary artery disease (review), *Med Eng Phys*, 2010.
- [17] Huizing, M.T., Misser, V.H.S., Pieters, R.C., Huinink, W.W.T., Vencor, C.H.N., Vermorken, J.B., Pinedo, H.M., Beijnen, J.H., 1995. Taxanes—a new class of anticancer agents. *Cancer Invest*. 4, 381–404.
- [18] Brannon-Peppas, L.; *Polymers in controlled drug delivery*. *Medical Plastics and Biomaterials Magazine*, 1997, (accessed November, 2013) (<http://www.devicelink.com/mpb/archive/97/11/003.html>).
- [19] Nair, L. S.; Laurencin, C. T.; *Biodegradable polymer as biomaterials*. *Progress in Polymer Science*, 2007, 32 (8-9), 762-798.
- [20] "Nanoscience and nanotechnologies: opportunities and uncertainties", The Royal Society and Royal Academy of Engineering, (2004)
- [21] Zach, M., Hagglund, C., Chakarov, D. & Kasemo, B. (2006). Nanoscience and nanotechnology for advanced energy systems. *Current Opinion in Solid State and Materials Science*, 10, 132-143.
- [22] Serrano, E., Rus, G. & Garcia-Martinez, J. (2009). Nanotechnology for sustainable energy

- [23] Sandhu,A. (2008). Data storage: One-track memory. *Nature Nanotechnology*.
doi:10.1038/nnano.2008.120.
- [24] D. W. Elliott, W.-X. Zhang, *Environ. Sci. Technol.* 2001, 35, 4922.
- [25] M. Takafuji, S. Ide, H. Ihara, Z. Xu, *Chem. Mater.* 2004, 16,1977.
- [26] Caruthers,S.D., Wickline,S.A. & Lanza,G.M. (2007). Nanotechnological applications in medicine. *Current Opinion in Biotechnology*,18, 26-30.
- [27] Q A Pankhurst¹, J Connolly² et al. Applications of magnetic nanoparticles in biomedicine. *Journal of physics d: applied physics*. June 2003, *J. Phys. D: Appl. Phys.* 36-R167–R181.
- [28] B. Fadeel, A. E.G. Bennett. Better safe than sorry: Understanding the toxicological properties of inorganic nanoparticles manufactured for biomedical applications. *Advanced Drug Delivery Reviews*. 2010, 62, 362–374.
- [29] Matsunaga, T.,Okamura,Y., Tanaka, T. *J. Mater. Chem.* 2004, 14, 2099.
- [30] Qiu H, Rieger B, Gilbert Ret al. PLA-coated gold nanoparticles for the labeling of PLA biocarriers. 2004, *Chem Mater* 16:850–856.
- [31] Gomez-Romero P. Hybrid organic-inorganic materials—in search of synergic activity. *Adv Mater* . 2001, 13:163– 174.
- [32] Lazaro FJ, Abadia AR, Romero MS, Gutierrez L, Lazaro J, Morales MP *Biochim Biophys Acta*. 2005, 1740:434–45.
- [33] T.K. Indira, P.K. Lakshmi. Magnetic Nanoparticles – A Review, *International Journal of Pharmaceutical Sciences and Nanotechnology*. 2010, Volume 3, Issue 3.

- [34] M. Shinkai, M. Yanase, M. Suzuki, et al. Intracellular hyperthermia for cancer using magnetite cationic liposomes. *Journal of Magnetism and Magnetic Materials*. 1999, 194, 176184.
- [35] D.G. Gadien, *NMR and its Applications to Living Systems*, Oxford University Press, New York, 2000.
- [36] Pardoe H, Clark PR, St Pierre TG, Moroz P, Jones SK, *Magnetic Resonance Imaging*. 2003 21:483–488.
- [37] J. Meng, E. Paetzell, A. Bogorad, W.O. Soboyejo, Adhesion between peptides/antibodies and breast cancer cells, *J. Appl. Phys.* 107 (2010) 114301.
- [38] C.C. Berry, A.S.G. Curtis, Functionalisation of magnetic nanoparticles for applications in biomedicine, *J. Phys. D. Appl. Phys.* 36 (2003) R198–R206.
- [39] Suzuki K. Activated CD4+ T cells preferentially take up lipid microspheres, but resting cells do not. *Clin Exp Immunol* 1994;99:479-485.
- [40] Liggins, R.T., D'Amours, S., Demetrick, J.S., Machan, L.S., Burt, H.M., 2000. Paclitaxel loaded poly(l-lactic acid) microspheres for the prevention of intraperitoneal carcinomatosis after a surgical repair and tumor cell spill. *Biomaterials* 21, 1959–1969.
- [41] Liggins, R.T., Burt, H.M., 2001. Paclitaxel loaded poly(l-lactic acid) microspheres: properties of microspheres made with low molecular weight polymers. *Int. J. Pharm.* 222, 19–33.
- [42] Gupte, A., Ciftci, K., 2004. Formulation and characterization of Paclitaxel, 5-FU and Paclitaxel + 5-FU microspheres. *Int. J. Pharm.* 276, 93–106.

- [43] Dordunoo, S.K., Jackson, J.K., Arsenault, L.A., Oktaba, A.M.C., Hunter, W.C., Burt, H.M., 1995. Taxol encapsulation in poly(caprolactone) microspheres. *Cancer Chemo. Pharmacol.* 36, 279–282.
- [44] C. M. Hoo, N. Starostin, P. West, M. L. Mecartney. "A comparison of atomic force microscopy (AFM) and dynamic light scattering (DLS) methods to characterize nanoparticle size distributions", *Journal of Nanoparticle Research*, 10:89-96, (2008).
- [45] S. Santra, R. Tapeç, N. Theodoropoulou, J. Dobson, A. Hebard, W. Tan. "Synthesis and Characterization of Silica-Coated Iron Oxide Nanoparticles in Microemulsion: The Effect of Nonionic Surfactants", *Langmuir*, 17 (10):2900–2906, (2001).
- [46] M. Ma, Y. Zhang, W. Yu, H. Shen, H. Zhang, N. Gu. "Preparation and characterization of magnetite nanoparticles coated by amino silane", *Colloid Surface Physicochem Eng Aspect*, 212:219-226, (2003).
- [47] J. Zhang, M. Oyama. "Gold nanoparticle arrays directly grown on nanostructured indium tin oxide electrodes: Characterization and electroanalytical application", *Analytica Chimica Acta*, 540(2):299-306, (2005).
- [48] Y. Hu, X. Jiang, Y. Ding, H. Ge, Y. Yuan, C. Yang. "Synthesis and characterization of chitosan–poly(acrylic acid) nanoparticles", *Biomaterials*, 23(15):3193-3201, (2002).
- [49] S. Santra, R. Tapeç, N. Theodoropoulou, J. Dobson, A. Hebard, W. Tan. "Synthesis and Characterization of Silica-Coated Iron Oxide Nanoparticles in Microemulsion: The Effect of Nonionic Surfactants", *Langmuir*, 17 (10):2900–2906, (2001).
- [50] M. Ma, Y. Zhang, W. Yu, H. Shen, H. Zhang, N. Gu. "Preparation and characterization of magnetite nanoparticles coated by amino silane", *Colloid Surface Physicochem Eng Aspect*, 212:219-226 , (2003).

Chapter 2

2.0 Literature Review

2.1 Introduction

Nanoparticles and drug-loaded polymer microspheres for disease (cancer) targeting and treatment have enormous potential to enhance the approaches that are used today. The National Nanotechnology Initiative (NNI) described nanotechnology as the study of all particles about 100 nanometers or less [1]. A nanometer is one billionth of a meter in size. The development of functionalized magnetite nanoparticles, a part of which this research addresses, has been the focal point of research lately [2-4].

Magnetite nanoparticles (MNPs) are engineered biomaterials particulate materials of size between 1 to 100 nm whose magnetic property can be manipulated under the influence of an external magnetic field to perform specific functions in biomedical applications [5-8]. Gold nanoparticles are chemically stable biocompatible particles whose sizes are between 1 and 100 nm with strong absorption in visible and near-infrared light regions (450–600 nm) that have the ability to scatter light and produce heat due to plasmon resonance. These properties make gold nanoparticles relevant in non-biomedical and biomedical applications.

In drug delivery, our previous work [9] explored the potential of an implantable anti-cancer treatment device that can locally deliver drugs and heat to the site of a tumor. Such a device can be used, following surgery to remove any remaining cancer tissue, by treatment with localized chemotherapy and hyperthermia. The above approach requires surgery for the insertion of the

device into the body. The current work in localized drug delivery explores the development prodigiosin-loaded microspheres in an effort to reduce the potential side effects of bulk systemic cancer treatment. In general, this chapter presents an overview of prior work on magnetic (magnetite) nanoparticles, adhesion of both magnetite and gold nanoparticles to surfaces that are relevant for the treatment of cancer. It also explores drug-loaded polymer microparticles, with a focus on specific targeting and localized drug delivery in the detection and treatment of breast cancer.

2.2 Magnetite and Gold Nanoparticles (AuNPs)

Magnetite, Fe_3O_4 , is a common magnetic iron oxide that has a cubic inverse spinel structure with oxygen forming an FCC closed packing and iron cations occupying interstitial tetrahedral sites and octahedral sites [10]. The electrons in the structure have the ability to hop between Fe^{2+} and Fe^{3+} ions in the octahedral sites at room temperature (See Figure 2.1). This makes magnetite an important class of half-metallic materials [11]. Magnetite nanoparticles (MNPs) are described as engineered particulate materials of size between 1 to 100 nm that can be manipulated under the influence of an external magnetic field to perform specific function for biomedical applications and diagnostics [12-15]. MNPs that range between size of 1 and 30 nm, have a single magnetic domain and do not retain any magnetism after removal of a magnetic field are referred to as superparamagnetic iron oxide nanoparticles (SPIONs). In other words, superparamagnetic materials are ferro- or ferri-magnetic materials of sizes on the order of tens of nanometers that become a single magnetic domain and maintain one large magnetic moment [16].

Gold nanoparticles are unique type of nanoparticles that have been used by many due to their shining color when interacted with visible light. Their optical and electronic properties have made them very relevant for both biomedical and non-biomedical applications. The interaction of gold nanoparticles with light is strongly influenced by their size, environment and morphology. Plasmon resonance is a phenomenon exhibited by gold nanoparticles as a result of the interaction of free electron and oscillating electric fields with a ray of light propagating causing a concerted oscillation of electron charge that resonate with the frequency of visible light [17-20].

Reflectance confocal microscopy [21] and optical coherence tomography [22,23], are microscopy techniques that image reflected light and provide detailed, three-dimensional images of tissue, without the need for physical sectioning. These techniques provide spatial resolutions of $\sim 1\text{-}10\ \mu\text{m}$ and a penetration depth, ranging from $\sim 300\ \mu\text{m}$ to $1\text{-}2\ \text{mm}$ [24]. Gold nanoparticles (AuNPs) are particularly attractive in cancer treatment because of their strong absorption of light in the visible and near infra-red (NIR) electromagnetic regions [25,26]. They are also biocompatible. The peak absorbance wavelength is in the visible range ($450\text{--}600\ \text{nm}$), NIR light is transmitted through normal tissue components with minimal absorption [25]. This optical absorption is strongly dependent on the shape and size of the gold nanoparticle [27]. In the next sections various methods of formation of magnetite and gold nanoparticles are highlighted.

2.2.1 Nanoparticle Synthesis

This section focuses on the synthesis of magnetite and gold nanoparticles with more emphasis on MNPs. In the case of magnetite nanoparticles, several methods are employed for the synthesis. These techniques include physical, chemical, biological and hybrid methods [28-31]. Physical methods of synthesis deal with generation of magnetic nanoparticles in the gas or solid phase using high-energy treatments including condensation methods and methods of nanodispersion of a compact material. In contrast, the chemical synthesis of nanoparticles involves reactions that are carried out in solutions at moderate temperature. Biological methods of synthesis involve the use plants and microorganisms in the synthesis of magnetic nanoparticles, while hybrid methods involve various combinations of any of the above methods. A review of some the conventional physical, chemical and biological syntheses are presented in this work.

2.2.1.1 Microemulsion Method

The method involves the use of thermodynamically stable isotropic liquid mixture of water or aqueous phases, (oil with surfactant and co-surfactant) in the formation of nanoparticles. In this method, surfactants tend to form reverse micelles, while the co-surfactants reduce the electrostatic repulsion force between the surfactant molecules. The particles size and morphology can be controlled under certain conditions in this method [32-35].

The microemulsion method can be direct, reverse or bi-continuous, depending on what solution is dispersed in the other. The most frequently used method for the synthesis of magnetic nanoparticles is the reverse microemulsion method also referred to as reverse micelle solution. In this method, water is dispersed in oil (w/o). The production of magnetic and nanosized particles

through this route has been proved to be adequate, versatile and simple [32-37].

Tartej *et al.* [35,36] in a related work have also observed that fine droplets at the micro level of the aqueous phase are trapped within the area in which surfactant molecules are dispersed in a continuous oil phase. They showed that the surfactant-stabilized microcavities tend to enhance a confinement effect that limits particle nucleation, growth and agglomeration. This was demonstrated by using a micellar solution (a ferrous sulfate, $\text{Fe}(\text{DS})_2$), producing nanosized magnetic particles whose sizes were controlled partially by the surfactant concentration and temperature [38]. The microemulsion method is therefore easy to scale up for large scale production using relatively inexpensive and simple equipment.

2.2.1.2 Sol-gel Method

This is a wet-chemical technique popularly used in the field of materials science and engineering. It is usually applicable in most technologies like ceramics technology, reactive material and separation, chromatography, nanotechnology [39], and is often used in the synthesis of magnetic nanoparticles (MNPs), heteroelement and some fused bimetallic particles [40]. Conventionally, sol-gel processing refers to the hydrolysis and condensation of metal alkoxide. The synthesis of magnetic nanoparticles starts from a colloidal reaction which serves as the precursor for an integrated network of either discrete particles or network polymers [41]. Klein *et al.* [42] revealed that the sol-gel method is a cheap and low temperature technique that controls the product's chemical composition. It can be used for the synthesis of nanoparticles for applications in biosensors, medicine, electronics, optics, electronics, and photovoltaics [42].

2.2.1.3 Co-precipitation Method

The co-precipitation method is one of the most widely used in the synthesis of magnetic nanoparticles. This is a water-based method, where metal oxide precipitation and a polymerization reaction are carried out at the same time. In this method, the developing particles are trapped inside tiny polymer beads. The synthesis process is divided into two parts. Firstly, ferrous metal hydroxide suspensions are partially oxidized with different oxidizing agents [43]. Secondly, stoichiometric mixtures of ferric and ferrous hydroxide are aged in aqueous media, yielding spherical magnetite particles with homogenous sizes [44]. The chemical equation for the second process is given by [45];



The sizes and shapes of the nanoparticles can be controlled by changing the pH, ionic strength, temperature and other pre-existing conditions [46]. However, the crystallinity and size uniformity of the magnetic nanoparticles are poor, and there seems to be a problem of aggregation produced by this method [46].

2.2.1.4 Thermal Decomposition

This method could also be referred to as *thermolysis*, which often involves a chemical decomposition that is caused by heat (endothermic reaction). The heat is used to break down the chemical bond in the compound. However, in cases in which the decomposition reaction is exothermic, a positive feedback loop is created [47]. This may lead to a thermal runaway and an explosion. The decomposition of iron precursors to obtain magnetic nanoparticles in the presence of hot organic surfactants results in samples with good size control, narrow size distribution (5-12 nm) and good crystallinity. The nanoparticles are also easily dispersed with a resulting

product that has good potential applications in nanomedicine e.g, in cell separation and magnetic resonance imaging [47].

Sun *et al.* [48] worked earlier on thermal decomposition of magnetic nanoparticles. Hence, the resulting method is often referred to as the Sun method. Their method [48] involves the high temperature ($> 220^{\circ}\text{C}$) decomposition of an organic iron precursor in the presence of oleic acid that decomposes to form organic ligands [48]. In this case, the nanoparticles produced avoid aggregation when the hydrophobic ligands form a dense coating around the nanoparticles. However, the nanoparticles that are synthesized are soluble only in nonpolar solvents due to the coatings involved. To solve this problem, hydrophilic polymer coatings have been proposed [49].

There are two popular adopted approaches in the production of magnetic nanoparticles by thermal decomposition [49]. In the first method, the thermal decomposition of metal carbonyl precursors is followed by an oxidation step in air [49] or oxidation by an oxidant at elevated temperatures [50]. The second method involves decomposition of precursors with a cationic metal center in the absence of reducing agents [51]. Another special case of thermolysis is called pyrolysis. It involves the simultaneous change of chemical composition and physical phase which is an irreversible process. It also involves thermochemical decomposition of organic materials at elevated temperatures, without the participation of oxygen.

2.2.1.5 Solvothermal Synthesis

This method involves the synthesis of nanoparticles from chemical reactions that occur under high temperature and pressure. The temperature is typically above the boiling point of the

solvent. Due to the high pressure involved, the reactions in most cases are carried out in an autoclave. Wang *et al.* [52,53], established this process as one of the reliable ways to grow crystals of many materials, one of which is magnetic nanoparticles. The resulting crystalline materials are dislocation free single crystal particles and grains that have a higher levels of crystallinity than particles produced from other methods [52-58]. However, the reaction typically occurs at a slow rate over a narrow regime of temperatures [55].

2.2.1.6 Biological Synthesis

Until recently, chemical and physical methods were the popular methods of synthesizing magnetic nanoparticles. These methods often require several processing steps, controlled pH, high temperature, controlled pressure and the use of expensive equipment. The chemical synthesis of nanoparticles may also involve the use of toxic chemicals as solvents and surfactants [59]. These tend to limit their potential greatly for biomedical applications like drug delivery system or magnetic resonance imaging (MRI). However, MNPs produced by some of the chemical and physical methods have been approved by the US Food and Drug Agency (FDA), as well as the Europe Medicine Agency (EMA) for biomedical applications [60,61].

Furthermore, most chemical synthesis procedures employ specialty chemicals and often yield particles in non-polar organic solutions [41]. These tend to preclude and limit their application in biomedicine. In contrast, the biosynthesis of nanoparticles from microorganisms has the ability to produce nanoparticles with controlled sizes and shapes under non-toxic conditions [59]. The formation pathways of these nanoparticles are non-toxic and low cost. These pathways can also be used to form magnetic nanoparticles with a range of sizes. The particles generated by these

processes have higher catalytic reactivity, greater specific surface area and an improved contact between the enzyme and metal salt in question, due to the bacterial carrier matrix [62, 63].

Biosynthesis of magnetic nanoparticles can be carried out using plants or micro-organisms. The nanoparticles can also form intracellularly or extracellularly on micro-organisms. Since the micro-organisms employ target ions from their environment or medium, they can process metal ions into the elemental metals using enzymes that are generated by cellular metabolism. The nanoparticles are formed intracellularly, when the process involves the transportation of ions into the microbial cell to form nanoparticles in the presence of enzymes. In contrast, the nanoparticles can also be formed extracellularly when metal ions that are trapped on the surfaces of cells are reduced in the presence of enzymes [63-65].

In the case of gold nanoparticles, they are synthesized in an aqueous solution through the reduction of chloroauric acid (HAuCl_4). The conventional methods for the synthesis of gold nanoparticles are the Turkevich method, the Brust method and the Reductant and stabilizer-free approach. Others methods involve biosynthesis. The Turkevich method involves the use of sodium citrate as a reducing agent and as a stabilizer. The presence of sodium citrate affects the particle size formed during this process. When the quantity of sodium citrate is reduced, the particle sizes increases and vice versa. The Brust method involves the use of sodium borohydride (NaBH_4) as a reducing agent and tetraoctylammonium (TOAB) as a stabilizer. In the Reductant and stabilizer-free approach, an electrochemical deposition (ED) technique is carried out. Here, gold nanoparticles are uniformly deposited on thin film by ED. Particles sizes and distribution

density can be well controlled by the potential of the ED. The methods described above are classified as physical and chemical methods of synthesis.

In contrast with the chemical and physical methods, the biosynthesis of gold nanoparticles provides a novel approach to the development of relatively non-toxic and environmentally benign methods [66,67]. Biosynthesis methods have the potential to replace the conventional methods of chemical synthesis that are normally used to synthesize gold nanoparticles [68-70]. Furthermore, the biosynthesis of gold nanoparticles can be achieved through the use of environmentally benign fungi, plants and bacteria, [66,68-78]. These provide useful new pathways and insights to the synthesis of particles with a variety of shapes and sizes [79,80].

2.3 Magnetite and Gold Nanoparticles for Cancer Detection and Treatment

2.3.1 Magnetic Nanoparticles for Cancer Detection and Treatment

Depending of their synthesis pathways, magnetite nanoparticles (MNPs) are explored for potential applications as contrast agents and drug delivery agents in localized cancer therapy [81,82]. In the case of potential applications as contrast agents in magnetic resonance imaging.[83,84], Meng *et al.* [85] have shown that superparamagnetic iron oxide contrast agents can provide sub-millimeter resolution in the imaging of breast cancer tissue in mice. Other researchers have shown that magnetic nanoparticles can be combined and conjugated together to cancer drugs [82]. Based on their unique magnetic, chemical, physical, optical, thermal, and mechanical properties, MNPs that are superparamagnetic nanoparticles offer a great potential for several biomedical applications including cancer detection and treatment [86–89], including:

- a) Drug delivery;

- b) Tissue repair;
- c) Cellular therapy such as cell labelling, targeting and as a tool to separate and purify cell populations;
- d) Hyperthermia;
- e) Magnetic resonance imaging (MRI);
- f) Magnetofection.

2.3.2 Gold Nanoparticles for Cancer Detection and Treatment

Gold nanoparticles have been used to enhance laser therapy through interactions that occur between gold nanoparticles and laser beams [90-92]. Similarly, anti-cancer drugs that are tethered to gold nanoparticles have been explored to treat targeted cancer cells/tissue and metastatic cancer cells in the blood stream [93,94]. Colloidal gold nanoparticles have been shown to have a good potential for cancer diagnosis and therapy [95]. These are attractive because gold has been approved and used for treatment of human disease. Gold nanoparticles have been used as contrast agents *in vitro* based on their ability to scatter visible light [96] and their strong absorption of light in the visible and near infra-red (NIR) electromagnetic regions [91,92].

Sokolov *et al.* [96] have shown the use of gold conjugated to EGFR antibodies to label cervical biopsies for identification of precancerous lesions for reflective imaging. Photoacoustic tomography has been used to image gold nanoparticles to a depth of 6 cm in a system [97]. This property of gold nanoparticles could be very useful for *in-vivo* imaging. Thorek *et al.* [98] have also shown that the cellular uptake of spherical gold nanoparticles is dependent on their size,

with 50 nm being the optimal diameter [30]. Furthermore, in a subcutaneous model of colon cancer, gold nanoparticles conjugated to tumor necrosis factor (TNF) have been shown to accumulate in tumors [95].

2.3.3 Passive and Active Targeting

Passive and active targeting strategies can be used to deliver nanoparticles and enhance the intracellular concentration of drugs in cancer cells while avoiding toxicity in normal cells [99,100,101]. Passive targeting (Figure 2.2) takes advantage of the size of nanoparticles and exploits the unique anatomical and pathological abnormalities of the tumor vasculature. In this case, nanoparticles (gold and magnetite) can accumulate and extravasate inside the interstitial space which contributes to an “enhanced permeability”. When lymphatic vessels are absent or ineffective in tumors, it leads to inefficiency in the drainage of the tumor tissue that contributes to an “enhanced retention”. Together these two phenomena constitute the “Enhanced Permeability and Retention” (EPR) effect. The EPR, considered as a gold standard in the design of new anti-cancer drug delivery system, was first explored by Matsumura *et al.*[102].

In the case of active targeting (Figure 2.2, Ref [103]), targeting ligands are grafted at the nanoparticle’s surface [103]. The ligand is chosen to bind specific receptors overexpressed by tumor cells or tumor vasculature that are not expressed by normal cells. Another important factor in the choice of targeting ligands is the homogeneity of the expression of the receptor on all targeted cells. Furthermore, to target cancer cells, several overexpressed receptors have been investigated e.g., the transferrin receptor, the LHRH receptor, the folate receptor, glycoproteins, the epidermal growth factor receptor (EGFR) or integrins [103]. To target tumoral endothelium,

targeting ligands have to recognize specific receptors such as the vascular endothelial growth factor receptors, the integrins, the vascular cell adhesion molecule-1 or the matrix metalloproteinases [103,104].

2.3.4 Magnetic Resonance Imaging (MRI)

Magnetic Resonance Imaging (MRI) in a more general sense is a technique that utilizes pulses of radio wave energy and magnetic fields to diagnose disease by creating images of structures and organs inside the body. It is also a non-destructive and non-invasive approach that reconstructs three-dimensional and two-dimensional pictures of internal living structures without restriction in depth or volume. It has been described as a process by which images are generated, based on the nuclear magnetic resonance signals of the water proton (^1H) nuclei in the specimen [105].

MRI, in some cases, gives some structural details that are not possible with other imaging methods like ultrasound; x-ray or computed tomography (CT) scans. When diagnosing with MRI, the part of the body involved is subjected to a strong magnetic field. MRI is essentially used to probe tumors, bleeding, injury, infection or blood vessel diseases [106-109]. Research has shown that, to enhance the images during MRI, a contrast material or agent is needed. This is why, in a standard clinical MRI scan, contrast media commonly used. The most commonly used contrast agents are gadolinium (Gd) chelates. Because of the problem of agglomeration or accumulation in the liver, incorporated with their non-specificity, they provide a short time imaging window [110,111]. For these reasons, magnetic nanoparticles (Fe_3O_4) are used *in-vivo* as contrast agents to produce local changes of the proton resonance in MRI for disease diagnosis. This makes MRI the most successful imaging method currently in use. Superparamagnetic iron

oxides have been reported to be effective as MRI agents [112].

Meng *et al.* [85] fully described *in-vivo* and *in-vitro* studies of the intake of LHRH–SPIONs and SPIONs into breast cancer cells. From their findings, they show how MNPs enter and accumulate in the breast cancer cells as a function of particle size and exposure time. Meng *et al.* also explained that the uptake of the LHRH–SPIONs is much greater than that of the unconjugated SPIONs in both *in-vitro* and *in-vivo* cases. The increased uptake of intracellular accumulated LHRH–SPIONs is shown to provide T2 contrast enhancement that could lead to improved spatial resolution in MRI by classical T2 imaging. Such improved detection could be very significant for the early detection of cancer [85].

Zhou *et al.* [113], in another approach see the effectiveness of MRI in breast cancers diagnosis and treatment with hormone-conjugated nanomaterials. Using TEM to measure sub-cellular distributions of SPIONs in the tumors and tissue, they showed that LHRH-SPIONs effectively have the potential to target cancer cells in both the primary breast tumors and the lung metastases. In a similar breast cancer study, Zhou *et al.* [114] revealed that accumulation of individual LHRH- magnetic nanoparticles in the nucleus of liver cells suggests that LHRH-MNPs are also potential carriers for effectively delivering drugs or DNA to liver cells with diseases.

2.3.5 Hyperthermia

The term hyperthermia simply referred to treatment by heat in cancer therapy [115]. It involves the exposure of cancer cells/tissue to temperatures of about 41 – 46 °C so as to kill or shrunk

them [116,117]. Hyperthermia can be used to treat cancer by local or regional means. These methods are called local and regional hyperthermia. Local hyperthermia also known as thermal ablation is used to destroy tumors in a specific area, while the regional hyperthermia occurs when the regional body temperature is raised beyond the normal body temperature, so as to destroy cancer cells/tissue.

Conventional hyperthermia, incorporated with magnetic nanoparticles (superparamagnetic nanoparticles) truly offers immense advantages in specific localized cancer treatment. Rosensweig [118] showed that superparamagnetic iron oxides nanoparticles have impressive levels of heating at low magnetic fields as compared to ferromagnetic material which require much higher magnetic field strength for effective heat generation. The amount of current resulting in heat generation is proportional to the size of the magnetic field and the size of the object [119].

Man Von Ardenne [120], in the eighteenth century, was the pioneer to specifically treat cancer patients by this method. This was followed by a chemotherapeutics approach in the treatment of cancer. The chemotherapeutic technique is known to damage normal organs and tissue by causing necrosis, coagulation and carbonization during the therapy. The reason is because the therapeutic temperature is 54 °C and the treatment is not localized [121]. However, studies have shown that the optimal temperature range for hyperthermia is between 43 – 44 °C [117] within this temperature regime, and the programmed cell death that occurs has been shown to be effective in cancer treatment [116]. More recently, Jordan *et al.* [120] in 1999 revealed that magnetic nanoparticles can be used to target cancer cells via immobile specific targeting

functional groups. This is due to their higher specific adsorption rates when compared to those of bulk particles.

2.3.6 Plasmon Resonance

This prominent spectroscopic feature of noble metal nanoparticles (NPs) is the surface plasmon resonance (SPR), which gives rise to a sharp and intense absorption band in the visible light range. The physical origin of the absorption is a collective resonant oscillation of the free electrons of the conduction band of the metal [122-124]. For a spherical nanoparticle, this is much smaller than the wavelength of the incident light. This response to the oscillating electric field can be described by the dipole approximation of Mie theory [122,125]. The large absorption cross-section values of the surface-plasmon resonance band imply that a NP is able to efficiently acquire a vast amount of energy when irradiated with light at the appropriate wavelength [122].

Gold as plasmonic nanoparticles exhibit interesting absorbance, scattering, and coupling properties based on their geometries and relative positions [126]. These unique properties have made them applicable in solar cells, signal enhancement for imaging, spectroscopy, and cancer treatment. The surface plasmon resonance can be tuned by varying the size or shape of the nanoparticles, leading to particles with tailored optical properties for different applications [126]. Research has shown that the absorption of gold nanorods functionalized with epidermal growth factor is sufficient to amplify the effects of low power laser light such that it can be used for targeted radiation cancer treatments [127].

2.3.7 Adhesion Mechanism and Theory

In classical Hertzian contact theory [128], it is assumed that no adhesion exists between elastic

spheres in contact. However, at small scales, such as those involved in tip-sample contacts in the AFM, the surface to volume ratio is high. Hence, the adhesion arising from attractive forces is generally not negligible and must be taken into account. Adhesion is the bonding of two phases on a micro or atomic scale [129]. Adhesion measurements at a nanoscale between particles can be achieved with the aid of Atomic Force Microscope (AFM).

The AFM invented in 1986 by Binnig, Quate and Gerber [130], is a high resolution scanning tool that is used to map the topography of a surface or to measure surface properties. The AFM can provide much more information on adhesion forces that are experienced by the micro-cantilever, as the probe tip is brought close to a sample surface and then pulled away. This technique can be used to measure the long range attractive or repulsive forces between the probe tip and the sample surface [131]. Samples can be investigated under ambient air or submerged liquid conditions, with no need for stiff or conductive surfaces with the aid of an AFM. The AFM has allowed for the characterization of biological samples, including living cells [132-134]. The AFM has also been used to study nanoparticles [135], drugs [136], ligand-receptor interactions [137-139], and nano-scale drug-delivery systems [140].

The adhesion of nanoparticles to drugs and biological materials usually provides a basis for the robustness of drug delivery or detection systems that are nanoparticle-based. Derjaguin-Muller-Toporov (DMT), Johnson-Kendall-Robert (JKR) and Maugis-Dugdale (MD) models form the basis for obtaining the adhesion energies from adhesion forces today. The while DMT model applies to weak interactions between stiff materials with small radii [141], JKR model considers strong interactions between compliant materials with large radii [142] and the MD model [143]

lies between the DMT and JKR models.

The operation mode of the AFM is described based on the type of interaction between the tip and the sample as well as the way the tip is moved across the sample surface. AFM operational mode could be categorized as contact, intermittent contact or tapping and non-contact mode. In the contact mode (Figure 2.3a, Ref [144]), the tip is in continuous contact with the sample surface, which causes the cantilever to deflect. As the tip is scanning across the surface, the feedback control system keeps the bending of the cantilever constant. This occurs by moving the cantilever toward or away from the sample surface to keep the laser position fixed on the photodiodes. The up/down movement of the cantilever is used to generate data on the surface topography [144].

In the case of the tapping mode (Figure 2.3b, Ref [144]), the first stage involves the bringing of the coated AFM tips close enough to the substrate for adhesive interactions to occur (A). The second stage involves jumps to contact with the surface when significant van der Waals forces are present (B). During the third stage, the tips then undergo elasticity as they are displaced further in the same direction (C). Upon their retraction, the displacements are reversed, as the loads are reduced to zero in the fourth stage (D). However, the tips do not detach at zero load, due to the effects of adhesion. Consequently, the retraction has to be continued until the adhesive interactions are overcome by the applied forces (See Figure 2.4). This finally results in the pull-off of the AFM tips from the substrates (E) [145].

From Hooke's law, the resulting pull-off force, F , is a measure of the adhesion. This is given as:

$$F = k\delta \quad (1)$$

Where k in equation (1) represents the stiffness of the AFM cantilever while d is the displacement of the AFM tip at the onset of pull-off [145] (represented as the length, EA in

Figure (2.4)).

2.4 Polymer Drug Microspheres

Microspheres are sometimes referred to as microparticles. They are spherical microscopic particles that are normally free flowing powders consisting of proteins or synthetic polymers which are biodegradable in nature with a size range from 1–1000 μm [146,147]. The use of microspheres as a drug-delivery system means that the system has an augmented effectiveness and reduced toxicity of the incorporated agents/drug to non-targeted cells and tissues. Polymeric microspheres as a drug delivery system are primarily developed for sustained release of drugs for prolonged systemic therapeutic effects after subcutaneous or intramuscular administration. Microsphere formulations of drug are particularly well suited to the local treatment of diseases as they are injectable; the drug encapsulates at high efficiency and is released slowly over a period of time [148-151].

Microspheres of poly(lactic acid) (PLA), and its co-polymer poly(lactic-co-glycolic acid) (PLGA) have been studied extensively due to the biocompatibility and biodegradation of these polymers [152-155]. Biodegradable microspheres can be utilized to direct drugs to organ(s) by releasing them to the site of interest. Its success depends on the size of the microsphere used and on the mode of administration (intravenous / intra-arterial) [156,157]. This work focuses on the development of PLGA-based injectable drug microspheres by the single emulsion solvent evaporation technique (SESET). This is also called emulsion-solvent extraction/evaporation method. Drug polymer (PLGA) microspheres for drug delivery systems have been fabricated by phase separation or precipitation, emulsion/solvent evaporation [158-163], and/or spraying

methods [164-168] or a combination of these techniques.

The SESET is essentially the most commonly used method in the preparation of microspheres because it is simple and easy [169-171]. The SESET involves the dissolution of polymer in a suitable organic solvent (water immiscible solvent), and the drug is dispersed or dissolved in this polymeric solution. The resultant solution of drug and polymer in the organic solvent is then emulsified in an aqueous continuous phase (stabilizer) to form discrete droplets. Microspheres are then formed when the organic solvent first diffuses into the aqueous phase and then evaporates at the water/air interface. As the solvent evaporates, the microspheres harden and free flowing microspheres can be obtained after suitable filtration and freeze drying.

2.4.1 Drug Delivery

There is a need to deliver the drugs precisely and safely to their target site at the right time and to control their release so as to achieve the maximum therapeutic effect. This is why localized cancer drug delivery systems offer numerous advantages over bulk chemotherapy. This includes the reduction of short and long term effects and a reduction in the amount of drug that is needed to have a therapeutic effect. These possibilities have stimulated extensive interest in the development of nanoparticles for localized cancer treatment. Some of the drug delivery systems available currently include liposome systems, drug conjugates, controlled delivery of cancer therapeutics and transdermal drug delivery patches using controlled released microchips [172].

In the case of magnetic nanoparticles, there have been numerous efforts in their use for drug delivery systems. Freeman *et al.* [173] in 1960 also proposed that magnetic particles (Fe_3O_4)

could be used for localized treatment, with the aid of magnetic field. One of the main limitations of magnetic drug delivery is the strength of the external field that can be applied to obtain the necessary magnetic gradients that are needed to control the residence times of the nanoparticles in the desired area or which triggers the drug desorption. Neuberger *et al.* [121] suggested that this can be overcome partly by the use of hybrid nanoparticles with permanent Nd-Fe-B shell that encapsulate superparamagnetic iron oxide nanoparticles core [174].

In the case of drug polymers, there have been significant research efforts to explore their efficacy for controlled drug release [141-151,154,160,162-166,171]. Polymeric drug-based particles have been used effectively in the treatment of prostate cancer [175], atherosclerosis [176] and breast cancer [177] by localized drug delivery. This is due to their uniqueness in the delivery of drugs at the required dosage and time [178, 179]. The use of polymeric cancer-based drug particles has limited the use of the conventional methods, which have severe side effects and are not cost effective [178-180]. The synthesized drug-based polymer microsphere is used for localized chemotherapy that can reduce the concentrations of cancer drugs that are needed for effective treatment.

Another advantage of using injectable polymer-based drugs is their low/minimal incidence of toxicity [178,179,181,182] and hypersensitivity reactions [179]. Paclitaxel is one of the best known effective anticancer drugs against breast cancer, ovarian cancer, colon cancer, small and non-small cell lung cancer, and neck cancer [183-186]. Paclitaxel has been encapsulated efficiently, prior to slow/controlled release over a period of months [150,187-192]. The release has shown to be controlled by diffusion and bulk erosion of the poly-lactic poly-glycolic acid

(PLGA) copolymers [180].

References

- [1] Nagavarma BVN, Hement KSY, Ayaz A, Vasudha LS, Shivakumar HG, Different techniques for preparation of polymeric nanoparticles –A review, *Asian J. of Pharm. and Clinical Research*, 5, 2012, 17-23.
- [2] J. W. M. Bulte, M. Cuyper, D. Despres and J. A. Frank, *Journal of Magnetism and Magnetic Materials* 194 (1999) 204.
- [3] H. Pardoe, P. R Clark, T. G St Pierre, P. Moroz, S. K Jones. *Magnetic Resonance Imaging*. (2003) 21:483–488.
- [4] F. J. Lazaro, A. R. Abadia, M. S. Romero, L. Gutierrez, J. Lazaro and M. P. Morales. *Biochim Biophys Acta*. (2005) 1740:434–45.
- [5] M. Ferrari, *Cancer nanotechnology: Opportunities and challenges*, *Nature Reviews. Cancer* 5 (2005) 161–171.
- [6] N. Sanvicens, M.P. Marco, *Multifunctional nanoparticles - properties and prospects for their use in human medicine*, *Trends in Biotechnology* 26 (2008) 425–433.
- [7] O.C. Farokhzad, R. Langer, *Nanomedicine: Developing smarter therapeutic and diagnostic modalities*, *Advanced Drug Delivery Reviews* 58 (2006) 1456–1459.
- [8] J. He, H.F. VanBrocklin, B.L. Franc, Y. Seo, E.F. Jones, *Nanoprobes for medical diagnosis: Current status of nanotechnology in molecular imaging*, *Current Nanoscience* 4 (2008) 17–29.

- [9] Y. Oni, C. Theriault, A.V. Hoek, W.O. Soboyejo, Effects of temperature on diffusion from PNIPA-based gels in a BioMEMS device for localized chemotherapy and hyperthermia, *Mater. Sci. Eng. C* 31 (2011) 67–76.
- [10] Cornelis K, Hurlburt CS. *Manual of Mineralogy*. New York: Wiley; 1977.
- [11] Kwei GH, von Dreele RB, Williams A, Goldstone JA, Lawson II AC, Warburton WK. Structure and valence from complementary anomalous X-ray and neutron powder diffraction. *J Molecul Struct* 1990;223:383–406.
- [12] Siegel RW. In: Siegel RW, Hu E, Roco MC, editors. *Nanostructure science and technology. A worldwide study*. WTEC, Loyola College in Maryland; 1999.
- [13] Uchegbu IF, Florence AT. Adverse drug events related to dosage forms and delivery systems. *Drug Saf* 1996;14(1):39–67.
- [14] Gilchrist RK, Medal R, Shorey WD, Hanselman RC, Parrot JC, Taylor CB. Selective inductive heating of lymph nodes. *Ann Surg* 1957;146:596–606.
- [15] Schwertmann U, Cornell RM. *Iron oxides in the laboratory: preparation and characterization*. Weinheim, Cambridge: VCH; 1991.
- [16] Q. A. Pankhurst, J. Connolly, S. K. Jones, and J. Dobson, “Applications of magnetic nanoparticles in biomedicine,” *Journal of Physics D*, vol. 36, no. 13, pp. R167–R181, 2003.
- [17] Kerker M. *The scattering of light and other electromagnetic radiation*. New York: Academic Press; 1969.

- [18] Papavassiliou GC. Optical properties of small inorganic and organic metal particles. *Prog Solid State Chem* 1979;12:185–271.
- [19] Bohren CF, Huffman DR. Absorption and scattering of light by small particles. New York: Wiley; 1983.
- [20] Kreibig U, Vollmer M. Optical properties of metal clusters. Springer;1995.
- [21] Smithpeter, C., et al., Penetration Depth Limits of In Vivo Confocal Reflectance Imaging. *Appl. Opt.*, 1998. 37: p. 2749-2754 79.
- [22] Tearney, G.J., et al., In Vivo Endoscopic Optical Biopsy with Optical Coherence Tomography. *Science*, 1997. 276(5321): p. 2037-2039.
- [23] Huang, D., et al., Optical coherence tomography. *Science*, 1991. 254(5035): p. 1178-1181.
- [24] Sokolov, K., et al., Real-Time Vital Optical Imaging of Precancer Using Anti-Epidermal Growth Factor Receptor Antibodies Conjugated to Gold Nanoparticles. *Cancer Research*, 2003. 63(9): p. 1999-2004.
- [25] X. Huang, P.K. Jain, I.H. El-Sayed, M.A. El-Sayed, Gold nanoparticles: interesting optical properties and recent applications in cancer diagnostics and therapy, *Nanomed. (Lond.)* 2 (2007) 681–693.
- [26] X. Huang, P.K. Jain, I.H. El-Sayed, M.A. El-Sayed, Plasmonic photothermal therapy (PPTT) using gold nanoparticles, *Lasers Med. Sci.* 23 (2008) 217–228.
- [27] D.P. O’Neal, L.R. Hirsch, N.J. Halas, J.D. Payne, J.L. West, Photo-thermal tumor ablation in mice using near infrared-absorbing nanoparticles, *Cancer Lett.* 209 (2004) 171–176.

- [28] J. Liu, S. Z. Qiao, Q. H. Hu, et al. Magnetic Nanocomposites with Mesoporous Structures: Synthesis and Applications. *Small*. 2011, 7, 425-443.
- [29] N. A. Luechinger, R. N. Grass, E. K. Athanassiou, et al. Bottom-up fabrication of metal/metal nanocomposites from nanoparticles of immiscible metals. *Chemistry of Materials*. 2007, 22, 155-160.
- [30] D. K. Tiwari, J. Behari, P. Sen. Time and dose-dependent antimicrobial potential of Ag nanoparticles synthesized by top-down approach. *Current Science*. 2008, 95, 647-655.
- [31] P. Mohanpuria, N. K. Rana, S. K. Yadav. Biosynthesis of nanoparticles: technological concepts and future applications. *Journal of Nanoparticle Research*. 2008, 10, 507-517.
- [32] Lisiecki I and Pileni M P 1993 *J. Am. Chem. Soc.* 7 115.
- [33] Zhang K, Chew C H, Xu G Q, Wang J and Gan L M 1999 *Langmuir* 15 3056.
- [34] Zarur A J and Ying J Y 2000 *Nature* 403 65.
- [35] Tartaj P and De Jonghe L C 2000 *J. Mater. Chem.* 10 2786.
- [36] Tartaj P and Tartaj J 2002 *Chem. Mater.* 14 536
- [37] Pileni M P 2003 *Nature Mater.* 2 145.
- [38] Pileni M P 1993 *J. Phys. Chem.* 97 6961.
- [39] D R Uhlmann, G Teowee, J Boulton J. *Sol-Gel Sci. Technol.* 8 1083 (1997).
- [40] Bose, S Bid, S K Pradhan, M Pal, D Chakravorty J. *Alloys Compd.* 343 192 (2002).

- [41] Brinker, C.J.; Scherer, G. W. Sol-Gel Science: The Physics and Chemistry of Sol-Gel Processing. Academic Press, 1990, ISBN 0121349705.
- [42] Klein, L. Sol-Gel Optics: Processing and Applications. Springer Verlag. 1994, ISBN 0792394240.
- [43] Sugimoto, T (1980). "Formation of uniform spherical magnetite particles by crystallization from ferrous hydroxide gels*1". Journal of Colloid and Interface Science 74: 227. doi:10.1016/0021-9797(80)90187-3.
- [44] Massart, R.; Cabuil, V.J.Chem.Phy.1987, 84,967.
- [45] Laurent, Sophie; Forge, Delphine; Port, Marc; Roch, Alain; Robic, Caroline; Vander Elst, Luce; Muller, Robert N. (2008). "Magnetic Iron Oxide Nanoparticles: Synthesis, Stabilization, Vectorization, Physicochemical Characterizations, and Biological Applications". Chemical Reviews 108 (6): 2064–110. doi:10.1021/cr068445e. PMID 18543879.
- [46] Jolivet J P 2000 Metal Oxide Chemistry and Synthesis: From Solutions to Solid State (New York: Wiley).
- [47] Laurent, Sophie; Forge, Delphine; Port, Marc; Roch, Alain; Robic, Caroline; Vander Elst, Luce; Muller, Robert N. (2008). "Magnetic Iron Oxide Nanoparticles: Synthesis, Stabilization, Vectorization, Physicochemical Characterizations, and Biological Applications". Chemical Reviews 108 (6): 2064–110. doi:10.1021/cr068445e.

- [48] S. Sun et al. "Nanoparticles," *Journal of the American Chemical Society*, 126, pp. 273–279, 2004.
- [49] F. Davar, Z. Fereshteh, M. Salavati-Niasari, *J. Alloys Compd.* 476 (2009) 797.
- [50] T. Hyeon, S.S. Lee, J. Park, Y. Chung, H.B. Na, *J. Am. Chem. Soc.* 123 (2001) 12798.
- [51] S. Sun, H. Zeng, D.B. Robinson, S. Raoux, P.M. Rice, S.X. Wang, G. Li, *J. Am. Chem. Soc.* 126 (2004) 273.
- [52] J. Wang, J. Sun, Q. Sun, Q. Chen, *Mater. Res. Bull.* 38 32 (2003) 1113.
- [53] J. Wang, F. Ren, R. Yi, A. Yan, G. Qiu, X. Liu, *J. Alloys Compd.* 479 (2009) 791.
- [54] K. Butter, K. Kassapidou, G.J. Vroege, A.P. Philipse, *J. Colloid Interface Sci.* 287 (2005) 485.
- [55] B. Mao, Z. Kang, E. Wang, S. Lian, L. Gao, C. Tian, C. Wang, *Mater. Res. Bull.* 41 (2006) 2226.
- [56] H. Zhu, D. Yang, L. Zhu, *Surf. Coat. Technol.* 201 (2007) 5870.
- [57] S. Giri, S. Samanta, S. Maji, S. Ganguli, A. Bhaumik, *J. Magn. Magn. Mater.* 285 (2005) 296.
- [58] F. Gözüak, Y. Köseoğlu, A. Baykal, H. Kavas, *J. Magn. Magn. Mater.* 321 (2009) 2170.
- [59] X. Li, H. Xu, Z. Chen, G. Chen, Biosynthesis of nanoparticles by microorganisms and their applications, *J. Nanomater.* 2011 (2011) 1–16 (Article No: 8).

- [60] V. Herynek, Z. Berkova, D. Horak, M. Babic, D. Jirak, F. Saudek, M. Hajek, Alternative labels for visualization of pancreatic islets, *Proc. Int. Soc. Magn. Reson. Med.* 18 (2010) 4200.
- [61] R. Provenzano, B. Schiller, M. Rao, D. Coyne, L. Brenner, B.J. Pereira, Ferumoxyl as an intravenous.
- [62] R. Bhattacharya, P. Mukherjee. Biological properties of —nakedll metal nanoparticles. *Advanced Drug Delivery Reviews.* 2008, 60, 1289–1306.
- [63] K. Simkiss, K.M. Wilbur. *Biom mineralization.* Academic, New York, 1989
- [64] S. Mann. *Biom mineralization: Principles and Concepts in Bioinorganic Materials Chemistry,* Oxford Univ. Press, Oxford, 2001.
- [65] X. Zhang, S. Yan, R. D. Tyagi, et al. Synthesis of nanoparticles by microorganisms and their application in enhancing microbiological reaction rates. *Chemosphere.* 2011, 82, 489–494.
- [66] Shukla, R., et al., Soybeans as a Phytochemical Reservoir for the Production and Stabilization of Biocompatible Gold Nanoparticles. *Small,* 2008. 4(9): p. 1425-1436.
- [67] Han, G., P. Ghosh, and V.M. Rotello, Functionalized gold nanoparticles for drug delivery. *Nanomedicine,* 2007. 2(1): p. 113-123.
- [68] He, S., et al., Biosynthesis of gold nanoparticles using the bacteria *Rhodospseudomonas capsulata.* *Materials Letters,* 2007. 61(18): p. 3984-3987.

- [69] He, S., et al., Biological Synthesis of Gold Nanowires Using Extract of *Rhodospseudomonas capsulata*. *Biotechnology Progress*, 2008. 24(2): p. 476-480.
- [70] Shankar, S.S., et al., Rapid synthesis of Au, Ag, and bimetallic Au core-Ag shell nanoparticles using Neem (*Azadirachta indica*) leaf broth. *Journal of Colloid and Interface Science*, 2004. 275(2): p. 496-502.
- [71] Southam, G. and T.J. Beveridge, The in vitro formation of placer gold by bacteria. *Geochimica et Cosmochimica Acta*, 1994. 58(20): p. 4527-4530.
- [72] Southam, G. and T.J. Beveridge, The occurrence of sulfur and phosphorus within bacterially derived crystalline and pseudocrystalline octahedral gold formed in vitro. *Geochimica et Cosmochimica Acta*, 1996. 60(22): p. 4369-4376.
- [73] Beveridge, T.J. and R.G. Murray, Sites of metal deposition in the cell wall of *Bacillus subtilis*. *J Bacteriol*, 1980. 141(2): p. 876-87.
- [74] Sastry, M., e. al, and et al., ChemInform Abstract: Bioreduction of AuCl₄ Ions by the Fungus, *Verticillium* sp. and Surface Trapping of the Gold Nanoparticles Formed. *ChemInform*, 2001. 32(51): p. no-no.
- [75] Mukherjee, P., et al., Extracellular Synthesis of Gold Nanoparticles by the Fungus *Fusarium oxysporum*. *ChemBioChem*, 2002. 3(5): p. 461-463.
- [76] Wen, L., et al., Extracellular biosynthesis of monodispersed gold nanoparticles by a SAM capping route. *Journal of Nanoparticle Research*, 2009. 11(2): p. 279-288.

- [77] Ahmad, A. and et al., Intracellular synthesis of gold nanoparticles by a novel alkalotolerant actinomycete, *Rhodococcus* species. *Nanotechnology*, 2003. 14(7): p. 824.
- [78] Kasthuri, J., K. Kathiravan, and N. Rajendiran, Phyllanthin-assisted biosynthesis of silver and gold nanoparticles: a novel biological approach. *Journal of Nanoparticle Research*, 2009. 11(5): p. 1075-1085.
- [79] Grzelczak, M., et al., Shape control in gold nanoparticle synthesis. *Chemical Society Reviews*, 2008. 37(9): p. 1783-1791.
- [80] Shankar, S.S., et al., Bioreduction of chloroaurate ions by geranium leaves and its endophytic fungus yields gold nanoparticles of different shapes. *Journal of Materials Chemistry*, 2003. 13(7): p. 1822-1826.
- [81] Meyers, P. H., et al., *Am. J. Roentgenol. Radium Ther. Nucl. Med.* 90: 1068, 1963.
- [82] Häfeli, U. O., *Int. J. Pharm.* 277: 19, 2004.
- [83] Lazaro FJ, Abadia AR, Romero MS, Gutierrez L, Lazaro J, Morales MP *Biochim Biophys Acta.* 2005, 1740:434–45.
- [84] T.K. Indira, P.K. Lakshmi. *Magnetic Nanoparticles – A Review*, *International Journal of Pharmaceutical Sciences and Nanotechnology.* 2010, Volume 3 • Issue 3.
- [85] J. Meng J. Fana, G. Galiana , R.T. Branca , P.L. Clasen , S. Ma , J. Zhou , C. Leuschner , C.S.S.R. Kumar ,J. Hormes , T. Otiti , A.C. Beye , M.P. Harmer , C.J. Kiely , W. Warren , M.P. Haataja a, W.O. Soboyejo “LHRH-functionalized superparamagnetic iron oxide

- nanoparticles for breast cancer targeting and contrast enhancement in MRI” *Materials Science and Engineering C* 29 (2009) 1467–1479.
- [86] Arbab AS, Bashaw LA, Miller BR, Jordan EK, Lewis BK, Kalish H, Frank JA. Characterization of biophysical and metabolic properties of cells labeled with superparamagnetic iron oxide nanoparticles and transfection agent for cellular MR imaging. *Radiology* 2003;229 (3):838–46.
- [87] Reimer P, Weissleder R. Development and experimental application of receptor-specific MR contrast media. *Radiology* 1996;36:153–63.
- [88] Pankhurst QA, Connolly J, Jones SK, Dobson J. Applications of magnetic nanoparticles in biomedicine. *J Phys D: Appl Phys* 2003;36:R167–81.
- [89] Häfeli U, Schütt W, Teller J, Zborowski M, editors. *Scientific and clinical applications of magnetic carriers*. New York: Plenum Press; 1997.
- [90] X. Huang, P.K. Jain, I.H. El-Sayed, M.A. El-Sayed, Gold nanoparticles: interesting optical properties and recent applications in cancer diagnostics and therapy, *Nanomed. (Lond.)* 2 (2007) 681–693.
- [91] X. Huang, P.K. Jain, I.H. El-Sayed, M.A. El-Sayed, Plasmonic photothermal therapy (PPTT) using gold nanoparticles, *Lasers Med. Sci.* 23 (2008) 217–228.
- [92] D.P. O’Neal, L.R. Hirsch, N.J. Halas, J.D. Payne, J.L. West, Photo-thermal tumor ablation in mice using near infrared-absorbing nanoparticles, *Cancer Lett.* 209 (2004) 171–176.
- [93] Melancon MP, Lu W, Li C. *MRS Bulletin* 2009;34:415-21.

- [94] Ramachandra RG, Mahaveer S, Ross BD. *Clin. Can. Res.* 2006;12:6677.
- [95] Paciotti GF, Myer L, Weinreich D, et al., Colloidal gold: a novel nanoparticle vector for tumor directed drug delivery: *Drug Deliv.* 11,169–183 (2004).
- [96] Sokolov K, Follen M, Aaron J, et al., Real-time vital optical imaging of precancer using anti-epidermal growth factor receptor antibodies conjugated to gold nanoparticles: *Cancer Res.* 63, 1999–2004 (2003).
- [97] Copland JA, Eghtedari M, Popov VL, et al., Bioconjugated gold nanoparticles as a molecular based contrast agent: implications for imaging of deep tumors using optoacoustic Tomography, *Mol Imaging Biol.*, 6, 341–349 (2004).
- [98] Thorek DL, Tsourkas A. *Biomaterials.* 2008; 29(26):3583-90.
- [99] B. Slutter, S. Bal, C. Keijzer, R. Mallants, N. Hagenaars, I. Que, E. Kaijzel, W. van Eden, P. Augustijns, C. Lowik, J. Bouwstra, F. Broere, W. Jiskoot, Nasal vaccination with N-trimethyl chitosan and PLGA based nanoparticles: nanoparticle characteristics determine quality and strength of the antibody response in mice against the encapsulated antigen, *Vaccine* 28 (2010) 6282–6291.
- [100] R.A. Jain, The manufacturing techniques of various drug loaded biodegradable poly(lactide-co-glycolide) (PLGA) devices, *Biomaterials* 21 (2000) 2475–2490.
- [101] M.F. Bachmann, G.T. Jennings, Vaccine delivery: a matter of size, geometry, kinetics and molecular patterns, *Nat. Rev. Immunol.* 10 (2010) 787–796.

- [102] Y. Matsumura, H. Maeda, A new concept for macromolecular therapeutics in cancer chemotherapy: mechanism of tumortropic accumulation of proteins and the antitumor agent smancs, *Cancer Res.* 46 (1986) 6387–6392.
- [103] F. Danhier, O. Feron, V. Preat, To exploit the tumor microenvironment: passive and active tumor targeting of nanocarriers for anti-cancer drug delivery, *J. Control. Release* 148 (2010) 135–146.
- [104] J. Folkman, Tumor angiogenesis: therapeutic implications, *N. Engl. J. Med.* 285 (1971) 1182–1186.
- [105] D.D. Stark, W.G. Bradley Jr., *Magnetic Resonance Imaging* (Mosby, St. Louis, 1999).
- [106] R. Lawaczeck, H. Bauer, T. Frenzel, M. Hasegawa, Y. Ito, K. Kito, N. Miwa, H. Tsutsui, H. Vogler, H.J. Weinmann, *Acta Radiol.* 38 (1977) 584–597.
- [107] S.C.A. Michel, T.M. Keller, J.M. Frohlich, D. Fink, R. Caduff, B. Seifert, B. Marincek, R.A. Kubik-Huch, *Radiology* 225 (2002) 527–536.
- [108] R.C. Semelka, T.K.G. Helmberger, *Radiology* 218 (2001) 27–38.
- [109] W.S. Enochs, G. Harsh, F. Hochberg, R. Weissleder, *J. Magn. Reson. Imaging* 9 (1999) 228–232.
- [110] Kubaska S, Sahani D V, Saini S, Hahn P F and Halpern E 2001 Dual contrast enhanced magnetic resonance imaging of the liver with superparamagnetic iron oxide followed by gadolinium for lesion detection and characterization *Clin. Radiol.* 56 410–5.

- [111] Low R N 2001 MR imaging of the liver using gadolinium chelates *Magn. Reson. Imag. Clin. N. Am.* 9 717–43.
- [112] R. Lawaczeck, H. Bauer, T. Frenzel, M. Hasegawa, Y. Ito, K. Kito, N. Miwa, H. Tsutsui, H. Vogler, H.J. Weinmann, *Acta Radiol.* 38 (1977) 584–597.
- [113] J. Zhou, C. Leuschner, C. Kumar, J.F. Hormes and W.O. Soboyejo // *Biomaterials* 27 (2006) 2001.
- [114] J. Zhou, C. Leuschner, C. Kumar, J. Hormes and W.O. Soboyejo // *Materials Science and Engineering: C* 26 (2006) 1451.
- [115] M. Shinkai, M. Yanase, M. Suzuki, et al. Intracellular hyperthermia for cancer using magnetite cationic liposomes. *Journal of Magnetism and Magnetic Materials.* 1999, 194, 176184.
- [116] Nielsen, O.S., Horsman, M. & Overgaard, J. (2001). A future for hyperthermia in cancer treatment? *European Journal of Cancer*, 37, 1587-1589.
- [117] Gonzales, M et al (2005). Synthesis of magnetoliposomes with monodispersed iron oxides nanocrystal cores for hyperthermia. *Journal of Magnetism and Magnetic Materials* 293(1): 265-270.
- [118] Rosensweig, R.E. (2002). Heating magnetic fluid with alternating magnetic field. *Journal of Magnetism and Magnetic Materials*, 252, 370–374.

- [119] Babincova, M., Leszczynska, D., Sourivong, P. & Babinec, P. (2000). Selective treatment of neoplastic cells using ferritin-mediated electromagnetic hyperthermia. *Medical Hypotheses*, 54, 177-179.
- [120] Jordan, A., et al, *Journal magnetism and magnetic materials* (1999) 201: pp 413-419.
- [121] Neuberger, T. et al, *Journal magnetism and magnetic materials* (2005) 293: pp 483-496.
- [122] Link, S.; El-Sayed, M. A. *Annu. Rev. Phys. Chem.* 2003, 54, 331-366.
- [123] Underwood, S.; Mulvaney, P. *Langmuir* 1994, 10, 3427-30.
- [124] Suppan, P. *Chemistry and Light*; The Royal Society of Chemistry: Cambridge, 1994.
- [125] Mulvaney, P. *Langmuir* 1996, 12, 788-800.
- [126] Zeng, Shuwen; Yu, Xia; Law, Wing-Cheung; Zhang, Yating; Hu, Rui; Dinh, Xuan-Quyen; Ho, Ho-Pui; Yong, Ken-Tye (2013). "Size dependence of Au NP-enhanced surface plasmon resonance based on differential phase measurement". *Sensors and Actuators B: Chemical* 176: 1128. doi:10.1016/j.snb.2012.09.073.
- [127] Rejiya, C.S., Kumar, J., Raji, V., Vibin, M., Abraham, A. "Laser Immunotherapy with Gold Nanorods Causes Selective Killing of Tumour Cells," *Pharmacological Research*, 2011.
- [128] H. Hertz, "Über die Berührung fester elastischer Körper", *Journal für die reine und angewandte Mathematik*, 92, 156-171, (1882)

- [129] K.W. Allen, Theories of Diffusion in Handbook of Adhesion by D.E. Packham, John Wiley and Sons, Inc. Hoboken, 2005.
- [130] G. Binnig, C. F. Quate, Ch. Gerber. "Atomic Force Microscope", Phys. Rev. Lett. 56, 930 - 933 , (1986)
- [131] M. B. Leon, A. Abizaid, J.W. Moses. "The CYPHER® stent: A new gold standard in the treatment of coronary artery disease". New York, NY : The cardiovascular research foundation,pp.90, (2003).
- [132] de Souza Pereira, R., Detection of the absorption of glucose molecules by living cells using atomic force microscopy. FEBS Lett, 2000. 475(1): p. 43-6.
- [133] Allison, D.P., et al., Atomic force microscopy of biological samples. Wiley Interdisciplinary Reviews: Nanomedicine and Nanobiotechnology, 2010. 2(6): p. 618-634.
- [134] Schneider, S.W., et al., Continuous detection of extracellular ATP on living cells by using atomic force microscopy. Proc Natl Acad Sci U S A, 1999. 96(21): p. 12180-5.
- [135] Kneuer, C., et al., A Nonviral DNA Delivery System Based on Surface Modified Silica-Nanoparticles Can Efficiently Transfect Cells in Vitro. Bioconjugate Chemistry, 2000. 11(6): p. 926-932.
- [136] Danesh, A., et al., An In Situ Dissolution Study of Aspirin Crystal Planes (100) and (001) by Atomic Force Microscopy. Pharmaceutical Research, 2001. 18(3): p. 299-303.
- [137] Wong, J., A. Chilkoti, and V.T. Moy, Direct force measurements of the streptavidin-biotin interaction. Biomolecular Engineering, 1999. 16(1-4): p. 45-55.

- [138] Radmacher, M., et al., Mapping interaction forces with the atomic force microscope. *Biophysical Journal*, 1994. 66(6): p. 2159-2165.
- [139] Florin, E., V. Moy, and H. Gaub, Adhesion forces between individual ligand-receptor pairs. *Science*, 1994. 264(5157): p. 415-417.
- [140] Davies, M., et al., Characterization of Drug Particle Surface Energetics and Young's Modulus by Atomic Force Microscopy and Inverse Gas Chromatography. *Pharmaceutical Research*, 2005. 22(7): p. 1158-1166.
- [141] B. V. Derjaguin, V. M. Muller, and Y. P. Toporov, *Prog. Surf. Sci.* 45: 131,1994.
- [142] K. L. Johnson, K. Kendall, and A. D. Roberts, *Proc. R. Soc. London, Ser. A* 324: 301, 1971.
- [143] D. Maugis, *J. Colloid Interface Sci.* 150: 243, 1992.
- [144] Sitterberg, J., et al., Utilising atomic force microscopy for the characterisation of nanoscale drug delivery systems. *European Journal of Pharmaceutics and Biopharmaceutics*, 2010. 74(1): p. 2-13.
- [145] V. Shahin, Y. Ludwig, C. Schafer, D. Nikova, and H. Oberleithner: Glucocorticoids remodel nuclear envelope structure and permeability. *J. Cell. Sci.* 118, 2881 (2005).
- [146] Freiberg, S.; Zhu, X.X. Polymer microspheres for controlled drug release. *Int. J. Pharm.* 2004, 282, 1-18.
- [147] Arshady, R. Preparation of polymer nano- and microspheres by vinyl polymerization techniques. *J. Microencapsul.* 1988, 5, 101-114.

- [148] Liggins, R.T., Burt, H.M., 2001. Paclitaxel loaded poly(l-lactic acid) microspheres: properties of microspheres made with low molecular weight polymers. *Int. J. Pharm.* 222, 19–33.
- [149] Liggins, R.T., D'Amours, S., Demetrick, J.S., Machan, L.S., Burt, H.M., 2000. Paclitaxel loaded poly(l-lactic acid) microspheres for the prevention of intraperitoneal carcinomatosis after a surgical repair and tumor cell spill. *Biomaterials* 21, 1959–1969.
- [150] Burt, H.M., Jackson, J.K., Bains, S.K., Liggins, R.T., Oktaba, A.M.C., Arsenault, A.C., Hunter, W.C., 1995. Controlled delivery of taxol from microspheres composed of a blend of ethylene-vinyl acetate copolymer and poly (d,l-lactic acid). *Cancer Lett.* 88, 73–79.
- [151] Dordunoo, S.K., Jackson, J.K., Arsenault, L.A., Oktaba, A.M.C., Hunter, W.C., Burt, H.M., 1995. Taxol encapsulation in poly(caprolactone) microspheres. *Cancer Chemo. Pharmacol.* 36, 279–282.
- [152] S. Pandey, U.V. Singh, N. Udupa, Implantable flurbiprofen for treating inflammation associated with arthritis, *Ind. Drugs* 31 (1994) 254–257.
- [153] A. Smith, I.M. Hunneyball, Evaluation of poly(lactic acid) as a biodegradable drug delivery system for parenteral administration, *Int. J. Pharm.* 30 (1986) 215–220.
- [154] Y.W. Chien, The use of biocompatible polymers in rate- controlled drug delivery systems. *Pharm. Tech.* May, (1985) 50–66.
- [155] C.C. Chu, Degradation phenonema of two linear aliphatic polyester fibre used in medicine and surgery, *Polymerization* 26 (1985) 591–594.

- [156] Jayaprakash S, Halith SM, Firthose PUM, Kulaturanpillai K, Abhijith, Nagarajan M. Preparation and evaluation of biodegradable microspheres of methotrexate. *Asian J Pharm* 2009;3(1):26-9.
- [157] The Internet Encyclopaedia of Science. Available from: <http://www.daviddarling.info/encyclopedia/M/microsphere.html>. [last cited on 2009 Jul 29].
- [158] M.A. Beboit, B. Baras, and J. Gillard. Preparation and characterization of protein-loaded poly(ϵ - caprolactone) microparticles for oral vaccine delivery. *Int. J. Pharm.*, 184:73–84, 1999.
- [159] L.Y. Chu, R. Xie, J.H. Zhu, W.M. Chen, T. Yamaguchi, and S.I. Nakao. Study of SPG membrane emulsification processes for the preparation of monodisperse core-shell microcapsules. *J. Colloid Interface Sci.*, 265: 187–196, 2003.
- [160] S.C. Lee, J.T. Oh, M.H. Jang, and S.I. Chung. Quantitative analysis of polyvinyl alcohol on the surface of poly(D,L-lactide-co-glycolide) microspheres prepared by solvent evaporation method: effect of particle size and PVA concentration. *J. Control. Rel.*, 59:123–132, 1999.
- [161] G.H. Ma, Z.G. Su, S. Omi, D. Sundberg, and J. Stubbs. Microencapsulation of oil with poly(styrene-N, Ndimethylaminoethyl methacrylate) by SPG emulsification technique: Effect of conversion and composition of oil phase. *J. Colloid Interface Sci.*, 266:282–294, 2003.

- [162] G. Wei, G.J. Pettway, L.K. McCauley, and P.X. Ma. The release profiles and bioactivity of parathyroid hormone from poly(lactic-co-glycolic acid) microspheres. *Biomaterials*, 25:345–352, 2004.
- [163] Y.Y. Yang, T.S. Chung, and N. Ng. Morphology, drug distribution, and in vitro release profiles of biodegradable polymeric microspheres containing protein fabricated by double-emulsion solvent extraction/evaporation method. *Biomaterials*, 22(3):231–241, 2001a.
- [164] F.J. Wang and C.H. Wang. Sustained release of etanidazole from spray dried microspheres prepared by non-halogenated solvents. *J. Control. Rel.*, 81:263–280, 2002.
- [165] F. Quaglia, G. De Rosa, E. Granata, F. Ungaro, E. Fattal, and M.I. La Rotonda. Feeding liquid, non-ionic surfactant and cyclodextrin affect the properties of insulin-loaded poly(lactide-co-glycolide) microspheres prepared by spray-drying. *J. Control. Rel.*, 86:267–278, 2003.
- [166] L. Mu and S.S. Feng. Fabrication, characterization and in vitro release of paclitaxel (Taxol r) loaded poly (lactic-co-glycolic acid) microspheres prepared by spray drying technique with lipid/cholesterol emulsifiers. *J. Control. Rel.*, 76:239–254, 2001.
- [167] P. He, S.S. Davis, and L. Illum. Chitosan microspheres prepared by spray drying. *Int. J. Pharma.*, 187:53–65, 1999.
- [168] S. Freitas, H.P. Merkle, and B. Gander. Ultrasonic atomisation into reduced pressure atmosphere—envisaging aseptic spray-drying for microencapsulation. *J. Control. Rel.*, 95:185–195, 2004.

- [169] Yeagy B. A, Prudencio A, Schmeltzer R. C, Uhrich KE, Cook TJ (2006) Characterization and in vitro degradation of salicylate-derived poly(anhydride-ester microspheres). *J Microencapsul* 23(6):643–653. doi:10.1080/02652040600776481.
- [170] Suzuki, K. and Price, J.C. Microencapsulation and dissolution properties of a neuroleptic in a biodegradable polymer, poly(dl-lactide), *J. Pharm. Sci.* 74 (1985) 21–24.
- [171] Jalil, R.U. Biodegradable poly (lactic acid) and poly (lactide- co-glycolide) polymers in sustained drug delivery, *Drug Dev. - Ind. Pharm.* 16 (1990) 2353–2367.
- [172] S Douang, C. Tang, H. Zhao (2004), Photochemical Synthesis of Gold Nanoparticles by the Sunlight Radiation Using A Seeding Approach.
- [173] Freeman, M.N, et al, *Journal of Applied Physics* (1960) 31, 732.
- [174] Hyeon, T., Lee, S. S., Park, J., Chung, Y., Na, H. B. *J Am. Chem Soc.* 2001, 123, 12798.
(b) Hyeon, T. *Chem. Commun.* 2003, 919.
- [175] David Martin. M and Boyle F. J: Drug eluting stents for coronary artery disease (review), *Med Eng Phys*, 2010.
- [176] Huizing, M.T., Misser, V.H.S., Pieters, R.C., Huinink, W.W.T., Vencor, C.H.N., Vermorken, J.B., Pinedo, H.M., Beijnen, J.H., 1995. Taxanes-a new class of anticancer agents. *Cancer Invest.* 4, 381–404.
- [177] Brannon-Peppas, L.; *Polymers in controlled drug delivery. Medical Plastics and Biomaterials Magazine*, 1997, (accessed November, 2013)
(<http://www.devicelink.com/mpb/archive/97/11/003.html>).

- [178] Nair, L. S.; Laurencin, C. T.; Biodegradable polymer as biomaterials. *Progress in Polymer Science*, 2007, 32 (8-9), 762-798.
- [179] Anderson, J. M. and Shive M. S. Biodegradation and biocompatibility of PLA and PLGA microspheres, *Adv. Drug Deliv. Rev.* 28 (1997) 5–24.
- [180] Govender, T., S. Stolnik, M.C. Garnett, L. Illum, S.S. Davis, PLGA nanoparticles prepared by nanoprecipitation: drug loading and release studies of a water soluble drug, *J. Control Release* 57 (1999) 171–185.
- [181] Okada, H.; Toguchi, H. Biodegradable microspheres in drug delivery. *Critical Reviews in Therapeutic Drug Carrier Systems*, 1995, 12, 1-99.
- [182] Jackson, J.K., Gleave, M.E., Yago, V., Beraldi, E., Hunter, W.L., Burt, H.M., 2000b. The suppression of human prostate tumor growth in mice by the intratumoral injection of a slow release polymeric paste formulation of paclitaxel. *Cancer Res.* 60, 4146–4151.
- [183] Winternitz, C.I., Jackson, J.K., Oktaba, A.M., Burt, H.M., 1996. Development of a polymeric surgical paste formulation for taxol. *Pharm. Res.* 13, 368–375.
- [184] Liggins, R.T., Burt, H.M., 2004. Paclitaxel-loaded poly (l-lactic acid) microspheres 3: blending low and high molecular weight polymers to control morphology and drug release. *Int. J. Pharm.* 282, 61–71.
- [185] Zhang, X., Jackson, J.K., Burt, H.M., 1996. Development of amphiphilic diblock copolymers as micellar carriers of taxol. *Int. J. Pharm.* 132, 195–206.

- [186] Demetrick, J.S., Liggins, R.T., Machan, L., Davis, N.L., Burt, H.M., Hunter, W.L., 1997. The development of a novel intraperitoneal tumor seeding prophylactic. *Am. J. Surg.* 173, 403–406.
- [187] Rajeev A. Jain: The manufacturing techniques of various drug loaded biodegradable poly(lactide-co-glycolide) (PLGA) devices, *Biomaterials* 21 (2000) 2475–2490.
- [188] Kawashima, Y., H. Yamamoto, H. Takeuchi, and Y. Kuno (2000) Micro-adhesive DL-lactide/glycolide copolymer nanospheres coated with chitosan to improve oral delivery of elcatonin. *Pharm. Develop. Technol.* 5: 77-85.
- [189] Kumari A., Yadav S.K., Yadav S.C., Biodegradable polymeric nanoparticles based drug delivery systems, *Colloids Surf. B Biointerfaces* 75 (2010) 1–18.
- [190] Prokop A., Davidson J.M., Nanovehicular intracellular delivery systems, *J. Pharm. Sci.* 97 (2008) 3518–3590.
- [191] Vert M., Mauduit J., Li S., Biodegradation of PLA/GA polymers: increasing complexity, *Biomaterials* 15 (1994) 1209–1213.
- [192] Wang, H. T., E. Schmitt, D. R. Flanagan, and R. J. Linhardt (1991) Influence of formulation methods on the in vitro controlled release of protein from poly(ester) microspheres. *J. Controlled Release* 17: 23-32.

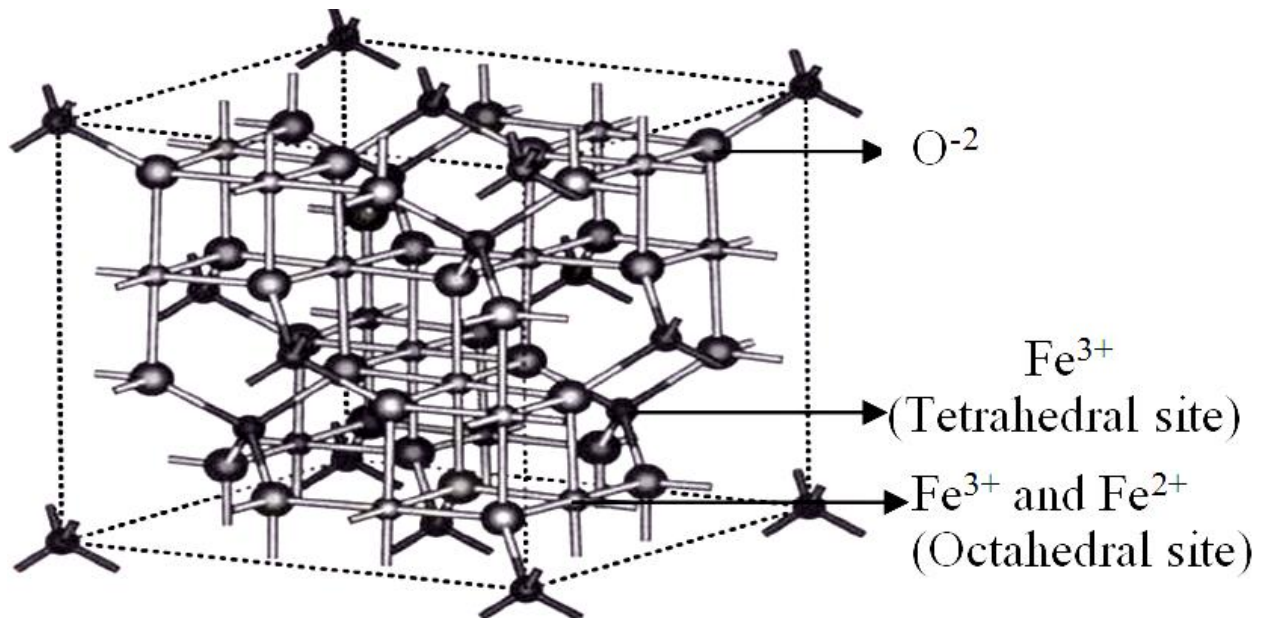


Figure 2.1: Inverse spinel structure of magnetite

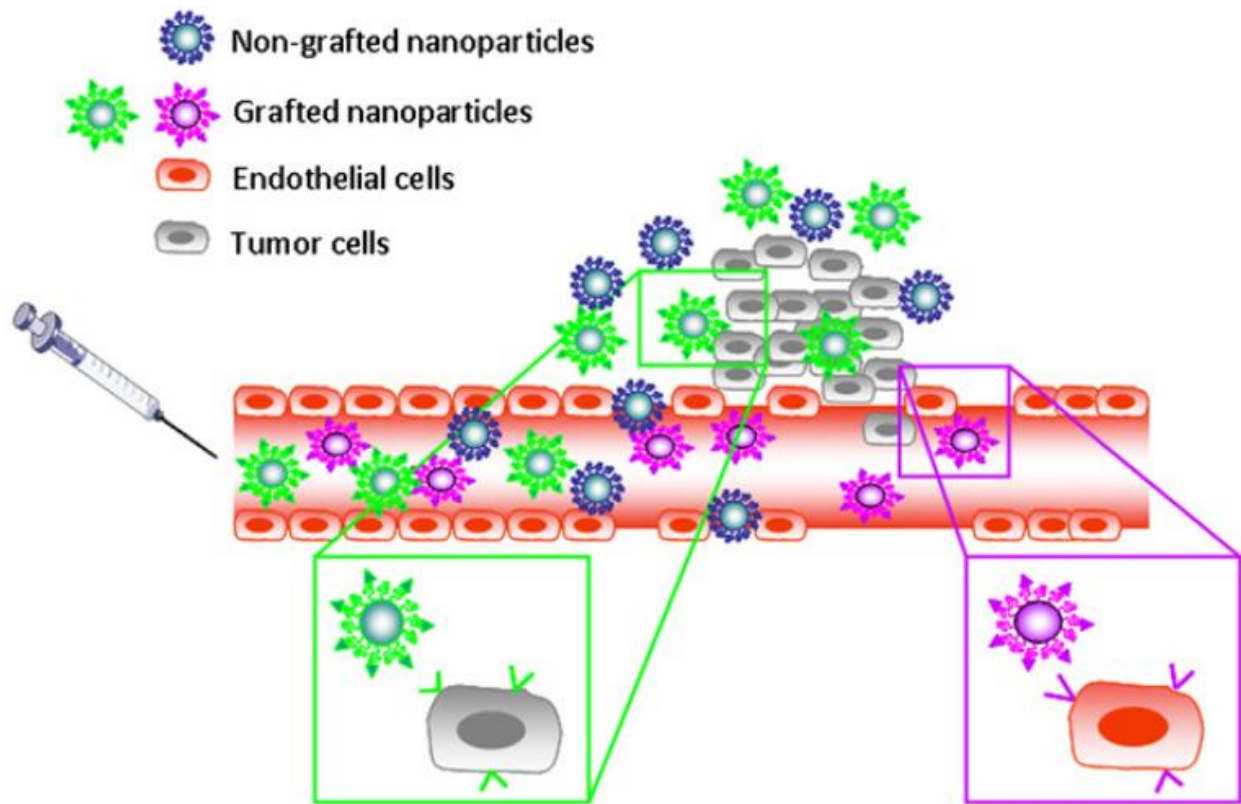


Figure 2.2: Passive and active targeting of nanocarriers. Nanocarriers can reach tumors selectively through the leaky vasculature surrounding the tumors. Ligands grafted at the surface of nanocarriers bind to receptors (over)-expressed by cancer cells (green) or angiogenic endothelial cells (pink). Adapted from Ref [103].

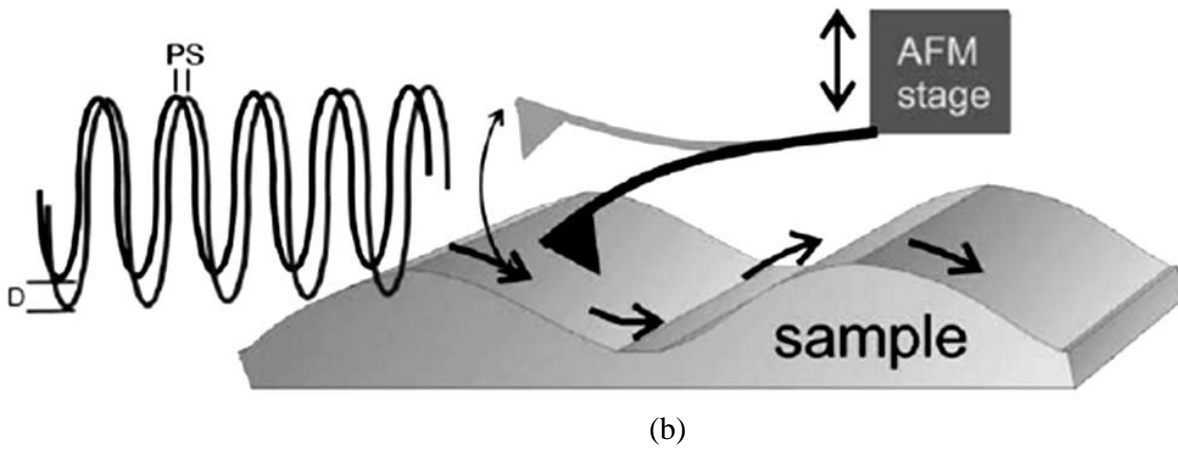
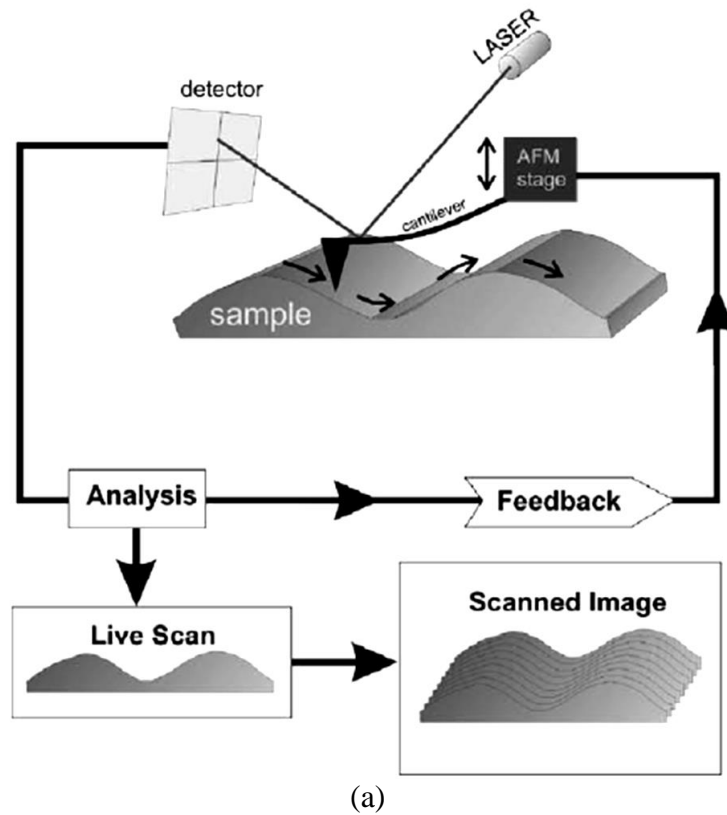


Figure 2.3: Schematic Setup of an AFM in (a) Contact Mode and (b) Tapping Mode (Adapted from Ref. [144]).

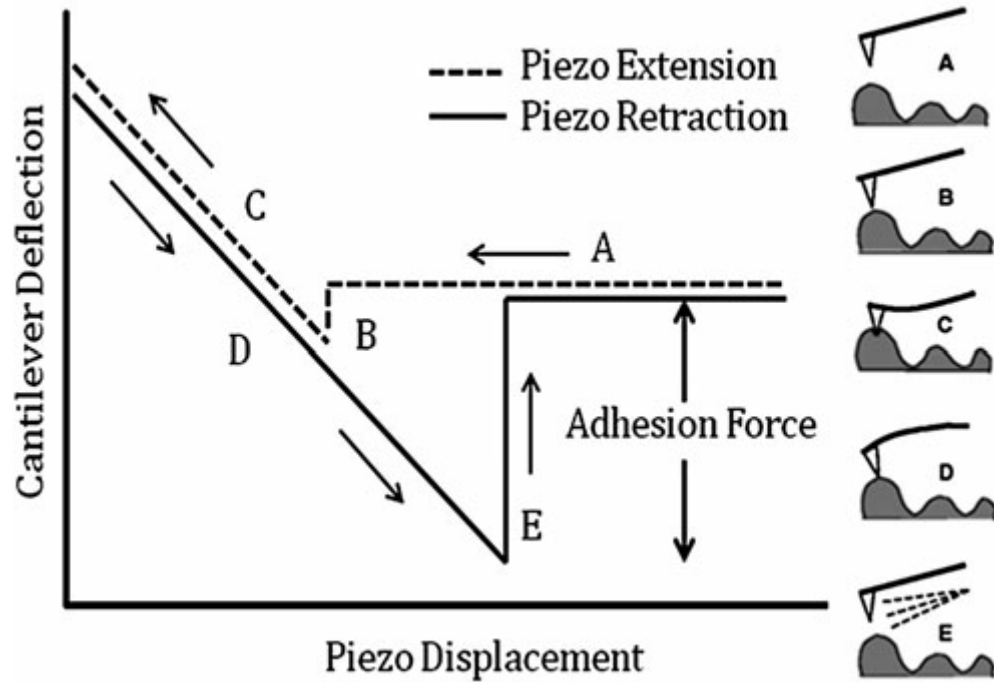


Figure 2:4: Schematic of Typical Deflection-Displacement Plot with Corresponding Stages of Force-Displacement Behavior (Adapted from Ref. [145]).

Chapter 3

3.0 Biosynthesis and the Conjugation of Magnetite Nanoparticles with Luteinizing Hormone Releasing Hormone (LHRH) for the Specific Targeting of Breast Cancer Cells

3.1 Introduction

Cancer is currently the second leading cause of death after cardiovascular diseases [1,2], while breast cancer is the second most common cause of cancer death in women [3,4]. The conventional methods for the diagnosis and treatment of breast cancer include: bulk systematic mammography; ultrasound; dynamic contrast-enhanced fast 3D gradient-echo (GRE) magnetic resonance imaging (MRI); surgery; chemotherapy and radiotherapy [3-6]. However, the current cancer detection methods have limited resolution, especially during the early stages of cancer [5,6]. Furthermore, most of the bulk systemic treatment methods are expensive, while resulting in severe side effects [5-7].

Hence, in recent years, there has been increasing interest in the development of magnetic nanoparticles for the detection and treatment of cancer [8-21]. These include: MRI enrichment/contrast agents [14-16] and the localized delivery of cancer drugs [5,22,23]. In the case of magnetite (Fe_3O_4) nanoparticles (MNPs), there have been significant efforts to explore their applications in cancer detection via magnetic resonance imaging (MRI) [12-19]. Their potential has also been examined for applications in contrast enhancement during MRI of tumor tissue [15].

Furthermore, a number of research groups have investigated the potential use of magnetite in localized hyperthermia for the treatment of cancer [19], while others have used the ability to conjugate magnetite nanoparticles to drugs, proteins, enzymes, antibodies, or nucleotides [15,20,24], to direct their specific attachment to specific cells, organs, tissues, or tumors [20,24]. Such attachment, which can also be facilitated by the use of external magnetic fields, can be used to induce localized heating via alternating magnetic fields that result in hyperthermia at temperatures between ~ 41 and 44 °C [9,10,15,19,21].

Some of the physical and chemical methods [23,25-33] that are often used for the synthesis of MNPs include: micro-emulsion [34,35]; sol-gel synthesis [31,36]; hydrothermal reactions [25,29]; thermal decomposition [34]; pyrolysis [37,38,39]; hydrothermal synthesis [32]; and chemical co-precipitation [34,37,38] methods. MNPs produced by some of the chemical methods have been approved by the US Food and Drug Agency (FDA), as well as the Europe Medicine Agency (EMA) for biomedical applications [40,41].

However, some of the chemical and physical methods (sol-gel synthesis, aerosol synthesis, template assisted synthesis, sonochemical synthesis, laser exposure synthesis, wet-chemical synthesis, thermal decomposition synthesis, plasma synthesis and hydrothermal synthesis) [25,29,31,32,34,36,42] often require several processing steps, controlled pH, high temperature, controlled pressure and the use of expensive equipment. The chemical synthesis of nanoparticles may also involve the use of toxic chemicals as solvents and surfactants. Furthermore, some of the chemical synthesis methods [31-39] may produce hazardous toxic wastes that are potentially

harmful to the environment and humans. Also, physical and chemical synthesis methods can be energy intensive and expensive [42].

There is, therefore, a need for alternative environmentally friendly methods for the synthesis of magnetite nanoparticles that are cost effective and produce biocompatible nanoparticles for biomedical applications. Such needs have stimulated the recent interest in the biological synthesis of MNPs from magnetotactic bacteria (MTB) [43-54]. Magnetite nanoparticles produced by magnetotactic bacteria are generally purely stoichiometric Fe_3O_4 [43-47]. They have been shown to be lacking in minor or significant trace elements, such as Ti, Cr, Mn and Al [43-50], that may have adverse side effects in humans. This is not true for all chemically and physically synthesized MNPs, in which these trace elements may be present.

Biosynthesis, also called biogenesis or anabolism, is an enzyme-catalyzed process that can occur in the cells of living organisms or in their immediate environment. Biosynthesis often involves enzymatic steps, in which the product of one step is used as the substrate for subsequent steps [55], to form more complex products [56]. Magnetotactic bacteria were first discovered by Blackmore in 1975 [43]. They are gram negative, microaerophilic and motile. They also exhibit aquatic life forms that swim along geomagnetic field lines of the earth [43]. They are cosmopolitan in distribution and are found in aquatic environments containing water with pH close to neutral values. Magnetotactic bacteria are generally found in water that is also well oxygenated and not strongly polluted with chemicals or contaminants [43,44]. Furthermore, they are magnetotactic in nature, meaning that they respond to magnetic fields. They also contain intracellular structures (magnetosomes) that encapsulate magnetic nanoparticles [43-45].

The *Magnetospirillum magneticum* (*M.M.*) AMB-1 strain is one of the best known MTB. They are major agents in the global iron cycle, converting iron in the environment to magnetite or greigite within the magnetosomes [45,46]. Magnetite particles can be produced in terrestrial samples, either abiotically or biogenically. The biomineralization of magnetite by bacteria occurs fundamentally by two different modes: biologically-controlled and biologically-induced mineralization (BCM and BIM, respectively) [47,48].

In BCM, magnetotactic bacteria produce well-ordered intracellular crystals of magnetite that exhibit narrow size distributions, consistent species and/or strain-specific morphologies [49-53]. Also, in the case of BIM, nanoparticles may be formed extracellularly by reactions between metabolic by-products and ferric chloride [42,51,53]. However, for BCM, the nanoparticles are synthesized intracellularly by reactions between the cell constituents and ferric chloride [51,53]. MTB have been suggested as agents for the genetic control of magnetic nanoparticle composition, size, morphology and crystallographic orientation [46-49,52-54]. They precipitate magnetite particles within small intracellular membrane vesicles in assemblages known as magnetosomes [42,46-54].

Some researchers [54] have also suggested that the components of intracellular organelles in the MTB may control the biomineralization processes. Furthermore, the pathways for the biosynthesis of magnetic nanoparticles (produced from MTB) are non-toxic, more specific and low cost [42]. The synthesis pathways are capable of producing superparamagnetic magnetite nanoparticles with well controlled sizes and shapes under nontoxic conditions [57]. This process can be used also to form magnetic nanoparticles with a range of sizes (1-100 nm). Such particles

have been shown to have higher catalytic reactivity [58], greater specific surface area [57] and improved contact between the enzyme and metal salts [57,58].

In an effort to ensure the specific targeting of receptors on the surfaces of breast cancer cells by magnetic nanoparticles, significant work has been carried out [13,16-20]. This includes efforts to conjugate and functionalize chemically-synthesized magnetite nanoparticles to luteinizing hormone releasing hormone (LHRH) [16-18]. These prior studies have shown that LHRH-conjugated magnetite nanoparticles can be used to enhance MRI contrast. They may also offer viable alternatives to existing commercially available MNPs for MRI contrast enhancement (Table 3.1). Meng *et al.* [16] have functionalized superparamagnetic iron oxide nanoparticles with LHRH. These have been used for targeting breast cancer cells and contrast enhancement in MRI. The work of Meng *et al.* [16] also suggests the potential of LHRH-SPIONs to enhance the T2 contrast of breast cancer tissue in nude mice models.

Prior work has also been carried out by Leuschner *et al.* [59] on LHRH-conjugated magnetic iron oxide nanoparticles for the early detection of breast cancer metastases. They concluded that LHRH conjugated SPIONs can serve as contrast agents for MRI imaging *in-vivo*. They also confirmed the sensitivity of LHRH-SPIONs for the detection of metastases and disseminated cells in lymph nodes, bones and peripheral organs. Zhou *et al.* [17] have also described superparamagnetic iron oxide nanoparticles (SPIONs) conjugated to LHRH. These have been shown to have the potential to target breast cancer cells/tissue in primary breast tumors and metastases in the lungs of nude mice models.

Transmission Electron Microscopy (TEM) images of distributions of SPIONs has also revealed the accumulation of LHRH-SPIONs in primary breast tumors and their metastases in the lungs [17]. Furthermore, Zhou *et al.* [18] have used TEM to study functionalized magnetic nanoparticles for the targeting breast cancer cells. They revealed the accumulation of individual LHRH-magnetic nanoparticles in the nuclei of breast cancer cells. Their work suggests that LHRH-MNPs are potential carriers that can deliver cancer drugs or DNA to cancer cells.

Prior work [42] has explored the potential applications of microorganisms to the synthesis of magnetite nanoparticles with different shapes and sizes (Table 3.2). Significant efforts have also been made to conjugate chemically synthesized magnetite nanoparticles to LHRH and antibodies [16–18,20,59,60]. Hampp *et al.* [61] have also explored the dip-coating of LHRH peptides to biosynthesized gold nanoparticles. However, there have been no prior efforts to conjugate biosynthesized magnetite nanoparticles to molecular recognition units, such as LHRH. Furthermore, there have been only limited studies of the magnetic properties of the biosynthesized magnetite nanoparticles under conditions that might be relevant to magnetic resonance imaging [29] or magnetically-induced hyperthermia [19]. There is, therefore, a need for further studies of the structure and magnetic properties of biosynthesized magnetite particles in conjugated and unconjugated configurations.

This chapter presents the results of an experimental study of the biosynthesis, structure and magnetic properties of magnetite nanoparticles. The magnetic nanoparticles are produced with different particle sizes and shapes in the presence of *M.M.* at controlled conditions. The effects of functionalization with LHRH are also explored by conjugating biosynthesized magnetite (Fe_3O_4)

nanoparticles (2–50 nm) with [D-Trp6]LHRH (Triptorelin). The magnetic properties of the biosynthesized magnetite nanoparticles are characterized along with their structure and chemistry. Furthermore, the polydispersity indices of the nanoparticles were measured using dynamic light scattering (DLS). The implications of the results are then discussed for the localized targeting and treatment of breast cancer.

3.2 Experimental Procedures

3.2.1 Sample Preparation:

The *Magnetospirillum magneticum* (*M.M.*) strain AMB-1 that was used in this study was obtained from ATCC, Manassas, Virginia, USA. The magnetotactic nature and purity of the strain was validated using hanging drop techniques (HDT) and the capillary race track method (CRTM) [62]. In the case of the CRTM, a capillary tube, closed at one end, was filled with a chemically-defined medium reported by Flies and Moench *et al.* [62,63]. This was done using a hypodermic syringe that was fitted with a Pasteur pipette at the smallest end. The other end of the pipette was used as a reservoir. It was plugged with wet sterile cotton wool. A permanent magnet, with high susceptibility, was placed at the smallest tip of the capillary tube for 3 hours. The bacteria were then observed to migrate towards the plugged tip, after which a sterile syringe was used to collect the bacteria for culturing in an enriched magnetic *spirillum* growth media (EMSGM) at buffered pH values of 4.0, 6.0, 6.5, 7.0, 7.5, 8.5, 9.0, 9.5 and 12.0.

3.2.2 Synthesis of Magnetite Nanoparticles

A standard 1 liter of enriched EMSGM was prepared with 0.74 g of succinic acid, 0.68 g of KH_2PO_4 , 0.12 g of sodium nitrate, 0.02% (0.2 g) of polypeptone, 0.01% (0.1 g) of yeast extract, 0.005% (0.1 g) of L-cysteine component, 2 mL of ferric quinate (obtained from Sigma Aldrich, St Louis, MO, USA). 5 mL of Wolfe's vitamin and 10 mL of Wolfe's mineral that were obtained from ATCC, Manassas, Virginia, USA were added. Subsequently, 1 mL of the *M.M* strain that was purified and cultured with an average population size was inoculated in the EMSGM broth in a standard solution with pH ranging between 4 and 12. This was done in a laminar-flow biosafety hood, under aseptic conditions, to avoid contamination. The samples were then placed in an incubator shaker (New Brunswick Innova 44 Incubator, Console Incubator Shaker, New Brunswick, NJ, USA). This was set to rotate at 141 revolutions per minute (rpm) at 29°C to ensure the uniform growth of the *M.M* for 24 hours within the incubator shaker.

During the 24 hours of exposure of ferric chloride to the MTB, the ferric chloride was exposed to enzymes and other biochemicals produced by the *M.M.* strain. At the end of 24, 48, 72, 96 and 120 hours of incubation, the samples were collected for further testing and characterization. 5 mL of the each sample was collected, washed three times and then centrifuged for 10 minutes at 12 000 rpm to obtain pellets. 100 μL of 20 % sodium dodecyl sulfate (SDS) obtained from Sigma Aldrich, St Louis, MO, USA, was added to each sample prior to mechanical agitation (sonication) to completely expose the nanoparticles within the cells. The entire samples were then washed for four times with PBS (poly butylene succinate). This was followed by washing in distilled water to remove impurities from the system.

3.2.3 Structure of Nanoparticles

An Evolution 300 UV-Visible (UV-Vis) spectrophotometer (Thermo Fisher Scientific, Waltham, MA) was used to characterize the nanoparticles that were synthesized. The sizes and shapes of the nanoparticles were also characterized using a CM100 transmission electron microscope (TEM) (Philips/FEI, Hillsboro, OR, USA). This was combined with electron diffraction (ED) and energy dispersive X-ray spectroscopy (EDS) techniques that were used, respectively, to characterize the structure and chemistry of the nanoparticles. The structure of the magnetite nanoparticles was characterized using powder X-ray diffraction (XRD), (Philips X'Pert powder diffractometer, X'Pert PRO, EA Almelo, Netherlands). This was done using copper $K\alpha$ radiation over 2θ steps of 0.02° , 1 s of counting time per step, and 2θ values between 15° and 60° .

Prior to UV-Visible spectroscopy analysis, 0.5 ml of 12 M HCl and 0.5 ml of 0.5 M potassium thiocyanate were added to the biosynthesized nanoparticles. Upon absorption of the light with a wavelength of ~ 450 (Figure 3.1), the resulting solution turned the pellets containing the nanoparticles red in color. This change of color confirmed the presence of intracellular magnetite nanoparticles, as reported by Meng *et al.* [16]. An Evolution 300 Double Beam Scanning Spectrophotometer (Thermo Fisher Scientific, Waltham, MA, USA) was used to measure the absorbance of each solution from the samples.

From *Beer Lambert's Law*, the absorbance is directly proportional to the path length, b , and the concentration, c , of the absorbing species. The concentrations of the magnetite in solution were also determined from a standard curve that was obtained for a maximum absorbance at a wavelength of ~ 450 nm [16,64]. A calibration curve was thus obtained by plotting the

absorbance at 450 nm against known concentrations of magnetite in solution. Corresponding concentrations of magnetite in solution were determined from the calibration curve. Thus, nanoparticles concentrations were obtained for particles produced over the range of pH conditions that was used in this study.

3.2.4 Ligand Conjugation

The process of ligand conjugation was achieved by carbodiimide reduction (activation), as illustrated in Figure 3.2 [16-18,59,65]. It is a well-established method that has been used to successfully conjugate MNPs [16-18,20,59-61]. However, it is not a green process. Biosynthesized magnetite nanoparticles produced at pH values of 6.5, 7.0, 7.5 and 9.5 were used for ligand conjugation. A [D-Trp6]LHRH (Triptorelin) molecular recognition unit was conjugated with the magnetite nanoparticles using a procedure reported by Kumar *et al.* [65]. Here, 30 mg of biosynthesized magnetite nanoparticles, with diameters between 2 and 30 nm, were dispersed in 3 ml of deionized water. This was done by sonication under nitrogen gas. Freshly prepared carbodiimide solution (30 mg in 1 ml of water) was then added, before further sonication for 10 minutes.

The mixed solutions were then cooled to 4°C before adding a solution of LHRH (3 mg in 1 ml of water). The reaction was maintained at 4°C for 2 h, with intervals of swirling of the conical flask. The flask was then placed on a permanent magnet (Sintered NdFeB Magnets, AA International Inc., Pomona, CA, USA). This was done to allow the conjugated particles to settle. The solution mixture was then decanted to enable the characterization of the functionalized nanoparticles that were formed. Fourier Transform Infra-Red Spectroscopy (FT-IR, Nicolet 5700, Thermo Fisher

Scientific, Waltham, MA, USA) was also used to analyze binding of the ligands to the particles and the surface characteristics of the biosynthesized nanoparticles before and after conjugation with LHRH ligands.

3.2.5 Characterization of Nanoparticle Sizes and Shapes

The morphologies, sizes and the polydispersity of the biosynthesized nanoparticles were characterized after the synthesis and functionalization of the nanoparticles. The characterization was done using TEM as well as the DLS. The nanoparticle samples were dropped onto the TEM carbon-coated copper grids (CF200-Cu, Electron Microscope Sciences, Hatfield, PA). The samples on the grids were then imaged in a model CM100 TEM (Philips/FEI, Hillsboro, OR, USA). Subsequently, images from the TEM were used in the quantitative analysis of the mean particle sizes and shapes. This was done using Adobe Photoshop (CS6 (13.0) Adobe, San Jose, CA, USA).

The hydrodynamic diameter and the polydispersity index (PDI) of the nanoparticles were measured using a Zetasizer-Nano Z590 instrument, DLS (Malvern Instruments, Worcestershire, UK) at Rutgers University, Piscataway, New Jersey, USA. The Zetasizer instrument included a 20 mW, 532 nm diode-pumped solid state laser module and an avalanche photo diode detector. The hydrodynamic diameters and the polydispersity indices (PDIs) were obtained for biosynthesized magnetite nanoparticles (BMNPs) that were synthesized at acidic (pH 6.5), neutral (pH 7.0) and basic (pH 9.5) pH. The PDI were also obtained for ligand (LHRH)-conjugated BMNPs.

Prior to DLS measurements, the synthesized and conjugated BMNP solutions were diluted initially with 0.05 mL of pH 7.4 PBS and subsequently with 0.1 mL of the same solution. This was done to explore the effects of sample concentration on the hydrodynamic diameters and the polydispersity indices. They were then filtered through 0.45 μm polytetrafluoroethylene (PTFE) syringe filters (Whatman, Clifton, NJ) before conducting triplicate DLS measurements. The DLS measurements were performed at room-temperature (25 $^{\circ}\text{C}$) and an incident laser angle of 90° . Particle sizes and size distributions were then generated using the Nicomp number-weighted analysis and multimodal Laplace transform analysis.

3.2.6 Vibrating Sample Magnetometry (VSM)

The magnetic properties of the nanoparticles were measured using Vibrating Sample Magnetometry (VSM). During VSM, 0.5 mg of the samples was placed on a silicon wafer with a cross-sectional area of 5 x 5 mm. This was then fixed in the VSM (Model 740 VSM, Lake Shore Cryotronics, Inc., Westerville, Ohio, USA) at the National University of Singapore (NUS). The magnetic properties of the biosynthesized nanoparticles were compared with those of a chemically synthesized nanoparticle produced by one-pot synthesis in a pyrolysis reaction [66]. The magnetization curves of the biosynthesized magnetite nanoparticles were then measured in response to a magnetic field. The resulting plots obtained were used to characterize the magnetic properties of the biosynthesized and chemically synthesized magnetite nanoparticles, which were studied as a control.

3.3 Results and Discussion

3.3.1 Nanoparticle Synthesis and Structure

The standard absorbance-concentration curve that was obtained for magnetite nanoparticles of known concentrations is presented in Figure 3.3. This shows a plot of absorbance versus known concentrations of magnetite. The linear plot ($r^2 = 0.9962$) is consistent with prior work by Meng *et al.* [16] on chemically synthesized magnetite nanoparticles. This will be used in subsequent sections of this paper to estimate the concentrations of magnetite in solution. The calibration was obtained for absorbance at a wavelength of 450 nm, where the maximum absorbance is known to occur [16].

Plots of the concentration of magnetite nanoparticles (in solution) versus pH are presented in the Figure 3.4. These are presented for exposure of *M.M.* at different pH values. The plots show that the highest concentration of magnetite occurs at a pH of 7.0. This is in agreement with prior reports in the literature [21]. However, in contrast, a pH of 6.5 is least favorable for the formation of magnetite nanoparticles. The slight change in pH between 6.5 and 7.0 clearly had a drastic effect on the BMNP formation. The reasons for this trend are not well understood at the moment. In any case, the concentration of BMNPs formed was found to depend strongly on pH and exposure time.

Selected TEM images of the biosynthesized nanoparticles that were produced from *M.M.* strain are presented in Figures 3.5, 3.7 and 3.8. These were obtained for pH values of 6.5, 7.5 and 9.5, respectively. Figures 3.6 (a-f) present the TEM micrographs of BMNPs produced after growth in medium at a pH of 7.0 for durations of: (a) 24 hours: (b) 48 hours: (c) 72 hours: (d) 96 hours,

and (e)/(f) 120 hours, respectively. The pH values 6.5, 7.0, 7.5 and 9.5 were chosen to represent slightly acidic (pH 6.5), neutral (pH 7.0) and basic (pH of 7.5 and 9.5) conditions. The micrographs also provide interesting insights into the effects of pH on particle size and shape.

The particle shapes were found to include cuboidal and rectangular prisms, and many nearly spherical faceted nanoparticles. The particle sizes also depend on the duration of exposure, as shown in Tables 3.3-3.6. The TEM results show that the BMNPs were formed intracellularly, with a range of particle sizes and shapes. This is because *M.M.* bacteria were recovered after synthesis process, lysed and imaged. However, analysis of the broth in which the bacteria were grown showed that there was a small amount of MNPs present. It is important to note here the low MNP content could be attributed largely to the spillage of the nanoparticles into the broth solution, during the separation or extraction of the bacterial pellet from the media.

The TEM images in Figures 3.5 (a) – 3.5 (e) show the evolution of particle shapes, while the histogram in Figure 3.5 (f) show the distribution of particle sizes. The mean particle sizes ranged from 15 to 30 nm, for exposure durations of up to 120 hours at a pH of 6.5. The particles formed were predominantly faceted and nearly spherical. After exposure to a pH of 7.5, the mean particle sizes ranged from 20 to 50 nm, for the durations of 24, 48, 72, 96 and 120 hours, respectively.

Furthermore, the TEM micrographs in Figure 3.7 (a) to 3.7 (e) show that the nanoparticles that were synthesized at a pH of 7.5 were faceted and more spherical than those formed at a pH of 6.5 (Figure 3.5). Furthermore, the nanoparticles that were formed after exposure to a pH of 9.5

(Figure 3.8), were also faceted and more spherical than those formed at lower pH values of 6.5, 7.0 and 7.5. The slight aggregation of particles at pH 6.5, 7.0, 7.5 and well-defined particles at pH 9.5, may be associated with differences in the distribution of surface charge.

The DLS measurements of hydrodynamic diameters, as well as polydispersity indices (PDIs), are presented in Table 3.7 and Figure 3.9. The measured PDIs show clearly that the representative samples of the biosynthesized nanoparticles were essentially monodispersed (Table 3.7). The PDI values were 0.17 for a pH of 6.5, 0.14 for a pH of 7.0 and 0.19 for a pH of 9.5 for a PBS dilution of 0.05 mL and 0.015 for a pH of 6.5, 0.108 for a pH of 7.0, 0.232 for a pH of 9.5 for a PBS dilution of 0.1 mL. Furthermore, the lowest PDI of 0.07 was obtained for the LHRH-conjugated BMNPs. The trend was different when the sample was diluted to reduce the sample concentration. The monodispersity of the ligand-conjugated BMNPs nanoparticles is consistent with the TEM images presented in Figure 3.10.

The hydrodynamic diameters of the nanoparticle are presented in Figure 3.9. These provide the dimensions of spheres that have the same diffusion coefficients within the same viscous environment of the nanoparticles. The diameters of the BMNPs obtained from TEM and DLS are summarized in Table 3.7. The hydrodynamic diameters were generally much greater than the effective diameters obtained from the TEM images. This could be partly attributed to the adsorption of unknown proteins and biological/organic molecules onto the surfaces of the nanoparticles [67-69]. Such adsorption can promote the formation of nanoparticle clusters that increase the hydrodynamic radii [70]. However, the high magnification TEM images required for

the measurement of individual nanoparticle sizes may not necessarily reveal the statistical variations in the cluster sizes that are formed due to nanoparticle aggregation [70].

In any case, in the current work with a dilution of 0.05 mL (dilution of 1:5) of PBS, the smallest hydrodynamic diameter of $\sim 82.44 \pm 2.00$ nm was associated with biosynthesis at a pH of 6.5. This is comparable to that obtained at a pH of 7.0, where the hydrodynamic diameter was $\sim 83.45 \pm 1.00$ nm. When the dilution was increased to 0.1 mL (dilution of 1:10), the hydrodynamic diameters decreased to a lower values, as shown in Table 3.7. Similar trends have also been reported by other researchers that the measured hydrodynamic diameters depend strongly on sample concentration [67,71,72]. In the current study, the smallest hydrodynamic diameter of $\sim 17.7 \pm 3.00$ nm was associated with biosynthesis at a pH of 7.0, while the highest hydrodynamic diameter of $\sim 100.7 \pm 1.00$ nm occurred at pH 6.5.

In all cases, the semi-quantitative Energy Dispersive X-ray spectroscopy (EDS) analyses revealed that the nanoparticles consisted on Fe, O and C. A typical EDS spectrum is presented in Figure 3.11 for nanoparticles that were biosynthesized at a pH of 7.0 for a duration of 96 hours. Note that the carbon and silicon peaks in the spectrum obtained could be attributed to the specimen mount in the Environmental Scanning Microscope (ESEM) (Model FEI Quanta 200F with Oxford-EDS system IE 250 X Max 80, Philips/FEI, Hillsboro, OR, USA). The presence of iron peaks and oxygen peaks is consistent with the existence of iron oxide nanoparticles (Figure 3.11).

The structure of the iron oxide nanoparticles, elucidated via X-ray diffraction analysis, is presented in Figure 3.12. The noise in the XRD pattern is consistent with the presence of organic materials on the surfaces of the nanoparticles. However, the intensities and locations of the diffraction peaks are consistent with the standard pattern for Fe₃O₄ in the JCPDS card No (79-0417) for magnetite. It is also important to note here that a smaller hematite peak was also observed, as shown in Figure 3.12. However, this peak was within the noise levels in the XRD peaks. In contrast, the dominant peaks in the XRD analyses corresponded to those of magnetite.

3.3.2 Magnetic Properties

Typical magnetization curves obtained for biosynthesized and chemically synthesized uncoated magnetite nanoparticles are presented in Figures 3.13 (a) and 3.13 (b). Figure 3.13 (a) presents the results obtained for nanoparticles that were biosynthesized at a pH of 7.0 for 96 hours. It shows that the particles rapidly approach a saturation magnetization of 2.5 electromagnetic units per gram (emu/g) Fe, compared to the bulk value of 90 emu/g Fe [73,74]. This value is much lower than that of the corresponding bulk because of the smaller size of the particles. Furthermore, the magnetic particles exhibit no diamagnetic contributions and are small enough to exhibit superparamagnetic behavior. Also, the nanoparticles retain negligible remnant magnetization (M_r), after the removal of the magnetic field.

Similar characteristics were observed in the magnetization curves that were obtained from the chemically synthesized magnetite nanoparticles that were produced using a pyrolysis reaction (Figure 3.13 (b)). However, the saturation magnetization levels of the chemically synthesized magnetite were much lower than those of the biosynthesized magnetite (Figure 3.13 (a)).

Furthermore, both the chemically synthesized and biosynthesized magnetite nanoparticles exhibited negligible hysteresis in their magnetization curves, which decreased from the saturation values to almost zero (negligible remnant magnetization), when the applied magnetic fields were removed. Finally, the M-H loops (with coercivity $H_c = \sim 15$ Oe) are very similar, suggesting that a similar magnetization reversal mechanism was responsible for the observed switching behavior. This result indicates strongly that biosynthesized magnetite nanoparticles and chemically synthesized magnetite nanoparticles have equivalent magnetic properties. This suggests that both chemically and biologically synthesized magnetic nanoparticles may be used for contrast enhancement in MRI imaging, or targeted cancer and cardiovascular drug delivery.

3.3.3 Characterization of Conjugated Magnetite Nanoparticles

The conjugation of the biologically synthesized magnetite nanoparticles, BMNPs (Figure 3.10) with Luteinizing Hormone Releasing Hormone (LHRH) was carried by carbodiimide reduction process [16-18,59,65]. The figures show the TEM micrographs of ligand-conjugated BMNPs produced at selected pH and exposure durations. It is interesting to note here that the unconjugated nanoparticles have typical sizes in a range (10-60 nm) (Figure 3.5-3.8). They also appear to have faceted and nearly spherical morphologies, with varying size dispersions. In contrast, the LHRH-conjugated magnetite nanoparticles were less faceted and more spherical in their morphologies (Figure 3.10 b, d and f). They also exhibited a wider range of cluster sizes than the unconjugated BMNPs. However, the individual nanoparticle sizes of the LHRH-conjugated BMNPs were similar to those of the unconjugated BMNPs. The BMNPs sizes were, therefore, in the range that could allow receptor-mediated endocytosis to facilitate the use of LHRH-conjugated MNPs as contrast agents during MRI [16].

The Fourier Transform Infrared (FTIR) spectra obtained from ligand-conjugated biosynthesized iron oxide nanoparticles (BMNPs-LHRH) (in the transition mode) exhibited strong bands in the low frequency region (Figure 3.14). These are due to the iron oxide skeleton [59]. In other regions, the iron oxide spectra have weak bands. The spectra obtained from 4100 to 500 cm^{-1} were found to be consistent with those of magnetite (Fe_3O_4) [75-77]. FTIR spectral analysis of LHRH peptide bound magnetite nanoparticles (Figure 3.14) also revealed the presence of characteristic bands of $-\text{NH}_2$ (3400 and 2850 cm^{-1}) and the signatures of LHRH. The results, therefore, suggest the attachment of LHRH to amines on the magnetite nanoparticles. This result is similar to the chemically synthesized MNPs conjugated with LHRH [16,21,59,65]. The FTIR spectral analysis of peptide bound MNPs reveals the absence of $-\text{NH}_2$ (3200 and 16525) presence in unbound nanoparticles (Table 3.8). Also, it was clear from the TEM micrographs that the LHRH-conjugated BMNPs are nearly monodisperse and non-aggregated, with a mean diameter of $\sim 30 \pm 4$ nm.

3.3.4 Nanoparticle Formation

The current results suggest that biosynthesized magnetite nanoparticles form predominantly by an intracellular mechanism in the presence of *M.M.*. Prior work has shown that the particles are formed by biomineralization [43-46,78]. The studies, based also on prior work, suggest that the nanoparticle formation is facilitated by intracellular organelles (magnetosomes) in the bacteria [42,46-54]. The membrane of the magnetosomes contain a protein called ferritin, which is a globular protein complex, consisting of about 24 sub-unit capable of storing iron in soluble and

non-toxic form [78,79]. These proteins are thought to play a vital role in the formation of the iron oxide nanoparticles, as well as the nucleation of minerals and their redox and pH control [79].

In the EMSGM, the entire reagents play a vital role in the formation of the magnetite nanoparticles [80]. Just as the L-cysteine induces cell growth, the polypeptide increases the final cell density, while the vitamins enrich the growth media [80]. Furthermore, during the nanoparticle nucleation and growth process, ferric chlorides dissociate to form Fe^{3+} in solution. OH^- ions are also present in the aqueous medium. The Fe^{3+} is taken up by the cell through the cytoplasm membrane and reduced to Fe^{2+} . The reduced Fe^{2+} is then taken up and reoxidized through the magnetosomes to form hydrous ferric oxide through passive sorption of dissolved iron in the magnetosomes. This is thought to be dehydrated to form the hydrated form of iron oxide $\text{Fe}(\text{OH})_3$ [81,82]. The ferritins present in the magnetosomes then aid the dehydration to enable the formation of iron oxide (Fe_3O_4) nanoparticles [45-54,78].

3.4 Implications

The implications of the current work are quite significant for the synthesis of magnetic nanoparticles from biological systems, for a variety of applications [8,13,16-19,21,29,58,59,65,83]. First, the current results show that the *M.M.* strain promotes the intracellular formation of mostly spherical and faceted magnetite. The biosynthetic approach is also simple, economical and environmentally friendly, compared to the conventional chemical and physical methods of producing magnetite [42].

Furthermore, some chemically- and physically-synthesized magnetite nanoparticles often may involve the use of toxic chemicals that may produce hazardous toxic wastes that are harmful, not only to the environment, but also to human health [42]. Thus, such nanoparticles could be associated with high cost, due to the relatively high energy cost of some synthesis techniques. This suggests that the development of low cost biosynthetic pathways could facilitate a more economical application of magnetite nanoparticles in the detection and treatment of diseases such as cancer [84] and cardiovascular disease [85]. The methods can also be extended to the detection of some poverty-related diseases such as malaria [8, 86] and tuberculosis [87].

The current work describes the biosynthesis of magnetite nanoparticles at different pH and exposure growth durations as well as the conjugation with LHRH for possible applications in the specific targeting of breast cancer cells. The nanoparticles sizes obtained from the TEM and the DLS measurements for the less concentrated solutions suggest that the LHRH-conjugated BMNPs may be suitable for biomedical applications. In the case of cancer, biosynthesized magnetite nanoparticles have been conjugated with LHRH, a molecular recognition unit (MRU) that can attach specifically to over-expressed receptors on the surfaces of cancer cells [88-90]. MRUs, such as LHRH, could therefore facilitate the specific attachment of nanoparticles to cancer cells/tumors, thereby promoting potential applications in magnetic resonance imaging [29,91] and localized drug delivery from tumor shrinkage [17,18,88].

Similar approaches could also be used to target fatty cells in atherosclerotic blood vessels [92]. As in the case of cancer, over-expressed receptors on the fatty cell surfaces could be targeted with specific ligands [93]. These could, therefore, be used to promote the attachment of

magnetite for enhanced magnetic resonance imaging (MRI) of blocked arteries. The MRUs could also be attached to drug nano-carriers that could dissolve or destroy fatty cell build-up in blood vessels before they induce vessel blockage and death.

Further research is needed to determine the optimal concentration of BMNPs from DLS measurements and *in-vitro/in-vivo* studies. There is also need to explore the effectiveness of the ligand conjugated BMNPs in the targeting of diseased cells under *in-vitro and in-vivo* conditions. These are clearly some of the challenges and opportunities for future work.

3.5 Summary and Concluding Remarks

1. A *Magnetospirillum magneticum* strain was used for the biosynthesis of magnetite nanoparticles with sizes between 10 and 60 nm. The formation of magnetite was promoted by the reaction between ferric chloride and the *M.M* bacteria. The formation of magnetite was confirmed via X-ray analysis and UV-Visible spectrophotometry at a maximum absorbance that was identified for magnetite at a wavelength of ~ 450 nm. The results show that *M.M.* bacteria in the presence of ferric chloride, promote the formation of magnetite nanoparticles. Further work is needed to develop a basic understanding of how the observed shapes and sizes change are controlled by nucleation and growth processes in biochemical environments.
2. The TEM analyses revealed that the mean particle sizes and shapes depend strongly on the pH and durations of growth. The resulting particles had size ranges between ~ 10 and 60 nm, after synthesis for durations between 24 and 120 hours. Most of the nanoparticles were

faceted. However, an increasing incidence of nearly spherical nanoparticles was observed with increasing pH between 6.5 and 9.5. Furthermore, EDS analyses revealed that the MNPs contained iron and oxygen peaks, while the XRD analysis showed that the incidence of magnetite nanoparticles was much greater than that of hematite.

3. Dynamic light scattering (DLS) studies of nanoparticles revealed interesting trends in the hydrodynamic diameter and the polydispersity indices of the BMNPs. The higher sample concentration in 0.05 mL PBS solution (1:5) resulted in a higher hydrodynamic diameter of 735.9 ± 5 nm, while the lower sample concentration in 0.1 mL PBS solution (1:10) resulted in a hydrodynamic diameter of 58.6 ± 2 , in the case of the LHRH-conjugated BMNPs. The DLS results also showed that the synthesized BMNPs were essentially monodispersed, with polydispersity indices in a range that is suitable for biomedical applications. Future efforts are needed to establish the optimum concentration of BMNPs for potential applications in nano-medicine.
4. VSM was used to study the magnetic properties of the BMNPs. The particles exhibited superparamagnetic behavior with no diamagnetic contribution. They are of particular interest as they do not retain any magnetism after removal of a magnetic field. This suggests that they may be used to enrich the MRI images associated with the early detection and localized treatment of cancer and arteriosclerosis.
5. The LHRH-conjugation of the BMNPs resulted in individual nanoparticles with sizes in the range between 10 and 60 nm. The FTIR results also suggest that the LHRH MRUs are chemically bound to the magnetite nanoparticles through amines. Further work is needed to explore their potential applications in cancer/cardiovascular disease and treatment.

References

- [1] B. Peter and L. Bernard. “The World Cancer Report” World Health Organization. 2008.
- [2] J. Mackay and G.A. Mensah “The Atlas of Disease and Stroke” Published by the World Health Organization in Collaboration with the Centers for Disease Control and Prevention, (2004). ISBN-13 97892415.
- [3] D. Cutierrez. “Cancer Facts and Figures. 2nd Edition. America Cancer Society, 2008.
- [4] A. Jemal, T. Murray, A. Samuels, A. Ghafoor, E. Ward, M. J Thun. “Cancer statistics”, 2003. *CA Cancer J Clin* (2003) 53:5–26.
- [5] D. Needhama and M. W. Dewhurst. “The Development and Testing of a New Temperature-Sensitive Drug Delivery System for the Treatment of Solid Tumors”. *Advanced Drug Delivery Reviews*. Elsevier, (2001) 53, 285–305.
- [6] B. Hildebrandt, W.P. Ceelen and P. Wust in: (Ed), “Peritoneal Carcinomatosis: A Multidisciplinary Approach”, Springer, New York, (2007) 185.
- [7] A. V. Hoek, C. Theriault, Y. Oni and W. O Soboyejo. “Effects of Temperature on Diffusion from PNIPA-Based Gels in a BioMEMS Device for Localized Chemotherapy and Hyperthermia”. *Materials Science and Engineering C*, (2010) 2011.
- [8] Q. A. Pankhurst, J. Connolly, S. K. Jones and J. Dobson. “Topical Review: Applications of Magnetic Nanoparticles in Biomedicine”. June (2003) *J. Phys. D: Appl. Phys.* 36-R167–R181.
- [9] I. Hilger, W. Andra, R. Hergt, R. Hiergeist, H. Schubert and W.A. Kaiser. “Electromagnetic Heating of Breast Tumors in Interventional Radiology: *In-Vitro* and *In-Vivo* Studies in Human Cadavers and Mice”. *Radiology* 218 (1997) 570.

- [10] A. Jordan, P. Wust, H. Fahling, W. Jonh, A. Hinz, and R. Felix. *International Journal of Hyperthermia* 9 (1997) 51.
- [11] P. Moroz, S. K. Jones and B. N. Gray, *International Journal of Hyperthermia* 18 (2002) 267.
- [12] C. Lok, *Nature* 412 (2001) 372.
- [13] A. Petri-Fink, M. Chastellain, L. Juillerat-Jeanneret, A. Ferrari and H. Hofmann. “Development of Functionalized Magnetic Nanoparticles for Interaction with Human Cancer Cells”. *Biomaterials* 26 (2005) 2685.
- [14] J. W. M. Bulte, M. Cuyper, D. Despres and J. A. Frank, *Journal of Magnetism and Magnetic Materials* 194 (1999) 204.
- [15] H. Pardoe, P. R Clark, T. G St Pierre, P. Moroz, S. K Jones. *Magnetic Resonance Imaging*. (2003) 21:483–488.
- [16] J. Meng J. Fana, G. Galiana, R.T. Branca , P.L. Clasen, S. Ma , J. Zhou , C. Leuschner, C.S.S.R. Kumar, J. Hormes, T. Otit, A.C. Beye, M.P. Harmer, C.J. Kiely, W. Warren, M.P. Haataja and W.O. Soboyejo “LHRH-Functionalized Superparamagnetic Iron Oxide Nanoparticles for Breast Cancer Targeting and Contrast Enhancement in MRI” *Materials Science and Engineering C* 29 (2009) 1467–1479.
- [17] J. Zhou, C. Leuschner, C. Kumar, J.F. Hormes and W.O. Soboyejo. *Biomaterials* 27 (2006) 2001.
- [18] J. Zhou, C. Leuschner, C. Kumar, J. Hormes and W.O. Soboyejo. *Materials Science and Engineering C* 26 (2006) 1451.

- [19] M. Shinkai, M. Yanase and M. Suzuki. "Intracellular Hyperthermia for Cancer Using Magnetite Cationic Liposomes". *Journal of Magnetism and Magnetic Materials*. (1999) 194, 176184.
- [20] J. Meng, E. Paetzell, A. Bogorad, and W. O. Soboyejo, "Adhesion between Peptides/Antibodies and Breast Cancer Cells". *Journal of Applied Physics* (2010): 107, 114301.
- [21] W. Zhou, W. He, and S. Zhong. "Biosynthesis and Magnetic Properties of Mesoporous Fe₃O₄ Composites". *Journal of Magnetism and Magnetic Materials*. (2009) 321, 1025–1028.
- [22] F. J. Lazaro, A. R. Abadia, M. S. Romero, L. Gutierrez, J. Lazaro and M. P. Morales. *Biochim Biophys Acta*. (2005) 1740:434–45.
- [23] Y. Zhao, Z. Qiu and J. Huang, "Preparation and Analysis of Fe₃O₄ Magnetic Nanoparticles Used as Targeted-drug Carriers". *Chinese J. Chem. Eng.* (2008) 16 (3), 451-455.
- [24] C. C. Berry and A. S. G. Curtis. "Functionalisation of magnetic nanoparticles for applications in biomedicine". *J Phys D: Appl Phys* (2003); 36:R198–206.
- [25] P. Tartaj, M.P Morales, S. Veintemillas-Verdaguer, T. Teresita Gonzalez-Carreno and J. Carlos Serna. "The Preparation of Magnetic Nanoparticles for Applications in Biomedicine". *J. Phys. D: Appl. Phys.* (2003) 36, R182– R197.
- [26] L. Vekas, D. Bica and M. V. Avdeev. "Magnetic Nanoparticles and Concentrated Magnetic nanofluids: Synthesis, Properties and some Applications" *China Particu.* (2007) 5, 43-49.

- [27] S. Wang, Z. Yang and W. Sun. "Preparation and Characterization of Antifouling Thermosensitive Magnetic Nanoparticles for Applications in Biomedicine", *Mater. Sci. Engin. C* (2009) C (29), 1196–1200.
- [28] S. P. Gubin, Yu. A. Koksharov, G. B. Khomutov, G. Yu. Yurkov. *Russian Chemical Reviews* (2005).74 (6) 489 ± 520
- [29] T.K. Indira and P.K. Lakshmi. "Magnetic Nanoparticles – A Review". *International Journal of Pharmaceutical Sciences and Nanotechnology*, December (2010) Volume 3 - Issue 3-October -.
- [30] Y. F. Shen, J. Tang, Z. H. Nie, Y. D Wang, Y. Renc and L. Zuo, "Preparation and Application of Magnetic Fe₃O₄ Nanoparticles for Wastewater Purification". *Sep. Purif. Technol.* (2009) 68, 312–319.
- [31] H. Yang, W. Fu, K. Du, Y. Sui, J. Chen, Y. Zeng, M. Li and G. Zou. "Preparation and Magnetic Properties of Magnetite Nanoparticles by Sol–gel Method". *J. Magn. Magn. Mater.* (2007) 309, 307-311.
- [32] A.K. Gupta and M. Gupta. "Synthesis and Surface Engineering of Iron Oxide Nanoparticles for Biomedical Applications". *Biomaterials* (2005) 26, 3995–4021.
- [33] K. Aslam, "Preparation and Characterization of Magnetic Nanoparticles Embedded in Microgels". *Mater. Lett.* (2008) 62, 898–902.
- [34] A.-H. Lu, E. L. Salabas and F. Schüth "Magnetic Nanoparticles: Synthesis, Protection, Functionalization, and Application". *Angew. Chem. Int. Ed.* 46 (8): (2007). 1222–1244. doi:10.1002/anie.200602866.

- [35] S S.Rana, J. Philip and B. Raj "Micelle Based Synthesis of Cobalt Ferrite Nanoparticles and its Characterization using Fourier Transform Infrared Transmission Spectrometry and Thermogravimetry". *Materials Chemistry and Physics* 124: (2010). 264–269.
- [36] D. Bose, S. Bid, S. K. Pradhan, M. Pal and D. Chakrovorty *J. Alloys Compd.* 343 (2002).
- [37] M. Fang, V. Ström, R. T. Olsson, L. Belova, K. V. Rao, *Appl. Phys. Lett.* 99, 222501 (2011)
- [38] R. N. Grass, N. Robert and W. J. Stark "Gas Phase Synthesis of FCC-Cobalt Nanoparticles". *J. Mater. Chem.* (2006). 16 (16): 1825. [doi:10.1039/B601013J](https://doi.org/10.1039/B601013J).
- [39] E. K. Athanassiou, K. Evagelos, R. N. Grass and W. J. Stark "Chemical Aerosol Engineering as a Novel Tool for Material Science: From Oxides to Salt and Metal Nanoparticles". *Aerosol. Sci. Tech.* 44 (2): (2010) 161–72.
- [40] V. Herynek, Z. Berkova, D. Horak, M. Babic, D. Jirak, F. Saudek, M. Hajek; Alternative Labels for Visualization of Pancreatic Islets. *Proc. Intl. Soc. Mag. Reson. Med.* 2010;18:4200.
- [41] Provenzano R., Schiller B., Rao M., Coyne D., Brenner L., Pereira B.J. Ferumoxytol as an Intravenous Iron Replacement Therapy in Hemodialysis Patients. *CJASN.* 2009;4:386–393.
- [42] X. Li, H. Xu, Z. Chen and G. Chen., "Biosynthesis of Nanoparticles by Microorganisms and their Applications". *Journal of Nanomaterials* vol (2011), Article ID 270974.
- [43] R. P. Blackmore, *Science*, (1975), 190, 377.
- [44] R. P. Blakemore, D. Maratea and R. S. Wolfe. 1979 *Journal of Bacteriol.* 140 720
- [45] D. A. Bazyliniski, R.B. Frankel and K. O., Konhauser. (2007) *Journal of Geomicrobiol.* 24 465

- [46] R. B. Frankel and D. A. Bazylinski, "Magnetosome Mysteries-Despite Reasonable Progress Elucidating Magnetotactic Microorganisms, Many Questions Remain," *ASM News*, (2004), Volume 70, Number 4, p.176-183
- [47] H. A. Lowenstam "Minerals formed by organisms". *Science* (1981). 211, 1126–1131.
- [48] S. Mann. "On the Nature of Boundary-Organized Biomineralization". *J. Inorg. Chem.* 28, (1986) 363–371
- [49] S. Mann, T. T. Moench and R. J. P. Williams. "A High Resolution Electron Microscopic Investigation of Bacterial Magnetite: Implications for Crystal Growth". *Proc. R. Soc. Lond. Ser. B* 221, (1984b), 385–393.
- [50] K. M. Towe and T. T. Moench. "Electron-optical Characterization of Bacterial Magnetite". *Earth Planet. Sci. Lett.* 52, (1981), 213–220.
- [51] S. Mann and R. B. Frankel. "Magnetite Biomineralization in Unicellular Organisms. In *Biomineralization: Chemical and Biochemical Perspectives*" (eds. S. Mann, J. Web, R. J. P Williams) (1989) p. 426. VCH Press, Weinheim, Germany.
- [52] D. A. Bazylinski. "Structure and Function of the Bacterial Magnetosome". *ASM News* 61, (1995) 337–343.
- [53] D. A. Bazylinski. and B. M. Moskowitz. "Microbial Biomineralization of Magnetic Iron Minerals: Microbiology, Magnetism, and Environmental Significance. In *Geomicrobiology: Interactions between Microbes and Minerals*" (eds. J. F. Banfield and K. H. Nealson). (1997) pp.181– 23. Mineralogical Society of America, Washington, DC.
- [54] Y. A. Gorby, T. J. Beveridge and R. P. Blakemore. "Characterization of the Bacterial magnetosome membrane". *J. Bacteriol.* (1988) 170, 834–841.

- [55] Jones, R. Celyn, Buchanan, B. Bob, Gruissem, and Wilhelm, “Biochemistry and Molecular Biology of Plants”. Rockville, Md: American Society of plant Physiologist. Pp. 371-2. ISBN 0-943088-39-9.
- [56] Albert and Bruce, Molecular Biology of the Cell. New York: Garland Science. (2002) ISBN 0-8153-3218-1.
- [57] R. Bhattacharya and P. Mukherjee, “Biological Properties of Naked Metal Nanoparticles”. Advanced Drug Delivery Reviews. (2008) 60, 1289–1306.
- [58] K. Simkiss and K.M. Wilbur, Biomineralization. Academic, New York, 1989.
- [59] C. Leuschner, C.S.S.R. Kumar, W. Hansel, J. Zhou, W. O. Soboyejo, J. Hormes, Breast Cancer Res. Treat. Springer 2006 DOI 10.1007/s10549-006-9199-7. 99 (2006) 163–176.
- [60] R. Lawaczeck, H. Bauer, T. Frenzel, M. Hasegawa, Y. Ito, K. Kito, N. Miwa, H. Tsutsui, H. Vogler and H.J. Weinmann, Acta Radiol. 38 (1977) 584–597.
- [61] E. Hampp, R. Botah, S. O. Odusanya, N. Anuku, K. Malatesta and W.O. Soboyejo. “Biosynthesis and Adhesion of Gold Nanoparticles for Breast Cancer Detection and Treatment” Journal of Materials Research; Nov (2012) Vol. 27 Issue 22, p2891.
- [62] T. T. Moench and W. A. Konetzka, “A Novel Method for the Isolation and Study of a Magnetotactic Bacterium”. Arch. Microbiol., (1978) 119, 203–212.
- [63] C. B. Flies, J. Peplies and D. Schuler. “Combined Approach for Characterization of Uncultivated Magnetotactic Bacteria from various Aquatic Environments”. Appl. Environ. Microbiol., (2005) 71, 2723–2731.
- [64] P. Kesarwani, K. T. Rakesh and N. K. Jain, “Spectrophotometric Estimation of Paclitaxel” International Journal of Advances in Pharmaceutical Sciences 2 (2011) 29-32.

- [65] C.S.S.R. Kumar, C. Leuschner, E.E. Doomes, L. Henry, M. Juban and J. Hormes, *Journal of Nanoscience and Nanotechnology* 4 (2004) 245.
- [66] W. S. Chiu, S. Radiman, M. H. Abdullah, P. S Khiew, N. M Huang, and R. Abd- Shukor. “One Pot Synthesis of Monodisperse Fe₃O₄ Nanocrystals by Pyrolysis Reaction of Organometallic Compound” *Journal of Materials Chemistry and Physics* 106 (2007) 231-235.
- [67] J. Lim, S. P. Yeap, H. X. Che and S. C. Low; Characterization of magnetic nanoparticle by dynamic light scattering. *Nanoscale Research Letters* 2013 8:381
- [68] L. Zhang, R. He, H. C. Gu: Oleic acid coating on the monodisperse magnetite nanoparticles. *Appl Surf Sci* 2006, 253:2611–2617.
- [69] Z. Wang, X. D. Wen, R. Hoffmann, J. S. Son, R. Li, C. C. Fang, D. M. Smilgies, T. H. Hyeon: Reconstructing a solid-solid phase transformation pathway in CdSe nanosheets with associated soft ligands. *Proc Natl Acad Sci USA* 2010, 107:17119–17124.
- [70] F. D. Sikkema, M. Comellas-Aragone`s, R. G.Fokkink, B. J. M.Verduin, J. J. L. M. Corn elissen, R. J. M.Noltea, *Org. Biomol. Chem.* **2007**, 5, 54.
- [71] M. Elimelech, J. Gregory, X. Jia, R. A Williams: *Particle Deposition and Aggregation: Measurement, Modeling and Simulation*. Stoneham: Butterworth-Heinemann; 1998.
- [72] M. R Gittings, D. A Saville: The determination of hydrodynamic size and zeta potential from electrophoretic mobility and light scattering measurements. *Colloid Surface A: Physiochem Eng Aspects* 1998, 141:111–117.
- [73] C. Hu, Z. Gao and X. Yang, *J. Magn. Mater.* 320 (2008) 70.

- [74] X. Liu, M. D. Kaminski, Y. Guan, H. Chen, H. Liu and A. J. Rosengart. "Preparation and Characterization of Hydrophobic Superparamagnetic Magnetite Gel". *J. Magn. Magn. Mater.* (2006) 306, 248–253
- [75] A.K. Gupta and S. Wells, "Surface-Modified Superparamagnetic Nanoparticles for Drug Delivery: Preparation, Characterization, and Cytotoxicity Studies", *IEEE Transactions on Nanobioscience*, March (2004). Vol. 3, No. 1
- [76] R. M. Cornell and U. Schwertmann, "The Iron Oxide: Structure, Properties, Reactions, Occurrence and Uses". Weinheim: VCH; 1996.
- [77] M. Ma, Y. Zhang, W. Yu, H-Y. Shen, H-Q. Zhang and N. Gu "Preparation and Characterization of Magnetite Nanoparticles Coated by Amino Silane". *Colloids Surf A: Physicochem Eng Aspects* (2003) 212:219–226.
- [78] D. Schuler. "Characterization of the Magnetosome Membrane in *Magnetospirillum gryphiswaldense*". In *Biom mineralization* (Baeuerlein, E., ed.), (2000) pp. 109–118, Wiley-VCH.
- [79] D. Schuler and R. B Frankel. "Bacterial Magnetosomes: Microbiology, Biom mineralization and Biotechnological Applications". *Appl. Microbiol. Biotechnology.* (1999) 52, 464–473.
- [80] C. Yang, H. Takeyama, T. Tanaka and T. Matsunaga. "Effects of Growth Medium Composition, Iron Sources and Atmospheric Oxygen Concentrations on Production of Luciferase-bacterial Magnetic Particle Complex by a Recombinant *Magnetospirillum magneticum* AMB-1". *Enzyme and Microbial Technology* (2001) 29: 13–19.
- [81] G.A Clegg *Proc. Biophys. Mol. Biol.* (1980) 36, 56-80.
- [82] R. R. Chrichton and F. Roman. (1978) *J. Mol. Catal.* 4, 75-82.

- [83] S. D. Caruthers, S. A. Wickline and G.M. Lanza. “Nanotechnological Applications in Medicine”. *Current Opinion in Biotechnology*, (2007) 18, 26-30.
- [84] A. Petri-Fink, M. Chastellain, L. Juillerat-Jeanneret, A. Ferrari and H. Hofmann. “Development of Functionalized Magnetic Nanoparticles for Interaction with Human Cancer Cells”, *Biomaterials* 26 (2005) 2685.
- [85] M. David and F. Boyle. “Drug Eluting Stents for Coronary Artery Disease (Review)”, *Med Eng Phys*, 2010.
- [86] F. Paul, D. Melville, S. Roath and D. Warhurst. “A Bench Top Magnetic Separator for Malarial Parasite Concentration” *IEEE Trans. Magn.* (1981) MAG-17 2822–4
- [87] A. L. Chun, “Nanoparticles Offer Hope for TB detection, *Nature Nanotechnology* 4, 698 - 699 (2009) doi:10.1038/nnano.(2009).322
- [88] C. Leuschner, C.S.S.R. Kumar, W. Hansel, J. Hormes, *J. Biomed. Nanotechnol.* 2 (2005) 229–233.
- [89] M. Bolla, L. Collette, L. Blank, P. Warde, J. B. Dubois, R. O. Mirimanoff, G. Storme, J. Bernier, A. Kuten, C. Sternberg, J. Mattelaer, J. L. Torecilla, J. R. Pfeffer, C. L. Cutajar, A. Zurlo, M. Pierart. *The Lancet* 360 (2002) 103-6.
- [90] G. Molema and D. K. F Meijer. *Drug Targeting*, WILEY-VCH, 2001.
- [91] J.W.M. Bulte, M. D. Cuyper, D. Despres. Preparation relaxometry, and biokinetics of PEGylated Magnetoliposomes as MRI agent. *Journal of Magnetism and Magnetic Materials* 194 (1999) 204-9 .
- [92] P. Kurtzhals, S. Havelund, I. Jonassen, J. Markussen, “Effect of Fatty Acids and Selected Drugs on the Albumin Binding of a Long Acting, Acylated Insulin Analogue”. *J Pharm Sci* (1997) 86:1365-1368

- [93] T. Lemberger, B. Desvergne, W. Wahli PPARs: “A Nuclear Receptor Signaling Pathway in Lipid Metabolism”. *Annu Rev Cell Dev Biol* (1996)12:335–363.
- [94] T. P. Gonzalez, C. J. Lopez, A. L. Neal, *et al.* “Magnetite Biomineralization Induced by *Shewanella oneidensis*”. *Geochimica et Cosmochimica Acta.* (2010) 74, 967–979.
- [95] K. Zhu, H. Pan, J. Li. “Isolation and Characterization of a Marine Magnetotactic *Spirillum* Axenic Culture QH-2 from an Intertidal Zone of the China Sea”. *Research in Microbiology.* (2010) 161, 276-283.
- [96] Y. Amemiyaa, A. Arakakia, S. Sarah, “Controlled Formation of Magnetite Crystal by Partial Oxidation of Ferrous Hydroxide in the Presence of Recombinant Magnetotactic Bacterial Protein Mms6”. *Biomaterials.* (2007) 28, 5381–5389.
- [97] W. Li, L. Yu, P. Zhou. “A Magnetospirillum strain WM-1 from Fresh Water Sediment with Intracellular Magnetosomes”. *World Journal Microbiol Biotechnol.* (2007) 23, 1489–1492.
- [98] C.T. Lefèvre, F. Abreu, M.L. Schmidt. “Moderately Thermophilic Magnetotactic Bacteria from Hot Springs in Nevada. *Applied and Environment Microbiology.* (2010) 76, 3740–3752.

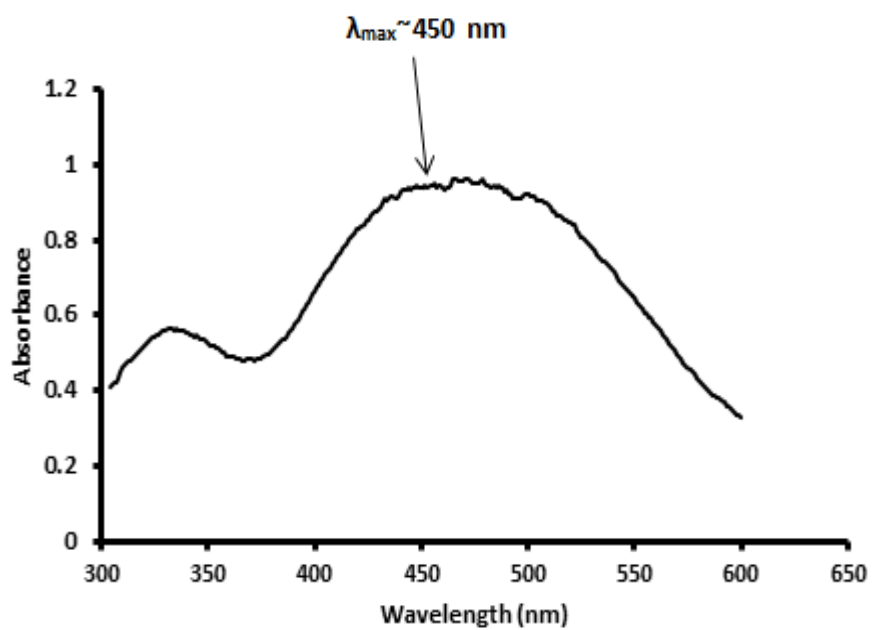


Figure 3.1: UV-Vis scan of magnetite nanoparticles. Arrow represents the existence of a peak at a wavelength, λ_{max} , of 450 nm.

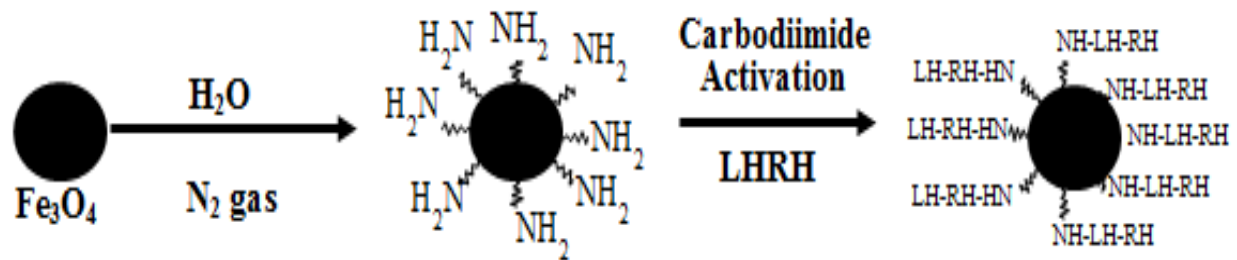


Figure 3.2: Schematic of reaction pathway for the functionalization of magnetite nanoparticles.

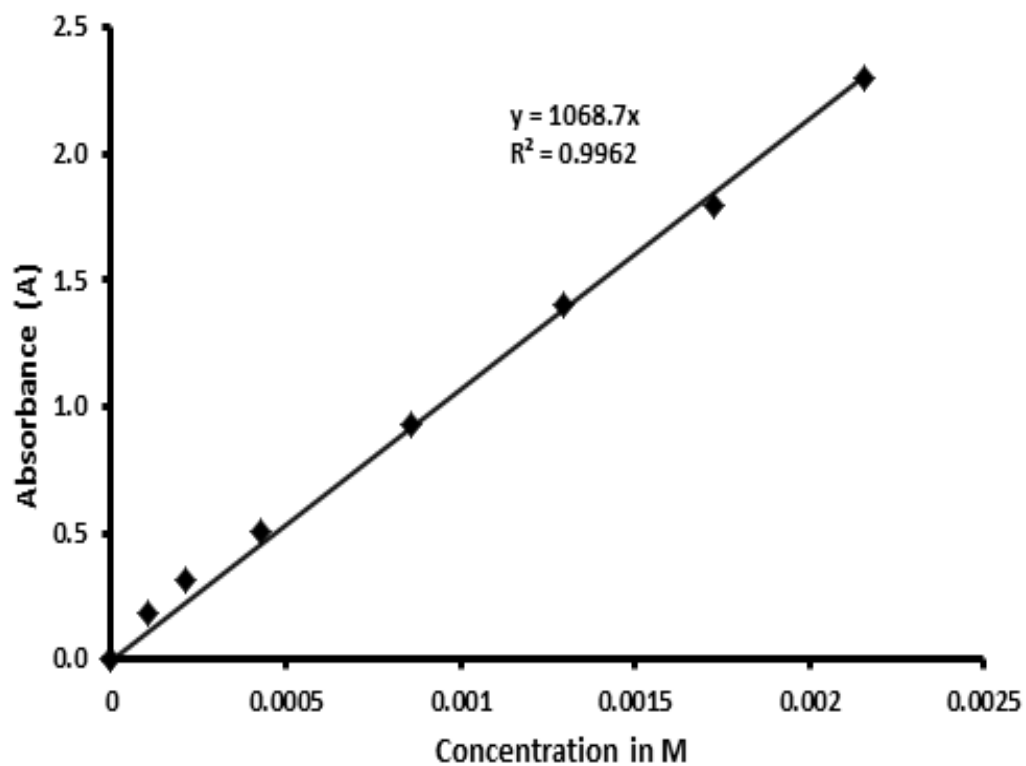


Figure 3.3: Standard absorbance-concentration curve for biosynthesized magnetite nanoparticles.

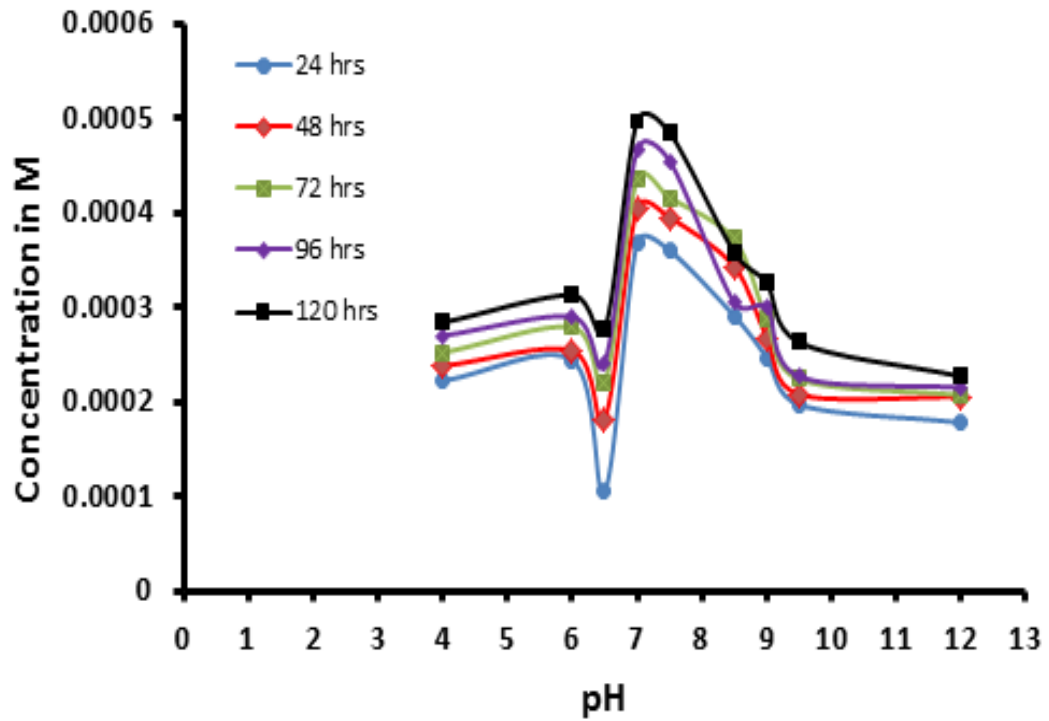


Figure 3.4: *Magnetospirillum magneticum* was grown at different pH values for different durations. The concentrations of BMNPs produced by *M. magneticum* under these different conditions are shown.

(a)

(b)

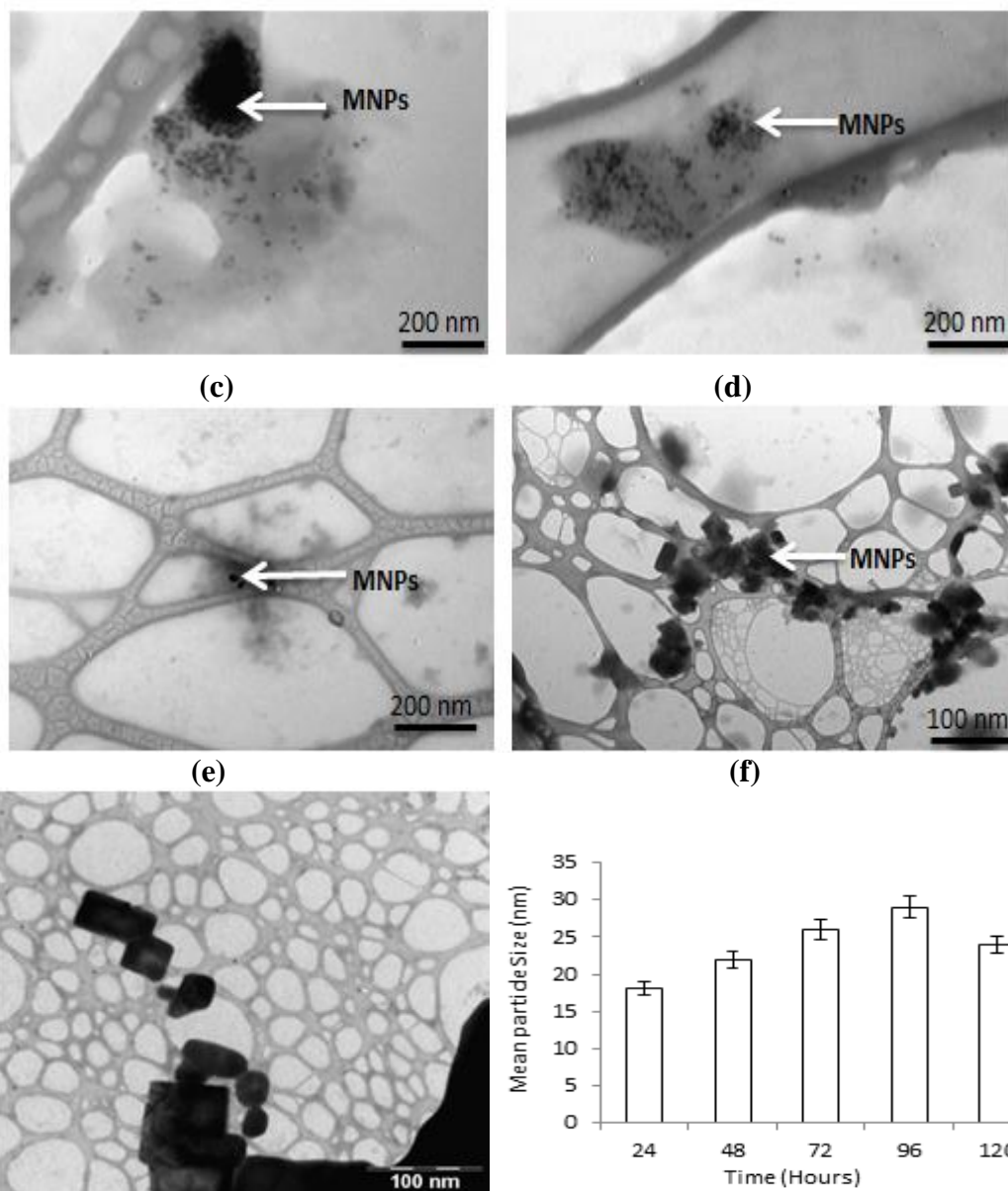


Figure 3.5: TEM micrographs of MNPs produced after exposure at a pH of 6.5 for (a) 24, (b) 48, (c) 72, (d) 96 and (e) 120 hours respectively. (f) Statistical analysis showing the mean particle size distribution after growth of *Magnetospirillum magneticum* at a pH of 6.5 for different durations.

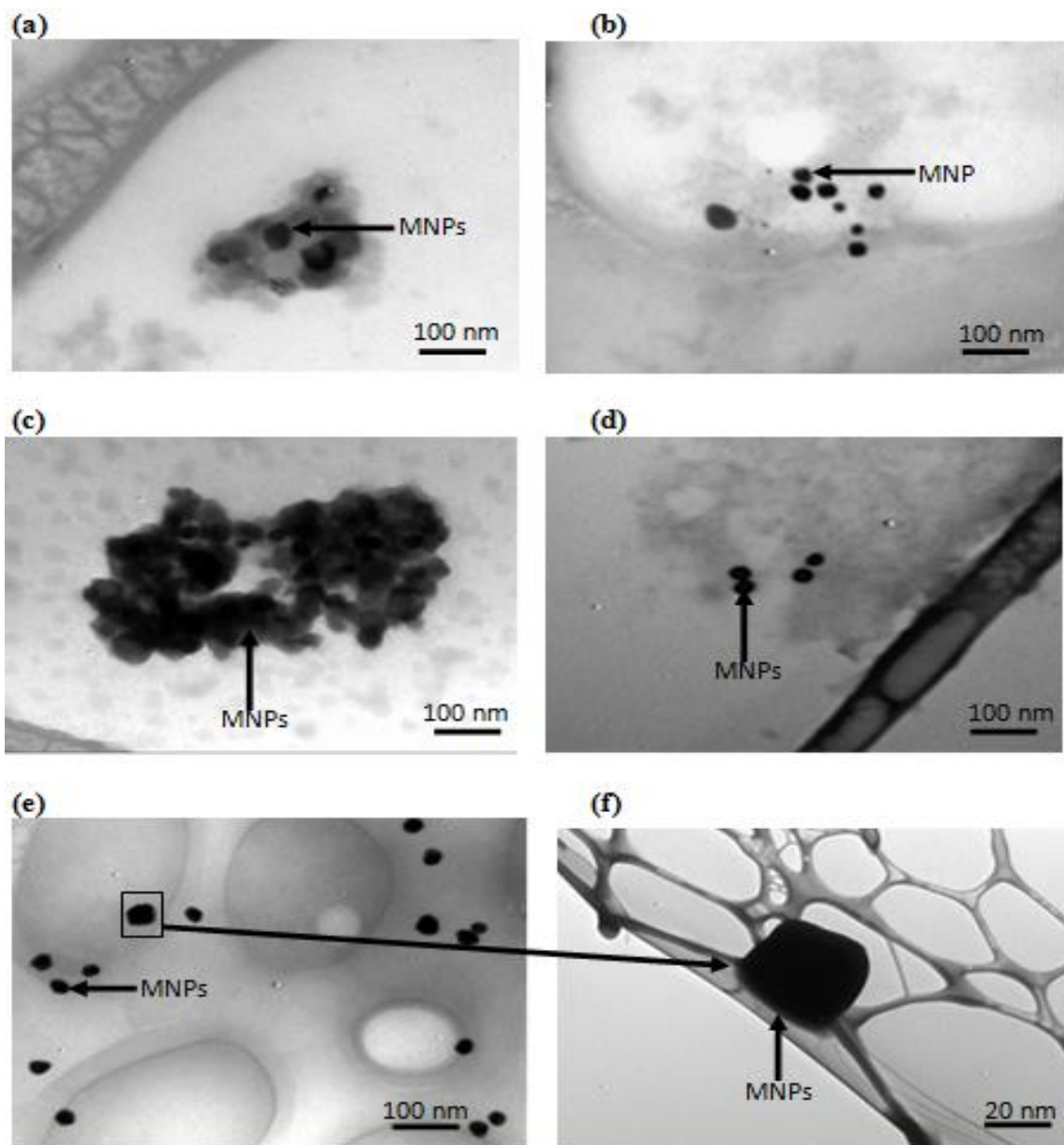


Figure 3.6: TEM micrographs of MNP shapes produced after growth in medium at a pH of 7.0 for durations of (a) 24, (b) 48, (c) 72, (d) 96 and (e)/(f) 120 hours, respectively.

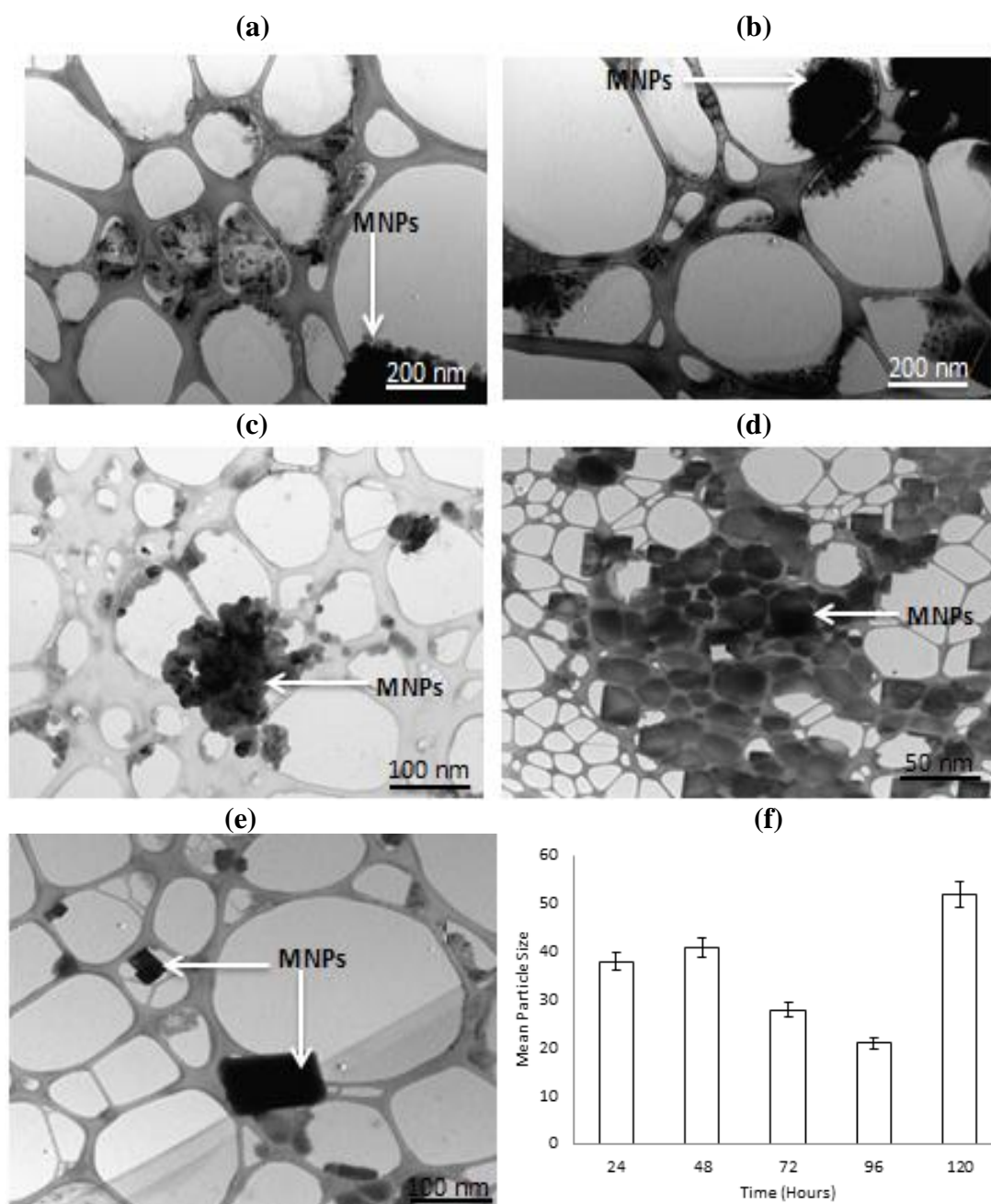


Figure 3.7: TEM micrographs of MNPs produced after growth at a pH of 7.5 for (a) 24, (b) 48, (c) 72, (d) 96 and (e) 120 hours respectively. (f) Statistical analysis showing the mean particle size distribution after growth of *Magnetospirillum magneticum* at a pH of 7.5 for different durations.

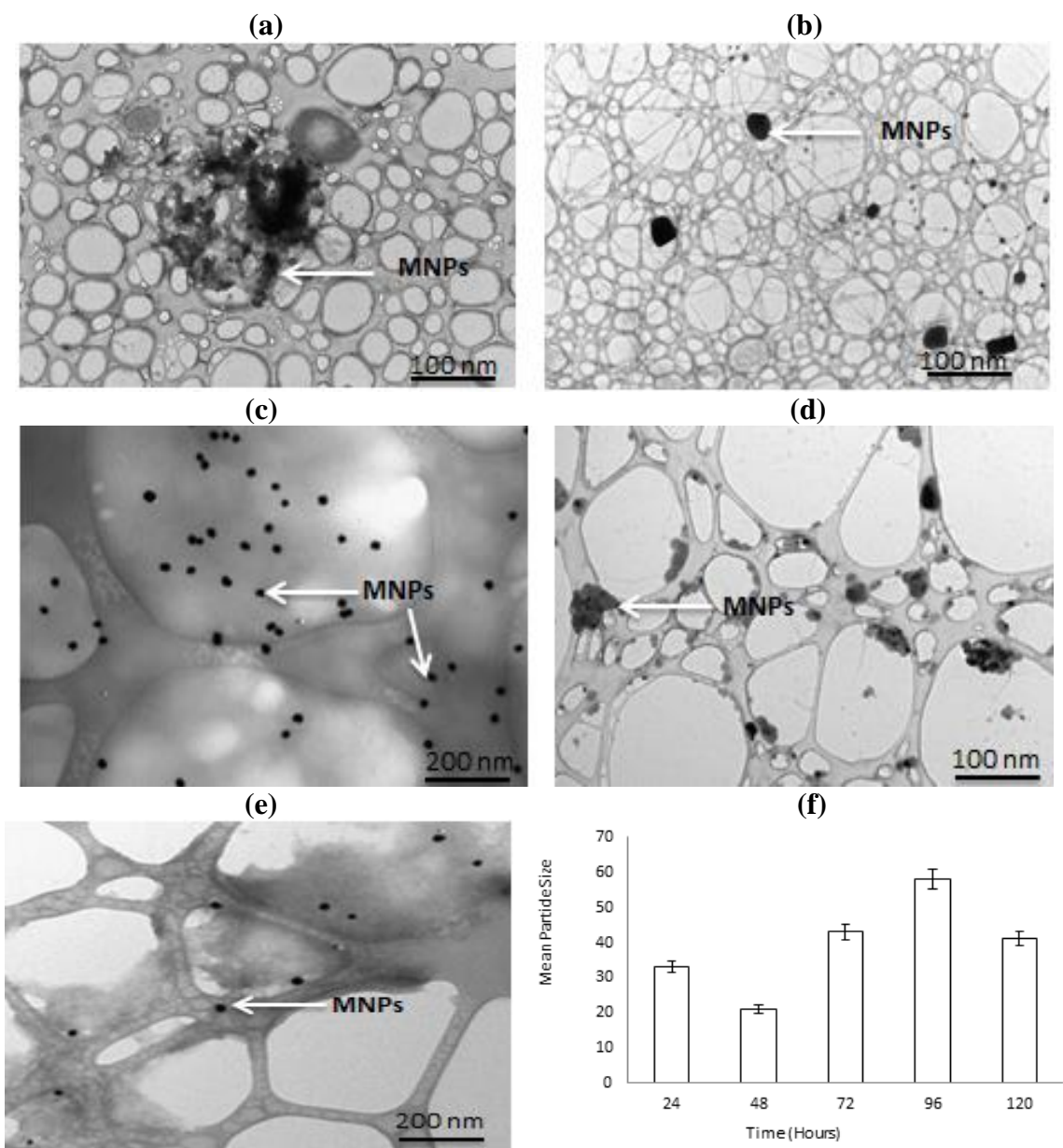


Figure 3.8: TEM micrographs of MNPs produced after growth at a pH of 9.5 for (a) 24, (b) 48, (c) 72, (d) 96 and (e) 120 hours respectively. (f) Statistical analysis showing the mean particle size distribution after growth of *Magnetospirillum magneticum* at a pH of 9.5 for different durations.

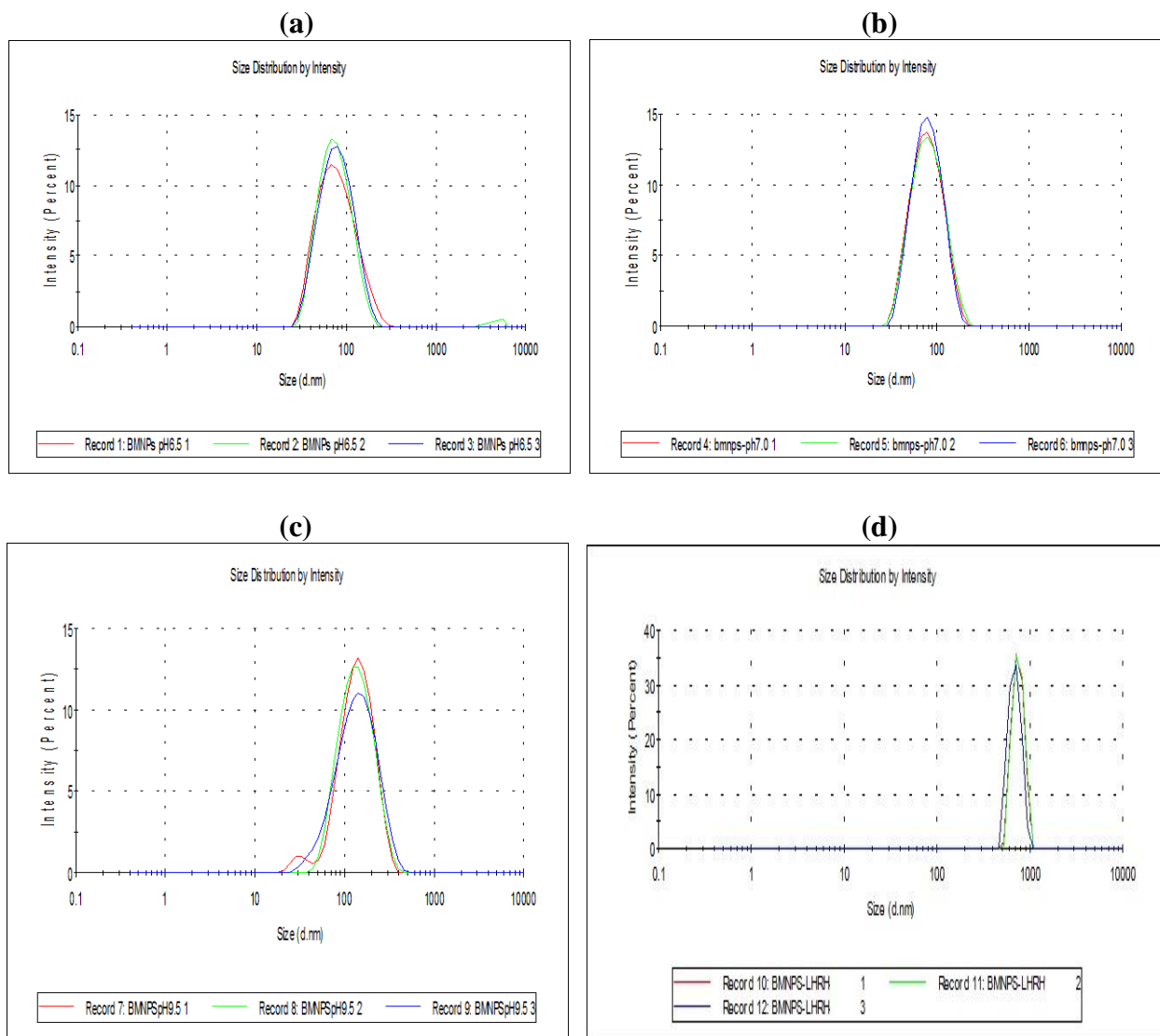


Figure 3.9 (a) Intensity particle size distributions of some selected BMNPs synthesized at pH (a) 6.5 (b) 7.0 (c) 9.5 and (d) functionalized BMNPs-LHRH particles for sample concentration diluted with 0.05 mL PBS solution (dilution of 1:5).

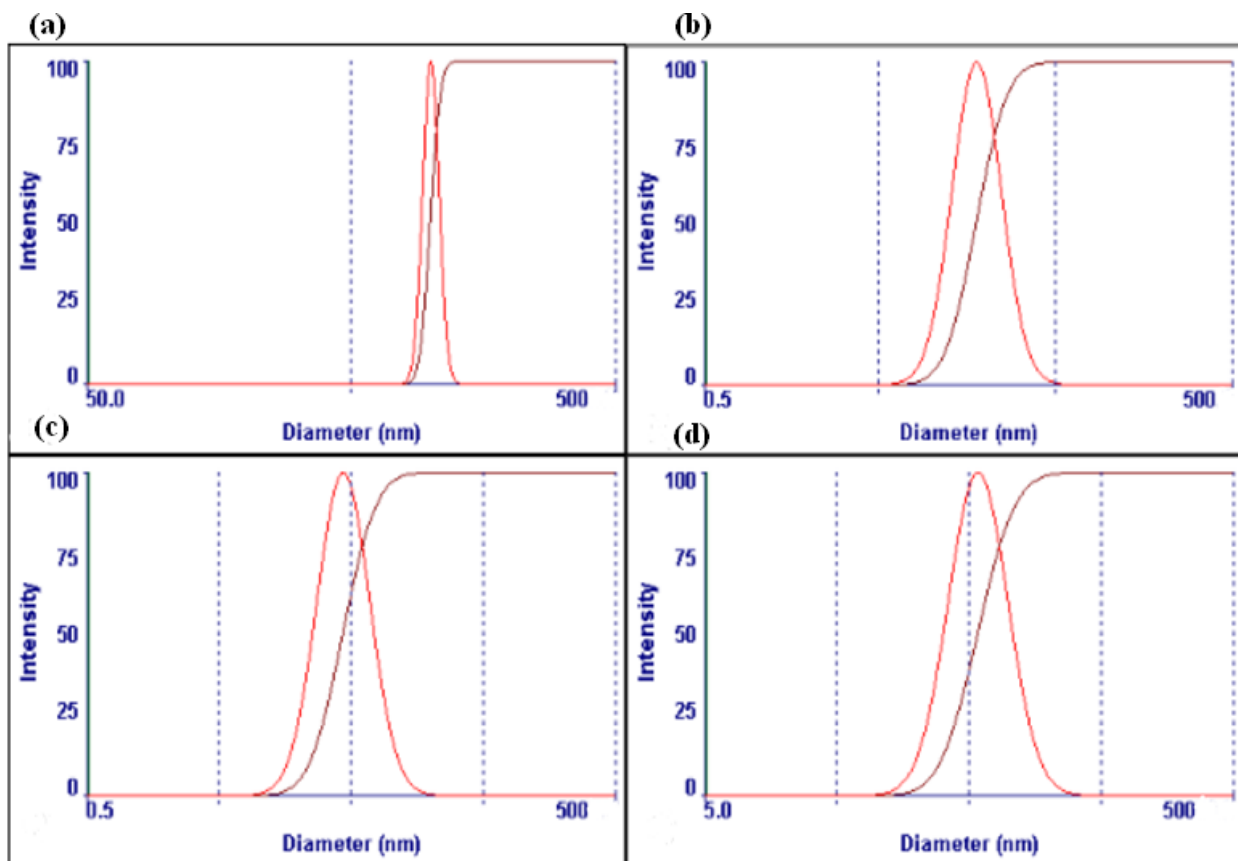


Figure 3.9 (b) Intensity particle size distributions of some selected BMNPs synthesized at pH (a) 6.5 (b) 7.0 (c) 9.5 and (d) functionalized BMNPs-LHRH particles for sample concentration diluted with 0.1 mL PBS solution (dilution of 1:10).

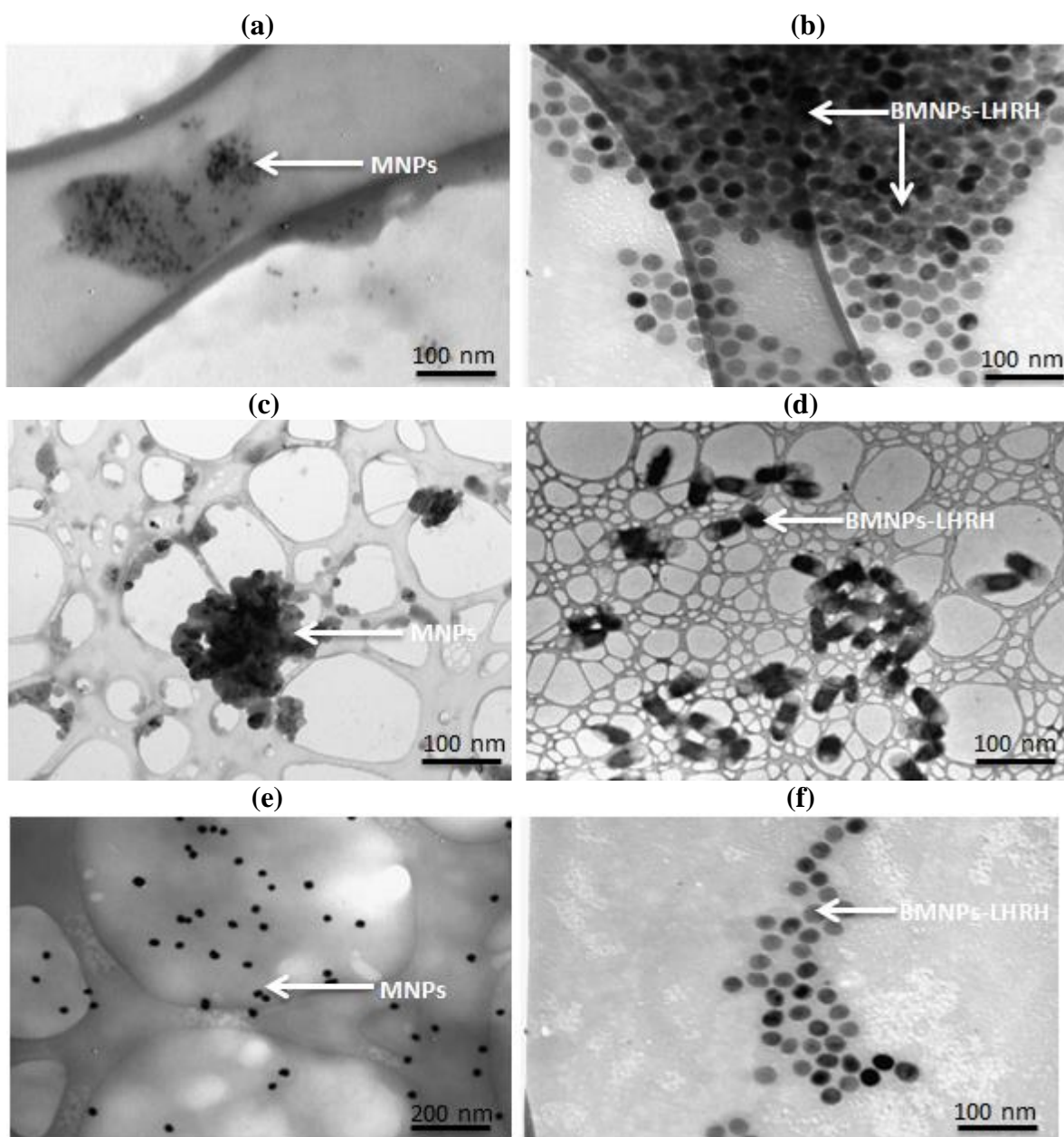


Figure 3.10: TEM micrographs of BMNPs produced by *M. magneticum* grown under the following conditions (a) pH of 6.5 for 48 hours (c) pH of 7.0 after 96 hours (e) pH of 9.5 after 72 hours. The TEM micrographs (b), (d) and (f) show ligand conjugated nanoparticles (BMNPs-LHRH) produced by *M. magneticum* after growth under the following conditions (b) pH of 6.5 for 48 hours (d) pH of 7.0 after 96 hours (f) 9.5 after 72 hours.

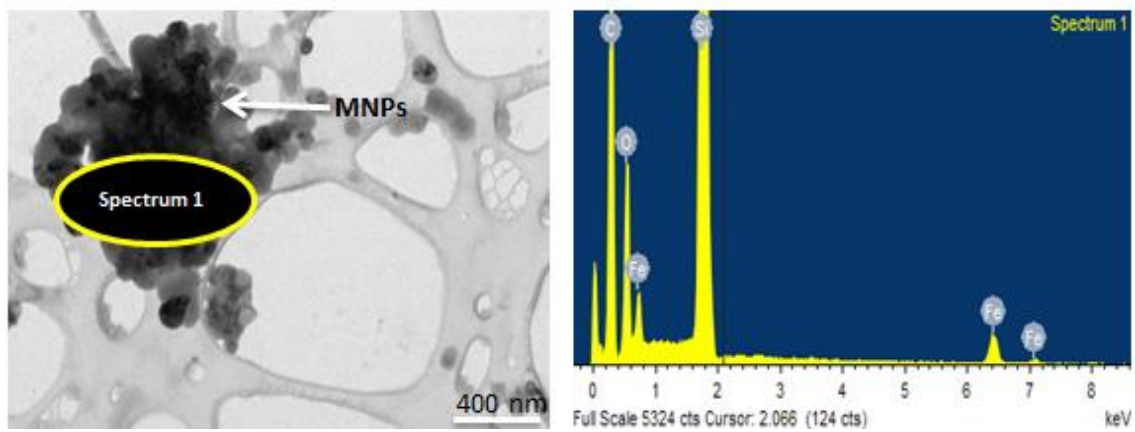


Figure 3.11: EDS of biosynthesized MNPs produced by *Magnetospirillum magneticum* at a pH 7.0 after exposure for 96 hours.

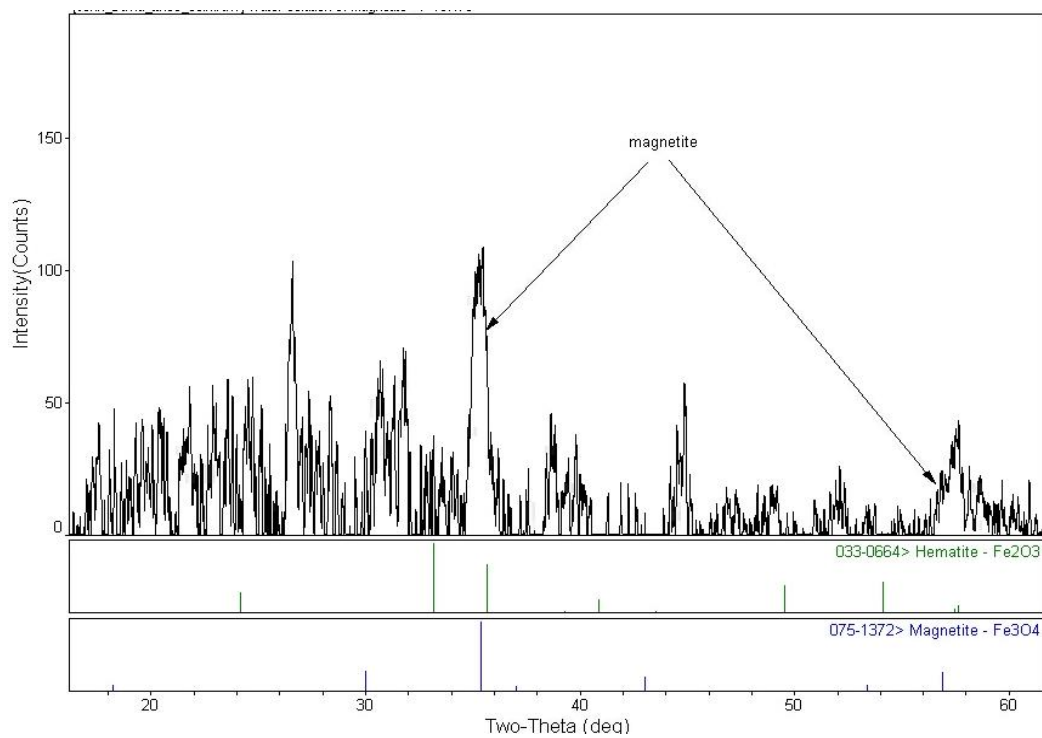


Figure 3.12: X - ray diffraction pattern of the biosynthesized magnetite particles (BMNPs).

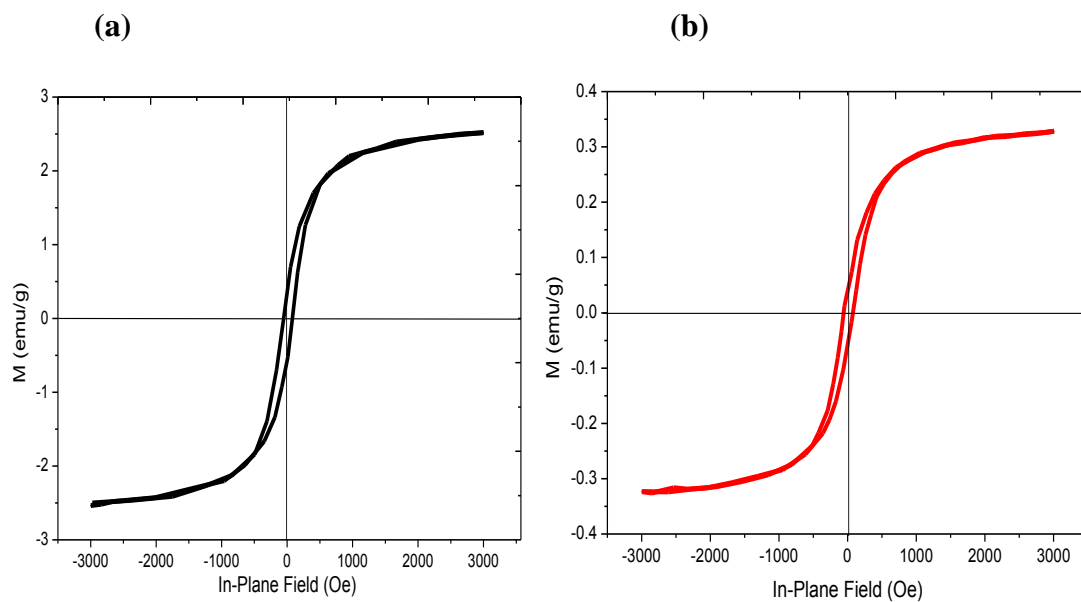


Figure 3.13: VSM results showing the hysteresis loops of the magnetic moments (emu/g) against the In-plane Field (Oe) for the (a) Biosynthesized magnetite nanoparticles obtained at pH 7.0 after 96 hours (b) Chemically synthesized magnetite nanoparticles (one pot synthesis).

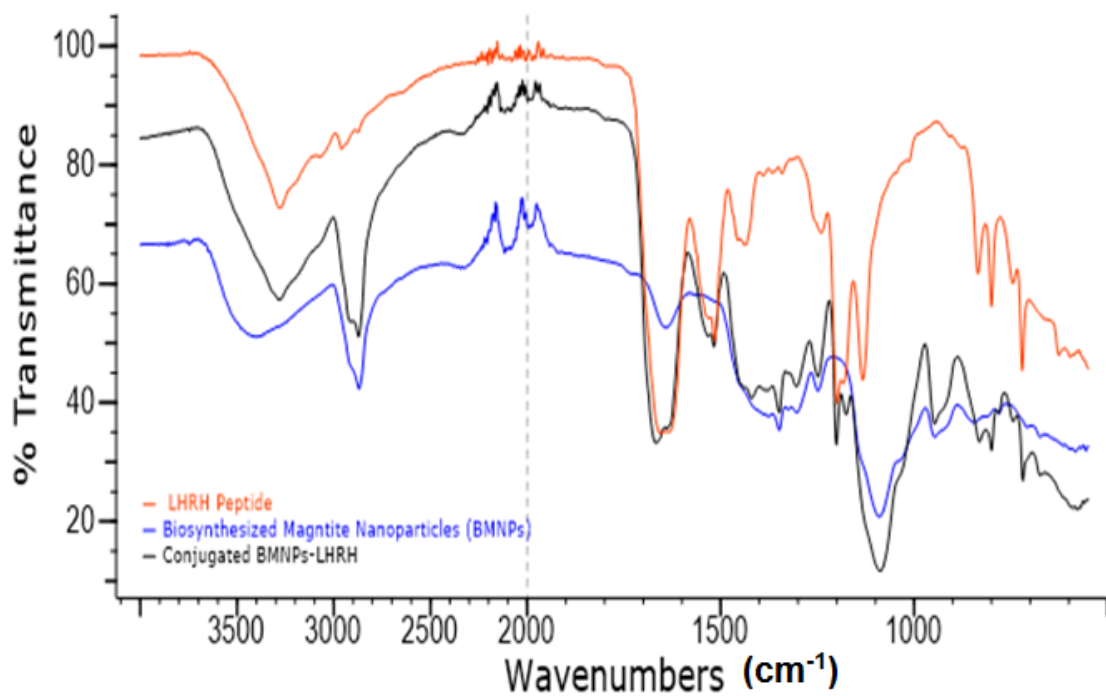


Figure 3.14: Fourier transformation infrared spectrum of LHRH, biosynthesized magnetite nanoparticles (BMNPs) synthesized at pH 7.0 after 96 hours and LHRH-BMNPs.

Table 3.1: Commercially available SPION/MNPs contrast enhancement and their specific indication place. (<http://mr-tip.com/>)

S/N	Name of Drug	Indication in MRI
1	Feridex®	Liver
2	Endorem™	Liver
3	GastroMARK®	Bowel marking
4	Lumirem®	Bowel marking
5	Sinerem®	MR angiography vascular, staging of RES-directed liver disease, lymph nodes
6	Resovist®	Liver lesions

Table 3.2: List of some microorganisms that have been used to synthesize magnetite nanoparticles

Microorganism	Product	Culturing tempt (°C)	Size range(nm)	Shape(s)	Location	References
Shewanella oneidensis	Fe ₃ O ₄	28	40-50	rectangular, rhombic, hexagonal	Extracellular	[94]
QH-2	Fe ₃ O ₄	22-26	81± 23×58±20	rectangular	Intracellular	[95]
Recombinant AMB-1	Fe ₃ O ₄	28	20	cubo-octahedral	Intracellular	[96]
yeast cells	Fe ₃ O ₄	36	Not Available	wormhole-like	Extracellular	[21]
WM-1	Fe ₃ O ₄	28	54 ± 12.3×43 ± 10.9	cuboidal	Intracellular	[97]
HSMV-1	Fe ₃ O ₄	63	113±34 ×40 ± 5	Bullet-shaped	Intracellular	[98]

Table 3.3: The mean particle size at pH 6.5 at different reaction times for *Magnetospirillum magneticum* strain

Time (hours)	Mean Particle Size (nm)
24	18 ± 2
48	22 ± 3
72	26 ± 4
96	29 ± 3
120	24 ± 4

Table 3.4: The mean particle size at pH 7.0 at different reaction times for *Magnetospirillum magneticum* strain

Time (hours)	Mean Particle Size (nm)
24	29 ± 6
48	19 ± 5
72	32 ± 3
96	21 ± 2
120	18 ± 4

Table 3.5: The mean particle size at pH 7.5 at different reaction times for *Magnetospirillum magneticum* strain

Time (hours)	Mean Particle Size (nm)
24	38 ± 2
48	41 ± 4
72	28 ± 3
96	21 ± 3
120	52 ± 4

Table 3.6: The mean particle size at pH 9.5 at different reaction times for *Magnetospirillum magneticum* strain

Time (hours)	Mean Particle Size (nm)
24	25 ± 4
48	22 ± 2
72	34 ± 3
96	42 ± 4
120	29 ± 3

Table 3.7: Diameter of some selected BMNPs from TEM and DLS (Z-average) characterization synthesized at pH (a) 6.5 (b) 7.0 (c) 9.5 and (d) functionalized BMNPs-LHRH with their polydispersity index for sample concentration diluted with 0.05 and 0.1 mL PBS solution respectively.

S/N	Sample	TEM (nm)	DLS (nm) @ a 0.05 mL PBS Dilution	DLS (nm) @ a 0.1 mL PBS Dilution	Polydispersity Index (PDI) @ a 0.05 mL PBS Dilution	Polydispersity Index (PDI) @ a 0.1 mL PBS Dilution
1	BMNPs at pH 6.5	26 ± 4	82.44 ± 2	100.7 ± 1	0.17	0.015
2	BMNPs at pH 7.0	32 ± 4	83.45 ± 1	17.7 ± 3	0.14	0.108
3	BMNPs at pH 9.5	34 ± 3	147.7 ± 3	43.9 ± 4	0.19	0.232
4	BMNPs-LHRH	39 ± 2	735.9 ± 5	58.6 ± 2	0.07	0.302

Table 3.8: Peaks that revealed the absence of characteristic bands of -NH₂ present in the LHRH, unbound nanoparticles and bound particles.

S/N	Sample	Wavenumber (cm ⁻¹)	Wavenumbers (cm ⁻¹)
1	LHRH Peptide	3280	1650
2	BMNP	3400	2850
3	Conjugated LHRH-BMNP	3280	2850

Chapter 4

4.0 Magnetite Nanoparticles for Cancer Detection and Treatment: The Role of Adhesion

4.1 Background and Motivation

Breast and prostate cancers are the second most common causes of cancer deaths in women and men, respectively [1]. Current trends also suggest that cancer will become the leading cause of death by 2030 [2,3]. The detection techniques used for breast cancer (mammograms, ultrasound, Magnetic resonance imaging (MRI) and different types of scan) are not yet considered effective. Even if the current trends in cancer should remain unchanged, the statistics suggest that two thirds of the entire global incidence of cancer will occur in low and middle income countries [4].

Cancer deaths are projected to result in more deaths than deaths from AIDS, tuberculosis and malaria combined per year [5]. In most cases, the major challenges are detection of cancer before metastasis [6,7] as well the side effects associated with current treatment methods [8-10]. Hence, the diagnosis is often too late for the current treatments to be efficacious [11,12]. Most patients that undergo the common bulk systemic cancer treatment, often experience excruciating pain, with significant short and long term side effects [11,13]. These treatments are also associated with high cost [8,10].

Furthermore, chemotherapy is known to affect normal cells as well as reduce the therapeutic index of the drugs used [14]. Many of the existing cancer therapeutic methods also lack selectivity and specificity. Hence, small or incremental improvements in breast cancer therapy

are unlikely to address the challenges associated with the cost and side effects of breast cancer treatment. In an effort to leverage the potential side effects associated with the bulk systemic cancer treatment, our previous research [10,15,16] reveals the potential of an implantable anti-cancer treatment device that can locally deliver drugs and heat to the site of a tumor. These devices can be used, after the removal of solid tumor by surgery, to treat cancer by the localized chemotherapy or/and hyperthermia. The potential of engineering synergy by the combination of the effect of heat and drug was the reason for the use of the device [17].

However, the approach described above requires surgery for the insertion of the device into the body. In any case, it could be difficult to treat metastatic cells that have escaped into the blood stream and other organs. This, therefore, has stimulated the need for novel approaches for the detection and treatment of cancer cells before and after metastases [6]. This stimulated our recent efforts in the development of functionalized nanoparticles for the early detection and treatment of cancer [18-22]. The biocompatible nanoparticles developed are functionalized with some molecular recognizing units (MRUs) [18-20,22]. When these functionalized nanoparticles are injected into the blood stream, they can diffuse through the capillaries and pores, until they reach receptors on cancer cells that can bind specifically to MRUs (such as antibodies and peptides) that are attached to nanoparticles [23].

There has also been increasing interest in the development of magnetic nanoparticles for the detection and treatment of cancer [20-32] as MRI enrichment/contrast agents [20,22-24,28] and

for the localized delivery of cancer drugs [27-29]. There have been significant efforts to explore the applications of magnetite nanoparticles (MNPs) in cancer detection via magnetic resonance imaging (MRI) [20,20-22,28]. Their potential has also been examined for applications in contrast enhancement during MRI of tumor tissue [28]. Recent work has been carried out to test the ability of binding magnetite nanoparticles to drugs, proteins, enzymes, antibodies, or nucleotides, [28,33,34] to direct their selective attachment to specific cells, organs, tissues, or tumors [33,34]. Such attachment, which can also be facilitated by the use of external magnetic fields, can also be used to induce localized heating via alternating magnetic fields that result in hyperthermia at temperatures between ~ 41 and 44 °C [28,29,31,35,36].

Furthermore, recent studies have shown that particularly invasive forms of breast cancer overexpress EphA2 tyrosine kinase receptors [37-42]. In normal breast cells, ephrin1, a ligand on neighboring cells, attaches to EphA2, leading to the downregulation of cell growth and migration [40]. However, breast cancer cells have higher levels of EphA2 receptors and lower levels of ephrin1-EphA2 contacts, favoring the growth and survival of tumor cells [40]. Current efforts have been targeting this receptor using antibody [41] or peptide [42] conjugates to achieve novel detection and treatment modalities for breast cancer. These strategies and approaches have been leveraged and explored for potential targeting of breast cancer cells using functionalized nanoparticles with the target of antibody and peptide [41,42]. However, during transport in the body, the functionalized nanoparticles are subjected to hydrodynamic and shear forces that can cause them to detach from their bonded receptors. Therefore, nanoparticles must be bound by significant adhesive and cohesive forces with their targets such that it cannot be overcome by the

detachment forces encountered during their transportation in the body. To solve this problem, it is crucial understand the adhesion forces, interaction and mechanism between the constituents of functionalized magnetite nanoparticles and breast cancer cells that are relevant to cancer detection and treatment.

Recent efforts [21,30,33] have explored the potential adhesion forces between the receptors on breast cancer cells specific to human luteinizing hormone-releasing hormone (LHRH) peptides and antibodies specific to the EphA2 receptor [33]. The pull off forces associated with interaction between breast cancer cells and LHRH/EphA2 that are over-expressed on breast cancer cells, are about five times greater than the adhesion to normal breast cells. In one of our recent study, we explored the effects of adhesion between gold nanoparticles and surfaces that are relevant to the potential applications in cancer detection and treatment [30]. Also, Hampp *et al.* [21] studied the adhesion of conjugated-biosynthesized gold nanoparticles to normal and breast cancer cells.

Furthermore, there has been significant work done in the conjugation of chemically synthesized magnetite nanoparticles (CMNPs) to LHRH and antibodies [18-20,22,33,43]. Obayemi *et al.* [44] recently studied the biosynthesis and the conjugation of magnetite nanoparticles with luteinizing hormone releasing hormone (LHRH) for the specific targeting of breast cancer cells. However, there have not been any known efforts to study the adhesion forces of biosynthesized and conjugated magnetite nanoparticles to surfaces that are relevant to the potential applications in cancer detection and treatment using a simple AFM technique.

In this chapter, experimental study of the adhesion of biosynthesized magnetite nanoparticles, chemically synthesized magnetite nanoparticles as well as their conjugates (LHRH and Breast Specific Antibody (BSA) that have receptors which are overexpressed on breast cancer cells; i.e., BMNPs–LHRH, CMNPs-LHRH, BMNPs-BSA or CMNPs-BSA) to breast cancer cells are demonstrated and explored. Some results from prior efforts by Meng *et al.* [33], Hampp *et al.* [21] and Oni *et al.*[30,45] are also discussed in the context of the current work. The implications of the results are then discussed for potential clinical applications of robust biosynthesized magnetite nanoparticle clusters for specific targeting and the treatment of breast cancer.

4.2 Adhesion Theory

AFM is a useful technique for the measurement of adhesion forces between AFM tips and substrates [46,47]. The detail of the theory applied is described in in the next chapter (chapter 5). Figure 4.1 gives typical schematics of the interaction of BMNPs-ligands on a dip-coated AFM tip with surface receptors on breast cancer and normal breast cells. The adhesion between the functionalized nanoparticles on the AFM tip and the cancer cells can provide a basis for cancer detection and insights into the optimum nanoparticle sizes for cancer therapeutics.

Figure 4.2 gives a schematic of an atomic force microscope force-displacement behavior: (I) Load displacement plot, (II) Tip/Surface Interaction [47]. The force microscopy method operates in the tapping mode. The stages in the interaction are described in Chapter 5.

4.3 Experimental Procedures

4.3.1 Materials

The biosynthesized magnetite nanoparticles (BMNPs) used were synthesized with *Magnetospirillum magneticum* (*M.M.*) strain AMB-1 that was obtained from ATCC, Manassas, Virginia, USA. Whereas, the chemically synthesized magnetite nanoparticles (CMNPs) used were synthesized by one-pot synthesis method in a pyrolysis reaction [48]. The LHRH peptide was purchased from California Peptide Research Inc. (Napa, CA, USA), and the monoclonal antibody specific to the EphA2 (breast specific antibody; BSA) receptor was purchased from Invitrogen (Carlsbad, CA, USA). Furthermore, uncoated AFM tips (MPP-31100) were procured from Veeco (Memphis, TN). MDA-MB-231 cell line, growth media (L-15, respectively), and medium supplements (fetal bovine serum and penicillin/streptomycin) were purchased from American Type Culture Collection (ATCC, Manassas, VA, USA), Sigma-Aldrich (St. Louis, MO, USA), and Thermo Fisher Scientific, Inc. (Waltham, MA, USA).

4.3.2 Adhesion and Characterization of Conjugated Nanoparticles to Breast Cancer Cells

In this work, the BMNPs used were synthesized and purified from *Magnetospirillum magneticum* (*M.M.*) strain AMB-1 using the methods as adapted from our previous work [44]. The magnetite nanoparticles synthesized were conjugated using the method as described by Meng *et al*[33]. and Obayemi *et al.* [18]. A simple dip-coating techniques as described by Hutter and Bechhoefer [49] was adopted to coat bare phosphorus n-doped silicon atomic force microscopy (AFM) tips with LHRH, BSA, BMNPs, CMNPs, as well as BMNPs–LHRH, CMNPs-LHRH, BMNPs-BSA or CMNPs-BSA conjugates. LHRH peptides were provided in a powder form and were dissolved in sterile double-distilled water to a concentration of 10 mg/ml,

while the antibodies were used as provided by the manufacturer at a concentration of 0.5 mg/ml [21].

The AFM tips were immersed in solutions containing the materials/particles of interest (LHRH, BSA, BMNPs, CMNPs, BMNPs–LHRH, CMNPs-LHRH, BMNP-BSA or CMNPs-BSA) and then air-dry for about 15 seconds. The tips were dipped three times afterwards and air-dried to ensure the tip was adequately covered with the materials of interest. Generally, then the tips were then allowed to air-dry for a minimum of 24 h before being used for AFM adhesion measurements. The interactions and adhesion forces were measured using a Multimode Dimension DI Nanoscope IIIa Atomic Force Microscope (Bruker Instruments, Woodbury, NY, USA).

The sample of the breast cancer cells (MDA-MB-231) were prepared for the AFM by fixation in 3.7 wt% formaldehyde (Sigma-Aldrich, St. Louis, MO, USA) using the method as described by Hampp *et al.* [21]. The breast cancer cells were cultured in 60 x15 mm Falcon Petri dishes (Falcon, Franklin Lakes, NJ, USA) for 48 h at high confluence and incubated at 37 °C at normal atmospheric pressure levels for breast cancer cells. The MDA-MB-231 cells were grown in L-15 medium (ATCC, Manassas, VA, USA), supplemented with 100 I.U./mL penicillin/100 I.U./mL streptomycin and 10% FBS (ATCC, Manassas, VA, USA). The samples were rinsed with sterile Dulbecco phosphate buffered saline (DPBS; Invitrogen, Carlsbad, CA) and fixed with a 3.7 wt% formaldehyde solution for 15 min at a temperature of 23 °C. They were then rinsed again with DPBS before a final rinse with purified water. Finally, the samples were placed in a vacuum desiccator for 2 h to dry at room temperature.

To determine whether the AFM tips were coated with BMNPs, bare (uncoated) AFM tips and the coated AFM tips were imaged using environmental scanning electron microscopy (ESEM). A Phillips FEI Quanta 200 FEG Environmental-SEM (Philips Electronics N.V., Eindhoven, The Netherlands) was used to obtain secondary/backscattered electron images of coated and bare AFM tips. An energy dispersive x-ray spectrometer, EDS (Inca, Oxford Instruments, UK), was used to acquire an elemental spectrum at the apex of the cantilever tip to confirm the presence of MNPs and antibodies.

Since weak adhesion between the AFM tips and the coatings could result in the detachment of the coatings from the AFM tips during handling or pull-off testing, the AFM tips were checked in the ESEM before and after AFM testing. Thus, the pull-off forces were related only to the coatings on the AFM tips since no detachment of the dip coatings from the coated AFM tips occurred. The spring constants of the coated and uncoated AFM tips were measured experimentally using the thermal tune method [49,50]. This was done to ensure that the actual spring constants were used to calculate the pull-off forces. Such measurements are also required to account for batch-to-batch variations in the spring constants, as well as the effects of coatings on the cantilever stiffness.

All AFM experiments were carried out using a Dimension 3100 AFM (Bruker Corporation, Billerica, MA, USA) under ambient conditions (23 °C) and relative humidity of 36–45 %. In any case, before the adhesion force measurements, the photodetector sensitivity was calibrated using a stiff quartz platform [51]. The BMNPs used for the experiment are the ones synthesized at a pH

of 7.0. The adhesion forces/interactions were measured for the following nine configurations using the AFM technique adopted by Ref. [21,33,45].

- (i) Bare AFM tip to normal breast cancer cells
- (ii) LHRH-coated AFM tip to breast cancer cells
- (iii) BSA-coated AFM tip to breast cancer cells
- (iv) BMNPs to breast cancer cells
- (v) CMNPs to breast cancer cells
- (vi) BMNPs–LHRH to breast cancer cells
- (vii) CMNPs–LHRH to breast cancer cells
- (viii) BMNPs–BSA conjugate to breast cancer cells
- (ix) CMNPs–BSA conjugate to breast cancer cells

Adhesion measurements of each of these components were carried out and recorded for each configuration on the prepared breast cancer cells. For each pair of interactions, 150 adhesion measurements were obtained from 3 AFM tips with 50 measurements obtained for each tip at 5 different positions on the substrate. This method of measurement is fully described in the next chapter (See Figures 4.1 and 4.2).

4.4 Results and Discussion

4.4.1 AFM Tip and Substrate Characterization

In each case, back-scattered SEM images of the uncoated AFM tip is presented in Figures 4.3 with the electron diffraction spectroscopy (EDS) spectrum showing 98.9 wt % Si. It clearly shows that silicon and slight traces of carbon are detected in the EDS scan. Figures 4.4 (a) to 4.4(h) show the SEM images of the tips coated with LHRH, BSA, CMNPs-LHRH and BMNPs-LHRH before and after adhesion. The SEM images also showed the surface morphologies of AFM tips that are coated with nanoscale layers of LHRH, BSA, CMNPs-LHRH and BMNPs-LHRH. These verify and demonstrate that there is no loss of particles during adhesion testing. The images of coated AFM tips before and after adhesion (See Figure 4.4) clearly suggest that there is no evidence of coating delamination observed in the pull-off experiments. Hence, the measured pull-off forces are due to interactions between the coated AFM tips and the substrates.

Furthermore, the EDS result of our particle of interest (BMNPs-LHRH) clearly shows the presence of BMNPs on the apex of the cantilever (Figure 4.5) with spectrum processing on coated AFM tip showing 28.5 wt% Si, 53.1 wt% C, 10.5 wt% O and 7.9 wt% Fe.

4.4.2 Adhesion Measurements

The measured pull-off forces for different AFM tips and/or their configuration with breast cancer cells are presented in Figure 4.6 and Table 4.2 with their respective tip stiffness (Table 4.1). There was a relatively low level of adhesion (23.5 ± 13 nN) between AFM tip and breast cancer cells. However, the average adhesion forces between an AFM tip coated with BMNPs and

breast cancer cells is 78.8 ± 11 nN, which is more than three times greater than the adhesion using the bare tip. The adhesion between the AFM tip coated with BMNPs and breast cancer cells is also greater than the average adhesion forces between the AFM tips coated with CMNPs, which is 53.2 ± 16 nN. This suggests that there could be proteins that are within the BMNPs that promote the binding to the breast cancer cells. There are possibilities that without these capping protein(s), the BMNPs will have reduced adhesive interactions with the cancer cells. In the case of the AFM tip coated with LHRH or BSA, the adhesion forces to the breast cancer cells were found to be relatively similar, 105.2 ± 9 and 110.9 ± 7 nN respectively (see Table 4.2).

The adhesion forces for the BMNPs-LHRH (126.1 ± 26 nN) with breast cancer cells is about one and a half times greater than that of CMNPs-LHRH (98.4 ± 39). Similarly, the adhesion forces for the BMNPs-BSA (142.7 ± 3) with breast cancer cells is slightly greater than that of BMNPs-LHRH. This value is about a one and half times greater to that of CMNPs-BSA as well. In addition, the adhesion configurations of BMNPs-BSA and CMNPs-BSA with breast cancer cells are greater than that of BMNPs-LHRH and CMNPs-LHRH. This could be due to the presence of amine group and protein coatings on the surfaces of the BMNPs. The increase in adhesion values of the conjugated BMNPs-LHRH(BSA) and CMNPs-LHRH(BSA) to breast cancer cells compared to the bare BMNPs and CMNPs can be attributed to the overexpression of receptors for LHRH and BSA on breast cancer cells.

The results obtained above suggest that the adhesive forces between BMNPs/CMNPs and cancer cells are attributed to a combination of van der Waals forces and hydrogen bonding. However, the high adhesion forces between the BMNPs-LHRH(BSA) and CMNPs-LHRH(BSA) and the

breast cancer cells are attributed to the van der Waals interactions between the peptide/antibody and its particular overexpressed receptor on the surface of the cancer cells. The results obtained are in agreement with the results of Hampp *et al.*[21] and Oni *et al.*[30].

Furthermore, the differences in adhesion values between the biosynthesized and chemically synthesized conjugated magnetite nanoparticles to cancer cells are thought to be attributed to the presence of capping protein(s) present on the biosynthesized magnetite nanoparticles as explored by Hampp *et al.*[21]. It is really necessary in future work to explore the presence and composition of the capping proteins. Also, further work is also needed to characterize and compare the biocompatibility of the biosynthesized magnetite nanoparticles to chemically synthesized magnetite nanoparticles. Finally, there is also a recommendation for toxicity studies for both types of synthesized magnetite nanoparticles (BMNPs and CMNPs) in breast cancer cells and normal breast cells. This will certainly pave the way for animal work and clinical trials.

4.5 Implications

One of the objectives of the current work is to understand the adhesive forces between the different configurations. This gives us insights of the forces that must be overcome by the forces encountered during nanoparticle transport in the body. Also, the implication of force microscopy measurements described above is quite significant in understanding the adhesion forces between functionalized BMNPs with surfaces that are relevant in the detection and treatment of cancer.

Furthermore, greater targeting selectivity is a major goal in the development of therapeutic agents or imaging contrast formulations for the detection and treatment of breast cancer. Ideally, functionalized/conjugated BMNPs should be selectively enriched in the tumor tissue. Thus, the adhesion techniques presented in this study may be used to screen the effectiveness of potential novel functionalized/conjugated BMNPs that are being developed for the targeting of breast cancer. The high adhesive forces that exist between BMNPs and breast cancer cells suggest their potential for increased selectivity in the targeting of cancer cells. Therefore, such improved screening could significantly reduce the cost of identifying new nanotargets through conventional in vitro and in vivo studies. This strategy may furthermore facilitate the attachment, entry, and uptake of BMNPs into cancer cells.

The average adhesive forces between the conjugated biosynthesized magnetite nanoparticles and cancer cells are almost one and half times greater than those between chemically synthesized magnetite. Thus, the results of adhesive forces obtained suggest the potential of the articles to improve the selectivity of conjugated BMNPs in cancer detection and treatment.

Finally, it is crucial to know that the adhesion methods used in this study may be used to screen the effectiveness of other potential configurations of functionalized/conjugated magnetite nanoparticles that are being developed for the specific targeting of breast cancer. This is clearly a part of the future work needed to explore such possibilities. This is because such screening may

enable the rapid identification of particles and/or targeting ligands that are more likely to specifically attach to overexpressed receptors on breast cancer and other types of cancer cells.

4.6 Summary and Concluding Remarks

This chapter presents the results of an experimental study of the adhesion forces between components of a model generic nanoparticle systems/configuration that includes, LHRH, BSA, BMNPs, CMNPs, BMNPs-LHRH, CMNPs-LHRH, BMNPs-BSA, CMNPs-BSA to breast cancer cells (MDA-MB-231 cell line). The results clearly show the potential application of conjugated BMNPs when the comparison of the adhesion of conjugated BMNPs and CMNPs to breast cancer cells was done.

Finally, chemically synthesized magnetite nanoparticles had adhesion forces to breast cancer cells that were about one and half times less than those of biosynthesized magnetite nanoparticles. These results suggest that BMNPs and BMNPs-LHRH conjugates are superior to CMNPs and CMNPs-LHRH conjugates in rapid screening of potential ligands for the specific targeting of breast cancer cells. This also means that BMNPs may also be used to design novel types of magnetite nanoparticles for the early diagnosis and treatment of cancer. Future work is clearly needed to carry out *in-vitro* experiments with at least two different cell lines of normal and cancer cells to ascertain and compared the efficacy of conjugated BMNPs and CMNPs. The effect of magnetization (superparamagnetic behavior) and nanoparticle sizes with respect to

adhesion on the breast cancer cells is also needed to predict the right design configuration.

Finally, further work is needed to extend the current work to preclinical and clinical scenarios.

References

- [1] Jemal, Murray T, Samuels A, Ghafoor A, Ward E, Thun MJ. Cancer statistics, 2003. *CA Cancer J Clin* 2003; 53:5–26.
- [2] Boyle Peter and Levin Bernard. *The World Cancer Report*. World Health Organization. 2008.
- [3] David Cutierrez., *Cancer facts and figures*. 2nd edition. America Cancer Society, 2008.
- [4] J. Ferlay, H. R. Shin, F. Bray, D. Forman, C. D. Mathers and D. Parkin. *GLOBOCAN 2008, Cancer Incidence and Mortality Worldwide: IARC Cancer-Base No.10* [Internet]. Lyon, France: International Agency for Research on Cancer. 2010; Available from: <http://globocan.iarc.fr>.
- [5] D. C. Mathers and D. Loncar. *Updated Projections of Global Mortality and Burden of Disease, 2002-2030; Data Sources, Methods and Results*. World Health Organization. (2005) 6.
- [6] L. A Nagahara, Ferrari M, Grodzinski P. *MRS Bulletin* 2009;34:406-14.
- [7] P. Grodzinski, Silver M, Molnar LK. *Expert Rev Mol Diagn* 2006;6:307-18.
- [8] David Needhama, Mark W. Dewhirst. The development and testing of a new temperature-sensitive drug delivery system for the treatment of solid tumors. *Advanced Drug Delivery Reviews*. ELSEVIER, 2001; 53, 285–305.
- [9] B. Hildebrandt, Ceelen W.P., Wust P. in: (Ed), 2007, *Peritoneal Carcinomatosis: A Multidisciplinary Approach*, Springer, New York, 185.

- [10] A. V. Hoek, C. Theriault, Y. Oni and W. O Soboyejo. “Effects of Temperature on Diffusion from PNIPA-Based Gels in a BioMEMS Device for Localized Chemotherapy and Hyperthermia”. *Materials Science and Engineering C*, (2010) 2011.
- [11] Irvine D, Vincent L, Graydon JE, Bubela N and Thompson L. *Cancer Nursing* 1994;17(5):367-78.
- [12] Stewart BW, Kleihues. *Le Cancer Dans le Monde*, ed. C.I.d.R.s.I.C. (CIRC).
- [13] *Le Cancer Dans le Monde* edited by B. W. Stewart and P. Kleihues (C.I.d.R.s.I.C. (CIRC), IARC Press, Lyon, 2005).
- [14] Ms Rajput et al: *Microspheres in cancer therapy*, *Indian journal*, 2010.
- [15] Y. Oni, C. Theriault, A. V. Hoek, and W. O. Soboyejo, *Mater. Sci. Eng. C* 31(2), 67–76 (2011).
- [16] Y. Danyuo, J. D. Obayemi, S. Dozie-Nwachukwu, C. J. Ani, O. S. Odusanya, Y. Oni, N. Anuku, K. Malatesta and W. O. Soboyejo. “Prodigiosin Release From an Implantable Biomedical Device: Kinetics of Localized Cancer Drug Release”. *Journal of Materials Science & Engineering C*. (2014) Vol/Issue 42C pp. 734-745, doi:10.1016/j.msec.2014.06.008
- [17] R. Kurzrock and M. Markman, *Targeted Cancer Therapy* (Humana Press, Clifton, 2008).
- [18] J. Meng J. Fana, G. Galiana, R.T. Branca , P.L. Clasen, S. Ma , J. Zhou , C. Leuschner, C.S.S.R. Kumar, J. Hormes, T. Otit, A.C. Beye, M.P. Harmer, C.J. Kiely, W. Warren, M.P. Haataja and W.O. Soboyejo “LHRH-Functionalized Superparamagnetic Iron Oxide

- Nanoparticles for Breast Cancer Targeting and Contrast Enhancement in MRI” *Materials Science and Engineering C* 29 (2009) 1467–1479.
- [19] J. Zhou, C. Leuschner, C. Kumar, J.F. Hormes and W.O. Soboyejo. *Biomaterials* 27 (2006) 2001.
- [20] J. Zhou, C. Leuschner, C. Kumar, J. Hormes and W.O. Soboyejo. *Materials Science and Engineering C* 26 (2006) 1451.
- [21] E. Hampp, R. Botah, S. O. Odusanya, N. Anuku, K. Malatesta and W.O. Soboyejo. “Biosynthesis and Adhesion of Gold Nanoparticles for Breast Cancer Detection and Treatment” *Journal of Materials Research*; Nov (2012) Vol. 27 Issue 22, p2891.
- [22] C. Leuschner, C.S.S.R. Kumar, W. Hansel, J. Zhou, W. O. Soboyejo, J. Hormes, *Breast Cancer Res. Treat. Springer* 2006 DOI 10.1007/s10549-006-9199-7. 99 (2006) 163–176.
- [23] M. P. Melancon, W. Lu, and C. Li, *MRS Bull.* 34, 415–421 (2009).
- [24] J. W. M. Bulte, M. Cuyper, D. Despres and J. A. Frank, *Journal of Magnetism and Magnetic Materials* 194 (1999) 204.
- [25] D. Needhama and M. W. Dewhirst. “The Development and Testing of a New Temperature-Sensitive Drug Delivery System for the Treatment of Solid Tumors”. *Advanced Drug Delivery Reviews.* Elsevier, (2001) 53, 285–305.
- [26] F. J. Lazaro, A. R. Abadia, M. S. Romero, L. Gutierrez, J. Lazaro and M. P. Morales. *Biochim Biophys Acta.* (2005) 1740:434–45.

- [27] Y. Zhao, Z. Qiu and J. Huang, "Preparation and Analysis of Fe₃O₄ Magnetic Nanoparticles Used as Targeted-drug Carriers". *Chinese J. Chem. Eng.* (2008) 16 (3), 451-455.
- [28] H. Pardoe, P. R Clark, T. G St Pierre, P. Moroz, S. K Jones. *Magnetic Resonance Imaging.* (2003) 21:483–488.
- [29] M. Shinkai, M. Yanase and M. Suzuki. "Intracellular Hyperthermia for Cancer Using Magnetite Cationic Liposomes". *Journal of Magnetism and Magnetic Materials.* (1999) 194, 176184.
- [30] Y. Oni, K. Hao, S. Dozie-Nwachukwu, J. D. Obayemi, O. S. Odusanya, N. Anuku, and W. O. Soboyejo "Gold nanoparticles for cancer detection and treatment: The role of adhesion". *Journal of Applied Physics J. Appl. Phys.* 115, 084305 (2014).
- [31] W. Zhou, W. He, and S. Zhong. "Biosynthesis and Magnetic Properties of Mesoporous Fe₃O₄ Composites". *Journal of Magnetism and Magnetic Materials.* (2009) 321, 1025–1028.
- [32] C. C. Berry and A. S. G. Curtis. "Functionalisation of magnetic nanoparticles for applications in biomedicine". *J Phys D: Appl Phys* (2003); 36:R198–206.
- [33] J. Meng, E. Paetzell, A. Bogorad, and W. O. Soboyejo, "Adhesion between Peptides/Antibodies and Breast Cancer Cells". *Journal of Applied Physics* (2010): 107, 114301.

- [34] C. C. Berry and A. S. G. Curtis. “Functionalisation of magnetic nanoparticles for applications in biomedicine”. *J Phys D: Appl Phys* (2003); 36:R198–206.
- [35] I. Hilger, W. Andra, R. Hergt, R. Hiergeist, H. Schubert and W.A. Kaiser. “Electromagnetic Heating of Breast Tumors in Interventional Radiology: *In-Vitro* and *In-Vivo* Studies in Human Cadavers and Mice”. *Radiology* 218 (1997) 570.
- [36] A. Jordan, P. Wust, H. Fahling, W. Jonh, A. Hinz, and R. Felix. *International Journal of Hyperthermia* 9 (1997) 51.
- [37] R. C. Ireton and J. Chen, *Curr. Cancer Drug Targets* 5, 149 (2005).
- [38] B. P. Fox and R. P. Kandpal, *Biochem. Biophys. Res. Commun.* 318, 882 (2004).
- [39] D. P. Zelinski, N. D. Zantek, J. C. Stewart, A. R. Irizarry, and M. S. Kinch, *Cancer Res.* 61, 2301 (2001).
- [40] L. W. Noblitt, D. S. Bangari, S. Shukla, D. W. Knapp, S. Mohammed, M. S. Kinch, and S. K. Mittal, *Cancer Gene Ther.* 11, 757 (2004).
- [41] D. Jackson, J. Gooya, S. Mao, K. Kinneer, L. Xu, M. Camara, C. Fazenbaker, R. Fleming, S. Swamynathan, D. Meyer, P. D. Senter, C. Gao, H. Wu, M. Kinch, S. Coats, P. A. Kiener, and D. A. Tice, *Cancer Res.* 68, 9367 (2008).
- [42] K. E. Scarberry, E. B. Dickerson, J. F. McDonald, and Z. J. Zhang, *J. Am. Chem. Soc.* 130, 10258 (2008).
- [43] R. Lawaczeck, H. Bauer, T. Frenzel, M. Hasegawa, Y. Ito, K. Kito, N. Miwa, H. Tsutsui, H. Vogler and H.J. Weinmann, *Acta Radiol.* 38 (1977) 584–597.

- [44] J. D. Obayemi, S. Dozie-Nwachukwu, Y. Danyuo, O. S. Odusanya, N. Anuku, K. Malatesta and W. O. Soboyejo, 'Biosynthesis and the Conjugation of Magnetite Nanoparticles with Luteinizing Hormone Releasing Hormone (LHRH)' : Elsevier Journal of Materials Science and Engineering C, Volume 46, Pages 482–496, 1 January 2015, (46 (2015) 482–496).
- [45] K. V. Wolf, Z. Zong, J. Meng, A. Orana, N. Rahbar, K. M. Balss, G. Papandreou, C. A. Maryanoff, and W. Soboyejo, *J. Biomed. Mater. Res. Part A* 87A, 272 (2008).
- [46] C. B. Prater, P. G. Maivald, K. J. Kjoller, and M. G. Heaton, www.veeco.com.
- [47] V. Shahin, Y. Ludwig, C. Schafer, D. Nikova, and H. Oberleithner: Glucocorticoids remodel nuclear envelope structure and permeability. *J. Cell. Sci.* 118, 2881 (2005).
- [48] W. S. Chiu, S. Radiman, M. H. Abdullah, P. S Khiew, N. M Huang, and R. Abd- Shukor. "One Pot Synthesis of Monodisperse Fe₃O₄ Nanocrystals by Pyrolysis Reaction of Organometallic Compound" *Journal of Materials Chemistry and Physics* 106 (2007) 231-235.
- [49] J.L. Hutter and J. Bechhoefer: Calibration of atomic-force microscope tips. *Rev. Sci. Instrum.* 64, 1868 (1993).
- [50] G.A.Matei, E.J.Thoreson, J.R. Pratt, D.B.Newell, and N.A. Burnham: Precision and accuracy of thermal calibration of atomic force microscopy cantilevers. *Rev. Sci. Instrum.* 77, 083703 (2006).
- [51] B. Bhushan: *Handbook of Micro/Nanotribology* (CRC Press, Boca Raton, FL, 1995).

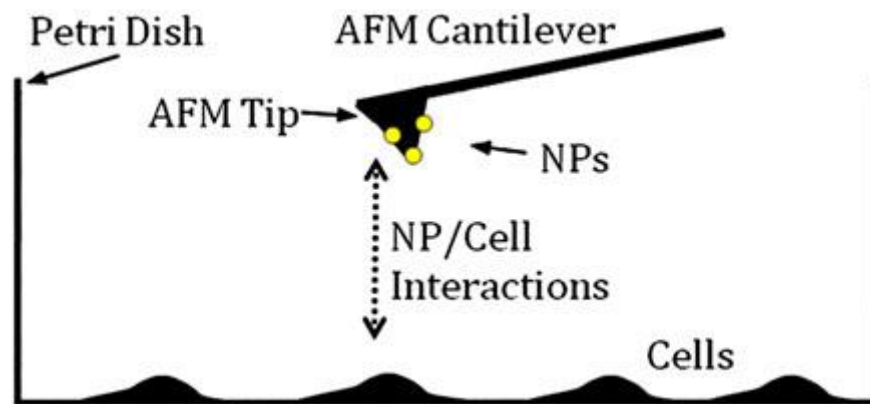


Figure 4.1: Ligand/receptor interactions. In the experimental setup, ligands on the dip-coated AFM tip interact with surface receptors on breast cancer cells (MDA-MB-231) seeded on a Petri dish ([Adapted from Ref [30]).

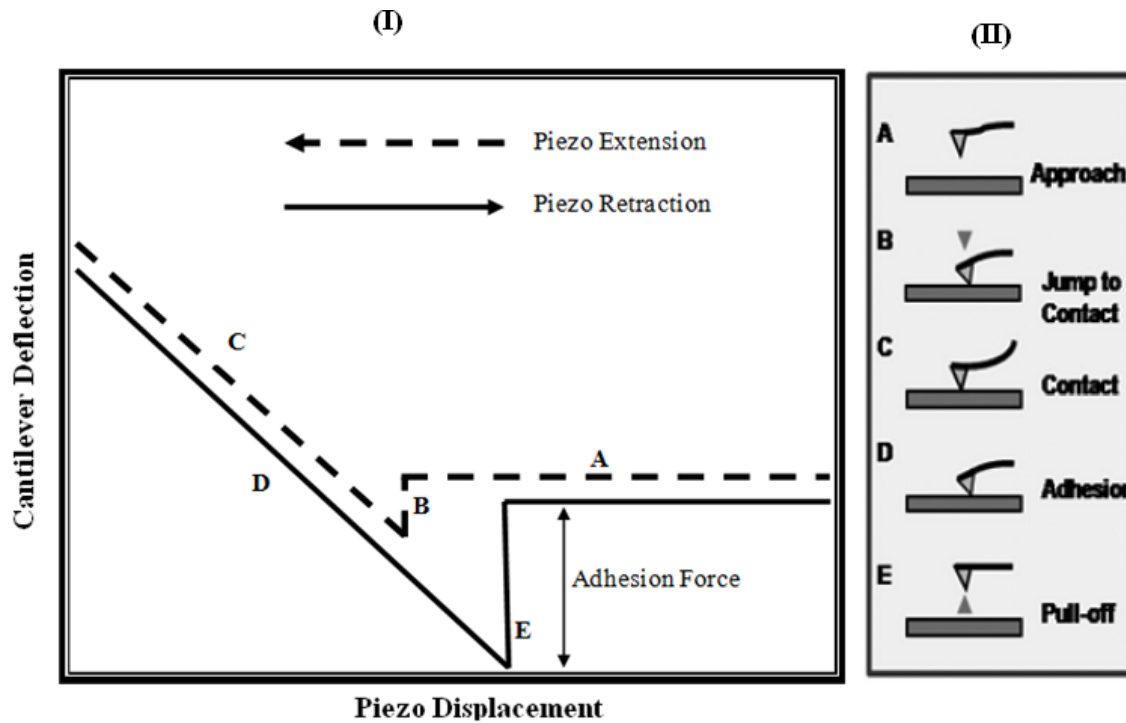


Figure 4.2: Schematic of typical force–displacement plot with corresponding stages of force displacement behavior (Modified from Ref. 56). In one approach–retract cycle, the AFM tip approaches the surface of the sample (A), jumps to contact with the surface when significant van der Waals forces are felt (B), and undergoes elastic bending and is retracted (C, D). Due to adhesive interactions, the tip does not detach from the substrate until a force sufficient to pull the tip off of the surface is achieved (E). (Adapted from Ref [45])

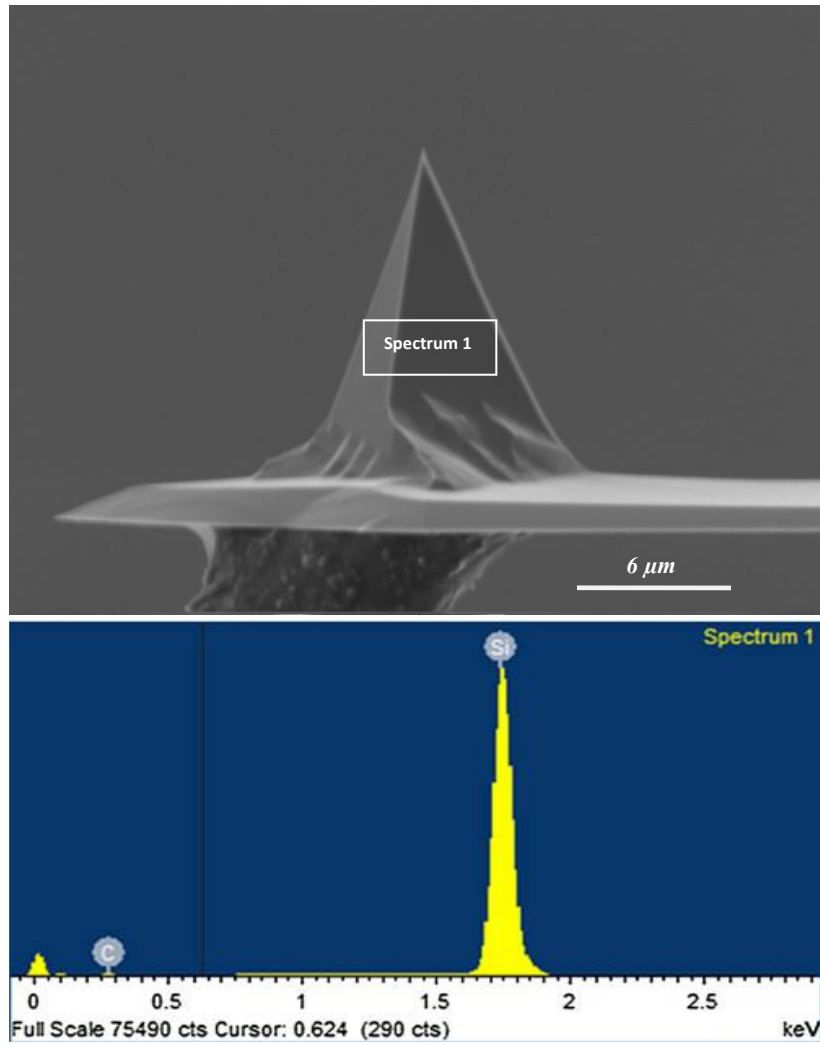


Figure 4.3: Electron diffraction spectroscopy (EDS) spectrum of a bare AFM tip showing 98.9 wt % Si.

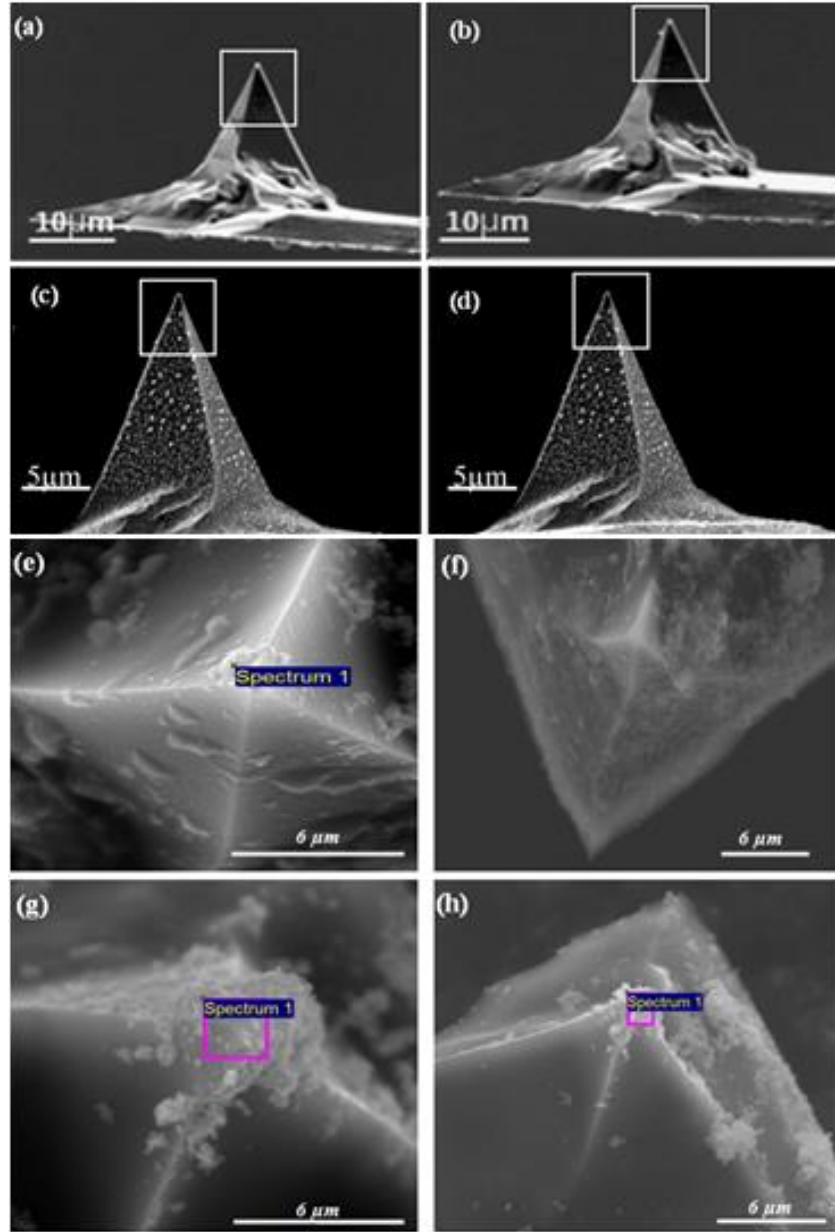


Figure 4.4: Sample SEM images of the AFM tips: (a) LHRH-coated AFM tip before adhesion measurement; (b) LHRH-coated AFM tip after adhesion measurement; (c) BSA-coated AFM tip before adhesion measurement; (d) BSA-coated AFM tip after adhesion measurement. Boxes show coating on apex tip and side edges. (e) Chemically synthesized magnetite nanoparticles-LHRH coated AFM tip before adhesion measurement; (f) Chemically synthesized magnetite nanoparticles-LHRH coated AFM tip after adhesion measurement; (g) Biosynthesized magnetite nanoparticles-LHRH coated AFM tip before adhesion measurement; (h) Biosynthesized magnetite nanoparticles-LHRH coated AFM tip after adhesion measurement.

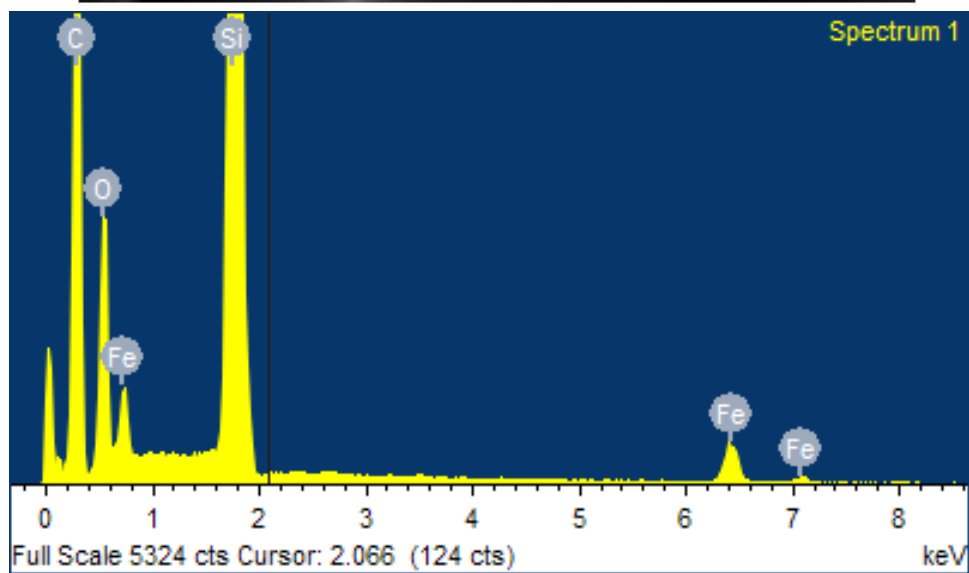
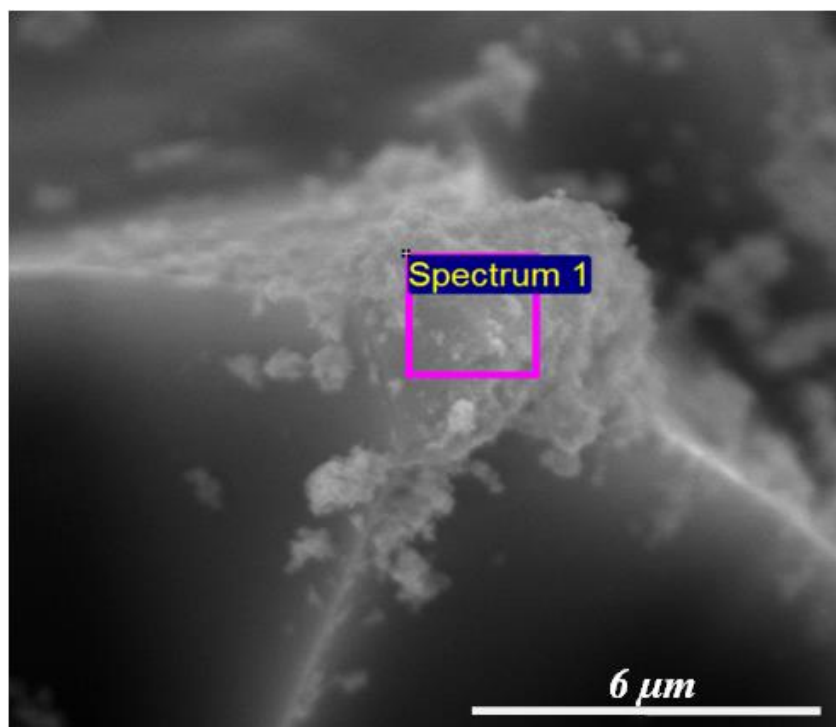


Figure 4.5: EDS Spectrum of LHRH conjugated biosynthesized magnetite nanoparticles (BMNPs-LHRH) coated on AFM tip showing 28.5 wt% Si, 53.1 wt% C, 10.5 wt% O and 7.9 wt% Fe.

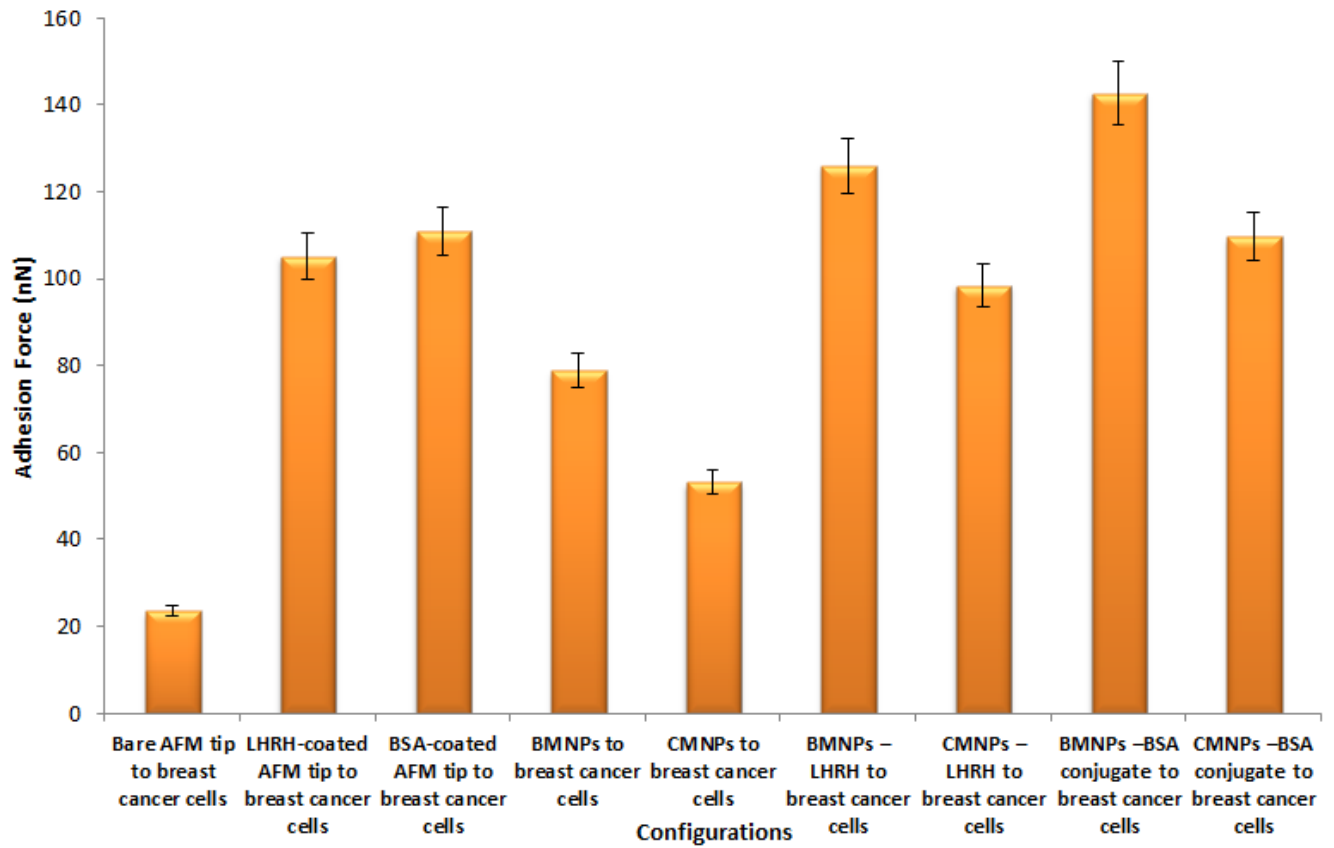


Figure 4.6: Summary of pull-off force measurements for different configurations of BMNPs and CMNPs with breast cancer (MDA-MB-231) cells.

Table 4.1: Spring constants of the bare/coated AFM tips

S/N	Coated/Uncoated AFM Tips	Average Spring Constant (N/m)
1	Bare tip	0.66 ± 25
2	LHRH-Coated tip	0.89 ± 19
3	BSA-Coated tip	0.94 ± 11
4	BMNPs-Coated tip	0.59 ± 22
5	CMNPs-Coated tip	0.55 ± 15

Table 4.2: Adhesion forces between coated/uncoated AFM tips and breast cancer cells.

Coated and uncoated AFM tip and breast cancer cell configuration		Average force (nN)
1	Bare AFM tip to breast cancer cells	23.5 ± 13
2	LHRH-coated AFM tip to breast cancer cells	105.2 ± 49
3	BSA-coated AFM tip to breast cancer cells	110.9 ± 71
4	BMNPs to breast cancer cells	78.8 ± 11
5	CMNPs to breast cancer cells	53.2 ± 26
6	BMNPs –LHRH to breast cancer cells	126.1 ± 21
7	CMNPs –LHRH to breast cancer cells	98.4 ± 39
8	BMNPs –BSA conjugate to breast cancer cells	142.7 ± 19
9	CMNPs –BSA conjugate to breast cancer cells	109.6 ± 51

Chapter 5

5.0 Gold Nanoparticles for Cancer Detection and Treatment: The Role of Adhesion

5.1 Introduction

The second leading cause of death in the world is cancer [1]. In most cases, the major challenge is the detection of cancer before metastasis [1,2]. Hence, the diagnosis is often too late to administer the current treatments that are available [3,4]. Consequently, more than 550 000 Americans and more than 7.5×10^6 worldwide die of cancer each year [5]. Furthermore, for the patients that undergo bulk systemic cancer treatment, the treatment is often painful, with significant short and long term side effects arising from common treatment methods that include: chemotherapy, radiotherapy, hyperthermia, and surgery [3,4].

In an effort to reduce the potential side effects of bulk systemic cancer treatment, our previous work [6] explored the potential of an implantable anti-cancer treatment device that can locally deliver drugs and heat to the site of a tumor. Such a device can be used, following surgery to remove cancer tissue, to treat cancer by the localized chemotherapy and hyperthermia. The combination of heat and drug was selected because of the potential of engineering synergy through the combined use of localized chemotherapy and hyperthermia [7].

However, the above device requires surgery for its insertion into the body. Furthermore, it may not treat metastatic cells that have escaped into the blood stream and other organs. There is, therefore, a need for novel approaches for the detection and treatment of cancer cells before and after metastases [1]. This has stimulated our recent efforts to use nanoparticles to facilitate the early detection and treatment of cancer [8–11]. The nanoparticles can be injected into the blood

stream, where they can also diffuse through the capillaries and pores, until they reach receptors on cancer cells that can bind specifically to MRUs (such as antibodies and peptides) that are attached to them [8].

Upon attachment, the nanoparticles can be used to facilitate the imaging [8–11] and treatment [8–11] of cancer. For example, magnetic nanoparticles may be used to facilitate the magnetic resonance imaging (MRI) of cancer cells/tissue, while gold nanoparticles may be used to enhance laser therapy through interactions that occur between gold nanoparticles and laser beams [8]. Similarly, anti-cancer drugs that are tethered to gold nanoparticles may be used to treat targeted cancer cells/tissue and metastatic cancer cells in the blood stream [8,11]. Designer nanoparticles, therefore, have the potential for localized detection and treatment of cancer.

Gold nanoparticles are particularly attractive in cancer treatment because of their strong absorption of light in the visible and near-infra red (NIR) electromagnetic regions. This optical absorption is strongly dependent on the shape and size of the gold nanoparticle [8]. Furthermore, it has been shown that the cell uptake of spherical gold nanoparticles is dependent on their size, with 50 nm being the optimal diameter [12]. Also, because smaller nanoparticles are expected to have a better chance of passing through tumor vasculature, they can attach to tumor tissue and then pass through the body prior to egestion and excretion. This prevents their long term accumulation in the body, while providing the basis for cancer detection and treatment during their attachment to specific cancer cells.

Since the interactions between nanoparticles and cancer cells can provide a basis for cancer detection and treatment, significant efforts have been made to design gold nanoclusters that can

improve our ability to detect and treat cancer [8,11,13–21]. In general, such nanoclusters consist of:

- An imaging core, such as gold that can undergo plasmon resonance under illumination with a laser;
- Encapsulated anti-cancer drugs, such as paclitaxel;
- Molecular recognition units, such as antibodies and peptides that bind specifically to receptors on cancer cells, ligand chemistry, and protective coatings that limit the interaction of the nanoparticles with surrounding tissue and blood during transport to target organs (Figure 5.1).

During transport in the body, the nanoclusters are subjected to hydrodynamic and shear forces that can cause them to fragment into smaller pieces. They must, therefore, be bound by significant adhesive and cohesive forces that cannot be overcome by the forces encountered during nanoparticle transport in the body. There is, therefore, a need to quantify the adhesion forces between the constituents of nanoclusters that are relevant to cancer detection and treatment. This can be done using Force Microscopy during Atomic Force Microscopy (AFM) [22–24]. This is a technique that can be used to study bi-material pairs [25] that simulate pairwise interactions between interacting nanoparticles [26]. It is the basis for force spectroscopy and the measurement of nano/molecular scale adhesion [27,28].

This chapter presents the results of an experimental study of the adhesion between the constituents of gold nanoclusters that are relevant to cancer detection and treatment. In the case of cancer detection, the adhesive interactions between gold nanoparticles and molecular recognition units (such as luteinizing hormone releasing hormone and a breast specific antibody)

are measured using force microscopy. The adhesion between gold nanoparticles and paclitaxel (an anti-cancer drug) is also measured along with the effects of thiols that are often used to improve the adhesion between gold and a number of organic materials [29]. The implications of the results are then discussed for the development of gold nanoclusters for future applications in cancer detection and treatment.

5.2 Theory

The force microscopy method involves bringing AFM tips close enough for adhesive interactions to occur (Figure 5.2(a)). This ultimately causes them to jump into contact (Figure 5.2(b)). The tips then undergo elasticity as they are displaced further in the same direction (Figure 5.2(c)). Upon their retraction, the displacements are reversed, as the loads are reduced to zero (Figure 5.2(d)). However, the tips do not detach at zero load, due to the effects of adhesion. Consequently, the retraction has to be continued until the adhesive interactions are overcome by the applied forces. This results in the pull-off of the AFM tips from the substrates (Figure 5.2(e)). The resulting pull-off force, F , is a measure of the adhesion. It is given by Hooke's law:

$$F = k\delta \quad (5.1)$$

where k is the stiffness of the AFM cantilever and δ is the displacement of the AFM tip at the onset of pull-off (represented as the length, EA in Figure 5.2(a)). Measurements of such pull-off forces have been applied in biology [30–33]. They have been shown to be sufficient to detect the differences between breast cancer cells and normal breast cells in recent work by Meng *et al.*, [25] who studied the adhesive interactions between the breast specific EphA2 antibodies and receptors on breast cancer or normal breast cells. Meng *et al.* [25] also studied the adhesion

between luteinizing hormone releasing hormone (LHRH) peptides and their receptors on breast cancer and normal breast cells. Their results show that the pull-off forces associated with breast cancer cells and LHRH/EphA2, which are over-expressed in breast cancer cells [34,35], are about five times the adhesion to normal breast cells [25].

It is important to note here that although the above results suggest that force microscopy can be used to measure the adhesive forces between the constituents of nanoclusters, there have been no prior efforts to use force microscopy to measure the adhesion between gold nanoparticles and the constituents of nanoclusters that are being designed for the specific detection and treatment of cancer via localized chemotherapy and hyperthermia. This will be explored in this study using a model nanocomposite system (Figure 5.1) that can deliver the anti-cancer drug, paclitaxel, while providing the basis for thermo-chemotherapy, by localized hyperthermia via plasmon resonance with optically tunable gold nanoparticle cores.

5.3. Materials and Methods

5.3.1 Materials

The gold nanoparticles were purchased from Nanopartz Inc. (Loveland, CO), while the uncoated AFM tips were procured from Veeco (Memphis, TN). Paclitaxel was obtained from Parenta Pharmaceuticals (West Columbia, SC), while LHRH was purchased from Thermo Scientific (Waltham, MA). The Breast Specific Antibody (BSA) and thiols were obtained from Sigma-Aldrich (St. Louis, MO).

5.3.2 AFM Experiments

5.3.2.1 AFM Tip and Substrate Coating/Characterization

A simple dip-coating method [25] was used to coat the AFM tips. The bare AFM tips were dip-coated with either gold nanoparticles, LHRH or BSA. This was done by immersing them into their respective solutions for about 10 s to maximize the AFM tip surface contact with the solution. The tips were then air-dried for less than a minute, after which they were dipped for a second time, again for 10 s. This procedure was repeated 3–5 times to complete the coating process. The nanoparticle concentrations in solution ranged from 22 to 46 ppm. These were used in the as received condition. Similarly, the BSA, thiols and LHRH solutions were used, as provided by the vendors, at a concentration of 0.5 mg/ml.

Subsequently, the coated AFM tips were air-dried for a minimum of 24 h. They were then observed under a scanning electron microscope. The paclitaxel, LHRH, and BSA substrates were prepared by spreading each of the solutions on glass sheets to form thin layers. These were then allowed to dry in air for a minimum of 24 h. The surface morphologies of the coated substrates and the uncoated glass substrates (control surfaces) [36] were then characterized using a Dimension 3100 Atomic Force Microscope (AFM) that was operated in the tapping mode (Dimension 3100, Bruker Instruments, Woodbury, NY, USA).

In order to confirm that the AFM tip samples were coated with gold nanoparticles, the coated and bare tips were imaged under a Phillips Model FEI XL30 field emission gun scanning electron microscope (SEM) (Phillips Electronics N.V., Eindhoven, The Netherlands). The images were obtained using secondary electron imaging. The images of the coated AFM tips

were obtained before and after the AFM experiments. In this way, possible detachment or delamination of the coatings was observed on the coated AFM tips.

Hence, since pull-off forces were only accepted for cases in which the coatings were still present after the pull-off experiments, the measured pull-off forces were confirmed to be due to the intended bi-material pairs. The spring constants of the coated and uncoated tips were measured using the thermal tune method [37,38]. This was measured because the actual spring constants are needed to obtain the true adhesion forces from Eq. (1). This also accounts for batch-to-batch variations in the spring constants, as well as the effects of coatings on the cantilever stiffness [25,36]. The pull-off measurements were obtained under ambient conditions (room temperature of 22–23 °C and a relative humidity of 40–45%).

5.3.2.2 AFM Force-Displacement Measurements

The interactions between the gold nanoparticle-coated AFM tips and the cell substrates or between the components of the drug delivery systems were measured using a Multimode Dimension DI Nanoscope IIIa Atomic Force Microscope (Bruker Instruments, Woodbury, NY, USA). The measurements were obtained under ambient conditions and relative humidity (40–45%). The photodetector sensitivity was calibrated on a stiff quartz surface before force microscopy measurements [39]. The Veeco probes were made from uncoated phosphorus (n)-doped silicon. They have a tip radius of curvature of 30 nm. For each pair of interactions, 150 adhesion measurements were obtained from 3 AFM tips with 50 measurements obtained for each tip at 5 different positions on the substrate. Table 5-I shows the different pairs used.

5.4 Results and Discussion

5.4.1 AFM Tip and Substrate Characterization

Back-scattered SEM images of the uncoated and dip-coated AFM tips are presented in Figures 5.3(a)–5.3(g). The images show tips before and after the AFM adhesion measurements. A typical uncoated AFM tip is shown in Figure 5.3(a). This shows that the bare tip is evenly smooth along the corners and surfaces of the tip. However, in the case of the coated tips, corners and apexes are covered with coatings that disrupt the smoothness of the surfaces. Typical AFM images of the dip-coated AFM tips are presented in Figures 5.3(b)–5.3(f). These show the surface morphologies of AFM tips that are coated with nanoscale layers of gold (Figure 5.3(b)), LHRH (Figure 5.3(c)), EphA2 breast specific antibody (Figure 5.3(d)). Furthermore, no evidence of coating delamination was observed on the surfaces of the coated AFM tips that were used in the pull-off experiments. Hence, the measured pull-off forces are due to interactions between the coated AFM tips and the substrates.

5.4.2 Adhesion Forces

Figure 5.4 shows a typical force-displacement plot for the adhesion between gold nanoparticles and LHRH. This plot has characteristics similar to the idealization presented in Figure 5.2. By multiplying the pull-off deflections with the tip stiffness shown in Table 5-II, the pull-off forces were obtained. There were no measurable forces for the control samples.

The adhesive force interactions between the different components of the designer drug delivery system (shown in Figure 5.1) are presented in Figure 5.5. The adhesion forces between the gold nanoparticles and LHRH and between gold nanoparticles and BSA are comparable and stronger than those obtained for paclitaxel-gold, paclitaxel-antibody or paclitaxel-LHRH complexes. The

weakest adhesive interactions within the drug nanocomposite systems (Figure 5.5) are with the drug (paclitaxel). These interactions result in pull-off forces of about 10 nN, compared to those without the drug ($F \sim 58$ nN). This suggests that the robustness of such systems will depend highly on the drug-component interactions. These above adhesion forces are generally related to Van der Waal's forces, with relatively large and short range interactions between the different components. Also, it can be observed that similar adhesion forces were obtained for the LHRH and BSA coated tips when measured against the same substrate (~ 60 nN against gold and ~ 10 nN against paclitaxel). This may be due to the amino acid sequence present in the peptide and polypeptide structures in the LHRH and BSA, respectively. The overall adhesion forces would, therefore, depend on the charge distributions and positions of the amino acid residues in the peptide and polypeptide structures of the LHRH and BSA structures.

The AFM force microscopy results (Figure 5.5) also show that gold nanoparticles are strongly attracted to biological compounds. The pull-off forces for gold-LHRH and gold-AB pairs are 6063 nN and 5763 nN, respectively. These forces are presented in Table 5-III.

These are far greater than those between gold and paclitaxel, which is 1260.6 nN. In contrast, there are weak adhesive interactions between paclitaxel and the molecular recognition units, LHRH and Antibody. The adhesive forces obtained for these interactions are 1061 nN and 961 nN, respectively. The results are shown in Table 5-IV.

The adhesion forces between taxol and gold, as well as taxol and thiol are generally less than the other interactions within the nanocomposite drug delivery system. Hence, the current results show that the drug is the weak link in the nanocomposite system. Careful nanocluster engineering must, therefore, be carried out to prevent the inadvertent release of the drug,

paclitaxel, before it is delivered to the tumor sites for controlled release and the treatment of cancer cells/tumor tissue.

Furthermore, the results show that the presence of thiols plays an important role in the overall robustness of the system. Figures 5.6–5.8 reflect increased adhesion forces, when compared with those with gold. In Figure 5.6, the thiolantibody couple has an adhesion force of 320640 nN, which is about three times the adhesion force between gold and the breast specific antibody. These results are summarized in Table 5-V.

Also, the adhesion force between thiol and gold is found to be almost double that between the gold and the BSA. These results clearly indicate a significant increase in the adhesive interactions when thiol is introduced between the gold and BSA. The increased adhesion forces between gold and thiol can be attributed to covalent bonds. Gold is known to form stable complexes with ligands which have “soft” or polarizable electron donating atoms such as phosphorus or sulfur [40]. Similarly, the stronger adhesive forces between BSA and thiol may be attributed to amine-thiol interactions.

Similar results were obtained for LHRH interactions. These resulted in a three-fold increase in the adhesion forces of gold-thiol structures, when compared with those of uncoated gold structures (Figure 5.7). Furthermore, the adhesion forces between gold and paclitaxel are about six times greater when thiols are present (Figure 5.8). The current results, therefore, confirm that thiols can improve the robustness of gold nanoparticle clusters, as is expected from prior work reported in the literature [41,42]. The current results are also presented in Table 5-VI.

The above results suggest that, with the exception of thiol-taxol interactions, the interactions between thiol and the other chemical species (LHRH, EphA2 and gold) generally result in increased adhesion. These results are shown in Table 5-VII.

The observed increase in adhesion forces (in the presence of thiols) is attributed to the effects of secondary bonds (Van der Waals forces or hydrogen bonds). Furthermore, the statistical variations in the measured adhesion forces seem to be less in the cases where the number of molecular species on the AFM tips is fewer. However, in cases with increased numbers of available molecular species on the AFM tips (taxol and LHRH), the variabilities in the measured adhesion forces may depend on the coverage of the AFM tips and the orientations of the molecules on the AFM tips and the substrates. Further work is clearly needed to explore the effects of molecular orientation and AFM tip coverage on the measured adhesion forces. These are clearly some of the challenges for future work.

The reasons for the variations in error ranges in the adhesion force measurements are not fully understood at the moment. We also note that the adhesive interactions between relatively large antibodies and gold nanoparticles result in smaller statistical variations, while those between organic structures with many possible sites of interactions result in larger variations in adhesive force.

Finally in this section, Figure 5.9 provides a comparison of the forces obtained for the different component pairs with thiols. As reported previously [43], proteins have the strongest affinity to thiols due to the possible disulfide intermolecular interactions.

Covalent bonds between gold and thiols [40] may be responsible for these strong adhesive interactions. Furthermore, the paclitaxel-thiol bi-material pair results in the smallest pull-off forces, suggesting the presence weak Van der Waal's interactions.

5.5 Implications

The implications of the current work are quite significant. They suggest that nanoparticles, peptides and antibodies can be coated on micro-cantilever tips and used to measure adhesion interactions that are relevant to drug delivery systems. Hence, the pairwise adhesive interactions between the drug components can be measured using force microscopy techniques. However, there is a need for further work to explore the extent to which the AFM adhesion measurements may vary due to interactions with liquids and different solvents that are relevant to in-vitro and in-vivo environments. In-vitro and in-vivo studies are also needed to understand the level to which the AFM adhesion measurements can be related to nanoparticle-drug component interactions and binding under experimental and clinical conditions. These are clearly some of the challenges for future work.

Based on the sizes of the rounded AFM tips with tip radii of about 30 nm, we estimate a total hemi-spherical volume of about 5656 nm² is available for the adhesive interactions with the substrates. Hence, in the case of the EphA2 antibodies, if we estimate the surface areas of the molecules to be approximately 1000 nm², then we would expect to have about 5.7 molecules interacting with the substrates. Consequently, partial coverage of the tip rounded AFM tips should result in about 3–5 molecules per rounded AFM tip. In the case of the smaller LHRH peptides, with surface areas of about 36 nm², about 157 LHRH peptides can be attached to the

rounded AFM tip, if it is fully covered. Similarly, the interactions with the taxol drug molecule with a surface area of 100 nm^2 could result in about 57 taxol molecules on the rounded AFM tip.

Furthermore, it is also clear that the adhesion methods that were used in this study can be used to screen the effectiveness of potential binding chemistry and coated nanoparticle targets before conducting expensive in-vitro and in-vivo studies that are needed for clinical use. However, the relatively weak bonds between the anti-cancer drugs (paclitaxel) suggest that nanocluster fragmentation may occur during transportation in the bloodstream to the target organs. Since such fragmentation may result in premature drug release from the nanoparticle clusters (before they reach the intended tumor tissue/target organs), there is a need for further experimental and computational work to study the resistance of the nanoparticle clusters to fragmentation under in-vitro and in-vivo conditions. Nevertheless, the results of the current study show clearly that thiols improve the adhesion between the constituents of nanoclusters that are relevant to early cancer detection and the localized treatment of cancer via hyperthermia and localized drug release.

5.6 Conclusions

This chapter presents the results of an experimental study of the adhesion forces between components of a model generic drug delivery/system that includes gold nanoparticles, paclitaxel, thiols, LHRH and breast-specific antibody, BSA. The results confirm that the robustness of such systems depends on the adhesion to paclitaxel, which is the weak link. In such cases, it is important to design nanoparticle clusters in which adhesion to the drug is increased to prevent premature release. The results suggest that the force microscopy technique can be used to rank the adhesion between different species in drug nanocomposites that are being developed to treat breast cancer and other forms of cancer. They also show that the presence of thiols can

significantly increase the adhesive forces between gold and the molecular recognition units or the drugs in these systems. Furthermore, the current work provides a tool for fast screening of potential binding chemistry for ligand conjugated nanoparticles that can also be used for cancer detection and treatment. Further work is clearly needed to measure the adhesion forces in biological environments and clinical settings.

References

- [1] L. A. Nagahara, M. Ferrari, and P. Grodzinski, *MRS Bull.* 34, 406–414 (2009).
- [2] P. Grodzinski, M. Silver, and L. K. Molnar, *Expert Rev. Mol. Diagn.* 6, 307–318 (2006).
- [3] D. Irvine, L. Vincent, J. E. Graydon, N. Bubela, and L. Thompson, *Cancer Nursing* 17(5), 367–378 (1994).
- [4] *Le Cancer Dans le Monde* edited by B. W. Stewart and P. Kleihues (C.I.d.R.s.I.C. (CIRC), IARC Press, Lyon, 2005).
- [5] A. Jemal, M. J. Thun, L. A. G. Ries, H. L. Howe, H. K. Weir, M. M. Center, E. Ward, X. C. Wu, C. Eheman, A. Anderson, U. A. Ajani, B. Kohler, and B. K. Edwards, *J. Nat. Cancer Inst.* 100, 1672–1694 (2008).
- [6] Y. Oni, C. Theriault, A. V. Hoek, and W. O. Soboyejo, *Mater. Sci. Eng. C* 31(2), 67–76 (2011).
- [7] R. Kurzrock and M. Markman, *Targeted Cancer Therapy* (Humana Press, Clifton, 2008).
- [8] M. P. Melancon, W. Lu, and C. Li, *MRS Bull.* 34, 415–421 (2009).
- [9] M. Ferrari, *Nat. Rev. Cancer* 5, 161–171 (2005).
- [10] M. V. Yezhelyev, X. Gao, Y. Xing, A. Al-Hajj, and O'. R. M. Nie Shuming, *Lancet Onco* 7(8), 657–667 (2006).
- [11] R. G. Ramachandra, S. Mahaveer, and B. D. Ross, *Clini. Can. Res.* 12, 6677 (2006).
- [12] D. L. Thorek and A. Tsourkas, *Biomaterials* 29(26), 3583–3590 (2008).
- [13] A. H. Lu, E. L. Salabas, and F. Schuth, *Angew Chem. Int. Ed. Engl.* 46(8), 1222–1244 (2007).
- [14] S. Laurent, D. Forge, M. Port, A. Roch, C. Robic, L. Vander Elst, and R. N.Muller, *Chem. Rev.* 108, 2064–2110 (2008).

- [15] Kim, S. Park, E. L. Ji, S. M. Jin, J. H. Lee, L. S. Lee, I. Yang, J. S. Kim, S. K. Kim, M. H. Cho, and T. Hyeon, *Angew. Chem. Int. Ed.* 45(46),7754–7758 (2006).
- [16] W. Stöber, A. Fink, and E. Bohn, *J Colloid Interface Sci.* 26(1), 62–69 (1968).
- [17] S. I. Stoeva, F. Huo, J. S. Lee, and C. A. Mirkin, *J. Am. Chem. Soc.* 127(44), 15362–15363 (2005).
- [18] V. Salgueirino-Maceira, M. A. Correa-Duarte, M. Farle, A. Lopez-Quintela, K. Sieradzki, and R. Diaz, *Chem. Mater.*18(11), 2701–2706 (2006).
- [19] M. Chen, Y. N. Kim, H. M. Lee, C. Li, and S. O. Cho, *Phys. Chem. C* 112, 8870–8874 (2008).
- [20] H. Wang, D. W. Brandt, F. Le, P. Nordlander, and N. J. Halas, *Nano. Lett.* 6(4), 827–832 (2006).
- [21] L. Wang, J. Bai, Y. Li, and Y. Huang, *Angew. Chem. Int. Ed. Engl.* 47(13), 2439–2442 (2008).
- [22] G. Binnig, C. F. Quate, and Ch. Gerber, *APS J. Phys. Rev. Lett.* 56,930–933 (1986).
- [23] R. Wiesendanger, *Scanning Probe Microscopy and Spectroscopy: Methods and Applications* (Cambridge University Press, Cambridge, 1994).
- [24] S. N. Magonov and M. H. Whangbo, *Surface Analysis with STM and AFM: Experimental and Theoretical Aspects of Image Analysis* (VCH, Weinheim, 1996).
- [25] J. Meng, E. Paetzell, A. Bogorad, and W. O. Soboyejo, *J. Appl. Phys.*107, 114301 (2010).
- [26] C. B. Prater, P. G. Maivald, K. J. Kjoller, and M. G. Heaton, *Force Spectroscopy*, “See www.braker.com.”

- [27] P. G. Hartley, F. Grieser, P. Mulvaney, and G. W. Stevens, *Langmuir* 15, 7282–7289 (1999).
- [28] H. J. Butt, B. Cappella, and M. Kappl, *Surf. Sci. Rep.* 59, 1–152 (2005).
- [29] C. C. Berry and A. S. G. Curtis, *J. Phys. D: Appl. Phys.* 36, R 198 (2003).
- [30] P. Hinterdorfer, G. Sch€utz, F. Kienberger, and H. Schindler, *Rev. Mol. Biotechnol.* 82, 25 (2001).
- [31] V. Dupres, F. D. Menozzi, C. Loch, B. H. Clare, N. L. Abbott, S. Cuenot, C. Bompard, D. Raze, and Y. F. Dufrene, *Nat. Methods* 2, 515–520 (2005).
- [32] E. Wojcikiewicz, X. Zhang, and V. Moy, *Biol. Proced. Online* 6, 1–9 (2004).
- [33] F. Li, S. D. Redick, H. P. Erickson, and V. T. Moy, *Biophys. J.* 84,1 252–1262 (2003).
- [34] W. R. Miller, W. N. Scott, R. Morris, H. M. Fraser, and R. M. Sharpe, *Nature* 313, 231–233 (1985).
- [35] D. P. Zelinski, N. D. Zantek, J. C. Stewart, A. R. Irizarry, and M. S. Kinch, *Cancer Res.* 61, 2301–2306 (2001).
- [36] K. V. Wolf, Z. Zong, J. Meng, A. Orana, N. Rahbar, K. M. Balss, G. Papandreou, C. A. Maryanoff, and W. Soboyejo, *Biomed. Mater. Res. Part A* 87A, 272–281 (2008).
- [37] J. L. Hutter and J. Bechhoefer, *Rev. Sci. Instrum.* 64, 1868–1873 (1993).
- [38] G. A. Matei, E. J. Thoreson, J. R. Pratt, D. B. Newell, and N. A. Burnham, *Rev. Sci. Instrum.* 77, 083703 (2006).
- [39] B. Bhushan, *Handbook of Micro/Nanotribology* (CRC, Boca Raton, 1995).
- [40] R. G. Pearson, *Struct. Bonding* 80, 1–10 (1993).
- [41] A. Kassam, G. Bremner, B. Clark, and B. R. Lennox, *J. Am. Chem. Soc.* 128(11), 3476–3477 (2006).

- [42] Z. M. Fresco and J. M. J. Frechet, *J. Am. Chem. Soc.* 127(23), 8302–8303 (2005).
- [43] N. Ohmura, K. Tsugita, J. I. Koizumi, and H. Saika, *J. Bacteriol.* 178(19), 5776–5780 (1996).

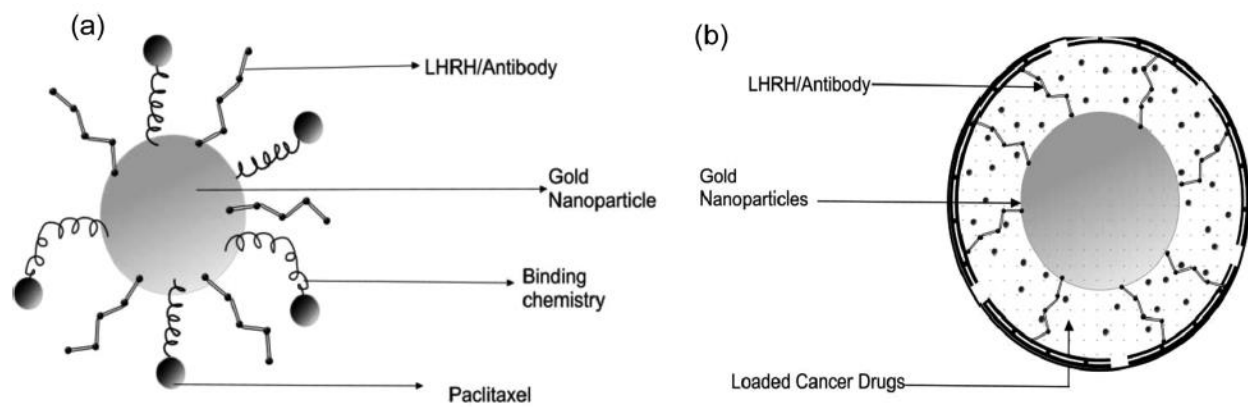


Figure 5.1: Possible schematics of a nanoparticle-based drug delivery/detection system.

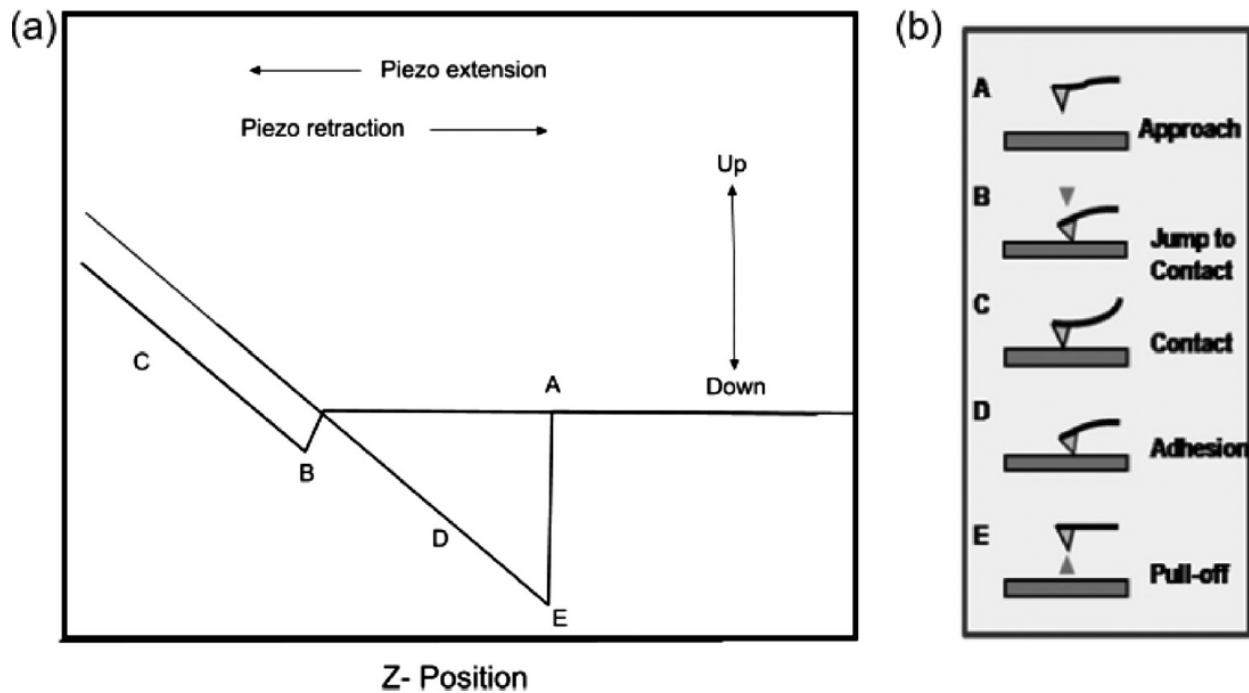


Figure 5.2: Schematic of an atomic force microscope force-displacement behavior: (a) Load-displacement plot, (b) Tip/Surface Interaction. In one cycle, tip approaches the surface of the substrate (A), jumps to contact with substrate as significant van der Waals forces are felt (B), undergoes elasticity as it is displaced further in the same direction (C), displacements are reversed upon retraction as loads reduce to zero (D), tip does not detach at zero load due to the effects of adhesion until sufficient force is applied to pull the tip off the surface (E).

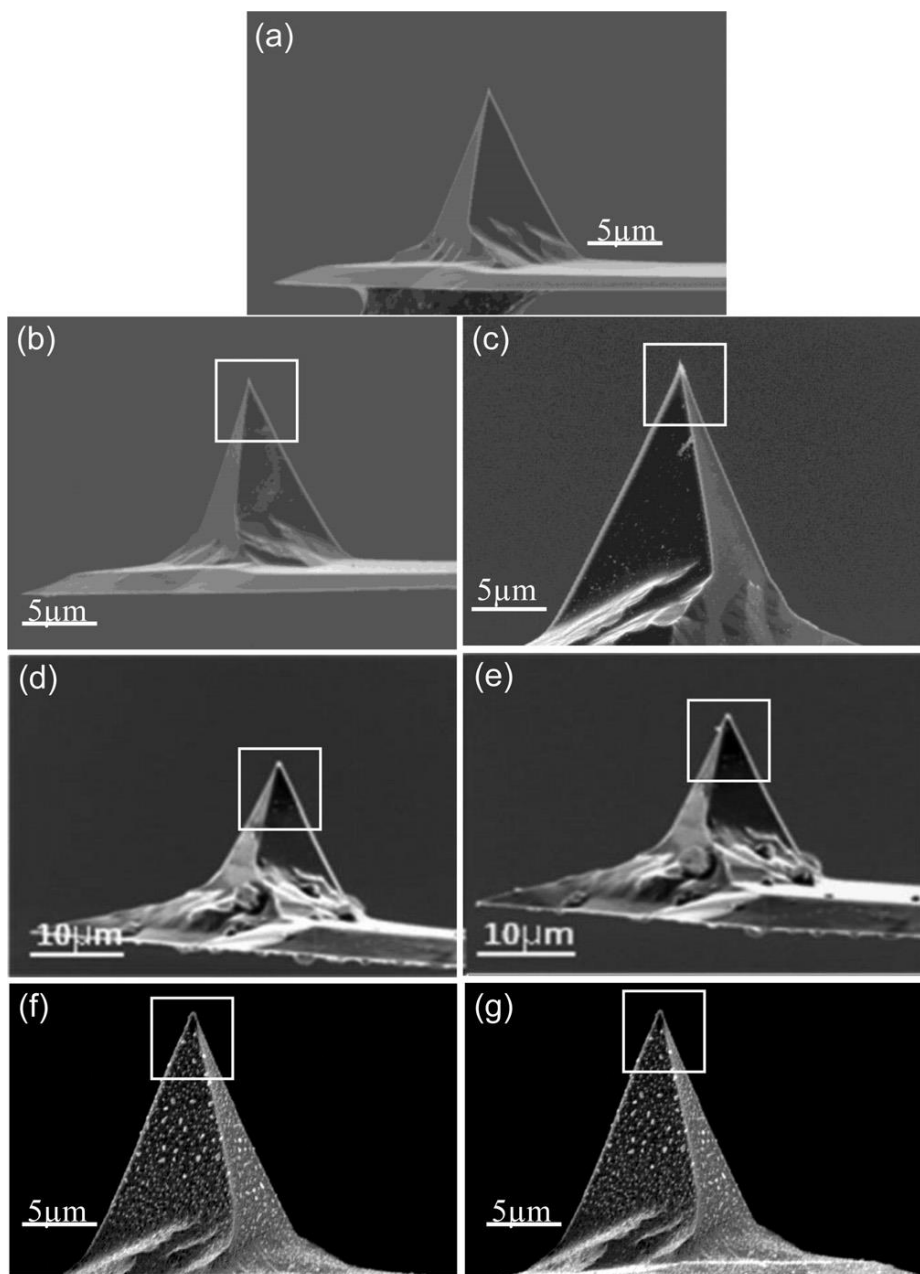


Figure 5.3: Sample SEM Images of the AFM tips: (a) Bare AFM tip; (b) Gold nanoparticles-coated AFM tip before adhesion measurement; (c) Gold nanoparticles-coated AFM tip after adhesion measurement; (d) LHRH-coated AFM tip before adhesion measurement; (e) LHRH-coated AFM tip after adhesion measurement; (f) BSA-coated AFM tip before adhesion measurement; (g) BSA-coated AFM tip after adhesion measurement. Boxes show coating on apex tip and side edges.

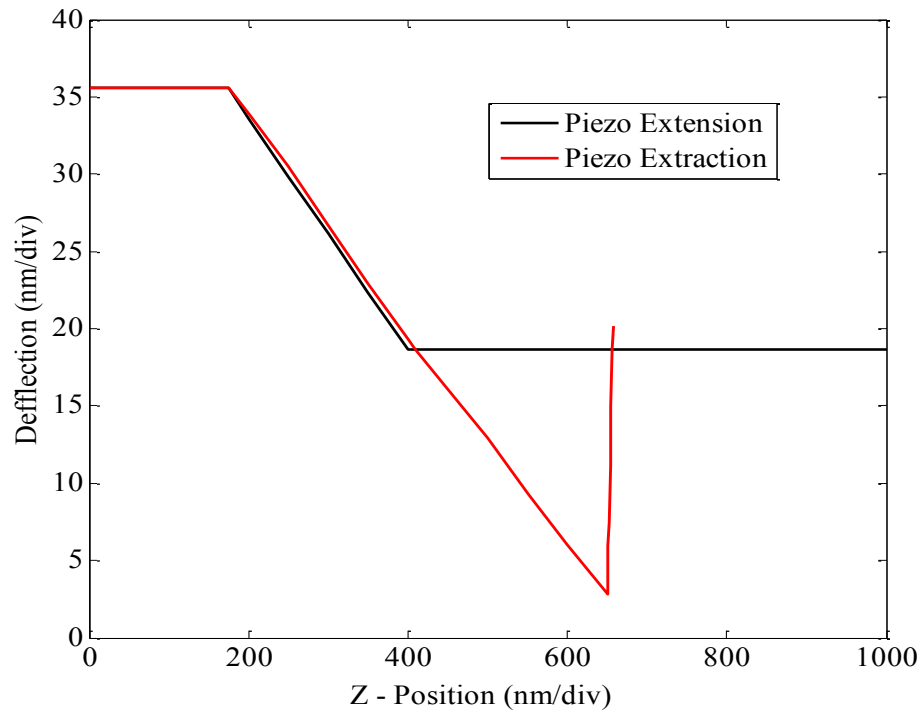


Figure 5.4: Typical AFM force-displacement behavior for coated tips on substrates.

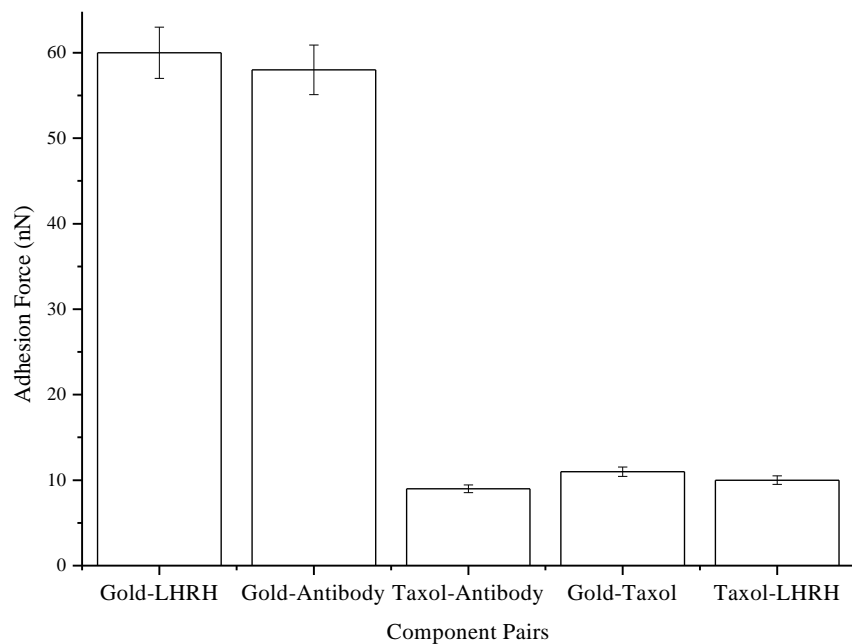


Figure 5.5: Adhesion interactions of components in a drug delivery system.

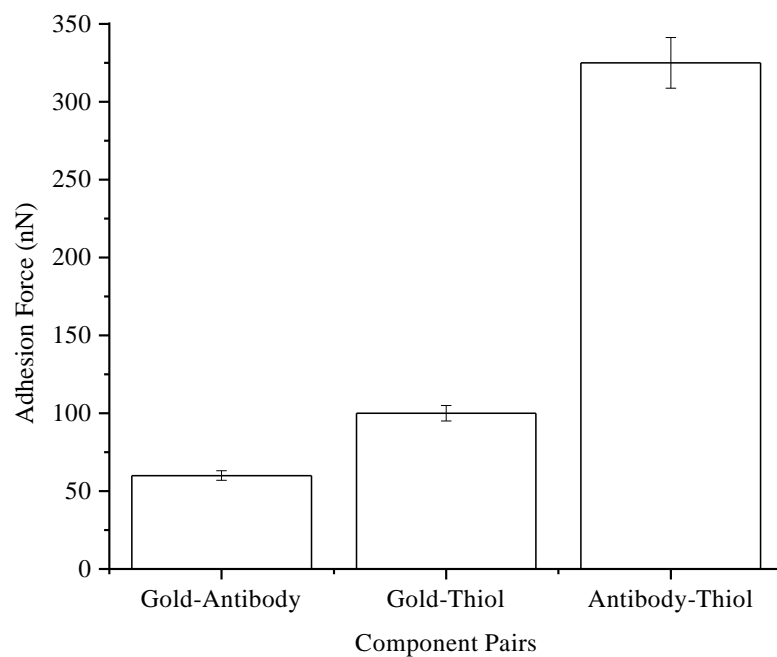


Figure 5.6: Comparison of adhesion interactions for gold with and without thiols.

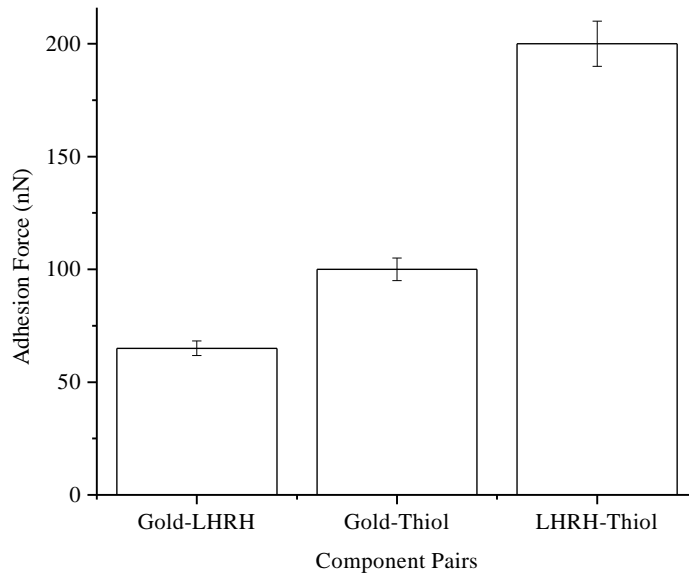


Figure 5.7: Comparison of adhesion interactions for LHRH with and without thiols.

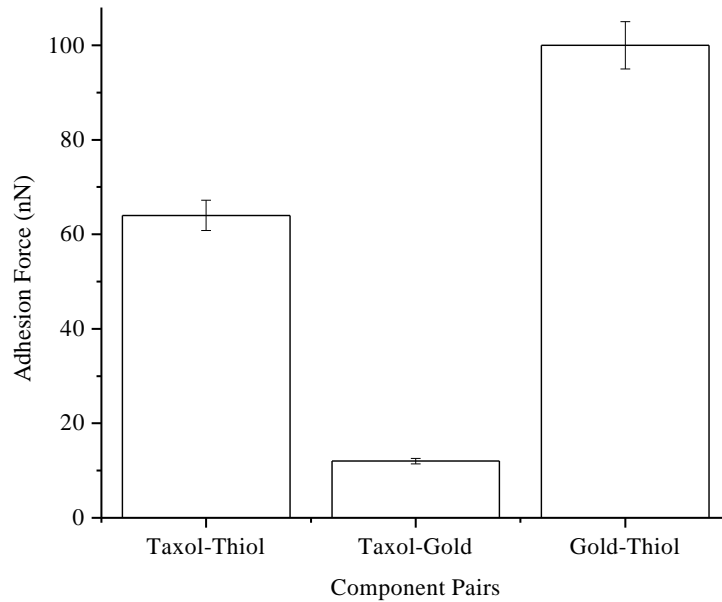


Figure 5.8: Comparison of adhesion interactions for paclitaxel (taxol) with and without thiols.

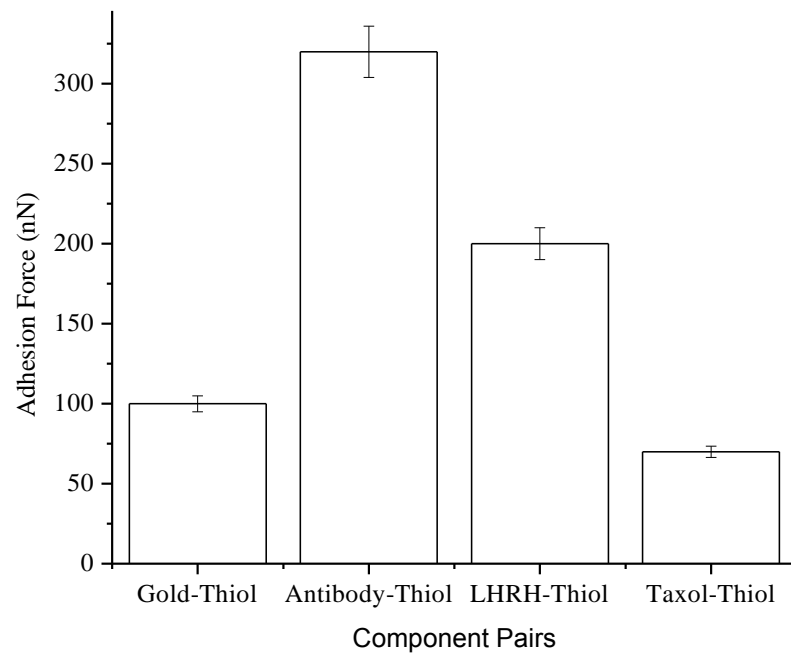


Figure 5.9: Comparison of adhesion interactions of the nanocomposite components with thiols.

Table 5-I: Substrates and coated tips used in AFM study

Coating on tip	Substrate
Gold	Taxol (Paclitaxel)
Gold	Taxol (Paclitaxel)
Gold	Antibody
Antibody	Taxol (Paclitaxel)
LHRH	Taxol (Paclitaxel)

Table 5-II: Spring constants of the bare and coated tips

LHRH-coated tip	0.71 ± 0.11
Gold-coated tip	0.48 ± 0.21
Antibody-coated tip	1.02 ± 0.32

Table 5-III: Comparison of adhesion interactions for LHRH with and without thiols

Component pairs	Average adhesion force (nN)
Gold-LHRH	60 ± 3
Gold-Antibody	57 ± 3
Gold-Thiol	100 ± 5
LHRH-Thiol	200 ± 10

Table 5-IV: Comparison of adhesion interactions for paclitaxel (taxol) with antibody, gold or LHRH.

Component pairs	Average adhesion force (nN)
Taxol-thiol antibody	9 ± 1
Taxol-gold	12 ± 0.6
Taxol-LHRH	10 ± 1

Table 5-V: Comparison of adhesion interactions for Gold with and without thiols.

Component pairs	Average adhesion force (nN)
Gold-antibody	60 ± 3
Gold-thiol	100 ± 5
Antibody-thiol	320 ± 40

Table 5-VI: Comparison of adhesion interactions for LHRH with and without thiols.

Component pairs	Average adhesion force (nN)
Gold-LHRH	60 ± 3
Gold-thiol	100 ± 5
LHRH-thiol	200 ± 10

Table 5-VII: Comparison of adhesion interactions of the nanocomposite components with thiols.

Component pairs	Average adhesion force (nN)
Gold-thiol	100 ± 5
Antibody-thiol	320 ± 6
LHRH-thiol	200 ± 10
Taxol-thiol	65 ± 3

Chapter 6

6.0 Injectable, Biodegradable Microparticles Loaded with Prodigiosin for Localized Anticancer Drug Delivery in the Treatment of Cancer

6.1 Background and Motivation

Cancer is currently the second leading cause of death [1,2]. Specifically, breast and prostate cancers are the second most common causes of cancer deaths in women and men, respectively [3]. Current trends also suggest that cancer will become the leading cause of death by 2030 [1,4]. The conventional methods for the treatment of breast cancer include: bulk systematic surgery, chemotherapy and radiotherapy. These are associated with high cost and severe side effects [5-7]. Chemotherapy also affects normal cells, while reducing the therapeutic indices of the drugs [8]. Many of the existing cancer drugs also lack selectivity and specificity [9-13]. Hence, incremental improvements in breast cancer therapy are unlikely to address the challenges associated with the cost and side effects of breast cancer treatment.

Prior work has shown that current cancer treatment procedures often result in short extensions of life [6]. In some cases, new tumors replace old ones, resulting in revisiting therapies [8]. To compliment these efforts, there is therefore, a need to develop localized controlled drug delivery cancer treatment techniques that can increase the effectiveness of cancer treatment, while reducing the cost and side effects (due to toxicity) of cancer treatment. This can be achieved by the direct injection of microspheres that are loaded with anti-proliferative and therapeutic cancer drugs that can release in a controlled manner [14]. Such microspheres can release cancer drugs

to breast cancer cells/tumors, through a controlled release by diffusion or as they degrade by hydrolysis or biodegradation.

Polymeric drug-loaded particles have been used effectively in the treatment of prostate cancer [15], atherosclerosis [16] and breast cancer [17], by localized drug delivery. This is due to their uniqueness in the delivery of drugs within the therapeutic window [18,19]. Unlike conventional bulk chemotherapy, which is relatively expensive and could have some side effects [18-20], polymeric drug-loaded microparticles can be injected directly into tumor regions to provide localized chemotherapy. This reduces the concentrations of cancer drugs that are needed for effective treatment. Injectable polymer-loaded drugs also result in low/minimal levels of toxicity [14,18,19,21] and hypersensitivity reactions [19].

This chapter presents the results of an experimental study of injectable poly (DL-lactide-co-glycolide) (PLGA)-loaded microspheres that are loaded with a biosynthesized apoptosis and anti-proliferative agent (prodigiosin) or a commercially available cancer drug (paclitaxel). This was achieved by single emulsion solvent evaporation technique (SESET) [22-24], in the presence of PLGA with a PVA emulsifier. The PLGA polymer and the PVA emulsifier are all approved by the World Health Organization (WHO) and the United States Food and Drug Administration (FDA) as implant materials for human therapy [25-27]. However, there are relatively few studies of low cost drug-loaded microparticles for cancer treatment [9-13].

Injectable PG-loaded PLGA microparticles were formed in this work which provides great potential for replacing PT-loaded microspheres for the sake of low costs. This is because

prodigiosin has been shown to have great potentials in the treatment of cancer [28-33]. PG has been used as an anticancer agent [28-32] and has been shown to have the ability to cause apoptosis [33] and as an immunosuppressant [28] agent. PT-loaded PLGA microspheres were developed as a positive control. Generally, the IC_{50} reported for PT against cancer cells lines is of the order of 10–100 nM (10–100 ng/mL) [15]. This provides a range of controlled PG or PT release over period that may be needed for elimination of cancer cells. Despite several efforts in the field of biodegradable polymeric drug-loaded microspheres, to the best our knowledge, no current work has explored the development of low cost injectable PG-loaded microspheres for localized treatment of cancer.

The resulting particles formed have sizes that were found to be influenced by the concentration of stabilizer/emulsifier and the homogenizer speed. The physicochemical characteristics, release studies were carried out to understand the drug loading efficiency, encapsulation efficiency and drug morphology with respect to release time were elucidated via a combination of scanning electron microscopy (SEM), differential scanning calorimetry (DSC), UV-visible spectrophotometry, optical microscope and AFM. The implications of the results are then discussed for the development of injectable and multi-functional low cost prodigiosin-loaded microparticles for cancer therapy. This PG-loaded PLGA microsphere will take advantage of the cost associated with PT-loaded microsphere by exploiting the unique anatomical and pathological abnormalities of the tumor vasculature for effective localized delivery of cancer drugs.

6.2 Materials

The chemicals that were used for the processing of the polymer-based microspheres include: polylactide-co-glycolide of different ratios of lactide-to-glycolide and polylactide (50:50 and molecular weight 30,000-60,000). These obtained from Sigma Aldrich, St Louis, MO, USA. The solvent, dichloromethane (DCM), that was used to dissolve the PLGA, was obtained from Fisher Scientific, Marietta, OH, USA. Poly vinyl alcohol (PVA) (98% hydrolyzed, MW= 13,000 – 23,000) was obtained from the Aldrich Chemical Co., Milwaukee, WI, while PT (anti-proliferative/anti-cancer drug) was obtained from LC Laboratories, Woburn, MA, USA. The anti-proliferative/anti-cancer drug (PG) was biosynthesized from *Serratia marcescens subsp. Marcescens* strains obtained from a soil at the Sheda Science and Technology Complex (SHESTCO), Abuja, Nigeria. Dimethyl sulfoxide (CH₃)₂SO (DMSO) was purchased from BDH Chemicals (Poole Dorset, England). This was used to dissolve the prodigiosin drug. Phosphate Buffered Saline (PBS) with solution with a pH of 7.4 was used for the drug delivery experiment. This was obtained from Life Technologies Corporation, Grand Island, NY, USA.

6.3 Experimental Methods

6.3.1 Synthesis and Purification of Prodigiosin (PG)

The PG that was used in this study was obtained from *Serratia marcescens subsp. Marcescens* bacteria at the Biotechnology and Genetic Engineering Advanced Laboratory, Sheda Science and Technology Complex (SHESTCO), Abuja, Nigeria. A method developed by Kamble *et al.* [34] was used for the synthesis and extraction of PG from *Serratia marcescens subsp. Marcescens* strains. The extracted samples were then purified using size exclusion chromatography prior to

characterization with High Performance Liquid Chromatography (HPLC) (Prominence, Shimadzu, Kyoto, Japan). During the purification process, the sample containing the pigment of PG was collected and placed in a rotary evaporator (BUCHI, Rotavapor® 114 with Water Bath B-480, Bristol, Wisconsin, USA) to remove the ethanol leaving the first extract of PG. This sample was then purified using column chromatography.

During the column chromatography, the stationary phase used was a silica gel (BDH Chemicals, 300624v, Poole Dorset, England), while the mobile phase was a mixture of ethyl acetate, chloroform and methanol in the ratio of 2:1:1, respectively. The PG extract was layered at the top of the gel in the column and fractions eluted by adding the mobile phase. Subsequently, 5 mL fractions of the sample were collected over several minutes. This was followed by UV-Vis spectrophotometric (UV-Vis) measurements of the fractions at a wavelength of ~ 535 nm. This was done using a UV-Vis spectrophotometer (CECIL 7500 Series, Buck Scientific Inc., East Norwalk, USA). Finally, the fractions that absorbed at this wavelength were pooled together and subsequently dried in a freeze dryer (LABCONCO, Kansas City, Missouri, USA).

High Performance Liquid Chromatography (HPLC) was carried out using an HPLC system with a dual wavelength absorbance detector (Waters 2695 with 2487 Absorbance Detector, LabX, Midland, ON, Canada) to determine the purity of the extracted prodigiosin samples by producing spectra at 535 nm. This was compared with a standard PG (purity = 95%, Mw = 323.4 g/mol) procured from Santa Cruz Biotechnology, CA, USA. Methanol and 10 mM triethylamine (17:3 v/v), with pH adjusted to 6.5 (using phosphoric acid), were used as the mobile phase at a flow

rate of 1.0 ml/min through a reverse column at 40°C. The acid was used to improve upon the chromatographic peak shape and also to provide a source of protons in the reverse phase.

Furthermore, the concentration of the standard solution was matched to the sample solution to avoid peak mis-assignment due to peak shape effects. 500 µg of each sample; standard PG and the sample PG were separately dissolved in 2 ml of methanol to obtain equal concentrations of 250 µg/ml. The PG content was determined from the HPLC analysis by comparing the peak areas (normalization), as well as the symmetrical increase of the peak areas as a function of the retention time. By comparing the retention time and response of the peak in the chromatogram of the standard solution, with the sample chromatogram, the peaks were assigned. The percentage peak, AP, areas and the amounts of PG present in the sample corresponding to a peak area were obtained from the work done by Dolan *et al.* [35-37].

6.3.2 Preparation of Polymer-loaded Microspheres

Prodigosin and paclitaxel-loaded PLGA microspheres were prepared using a single emulsion solvent evaporation technique (SESET) [22-24]. This technique is also referred to as the Single Emulsion Micro-encapsulation (SEME) method. It is a common method for the entrapment of hydrophobic drugs into polylactide-co-glycolide acids (PLGAs) [38]. The PG/PT-loaded PLGA microspheres were prepared using the SESET adapted from prior work by various research groups [39-43].

In this work, 100 ml each of 0.5 % and 3 % PVA emulsifier were prepared. Typically, two portions of 200 mg of PLGA were dissolved in 2.0 ml of dichloromethane (DCM). The solution

of PLGA and the DCM was then vortexed and mixed for 5 minutes to obtain a homogenous PLGA solution. To each portion of the PLGA solution, 0.2 ml of 7.5 mg/ml of PG and 0.2 ml of 7.5 mg/ml of PT that were freshly prepared with DMSO were gently poured, respectively. The resulting solutions were stirred with a homogenizer (Ultra Turrax T8, IKA Works Inc., Wilmington, NC, USA) for 1 minute at 18000 and 22000 rpm, respectively.

Each of the two separate resulting solutions of PG/PT and PLGA solution (solution of organic phase) was poured slowly into an aqueous solution containing 0.5 or 3 % PVA as surfactant, to form an oil-in-water (o/w) emulsion, respectively. The solutions were homogenized with an Ultra Turrax T8 homogenizer for 4 minutes at 18000 and 22000 rpm, respectively. The samples were then transferred into a magnetic stirrer, stirring at 600 rpm for 3 hours to evaporate the DCM and DMSO in the solution mixture. The residual solutions were then washed several times with deionized water before centrifuging them at 3,000 rpm to remove the emulsifier/stabilizer and recover the pellet drug-encapsulated microparticles that were formed. Finally, the microspheres were pre-frozen at -80°C for 20 minutes in dry ice for 10 minutes. This was followed by lyophilization for 16 hours at -80°C under 110 mmHg vacuum (2KBTXL-75 Benchtop SLC Freeze Dryer, Virtis, Warminster, PA, USA). Non-loaded PLGA microspheres were prepared at a homogenizer speed of 18000 and 22000 rpm, respectively as controls using the same approach but without the addition of PG and PT solutions.

6.3.3 Materials Characterization

The morphology of the PG/PT-loaded PLGA microspheres formed at a homogenizer speed of 18000, 22000 rpm and 0.5 % and 3 % PVA concentration, respectively, were characterized using a high-resolution field emission scanning electron microscope (AMRAY 1830 I SEM, AMRAY, Inc, Bedford, MA, USA). Prior to SEM, the samples were mounted on aluminum stubs and gold-coated using a sputter coater [44] for 1 minute. This was done to make the surfaces conductive without compromising the fine surface microstructures. These gold-coated particle samples were cooled over liquid nitrogen prior to SEM analysis. This was done to avoid their melting due to the electron beam exposure. The size distributions of the microspheres were then determined using the ImageJ software package (NIH Image, Scion Image for windows, National Institute of Health, Bethesda, Maryland, USA). This was used to analyze the SEM images of the microspheres. The polydispersity indices (PDI) of the nanoparticles were also measured using a Zetasizer-Nano Z590 instrument, DLS (Malvern Instruments, Worcestershire, UK).

The thermal characteristics of PG/PT-loaded microspheres formed at a homogenizer speed of 18000 rpm were analyzed using differential scanning calorimetry (DSC) (Q1000 DSC, Thermal Analysis Instruments, New Castle, DE). This measured the heat flow (in and out of both sample and reference) during a controlled temperature program. The crystalline nature of the pure drug and its thermal behavior were studied using DSC. The glass transition temperature (T_g) and the melting temperature (T_m) were obtained from the DSC measurements. All of the DSC measurements were conducted in crimped nonhermetic aluminum pans. The samples were heated at the rate of 10°C/min from 0°C to 200°C for plain PLGA microspheres, and from -10°C to 250°C, for the encapsulated microspheres. This was done using an empty crimped aluminum

pan as a reference. The glass transition temperature (T_g) was determined from the mid-point temperature of the endothermic drift in the heating curve.

A UV-Visible spectrophotometer (Lambda XLS, Perkin Elmer, Waltham, USA) was used to estimate the concentration of PG or PT in the microspheres. These were estimated from the spectroscopic measurements. The UV-vis spectrophotometer measures the absorbance of each solution of the samples. From *Beer Lambert's Law*, the absorbance, (A) is directly proportional to the path length, (L), and the concentration, (C), of the absorbing species and β is the molar absorptivity of the species.

$$A = \beta CL \quad 6.1$$

This gives concentrations of the PG and PT in the solution were determined from a standard curve that was obtained for a maximum absorbance at wavelengths of ~ 535 and 235 nm, respectively. The drug loading efficiency, DLE, of the microspheres was obtained from the expression [45].

$$DLE = \frac{M_D}{M(D+P)} \times 100\% \quad 6.2$$

where M_D is the mass of drug uptake into the microspheres and $M(D+P)$ is the mass sum of drug and polymer in the microsphere. Thus, the drug encapsulation efficiency, DEE, of the microparticles formed was calculated from the expression given below:

$$DEE = \frac{M_x}{M_z} \times 100\% \quad 6.3$$

where M_x is the amount of encapsulated drug and M_z amount of drug used for microparticles preparation.

6.3.4 Standard Curve and Drug Concentration

In order to estimate the exact drug content, there was a need to calibrate a standard curve. A 0.12 ml of stock solution of known concentration (7.5mg/ml) of PG was used to prepare a standard concentration curve. This was done using a method reported by Kesarwani *et al.* [46]. The solution was serially diluted and dissolved in DMSO (DMSO dissolve PG and PT completely and faster) to obtain standard PG drug solutions with concentrations of 0.01, 0.03, 0.06, 0.12 and 0.24 mg/ml. A UV spectrophotometer (Lamda XLS, Perkin Elmer, Waltham, USA) was used to determine the absorbance at ~ 535 nm (Figure 6.2 (a)) using DMSO as blank. The measured absorbances were then plotted against known concentrations (Figure 6.3 (a)). This was used to obtain a calibration curve for determining the concentrations of PG at any absorbance respectively.

A similar approach was used to quantify the concentration of paclitaxel at an absorbance of 235 nm. In this case, 7.5 mg of pure PG was dissolved in 1 ml of dichloromethane (DCM) to obtain standard PT solution. This was then serially diluted to obtain paclitaxel solutions with concentrations 0.01, 0.03, 0.06, 0.12 and 0.24 mg/ml. A UV spectrophotometer (Lamda XLS, Perkin Elmer, Waltham, USA) was used to determine the absorbance at 235 nm (Figure 6.2 (b)). The results were then plotted against concentration (Figure 6.3 (b)) to obtain a calibration curve for determining the concentration of paclitaxel. The calibration curves obtained above were used to determine the concentration of PG and PT. These were used in subsequent drug release experiments in which UV absorbance measurements were obtained from solutions containing the microspheres at wavelengths of 535 nm and 235 nm, respectively.

6.3.5 *In-vitro* Drug Release from Microparticles

This release of drugs (PG or PT) from the microspheres containing entrapped drugs was also characterized. 10 mg each of PG or PT drug-loaded microspheres (prepared under 18000 and 22000 rpm homogenizer speed using 0.5 % and 3 % PVA concentration) were suspended in 10 ml of phosphate buffered saline (PBS) (containing 0.1 % w/v Tween 80) in triplicate 16 ml screw-capped (Teflon) tubes at a pH of 7.4. This was done to mimic human blood for the period of 8 days (192 h). The resulting solution facilitates microsphere suspension and drug solubility. The tubes were placed in an incubator shaker (Innova 44 Incubator, Console Incubator Shaker, New Brunswick, NJ, USA) that was maintained at 37°C and shaken at 8 rpm. At time intervals of 12 hours and subsequently 24 hours towards the end of the experiment, the tubes were centrifuged at 3000 rpm for 5 minutes. 2.0 ml of the supernatant (referred to as release study samples) were then extracted and stored at -25°C for subsequent UV-Visible spectrophotometry. 2.0 ml fresh drug-free release media were added to the tubes to maintain sink conditions during the release study. The tubes were then inserted into the orbital shaker until the next sampling time.

The concentrations of drug from the release study were quantified using the UV-Visible standard curves prepared for the PG and PT. The changes in the morphologies, degradation and release rate of the microspheres were also characterized with respect to their structure using optical microscope (Nikon Eclipse E200, Nikon Instruments Inc., Melville, New York, USA) with an Edmond Optics EO-4010C and AFM (AFM, Multimode™ Scanning Probe Microscope, Digital Instruments, USA) of selected samples at different stages of drug release.

6.4 Results and Discussion

6.4.1 Microsphere Morphology and Physicochemical Properties

SEM micrographs of encapsulated prodigiosin polymer-loaded microspheres are presented in Figures 6.4 (a) and 6.4 (b) for samples prepared at homogenizer speeds of 18000 and 22000 rpm, respectively. These show porous PG-loaded microspheres with particle sizes that are between 5 and 50 μm (Figure 6.4 (c) and 6.4 (d)). In the case of PT-loaded PLGA microspheres formed at similar homogenizer speed of 18000 and 22000 rpm, respectively, the microparticle sizes were between 5 and 40 μm (Figure 6.5 (c) and 6.5 (d)) with their micrograph as shown in Figure 6.5 (a) and 6.5 (b). This clearly shows that as the homogenizer speed increases during the PG-loaded microspheres formulation, the particle sizes formed tend to decrease and vice versa.

The microparticles sizes were also influence by the concentrations of PVA (Figures 6.6 and 6.7). This is shown in Figures 6.6 (a) – 6.6 (d), for PG-loaded PLGA microspheres formed in the presence of 0.5 and 3 % PVA concentrations. The sizes formed ranges from $\sim 5 - 70 \mu\text{m}$ and $\sim 5 - 25 \mu\text{m}$ for microspheres formed in the presence of 0.5 % and 3 % PVA concentrations, respectively. Similar results were also obtained for PT-loaded microspheres with sizes ranges between ~ 10 and $50 \mu\text{m}$ for 0.5 % PVA and ~ 5 and $25 \mu\text{m}$ for 3 % PVA concentration (Figures 6.7 (a) – 6.7 (b)). These results are consistent with prior reports by Zambaux *et al.*[47], Stevanovi *et al* [48] and Niwa *et al.* [49]. As the PVA concentration increases, the particle sizes formed in the process decreases and vice versa. This is because a higher concentration of the emulsifier tend to decrease the interfacial energy of oil droplets, thus smaller droplets that correspond to larger surface area can be formed [50] (See Table 6.1).

In the case of the control (plain microspheres without drug encapsulated under the same conditions), the temperatures; glass transition, T_g , and melting temperature, T_m were ~ 45.35 °C and 48.5 °C, respectively (Figure 6.8 (a)). However, in the case of the encapsulated prodigiosin and paclitaxelTM microspheres, the T_g and T_m were ~ 31.13 °C, 35.5 °C and ~ 27.53 °C, 32 °C respectively (Figures 6.8 (b) and 6.8 (c)). The changes in the measured T_g and T_m values are attributed to the drug acting as a strong plasticizer for the polymer (PLGA). In other words, it suggests that the drug have a strong miscibility with the PLGA polymer used [51]. These above results are in agreement with prediction of T_g from the Flory-Fox equation [52].

$$\frac{1}{T_{gTheoretical}} = \frac{W_{PLGA}}{T_{g,PLGA}} + \frac{W_{Drug}}{T_{g,Drug}} \quad 6.4$$

Where $T_{gTheoretical}$ is glass transition temperature of the drug-loaded polymer microspheres, $T_{g,PLGA}$ and $T_{g,Drug}$ are glass transition temperature of the polymer, PLGA and drug, respectively. W_{PLGA} and W_{Drug} are weight fractions of polymer, PLGA and drug, respectively.

The porosity of the PG-loaded PLGA microspheres is associated to the diffusion of the inner phase, as a result of the removal of volatile solvents. These solvents diffuse into the aqueous medium and evaporate at the air/water interface under constant stirring, leaving only spherical polymer microspheres in the aqueous phase. It could be reasoned that the influx between the internal aqueous phase and external aqueous phase result in pore formation [53].

6.4.2 Purity of Extracted Prodigiosin and Standard Calibration Curves

From the chromatogram of both the test sample and the standard sample, single peaks were obtained. These indicate the presence of single components (Figure 6.9). For the sample, the

peaks (1-7) grow and retain symmetry, given a tentative confirmation of the sample (PG) [35,37]. The asymmetry factor for the peaks, 1, 2, 3, 4, 5, 6 and 7, were determined to be 1.26, 0.31, 1.26, 0.10, 0.70, 1.17 and 0.51, respectively. Meanwhile asymmetry factors, as of peaks at 1.0-1.4 are considered good, while As between 1.5- 2.5 are marginally accepted and As values above 3.0 are unacceptable [36]. Clearly, all the asymmetry factors reported here are considered to be good and hence peaks were considered for the analysis. Quantitatively, peak areas or heights were used to determine the concentration of PG in the sample [35,37].

In this chapter, the peak areas were used to determine the content of PG because the peaks were slightly tailed. The peak heights varied, while the areas remained constant. Peak symmetry is also a performance characteristic for a good quantitative result. The test sample shows good asymmetry based on the asymmetry factors determined. Other six smaller peaks were observed in the test samples due to unavoidable organic impurities that were present. Also, the greatest peak was obtained at 5.01 min of retention time, with a percentage area of 95.42, as compared to 4.87 min for the standard sample, which also had recorded a percentage area of 97.66. The purity of the standard sample was 95 %. This translates by ratio to a sample purity of 92.8 %.

The calibration curves obtained for prodigiosin and paclitaxel are presented in Figure 6.2 (a) and 6.2 (b), respectively, for absorbance at wavelengths of ~ 535 nm and 235 nm. The plots are consistent with prior reports in the literature [28,34]. These calibration curves were used to obtain the corresponding concentrations of the drugs in the microspheres.

6.4.3 *In-vitro* Drug Release From Prodigiosin/PaclitaxelTM-Loaded PLGA Microspheres

The average particle sizes and polydispersity indices of the microspheres used for the drug release experiment were 16.4, 15.5 μm and 0.21, 0.35 for PG and paclitaxel-loaded microsphere respectively (Table 6.1) at a homogenizer speed of 18000 rpm and a PVA concentration of 0.5 %. At a speed of 22000 rpm and PVA concentration of 0.5 %, the average particle sizes and polydispersity indices are 5.1, 10.2 μm and 0.26 and 0.38, respectively. This is crucial because controlled drug release rate depends upon nature and the polydispersity of the microparticles. Similar drug release was observed for the PVA concentration of 3 % with the homogenizer speed of 18000 and 22000 rpm, respectively. This implies that the PVA concentration does not significantly affect the release rate and the particle sizes [50], This is because the PVA were properly rinsed out.

For effective treatment of cancer, Wang *et al.* [53] have suggested that the continuous release of an anti-cancer (agent from a controlled delivery device) should be studied over a period between 1 week and 1 month. These have stimulates our efforts to understand the surface morphology during the release carried out for prodigiosin/paclitaxel-loaded microspheres. The results obtained for the *in-vitro* release of prodigiosin or paclitaxelTM from the PLGA microspheres are presented in Figure 6.10, respectively. These show the cumulative *in-vitro* release profiles of prodigiosin and paclitaxelTM up to 8 days.

Studies show that degradation period of PLGA is between 4 and 6 weeks [54,55]. This clearly indicates that drug release in the current research was more through diffusion and dissolution controlled rather than degradation controlled. This argument validates the microscopic structures

of the particles observed during the release studies (Figure 6.11). This is to truly ascertain that there is no surface change as a result of electron interaction with the surface of the microsphere when the SEM is used.

The porous PG-loaded PLGA microspheres exhibited somewhat slower and similar release behavior as the PT-loaded microspheres (Figure 6.10). However, both release profiles exhibited steady continual-release profile, with some initial burst release. In the case of PG, the initial released from the microspheres was fast in the first 40 h, while the release of PT from the microspheres was fast in the first 50 h. The initial release in the case of PG was ~ 55%, while that of paclitaxel was ~ 70% in line with the result as reported by Engineer *et al.* [56]. This is because the release of paclitaxel from the polymeric matrix has been reported to occur in two phases. 60-70% within 1 week of incubation in PBS and in the second phase, remaining percentage of drug tends to release in the next 7 weeks [56]. In any case, the release rate carried out for both PG and PT-loaded PLGA microspheres at homogenizer speeds of 18000 and 22000 rpm using a PVA of 0.5 % for durations of up to 192 h (8 days) was a sustained release.

The observed first phase of release in the current work can be attributed to the preferential location of the drugs at the hydrophobic–hydrophilic interfaces inside of the microspheres [57]. This results in the faster release of prodigiosin and paclitaxelTM from the particles to the medium. Prior work has also suggested that the drugs dissolve more readily in amorphous regions than crystalline regions of the microspheres [58] which will tend to accelerate their release.

The PG or PT release from microspheres was also influenced by the drug payload or drug density in the microparticles. The higher the drug payload in microparticles, the faster the prodigiosin and paclitaxelTM release from particles [53,57,58]. This is because the total *in-vitro* drug release from polymeric microspheres occurs by diffusion, bulk erosion and polymer degradation processes [20]. In the case of PG-loaded microspheres, the large surface area and the release of drug to the surrounding medium becomes easier at higher drug payloads hence have a higher initial burst [59,60]. This results in faster initial drug release at time, 25 hrs, in the case of prodigiosin (53 %) as compared to paclitaxel (45 %). However, since the drug density or payload becomes low at longer release times, the drug release rate becomes slower [53].

In the case of paclitaxel-loaded PLGA microspheres at a homogenizer speed of 18000 rpm and using a 0.5 % PVA concentration, the drug loading and encapsulation efficiencies were 2.4 and 82 %, respectively. The corresponding values for the PG-loaded microspheres were 4.2 % and 76 %, respectively. When 22000 rpm speed is used with a PVA concentration of 3 %, the loading and encapsulation efficiency are 3.8, 2.1 and 69.1, 74.6 % for PG and PT-loaded PLGA microspheres, respectively. The PG-loaded microspheres drug release rate is slightly slower due to the payload as compare to that of paclitaxel-loaded microspheres.

Figure 6.11 shows the gradual morphological changes in the structure of the microspheres during the *in vitro* release test as observed by a microscope. One day (24 hours) after dispersal in phosphate buffer at 37°C, the surface of the particles was still smooth with many small pores observed in the case of the PG-loaded microspheres (Figure 6.11 and 6.12). Slight surface change was observed after 1 week (168 hours) of incubation in PBS. These morphologies

observed inherently result to deformation that is apparent on both the surface and inside the microspheres. This process leads to progressive erosion and degradation of the microspheres afterwards.

6.5 Implications

The work demonstrates the potential for the controlled release of prodigiosin (PG) as an anticancer drug from porous PG-loaded PLGA microspheres. The implications of the current results are quite significant for the development of low cost injectable biodegradable PG-loaded polymer microspheres. This is because the bacterial synthesis and purification of PG would greatly reduce the cost of cancer drugs compared to conventionally manufactured drugs such as PT use as a control in the current work. Hence, it is possible to envisage injectable multifunctional microspheres as a cancer treatment system, in which PG is released at a controlled and localized rate for localized cancer treatment. Such drugs can find variety of applications in the treatment of cancers that require localized drug delivery [7,61]. These include solid tumors, such as breast cancers, that can be injected locally with porous micro-particles that can elute drugs into surrounding tissue. Such elution can be used locally to treat cancer cells, without many of the adverse effects associated with bulk chemotherapy. They could, therefore, minimize the adverse side effects associated with bulk chemotherapy and greatly reduce the amount of drugs that are needed for therapeutic cancer treatments.

The DLE and DEE for PG-loaded PLGA microspheres were relatively high and similar to that of PT-loaded PLGA microspheres. This release rate is within the range that is relevant for control localized drug delivery in the treatment of cancer. However, further work is needed to explore

the performance of the encapsulated PG microparticles with different cancer cell lines and under *in-vivo* conditions. The suggested studies will explore the localized release of cancer drugs (PG) within a controlled rate and their effects on cancer cells or tissue [62, 63].

6.6 Summary and Concluding Remarks

The current work explores the formation of porous prodigiosin-loaded microspheres that are within the domain which are injectable for localized delivery in the treatment of cancer. We have successfully prepared and characterized PG/PT-loaded injectable microspheres. The study reveals that PG-loaded PLGA microspheres were formed through a single solvent emulsion evaporation technique with relatively high and similar DEE with PT-loaded PLGA microspheres that are relevant for the localized release of a biosynthesized anticancer agent (PG) for the treatment of cancer. The results of controlled release of PG from PLGA microparticles were also compared to that of PT-loaded PLGA microparticles. The result shows that PG can be release at a controlled localized rate within a period of 192 hours for the treatment of cancer.

The formations of the microspheres sizes and the drug release are greatly influenced by the concentrations of homogenizer speed and slightly by the PVA concentration. The PT-loaded PLGA microspheres at a homogenizer speed of 18000 rpm and using a 0.5 % PVA concentration result to a loading and encapsulation efficiencies of 2.4 and 82 %, respectively. The corresponding values for the PG-loaded microspheres were 4.2 % and 76 %, respectively. When 22000 rpm speed is used with a PVA concentration of 0.5 %, the loading and encapsulation efficiency are 3.8, 2.1 and 69.1, 74.6 % for PG and PT-loaded PLGA microspheres, respectively. The properties of the PG-loaded microspheres formed suggest that they are relevant for

controlled localized drug delivery in treatment of cancer. Future work is clearly needed to explore the efficacy of PG-loaded PLGA microspheres as a replacement for PT-loaded PLGA microspheres under *in-vivo* conditions.

References

- [1] Boyle Peter and Levin Bernard. The World Cancer Report. World Health Organization. 2008.
- [2] Mackay J., Mensah G.A. The atlas of disease and stroke, published by the world health organization in collaboration with the centers for disease control and prevention, 2004. ISBN-13 97892415.
- [3] Jemal A, Murray T, Samuels A, Ghafoor A, Ward E, Thun MJ. Cancer statistics, 2003. *CA Cancer J Clin* 2003; 53:5–26.
- [4] David Cutierrez., Cancer facts and figures. 2nd edition. America Cancer Society, 2008
- [5] David Needhama, Mark W. Dewhirst. The development and testing of a new temperature-sensitive drug delivery system for the treatment of solid tumors. *Advanced Drug Delivery Reviews*. ELSEVIER, 2001; 53, 285–305.
- [6] Hildebrandt B., Ceelen W.P., Wust P. in: (Ed), 2007, *Peritoneal Carcinomatosis: A Multidisciplinary Approach*, Springer, New York, 185.
- [7] Y. Oni, C. Theriault, A.V. Hoek, W.O. Soboyejo, Effects of temperature on diffusion from PNIPA-based gels in a BioMEMS device for localized chemotherapy and hyperthermia, *Mater. Sci. Eng. C* 31 (2011) 67–76.
- [8] Ms Rajput et al: Microspheres in cancer therapy, *Indian journal*, 2010.
- [9] Ducry L. and Stump B. Antibody-Drug Conjugates: Linking Cytotoxic Payloads to Monoclonal Antibodies. *Bioconjugate Chem.* 2010, 21, 5–13.
- [10] Kratz, F., Müller, I. A., Ryppa, C., and Warnecke, A. (2008) Prodrug strategies in anticancer chemotherapy. *ChemMedChem* 3, 20–53.

- [11] Panchal, R. G. (1998) Novel therapeutic strategies to selectively kill cancer cells. *Biochem. Pharmacol.* 55, 247–252.
- [12] Chari RV, Targeted cancer therapy: conferring specificity to cytotoxic drugs. *Acc Chem Res.* 2008 Jan; 41(1): 98-107.
- [13] Ross J S, Schenkein D P, Pietrusko R, *et al.* Targeted therapies for cancer 2004. *Am J Clin Pathol* 2004;122:598–609.
- [14] Hideya Kimura, Yuichiro Ogura, Takeshi Moritera, Yoshihito Honda, Ryoichi Wada. Suong-Hyu Hyon, and Yoshito Ikada; Injectable Microspheres with Controlled Drug Release for Glaucoma Filtering Surgery; *Investigative Ophthalmology & Visual Science*, Vol. 33, No. 12, November 1992, *Vis Sci* 33: p. 3436-3441.
- [15] Jackson, J.K., Gleave, M.E., Yago, V., Beraldi, E., Hunter, W.L., Burt, H.M., 2000b. The suppression of human prostate tumor growth in mice by the intratumoral injection of a slow release polymeric paste formulation of paclitaxel. *Cancer Res.* 60, 4146–4151.
- [16] David Martin. M and Boyle F. J: Drug eluting stents for coronary artery disease (review), *Med Eng Phys*, 2010.
- [17] Huizing, M.T., Misser, V.H.S., Pieters, R.C., Huinink, W.W.T., Vencor, C.H.N., Vermorken, J.B., Pinedo, H.M., Beijnen, J.H., 1995. Taxanes—a new class of anticancer agents. *Cancer Invest.* 4, 381–404.
- [18] Brannon-Peppas, L.; *Polymers in controlled drug delivery. Medical Plastics and Biomaterials Magazine*, 1997, (accessed November, 2013) (<http://www.devicelink.com/mpb/archive/97/11/003.html>).
- [19] Nair, L. S.; Laurencin, C. T.; *Biodegradable polymer as biomaterials. Progress in Polymer Science*, 2007, 32 (8-9), 762-798.

- [20] Rajeev A. Jain: The manufacturing techniques of various drug loaded biodegradable poly(lactide-co-glycolide) (PLGA) devices, *Biomaterials* 21 (2000) 2475-2490.
- [21] Kabanov, A. V.; Gendelman, H. E. Nanomedicine in the diagnosis and therapy of neurodegenerative disorders. *Progress in Polymer Science*, **2007**, 32 (8-9), 1054-1082.
- [22] Yeagy B. A, Prudencio A, Schmeltzer R. C, Uhrich KE, Cook TJ (2006) Characterization and *in vitro* degradation of salicylate-derived poly(anhydride-ester microspheres). *J Microencapsul* 23(6):643-653. doi:10.1080/02652040600776481.
- [23] Suzuki, K. and Price, J.C. Microencapsulation and dissolution properties of a neuroleptic in a biodegradable polymer, poly(dl-lactide), *J. Pharm. Sci.* 74 (1985) 21-24.
- [24] Jalil, R.U. Biodegradable poly (lactic acid) and poly (lactide- co-glycolide) polymers in sustained drug delivery, *Drug Dev. - Ind. Pharm.* 16 (1990) 2353-2367.
- [25] Anderson, J. M. and Shive M. S. Biodegradation and biocompatibility of PLA and PLGA microspheres, *Adv. Drug Deliv. Rev.* 28 (1997) 5-24.
- [26] Govender, T., S. Stolnik, M.C. Garnett, L. Illum, S.S. Davis, PLGA nanoparticles prepared by nanoprecipitation: drug loading and release studies of a water soluble drug, *J. Control Release* 57 (1999) 171-185.
- [27] Okada, H.; Toguchi, H. Biodegradable microspheres in drug delivery. *Critical Reviews in Therapeutic Drug Carrier Systems*, 1995, 12, 1-99.
- [28] Han, S. B., H. M. Kim, Y. H. Kim, C. W. Lee, E.-S. Jang, K. H. Son, S. U. Kim, and Y. K. Kim.,) 1998), T-cell specific immunosuppression by prodigiosin isolated from *Serratia marcescens*, *International Journal of Immunopharmacology*, 20, pp 1-13.

- [29] Mekhael, R. and Yousif S.Y., (2009), The role of red pigment produced by *Serratia marcescens* as antibacterial and plasmid curing agent, *Journal of Duhok University*, 12(1), pp 268-274.
- [30] Perez-Tomas, R., Montaner, B., Llagostera, E., Soto-Cerrato, V., (2003), The prodigiosins, proapoptotic drugs with anticancer properties. *Biochem. Pharmacology*,
- [31] Kavitha, R., Aiswariya, S., Chandana, R. M., (2010), Anticancer activity of red pigment from *Serratia marcescens* in Human cervix carcinoma, *International Journal of Pharmaceutical Research*, 2(1), pp 784-787.66, pp 1447–1452.
- [32] Pandey, R. Chander, R., Sainis, K.B., (2009), Prodigiosins as anti-cancer agents: Living upto their name, *Current Pharmaceutical design*, 15, pp 732-741.
- [33] Montaner, B., Navarro, S., Pique M, Vilaseca M, Martinell, M., Giralt, E., Gil, J. and Perez-Thomas, R., (2000), Prodigiosin from the supernatant of *serratia marcescens* induce apoptosis in haematopoietic cancer cell lines, *British Journal of Pharmacology*, 131(3), pp 585-593.
- [34] Kamble K. D, Hiwarale V.D “Prodigiosin production from *Serratia marcescens* strains obtained from farm soil” *International Journal of Environmental Sciences* Volume 3 No.1, 2012.
- [35] LCLGC’s CHROMacademy. Crawfordscientific. Quantitative & Qualitative HPLC. Unpublished data.1-31.
- [36] J. W. Dolan (editor). *Why Do Peaks Tail? LC Troubleshooting*. LCGC North America. 21(7) (2003) 612.
- [37] L.R. Snyder, J. J. Kirkland, and J.L. Glajch, *Practical HPLC Method Development* (John Wiley & Sons, New York, 2nd ed., 1997), p. 180.

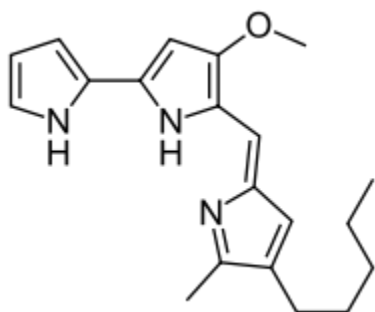
- [38] Yoon Yeo et al: Microencapsulation Methods for Delivery of Protein Drugs, *Biotechnol. Bioprocess Eng.* 2001, 6: 213-230.
- [39] Xuetao Shi et al : Enhancing Alendronate Release from a Novel PLGA/Hydroxyapatite Microspheric System for Bone Repairing Applications, *Pharmaceutical Research*, Vol. 26, No. 2, February 2009.
- [40] Meltem C,ETIN et al: Preparation and characterization of anticancer drug-loaded implantable PLGA microparticles, *Turk J Chem* 34 (2010) , 509 – 516.
- [41] Magdalena Stevanovi et al: Poly(lactide-co-glycolide)-based Micro and Nanoparticles for the Controlled Drug Delivery of Vitamins, *Current Nanoscience*, 2009, 5, 00-00.
- [42] Feng Qian et al: Fabrication and characterization of controlled release poly(D,L-lactide-co-glycolide) millirods, John Wiley & Sons, Inc., 2001.
- [43] Carlos Ernesto Astete R: Synthesis of Poly(DI-Lactide-Co-Glycolide) Nanoparticles with Entrapped Magnetite, Louisiana State University, December 2005.
- [44] Gupta, A. J.; Gupta, M. *Biomaterials* 2005, 26, 3995.
- [45] Park E. K., Lee S. B., Lee Y. M.. Preparation and characterization of methoxy poly (ethylene glycol)/poly (caprolactone) amphiphilic block copolymeric nanospheres for tumor-specific folate-mediated targeting of anticancer drugs. *Biomaterials* 2005, 26: 1053-1061.
- [46] Kesarwani P, Rakesh K. Tekade, N. K. Jain, Spectrophotometric Estimation of Paclitaxel *International Journal of Advances in Pharmaceutical Sciences* 2 (2011) 29-32.
- [47] Zambaux, M.; Bonneaux, F.; Gref, R.; Maincent, P.; Dellacherie, E.; Alonso, M.; Labrude, B.; Vigneron, C.; Influence of experimental parameters on the characteristics of

- poly(lactic acid) nanoparticles prepared by double emulsion method. *Journal of Controlled Release*, 1998, 50, 31-40.
- [48] Stevanovi, M.; Ignjatovi, N.; Jordovi, B.; Uskokovi, D. Stereological analysis of the poly (DL-lactide-co-glycolide) submicron sphere prepared by solvent/non-solvent chemical methods and centrifugal processing. *Journal of Materials Science: Materials in Medicine*, 2007, 18 (7), 1339-1344.
- [49] Niwa, T.; Takeuchi, H.; Hino, T.; Kunou, N.; Kawashima, Y. Preparation of biodegradable nanoparticles of water-soluble and insoluble drugs with D,L lactide/glycolide copolymer by a novel spontaneous emulsification solvent diffusion method, and the drug release behaviour. *Journal of Controlled Release*, 1993, 25, 89-98.
- [50] Qia Feng, Wua Jie, Fan Qingze, He Fan, Tian Guifang, Yang Tingyuan, Ma Guanghui, Zhiguo Su, Preparation of uniform-sized exenatide-loaded PLGA microspheres as long-effective release system with high encapsulation efficiency and bio-stability; *Colloids and Surfaces B: Biointerfaces* 112 (2013) 492–498.
- [51] Zhang Z., Sun A., Long L; Effect of Physicochemical Properties of Drug on the Morphology and Release of Microspheres *J. Med. Biol. Eng.* (May 29, 2013), doi: 10.5405/jmbe.1070.
- [52] T.G. Fox, *Bull. AM. Phys. Soc.*, 1(2), 123 (1956).
- [53] Wang YM, Sato H, Adachi I, Horikoshi I. Preparation and characterization of poly(lactic-co-glycolic acid) microspheres for targeted delivery of a novel anticancer agent, taxol. *Chem Pharm Bull* 1996;10:1935–40.
- [54] D.H. Lewis, In *Biodegradable Polymers as Drug Delivery Systems*, (Ed.) M. Chasin and R. Langer, Marcel Dekker: New York, 1-43 (1990).

- [55] R.L. Kronenthal, In *Polymers in Medicine and Surgery*, (Ed.) R.L. Kronenthal, Z. Oser and E. Martin, Plenum Press: New York, 119 (1975).
- [56] Engineer C., Parikh J., and Raval A. *Trends Biomater. Artif. Organs* Vol 24(3), pp 131-138 (2010).
- [57] Chen H., Kim S., Li L., Wang S., Park K., Cheng J., Release of hydrophobic molecules from polymer micelles into cell membranes revealed by Foster resonance energy transfer imaging, *PNAS* 105 (18) (2008) 6596–6601.
- [58] Zhang L., Hu Y., Jiang X., Yang C., Lu W., and Yang Y.H. Camptothecin derivative-loaded poly (caprolactone-co-lactide)-b-PEG-b-poly(caprolactone-co-lactide) nanoparticles and their biodistribution in mice, *J. Control. Release* 96 (1) (2004) 135–148.
- [59] Li, W. I., Anderson, K. W., Mehta, R. C., and DeLuca, P. P. Prediction of solvent removal profile and effect on properties for peptide-loaded PLGA microspheres prepared by solvent extraction/ evaporation method. *Journal of Controlled Release*, 37, 199-214 (1995b).
- [60] Yi-Yan Yang, Tai-Shung Chung, Xin-Lai Bai, Woon-Khiong Chan. Effect of preparation conditions on morphology and release profiles of biodegradable polymeric microspheres containing protein fabricated by double-emulsion method, *Chemical Engineering Science* 55 2223-2236 (2000).
- [61] G. Fu, W.O. Soboyejo, Swelling and diffusion characteristics of modified poly(N-isopropylacrylamide) hydrogels, *Mater. Sci. Eng. C* 30 (2010) 8–13.
- [62] Gao. D., H. Xu, M-A. Philbert, R. Kopelman. Ultrafine Hydrogel Nanoparticles: Synthetic Approach and Therapeutic Application in Living Cells. *Angew Chem Int Ed.* 46 (2007) 2224-2227.

- [63] H-Y. Hsieh, J-J. Shieh, C-J. Chen, M-Y. Pan, S-Y. Yang, S-C. Lin, J-S. Chang, A. Y-L. Lee and C-C. Chang. Prodigiosin Down-Regulates SKP2 to Induce P27kip1 Stabilization and Antiproliferation in Human Lung Adenocarcinoma Cells. *Br. J. of Pharmacol.* 166 (2012) 2095-2108.

(a)



(b)

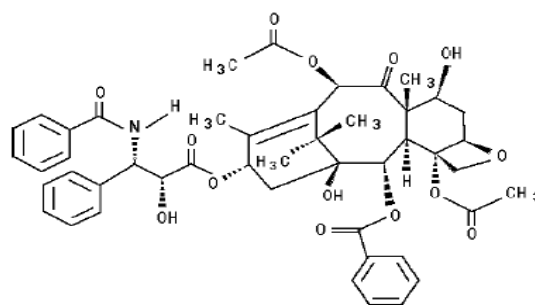
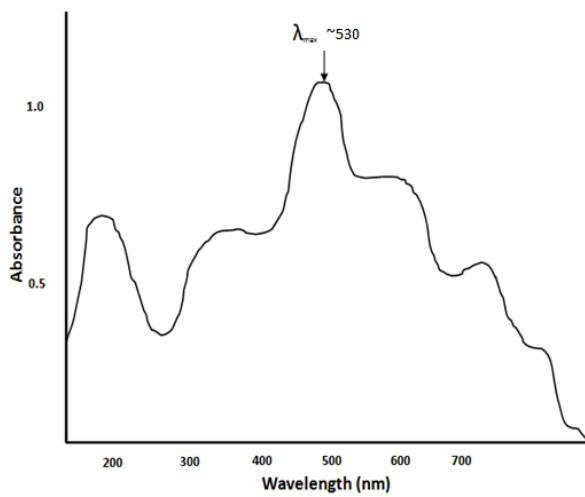


Figure 6.1: Structural formula of (a) prodigiosin (PG) (IUPAC/Chemical Name: 4-methoxy-5-[(Z)-(5-methyl-4-pentyl-2H-pyrrol-2-ylidene)methyl]-1H,1'H-2,2'-bipyrrole) (b) paclitaxel (PT).

(a)



(b)

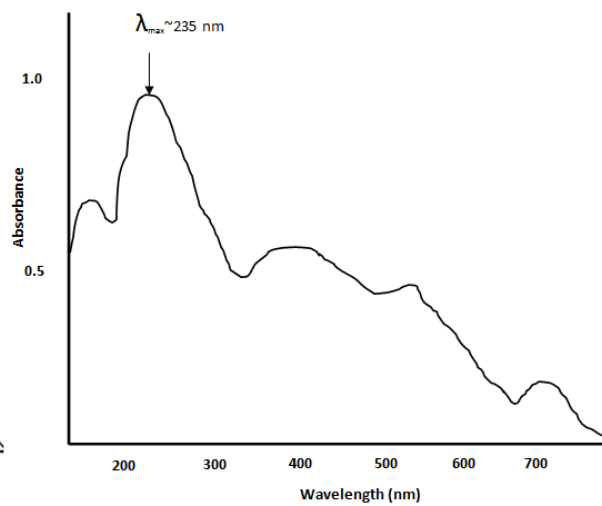
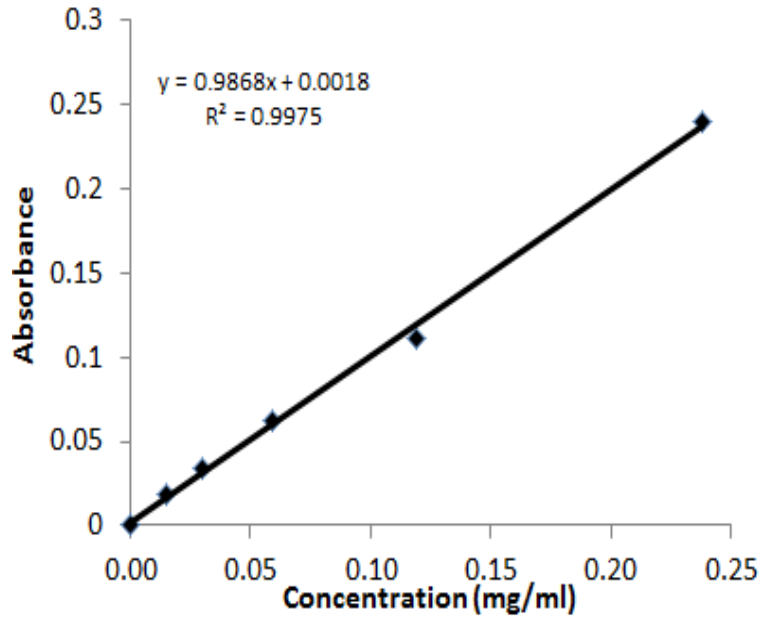


Figure 6.2: UV scans of (a) prodigiosin and (b) paclitaxelTM. Arrow represents the existence of respective peaks at wavelength corresponding to λ_{max} .

(a)



(b)

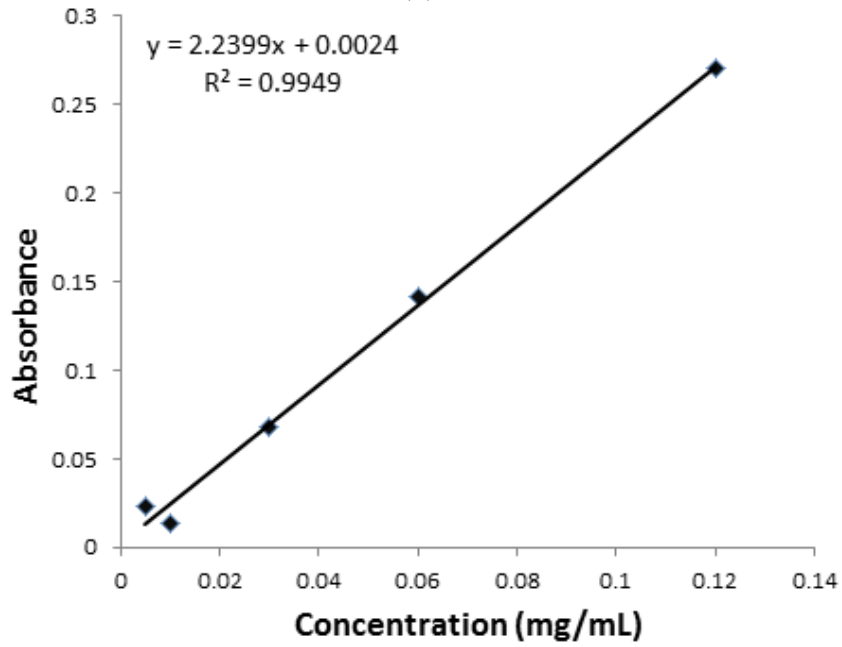


Figure 6.3: Concentration-Absorbance standard curves of (a) prodigiosin and (b) paclitaxelTM

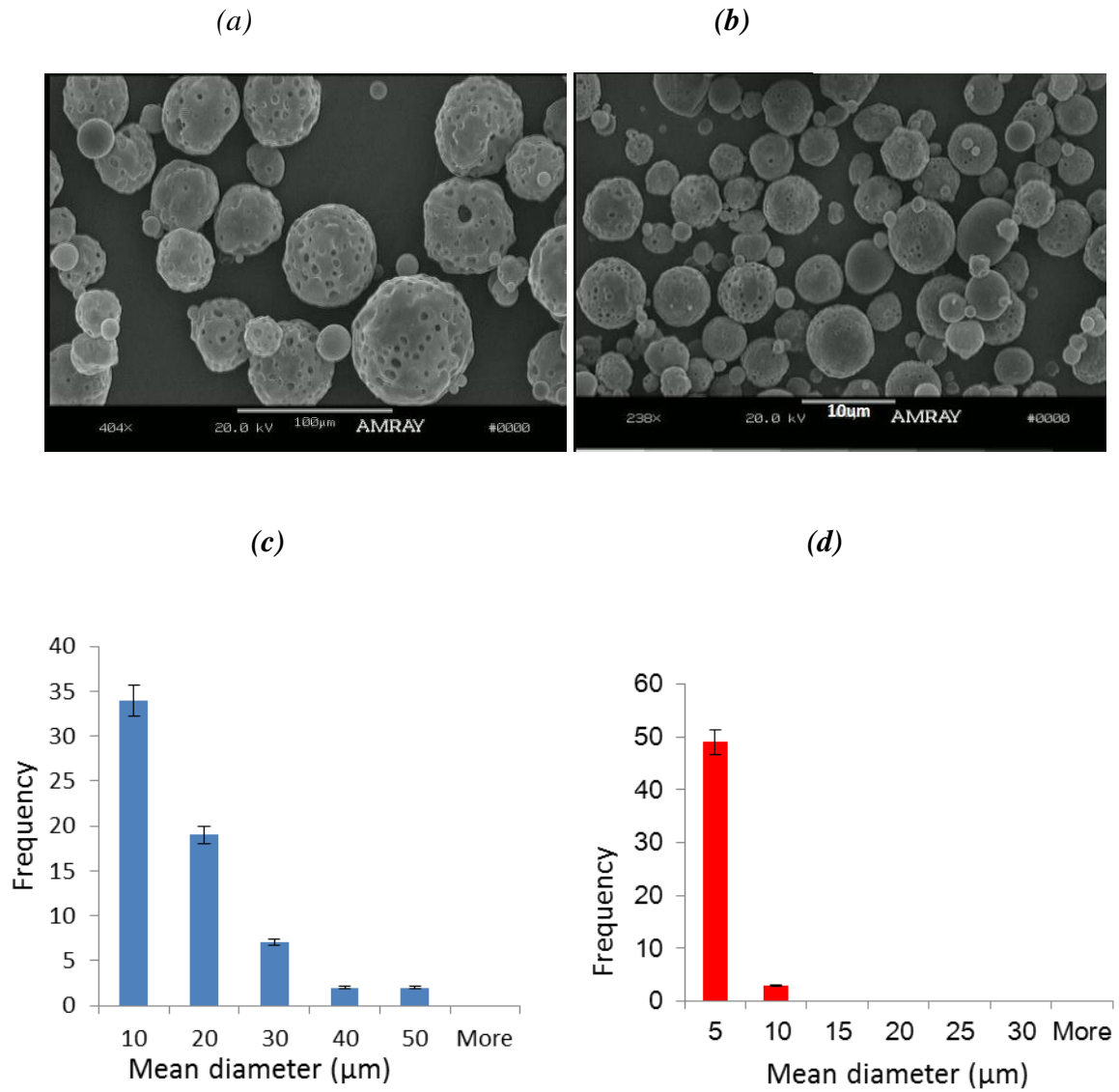


Figure 6.4: SEM micrographs (a and b) and mean particle size distributions (c and d) of PG-loaded PLGA microspheres at homogenizing speed of 18000 rpm ((a) and (c)) and 22000 rpm ((b) and (d)) with a uniform PVA concentration of 0.5 %, respectively.

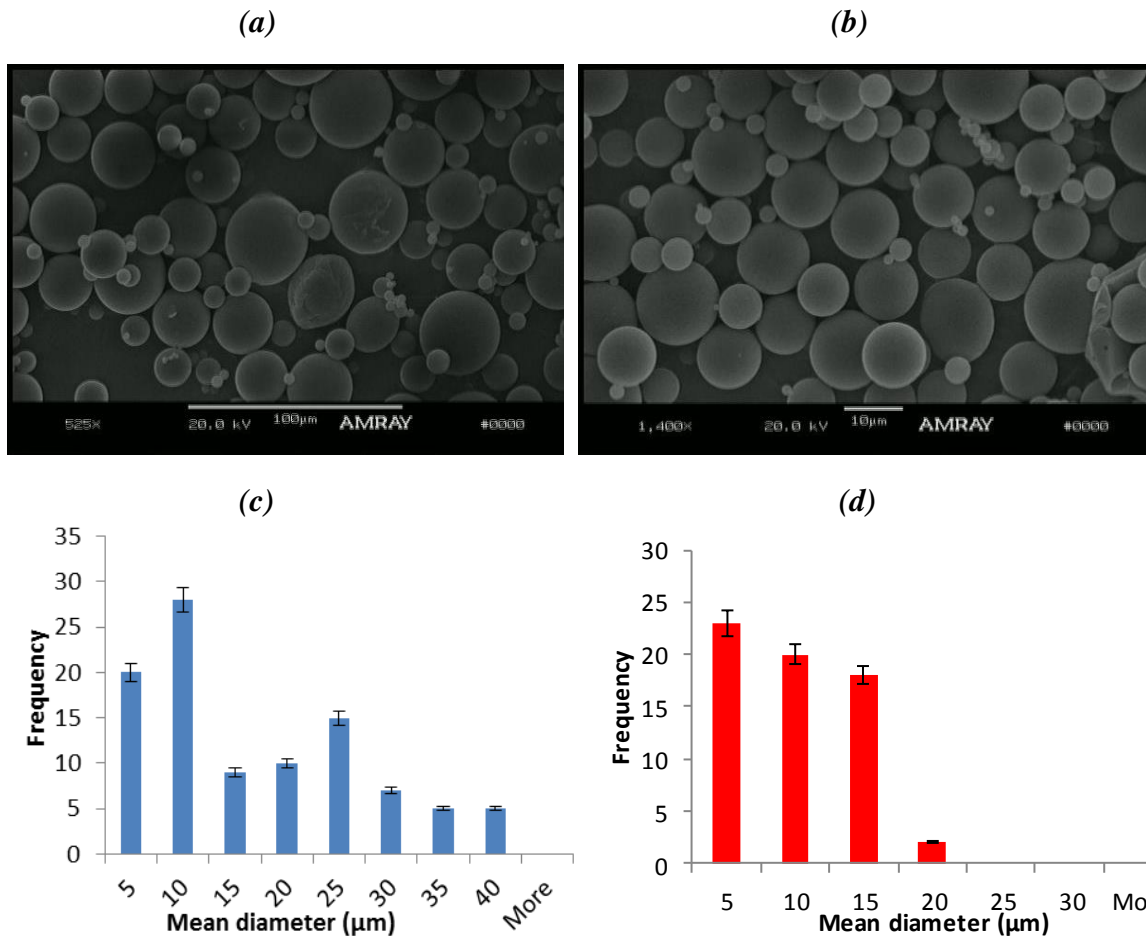


Figure 6.5: SEM micrographs (a and b) and mean particle size distributions (c and d) of PT-loaded PLGA microspheres at homogenizing speed of 18000 rpm ((a) and (c)) and 22000 rpm ((b) and (d)) with a uniform PVA concentration of 0.5 %, respectively.

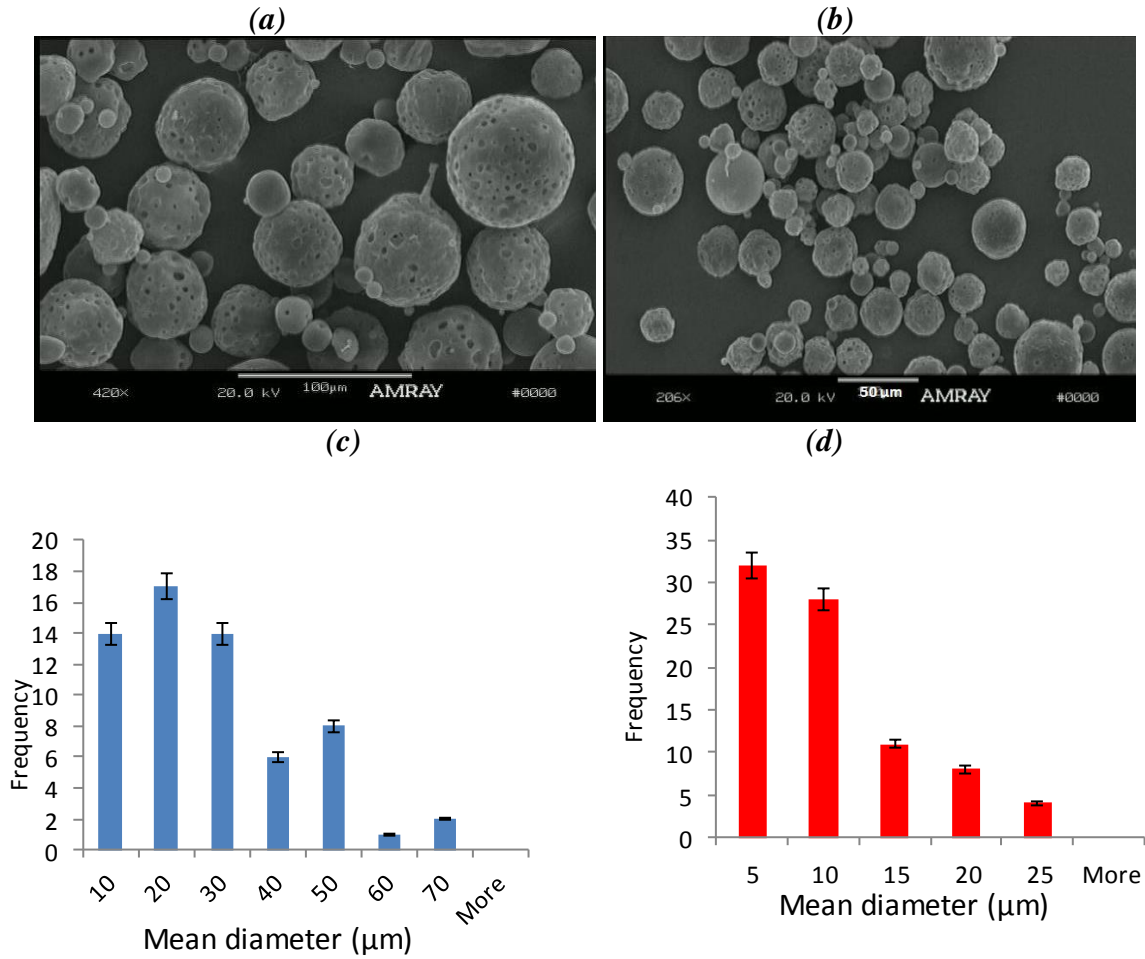


Figure 6.6: SEM micrographs (a and b) and mean particle size distributions (c and d) of PG-loaded PLGA microspheres for 0.5% PVA ((a) and (c)) and 3% PVA ((c) and (d)) with a uniform homogenizer speed of 18000 rpm, respectively.

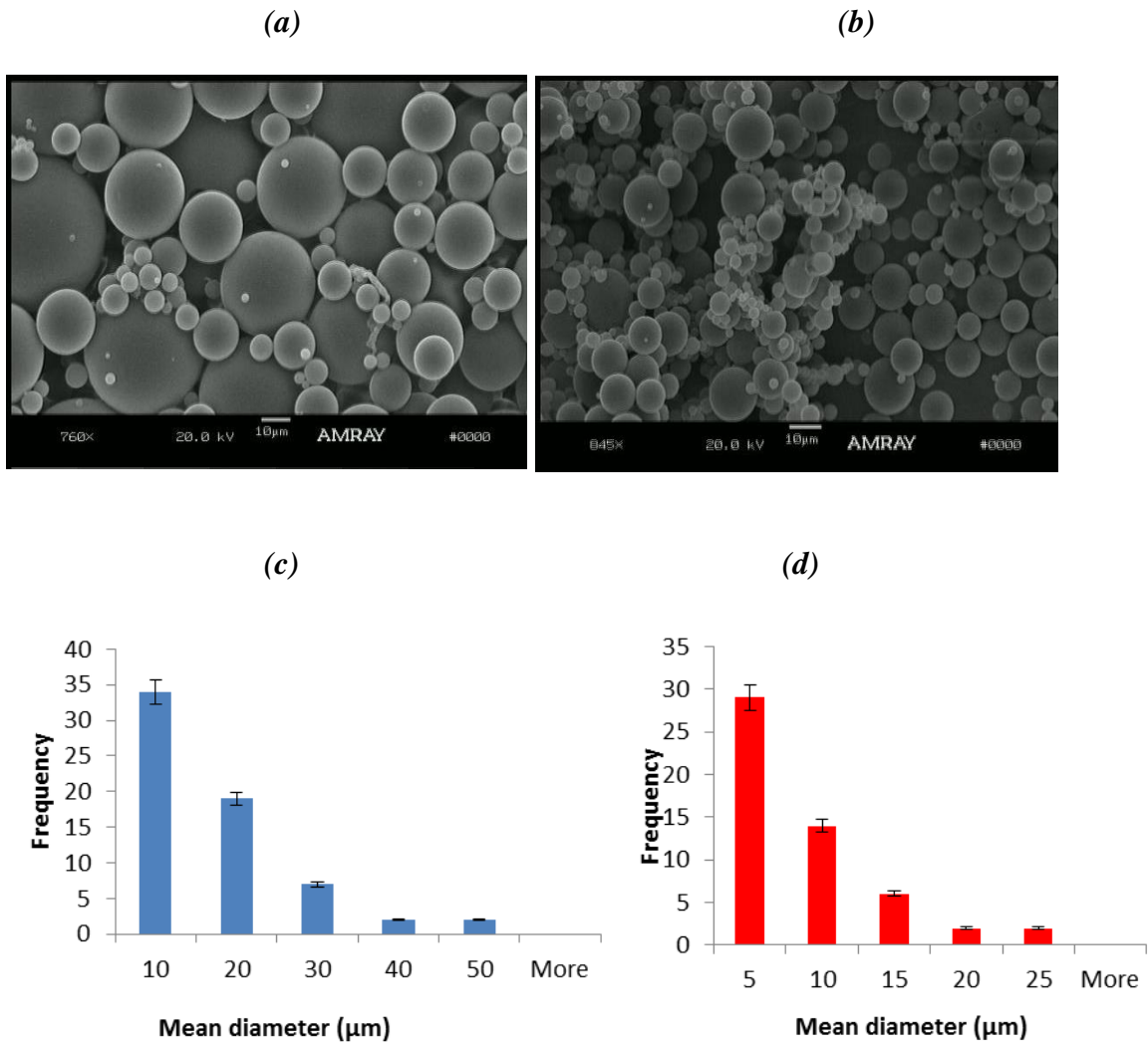


Figure 6.7: SEM micrographs (a and b) and mean particle size distributions (c and d) of PT-loaded PLGA microspheres using 0.5% PVA ((a) and (c)) and 3% PVA ((b) and (d)) with a uniform homogenizing speed of 18000 rpm, respectively.

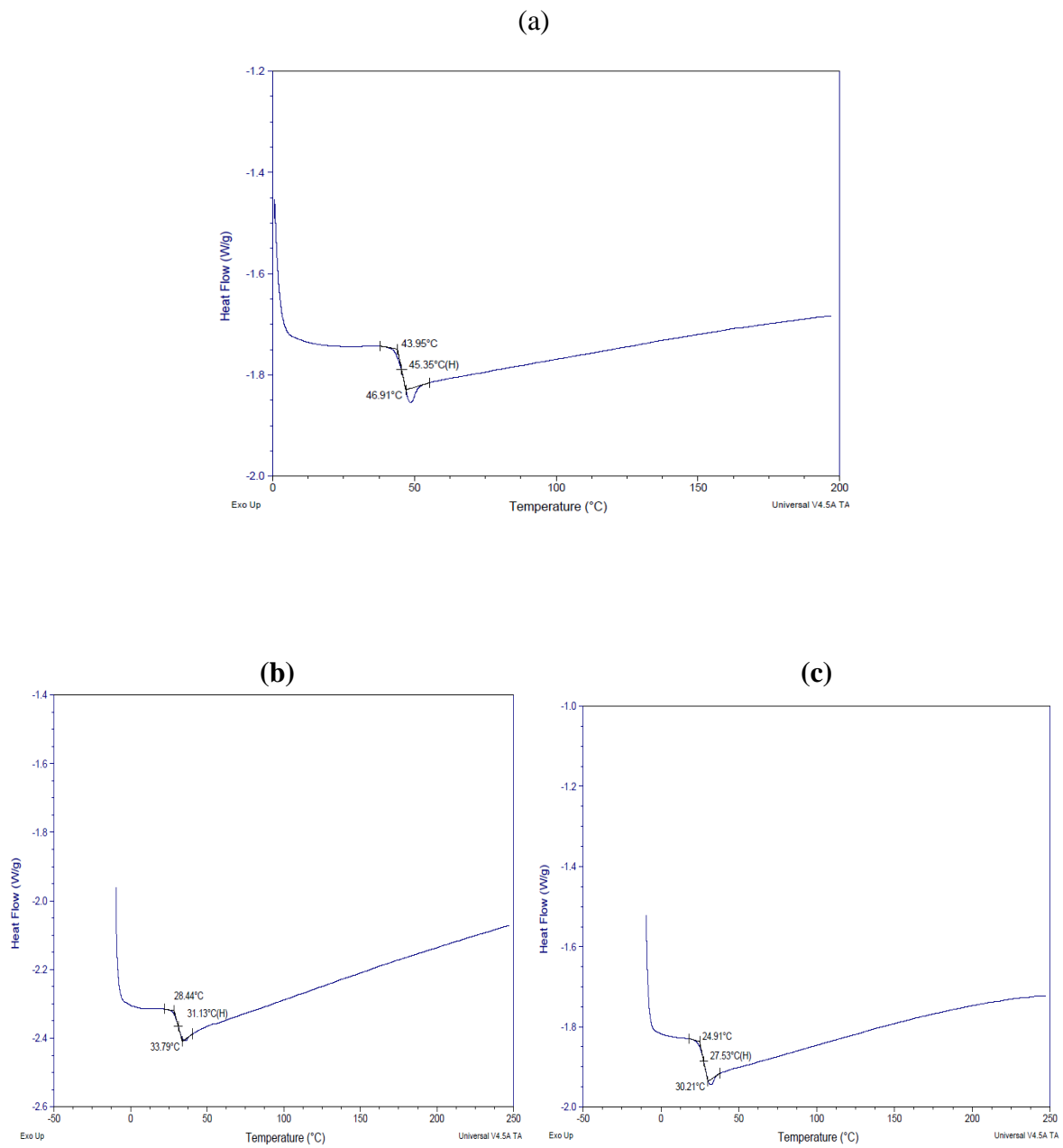


Figure 6.8: DSC results of (a) Plain (non-loaded) PLGA microspheres (b) PG-loaded PLGA and (c) PT-loaded PLGA microspheres.

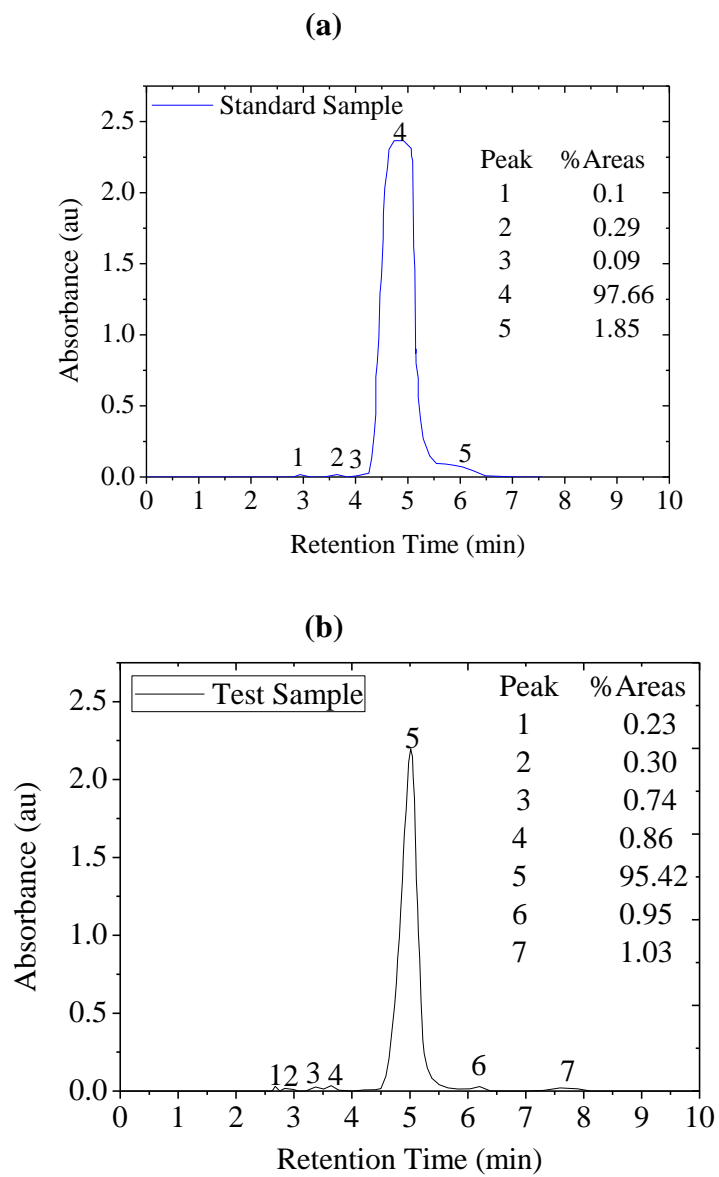


Figure 6.9: HPLC Analysis of Sample Purity: (a) Standard Prodigiosin and (b) Tested Sample (Prodigiosin), respectively at 535 nm.

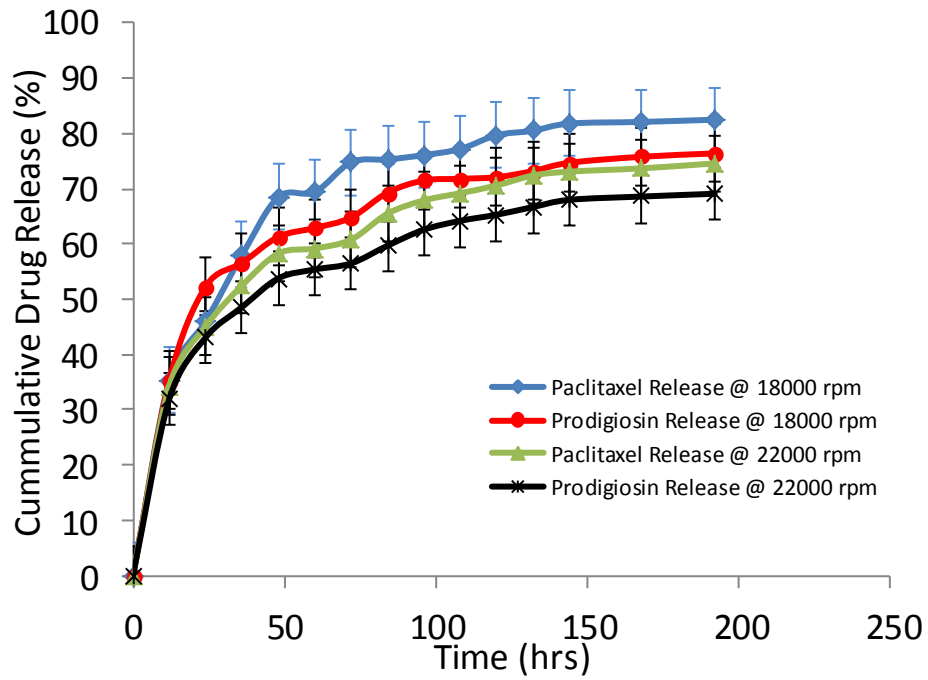
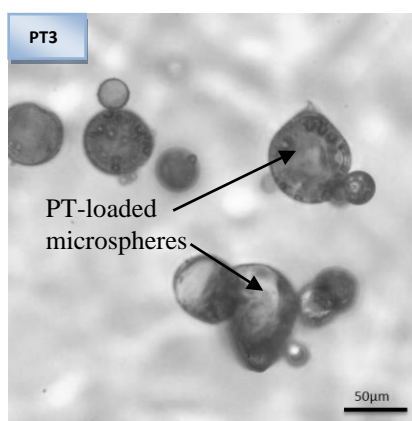
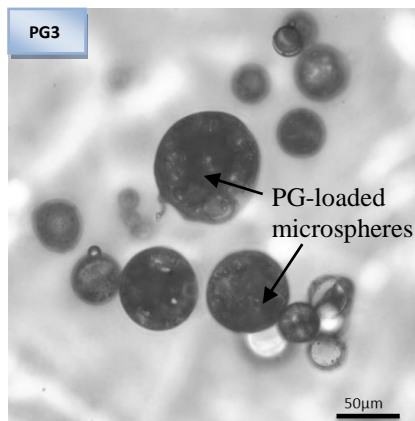
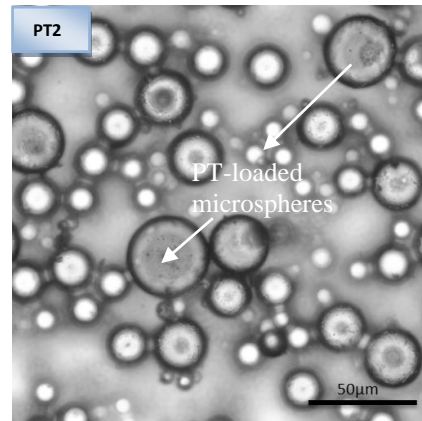
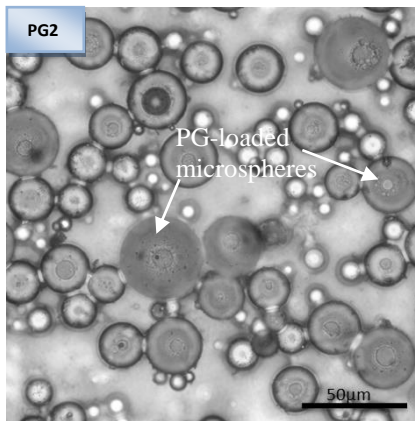
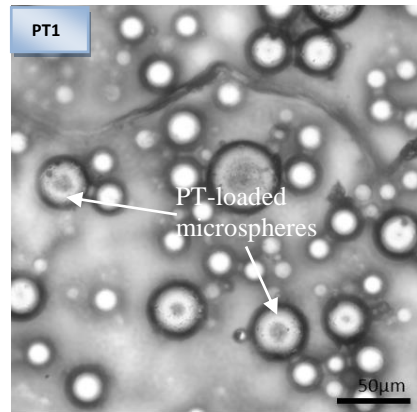
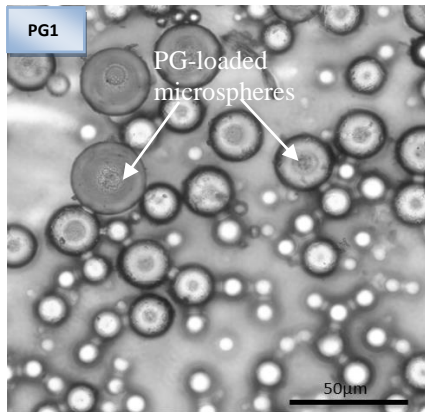
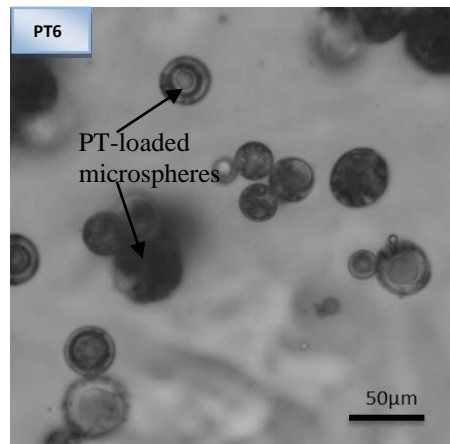
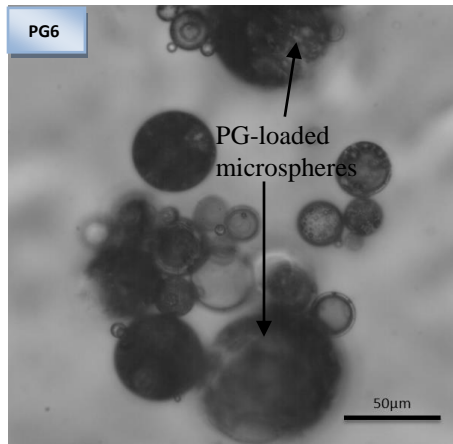
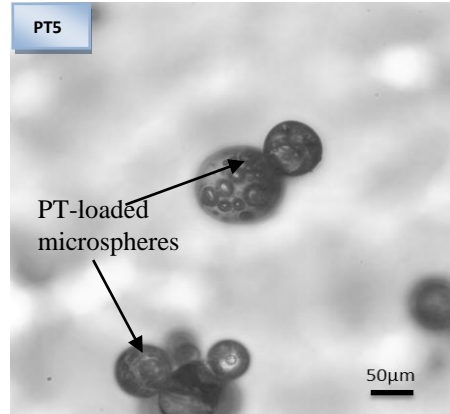
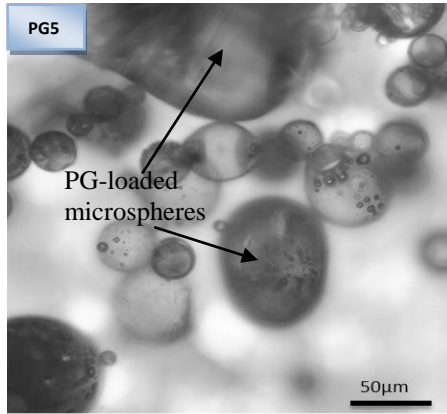
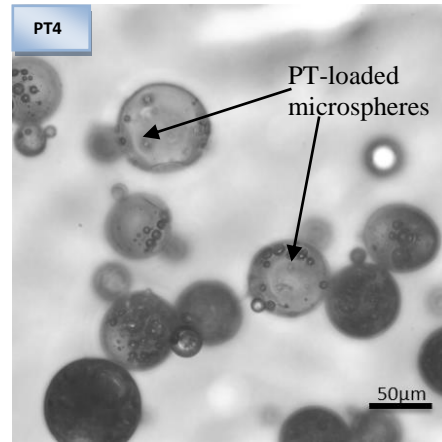
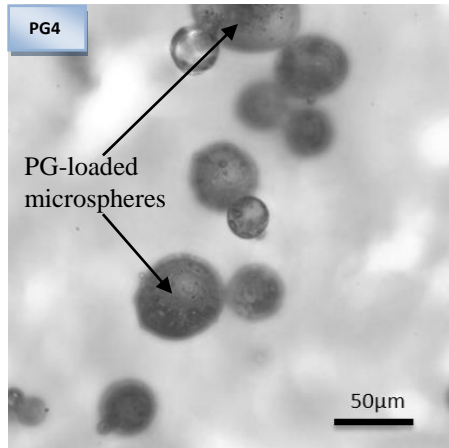
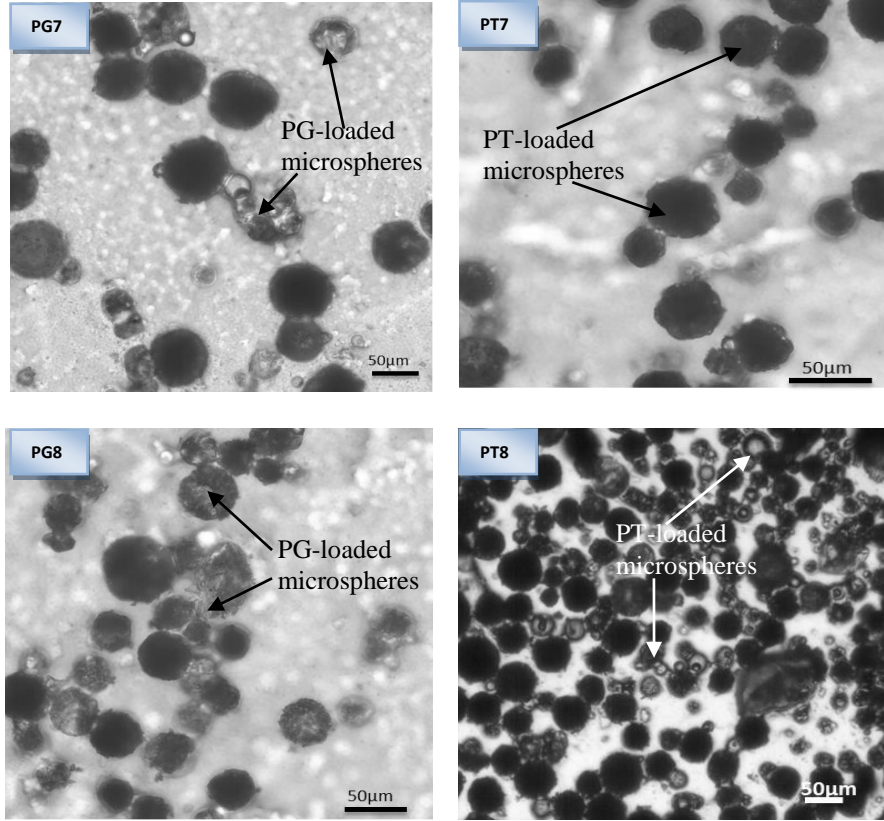


Figure 6.10: *In-vitro* release profiles of different formulations based on homogenization speed of 18000 and 22000 rpm for drug formulation 1 to 4 for 8 days, respectively.







PG1, PG2,PG8 Prodigiosin-loaded PLGA at day 1, 2, day 8.
 PT1, PT2,PT8 Paclitaxel-loaded PLGA at day 1, 2, day 8

Figure 6.11: Optical micrographs of prodigiosin (PG) and paclitaxel (PT) drug-loaded microspheres after day 1 (24 hours) to day 8 (192 hours) stages of drug release respectively.

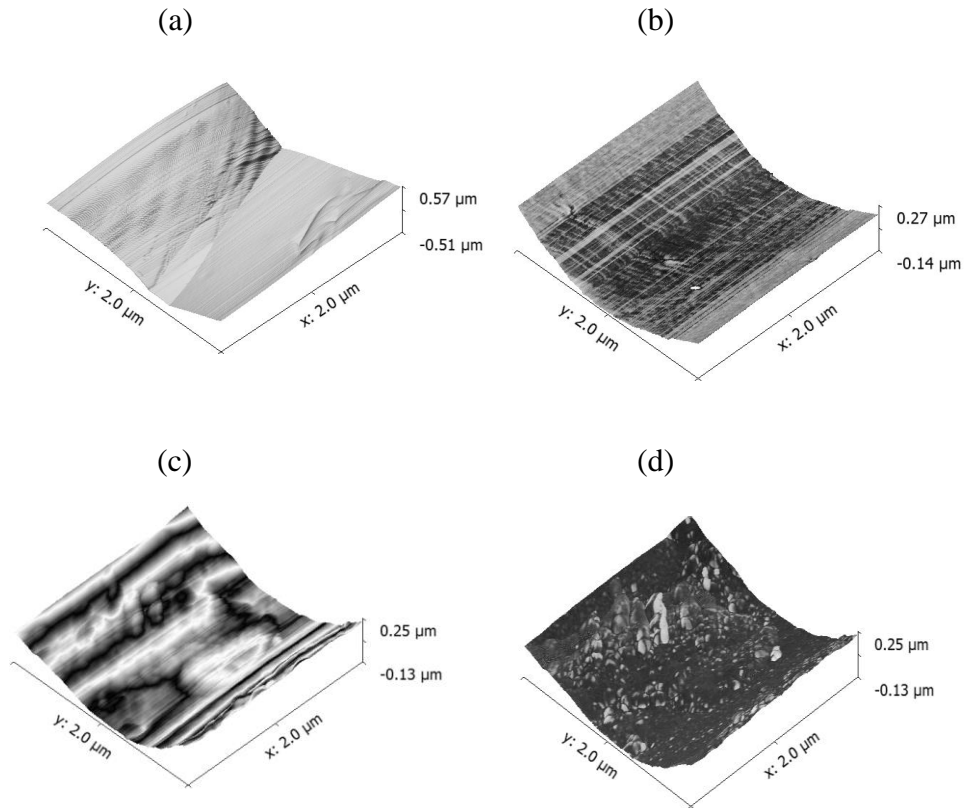


Figure 6.12: AFM images of a section of paclitaxel-loaded PLGA microsphere (a and c) and prodigiosin-loaded PLGA microsphere (b and d) after 1 day (24 hours) and 8 days (192 hours) of the drugs release, respectively.

Table 6.1: Formulations parameters and characteristics of investigated prodigiosin and paclitaxel –loaded PLGA microspheres

Drug Formulation	Homogenizer Speed (rpm)	PVA Concentration (W/V) %	Average Size (μm)	DLE (%)	DEE (%)	Polydispersity Index (PD)	Initial Burst (%)
A	18000	0.5	16.4	4.2	76	0.21	53
B	18000	0.5	15.5	2.4	82	0.35	46
C	22000	0.5	5.1	3.8	69.1	0.26	43
D	22000	0.5	10.2	2.1	74.6	0.38	45
E	18000	0.5	12.6	-	-	0.17	-
F	22000	0.5	8.3	-	-	0.19	-

^{PVA}Polyvinyl Alcohol, ^{DLE}Drug Loading Efficiency, ^{DEE}Drug Encapsulation Efficiency; ^AProdigiosin-loaded Microspheres formed at a homogenizer speed of 18000 rpm, ^BPaclitaxel-loaded Microspheres formed at a homogenizer speed of 18000 rpm, ^CProdigiosin-loaded Microspheres formed at a homogenizer speed of 22000 rpm, ^DPaclitaxel-loaded Microspheres formed at a homogenizer speed of 22000 rpm, ^EPLGA Microspheres formed at a homogenizer speed of 18000 rpm (Control), ^FPLGA Microspheres formed at a homogenizer speed of 22000 rpm (Control)

Chapter 7

7.0 Concluding Remarks and Suggestions for Future Work

7.1 Summary and Concluding Remarks

This dissertation has presented and explored the efforts to use material science and engineering approaches in developing solutions to problems in the life science with a focus on nano- and micro-particles for the detection and treatment of cancer. The topics that were covered in this thesis are: biosynthesis and the conjugation of magnetite nanoparticles for the specific targeting of breast cancer and fundamental studies on the adhesion between functionalized magnetite and gold nanoparticles to surfaces that are relevant in the detection and treatment of breast cancer. Finally, the development and the physicochemical characterization of injectable biodegradable prodigiosin-loaded microparticles for localized cancer drug delivery is the last topic presented. The main results from the studies and salient conclusions from the above topics are presented below.

One of the key goals in the development of therapeutic agents for early detection and treatment of cancer is development of selective targeting. To facilitate as well as achieve this goal for early detection and treatment of breast cancer, a new approach that gives us a fundamental understanding of the biosynthesis and the conjugation of robust magnetite nanoparticles with LHRH was carried out in chapter 3. The results showed that magnetite nanoparticles of clinically relevant sizes (10-60 nm) can be synthesized intracellularly by *Magnetospirillum magneticum*. The TEM analyses and the DLS results revealed that the mean particle sizes and shapes depend strongly on the pH and durations of growth of *Magnetospirillum magneticum*. The DLS results

also showed that the synthesized BMNPs were essentially monodispersed, with polydispersity indices in a range that is suitable for biomedical applications. The particles obtained exhibited superparamagnetic behavior with no diamagnetic contribution. This, therefore, suggests that these nanoparticles may be used effectively to enrich the MRI images associated with the early detection and localized treatment of cancer. The FTIR results also suggest that the LHRH MRUs are chemically bound to the biosynthesized magnetite nanoparticles through amines. This tends to improve the efficacy of these nanoparticles for selective targeting.

In chapter 4, the results of an experimental study of the adhesion forces between components of a model generic nanoparticle system/configuration that includes, LHRH, BSA, BMNPs, CMNPs, BMNPs-LHRH, CMNPs-LHRH, BMNPs-BSA and CMNPs-BSA to breast cancer cells (MDA-MB-231 cell line) are presented. The results clearly showed the superior adhesion of conjugated BMNPs to breast cancer cells when compared to the adhesion of conjugated CMNPs to breast cancer cells. Biologically synthesized magnetite nanoparticles had adhesion forces to breast cancer cells that were about one and half times more than those of chemically synthesized magnetite nanoparticles.

The results suggest that the biosynthesized magnetite nanoparticles may contain possible cap protein(s) that enhances the specific adhesion forces between the particles and cancer cells. Such high adhesive forces could improve the selectivity of conjugated BMNPs in cancer detection and treatment. These results also suggest that BMNPs and BMNPs-LHRH/BMNPs-BSA conjugates may be useful for rapid screening of potential ligands for the specific targeting of breast cancer

cells. Furthermore, this means that BMNPs may be used to design novel and robust types of magnetite nanoparticles for the early diagnosis and treatment of cancer. Finally the results suggest that force microscopy techniques may be used to detect breast cancer cell in biopsies.

Chapter 5 complements the studies carried out in chapter 4. These studies basically demonstrated the role of adhesion of gold nanoparticles for early cancer detection and treatment. This chapter also presented the results of an experimental study of the adhesion forces between components of a model generic drug delivery/system that includes gold nanoparticles, paclitaxel, thiols, LHRH and EphA2, a breast-specific antibody (BSA). The results obtained confirm that the robustness of such systems depends on the adhesion to paclitaxel, which is the weak link. Therefore, it is important to design nanoparticle clusters in which adhesion to the drug is increased to prevent premature release of the drug. The results also suggest that the force microscopy technique can be used to rank the adhesion between different species of drug nanocomposites that are being developed to treat breast cancer and other forms of cancer. The presence of thiols has been shown to significantly increase the adhesive forces between gold and the molecular recognition units or the drug systems.

Finally, chapter six explores the development of prodigiosin-loaded microparticles that are injectable for localized drug delivery in the treatment of cancer. The study reveals that porous PG-loaded PLGA microspheres were formed through a single solvent emulsion evaporation technique. These microspheres have relatively high and similar drug encapsulation efficiency to

PT-loaded PLGA microspheres. These particles are very effective for the localized release of a biosynthesized anticancer agent (PG) for the treatment of cancer. The results of controlled release of PG from PLGA microparticles were also compared to those of PT-loaded PLGA microparticles. The results also showed that initial release of PG at a controlled localized rate from the microparticles within a period of 192 hours have great potential for the treatment of cancer. In addition, the microparticle sizes and the drug release characteristics are greatly influenced by the homogenizing speed and also by the PVA concentrations.

7.2 Suggestions for Future Work

To further extend the work that has been presented in this dissertation, the following future directions are suggested.

7.2.1 Biosynthesized Magnetite Nanoparticles for Early Cancer Detection and Treatment

Further research is needed to determine the optimal concentration of BMNPs from DLS measurements with clinically relevant diameters for the detection and treatment of cancer. Also a deeper understanding of the reaction mechanisms involved in the formation and functionalization of BMNPs is required. In addition, there is a need to explore the effectiveness of the ligand conjugated BMNPs in the targeting of diseased cells under *in-vitro* and *in-vivo* conditions. In the case of *in-vitro* experiments, additional cell lines are required to ascertain the efficacy of conjugated BMNPs. The *in-vivo* studies will demonstrate the experimental results that showed how biosynthesized nanoparticles enter and accumulate in the breast cancer cells as a function of particle size and exposure time using an animal model.

Considering the use of BMNPs for early breast cancer detection, future work is also needed to study the interaction between BMNPs-LHRH and breast cancer cells/tissue or normal breast cells. MRI experiments on the healthy tissue and tumor with/without nanoparticles in this case will give specific insights of the potentials of BMNPs with respect to CMNPs. This comparison will be important to demonstrate the efficiency of BMNPs-LHRH as specific MRI contrast agents for breast cancer. That is to say, MRI studies are essential and should be conducted on live animals, before and after injection of BMNPs-LHRH. This will provide more convincing evidence for the efficacy and the potential side effects associated with the role of BMNPs as MRI contrast agents.

Finally, future work is very necessary in exploring the efficacy of other molecules/antibodies or peptide to functionalize BMNPs. These efforts will complement in targeting of other types of cancer such as prostate or brain cancer. A combination of thermodynamic and kinetic models is also needed to model the transport of the individual nanoparticles and nanoparticle clusters into cancer and non-cancer cells. This approach will consider the changes in surface and elastic energies, as well as the entropic changes associated with the recoiling of the receptors during the entry of nanoparticle clusters into the cells. Further research is also clearly needed to demonstrate the efficacy of the BMNPs for cancer treatment. This is possible by making a cocktail of nanoparticles (Mixture of BMNPs, gold nanoparticles drugs and MRU's) with drug for localized drug delivery in the treatment of cancer. Subjecting the BMNPs to an external magnetic field during *in-vitro* and animal experiments will increase the heat of the nanoparticles thereby heating up the surrounding cancer cells by regional hyperthermia.

7.2.2 AFM Adhesion Measurement for Cancer Detection and Treatment.

Future work is seriously needed in the use of the AFM adhesion method to establish the generality of this technique for rapid screening (RS) of ligand-conjugated nanoparticles. This RS technique can be used as specific targets in early detection and treatment of other types of cancer. Similar approaches can also be applied to target other diseased cells with over-expressed ligand receptors on their membranes.

Furthermore, the force microscopy measurements could be developed to enhance the detection of breast cancer cells in biopsy samples based on adhesion differences. It could be interesting to study cancer cells versus normal cells at different stages of breast, cervical and prostate cancer to elucidate how their adhesion properties differ at a nanoscale level with drugs, MRUs and nanoparticles. In this way, a better understanding of the configuration of materials that is needed for the early detection and treatment of cancer will be achieved. The adhesion studies presented in chapters 4 and 5 were carried out in the absence of aqueous conditions that exist *in vivo*. It would be interesting to check the influence or effect of aqueous conditions on the adhesion forces obtained using the AFM technique.

Finally, there is a need to study the possible use of cocktail of magnetite nanoparticles, gold nanoparticles and different types of cancer drug in the development of future methods for detecting and treating breast cancer. This could provide the basis for the future development of synergistic cancer diagnosis and treatment strategies. Such advancement can be achieved by exploring the interactions between laser beams and nanoparticle clusters that can contain different types of cancer drugs, nanoparticles and molecular recognition units.

7.2.3 Drug Polymer for Localized Drug Delivery in the Treatment of Cancer

Future work is clearly needed to explore the efficacy of PG-loaded PLGA microparticles as a replacement for PT-loaded PLGA microspheres under *in-vivo* conditions. This is important because these particles could significantly reduce the cost of treatment. Further work is also

needed to demonstrate the performance of the encapsulated PG microparticles with additional cancer cell lines and also under *in-vivo* conditions. The suggested studies will explore the localized release of cancer drug (PG) within a controlled rate as well as environments that mimic the human body system.

Finally, the purity of the prodigiosin drug used should be enhanced in future studies. This can be done by combining different methods of prodigiosin purification. A study of the possible cytotoxicity the PG-loaded microparticles/microspheres is also needed to determine their limitations in the treatment of cancer.